Estimating Earth's temporal gravity field from GRACE observations: Mitigation of thermal errors and the interplay between orbital characteristics, basis functions and spatial resolution

Rebecca McGirr

A thesis submitted for the degree of
Doctor of Philosophy of
The Australian National University

March, 2022

Declaration

This thesis is an account of research undertaken between February 2018 and March 2022 at The Research School of Earth Science, College of Science, The Australian National University, Canberra, Australia.

To the best of my knowledge, except where acknowledged, the material presented in this thesis is original and has not been submitted in whole or part for a degree in any university.

Rebecca McGirr

March, 2022

Acknowledgements

First and foremost, I would like to express my sincerest appreciation to my supervisor, Professor Paul Tregoning. Firstly, I'm very grateful for his willingness to take me on as a PhD student having no prior knowledge of geodesy. Building my knowledge to the point that I could produce this body of work took a significant time commitment from Paul over the last four years. I'm very aware that finding a suitable supervisor can be the luck of the draw; as such, I feel fortunate to have found such a supportive supervisor and mentor in Paul. Thank you for encouraging me and having confidence in my abilities when I had little.

I would also like to thank my supervisory panel, Dr Simon McClusky, Dr Herb McQueen and Professor Matt King at the University of Tasmania. Thank you for providing me with the necessary direction and reminding me of the big picture.

I'm also highly grateful to my colleagues within the GRACE group at RSES. I would specifically like to thank Dr Anthony Purcell and Dr Herb McQueen for their scientific direction, help to edit my manuscripts and assistance with Terrawulf. Also, thank you to my old colleagues, Dr Sebastian Allgeyer and Dr Julia Pfeffer.

To the late Leanne Armand, thank you for your mentorship during the beginning years of my research program. You reminded me of the bigger picture and were an unbiased sounding board when I was unsure of my career trajectory. You were such an inspiration to me and other early career researchers. Your advocacy for women in science influenced me to embark on the path of academia, and for that, I am incredibly grateful.

I would also like to specifically thank Nicky Wright, Jess Hargreaves, Sarah Jackson, Tharika Liyanage, Lu Alvarez and Mahdiyeh Razeghi. Thank you for the endless venting sessions and for always being available for a chat or a drink when I needed it. Thank you to the broader RSES community for making my time at ANU as a graduate student as enjoyable as it could be.

Finally, thank you to my family and friends. Specifically, to my partner Harry for supporting my move to Canberra even though it meant being apart for the last four years. Thank you to my parents for their love and encouragement and their sacrifices for my education. I hope I have made you proud.

Abbreviations

ACC	Accelerometer
AHK	Accelerometer Housekeeping
AMOC	Atlantic Meridional Overturning Circulation
ANU	Antarctic Circumpolar Current
AOD	Atmosphere Ocean De-aliasing
AIS	Antarctic Ice Sheet
ANU	Australian National University
CHAMP	CHAllenging Minisatellite Payload
CSR	Centre for Space Research
DLR	German Aerospace Centre
ENSO	El Niño Southern Oscillation
EWH	Equivalent Water Height
FFT	Fast Fourier Transform
GEBCO	General Bathymetric Chart of the Oceans
GFZ	German Research Centre Geosciences
GIA	Glacial Isostatic Adjustment
GIS	Greenland Ice Sheet
GLDAS	Global Land Data Assimilation System
GNSS	Global Navigation Satellite System
GNV	GPS Navigation
GMSL	Global Mean Sea Level
GOCE	Gravity and steady-state Ocean Circulation Explorer
GPS	Global Positioning System
GRACE	Gravity Recovery and Climate Experiment
GRACE-FO	Gravity Recovery and Climate Experiment Follow-On
ICRF	International Celestial Reference Frame
IERS	International Earth System and Rotation Service
ITRF	International Terrestrial Reference Frame

IPU	Instrument Processing Unit
JPL	Jet Propulsion Lab
KBR	K/Ka-Band Ranging System
LGM	Last Glacial Maximum
LRI	Laser Ranging Interferometer
Mascon	Mass concentration element
MCF	Minimum-Cost Flow
MWI	Microwave Instrument
NADW	North Atlantic Deep Water
NASA	National Aeronatauics and Space Administration
OBP	Ocean Bottom Pressure
ONERA	Office National d'Études et de Recherches Aérospatiales
PODAAC	Physical Oceanography Distributed Active Archive Center
RMS	Root Mean Square
SCA	Star Camera Assembly
SDS	Science Data System
SLR	Satellite Laser Ranging
SMOS	Soil Moisture Ocean Salinity
SNR	Signal-to-Noise Ratio
SU	Sensor Unit
SVD	Singular Value Decomposition
TWS	Terrestrial Water Storage
USO	Ultra-Stable Oscillator
XBT	eXpendable BathyThermongraph

Abstract

The Gravity Recovery and Climate Experiment (GRACE) mission measured the combined effect of the Earth's static and time-variable gravity fields globally and near-continuously over 15 years at unprecedented accuracy. Launched in 2002, the GRACE mission used a unique low-Earth orbit satellite-to-satellite tracking mission design. The time-variable gravity field is influenced by the movement of masses within the hydrosphere and the solid Earth. By directly monitoring mass balance changes due to flood, drought, groundwater extraction, ocean circulation, ocean mass increase and ice mass loss, results from the GRACE mission have increased understanding of the impacts of human activity, natural variation and climate change.

The accuracy of GRACE estimates of the time-variable gravity field and the associated mass anomaly time series is affected by several factors. These include orbital characteristics, quality of the observations and background forcing models and the processing strategies used for precise orbit determination and temporal gravity field estimation. This study aims to improve GRACE-based estimates of the time-variable gravity field to analyse mass anomalies by mitigating measurement errors and optimising the choices of processing strategies.

The precise calculation of GRACE satellite orbits is reliant on knowledge of accurate non-gravitational forces acting on the spacecraft. Optimal performance of the accelerometers requires a highly stable thermally controlled environment which was not maintained throughout the mission. In this study, I developed pre-processing and calibration strategies to account for thermally-induced errors in the non-gravitational acceleration measurements. Accurate time-variable gravity models could then be estimated from GRACE data even in the presence of thermally-induced error.

Some mathematical form, or basis function, must be assumed to parameterise the temporal gravity field on the surface of Earth. The choice of the inter-satellite observation and basis functions can also improve the recovery of the gravity field by better localising the mass variations. This study demonstrates how mass concentration (mascon) tiles can reduce signal leakage and intra-mascon variability (the variations of mass change signals within a mascon). I identified the optimal mascon parameterisation through simulation,

subsequently used to generate the ANU GRACE mass anomaly time series. Improved localisation of the mass variation signals was achieved using the range acceleration as the inter-satellite observation rather than the conventional approach of using range rate observations.

The GRACE processing strategies chosen to optimise the accuracy of the temporal gravity solutions tend to be used – without change – across the mission's duration. However, as the geometry of the orbits of the twin spacecraft vary throughout the mission, the ability of the observations to recover high-frequency spatial signals also varies. Through simulation, I assessed the impact of the changing orbital elements on the spatial resolution of the GRACE mascon solutions as a function of altitude and ground track density. With appropriate regularisation, mascons as small as $\sim$150 $\times$ 150 km yield the most accurate solutions even during periods of orbit resonance. Under realistic simulation conditions, the temporal gravity field solutions are significantly improved with decreased orbit altitude.

Many components of my work have been implemented into the ANU GRACE software, including pre-processing and calibration strategies that account for thermally-induced errors in the accelerometer measurements, filtering to mitigate high-frequency inter-satellite range acceleration noise, protocols to create mascon grids and the iteration procedure used to generate the ANU GRACE mass anomaly estimates. The results show substantial seasonal variations, ice sheet mass loss and global mean sea level increase consistent with previous studies.

Contents

List of Figures

List of Tables

Chapter 1

Introduction

Short-term changes in the strength of Earth's gravity field are caused mainly by changes in the distribution of water, snow and ice across the Earth. The time-variable gravity field is influenced by the movement of masses within the Earth's hydrosphere, including the atmosphere, cryosphere, oceans, surface and subsurface land hydrology (i.e. lakes and rivers, soil moisture, groundwater), and within the solid Earth due to seismic deformation and glacial isostatic adjustment (GIA). Satellite gravity missions remotely sense the combined effects of Earth's static and time-variable gravity field. Results from these missions have led to an increased understanding of the impacts of human activity, natural climate variation and climate change on the Earth's hydrosphere (e.g. Rodell et al., 2018; Tapley et al., 2019).

Launched in March 2002, the Gravity Recovery and Climate Experiment (GRACE) mission measured the effect of the Earth's time-variable gravity field globally and near-continuously, over 15 years (Tapley et al., 2004). The GRACE mission achieved this at an unprecedented accuracy using a unique low-Earth orbit satellite-to-satellite tracking mission design (Figure 1.1). The twin satellites were each equipped with a K/Ka-Band Ranging (KBR) system that detected changes in the relative distance between the satellites with sub-micrometre precision, providing the fundamental measurement to produce high fidelity temporal gravity field models. The scientific payload of each of the GRACE satellites included GPS receivers and a dual star camera assembly for attitude and orbital control, and a three-axis electrostatic accelerometer. Along with the KBR, these instruments provided the measurements necessary for precise orbit and gravity field estimation.

The GRACE mission ended in October 2017 after years of reduced operation to extend the mission's longevity despite power constraints. Having been recognised as a scientific priority (NASEM, 2018), the monitoring of Earth's mass variations was continued with the launch of the GRACE Follow-On (GRACE-FO) mission in May 2018 (Tapley et al., 2019). The GRACE-FO satellites were modelled on their predecessor, but with the addition of a

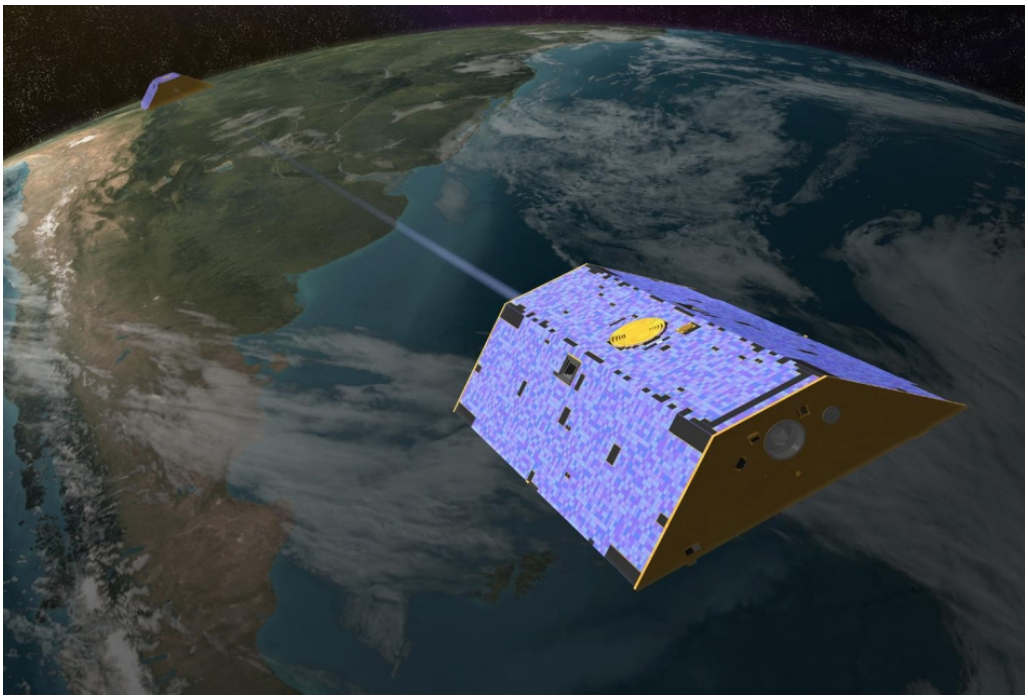

Figure 1.1: Artists impression of the mission concept of the Gravity Recovery and Climate Experiment (GRACE) (source: NASA, JPL)

Laser-Ranging Interferometer (LRI) which measures with significantly improved precision the inter-satellite range using a laser link in parallel with the microwave instrument (Sheard et al., 2012; Abich et al., 2019).

GRACE and GRACE-FO models of the time-varying gravity field are typically produced with monthly temporal resolution and ∼300 km spatial resolution (Tapley et al., 2004, 2019). However, the accuracy of individual GRACE and GRACE-FO solutions of the time-variable gravity field and the associated time-series of mass variations are affected by several factors. These include the altitude of the satellites and their ground track pattern; the precision and accuracy of the observations, being the fundamental measurement of the inter-satellite distance but also the quality of the non-gravitational acceleration observations and performance of the attitude and orbital control system on-board each satellite; the quality of the background forcing models which necessitate the identification of orbit perturbations induced by the static gravity field, solid Earth anomalies, ocean tides, atmosphere and planetary bodies; and the processing strategy used for GRACE and GRACE-FO analysis for precise orbit determination and temporal gravity field estimation.

The precise calculation of GRACE and GRACE-FO satellite orbits is reliant on knowledge of accurate non-gravitational accelerations acting on the spacecraft. Optimal performance of the accelerometers requires a highly stable and thermally controlled environment

for the instruments on-board the satellites (Touboul et al., 1999). Thermal control was not maintained in the latter part of the GRACE mission due to power constraints, degrading the quality of accelerometer observations (Tapley et al., 2015). These thermal effects must be accounted for in a pre-processing step and/or calibrated during orbit and gravity field estimation (e.g. Klinger and Mayer-Gürr, 2016). Without adequate mitigation of thermal noise in the accelerometer observations, the calculated satellite orbits contain errors that may propagate into the temporal gravity field estimates.

Some mathematical form, or basis function, must be assumed to parameterise the temporal gravity field on the surface of Earth. Traditionally, the temporal gravity field has been represented using spherical harmonics (e.g. Lemoine et al., 2007; Save et al., 2012). These solutions contain significant north-south striped errors that must be mitigated using filtering (e.g. Swenson and Wahr, 2006; Kusche, 2007). However, filtering increases signal leakage and attenuation, which has led to the development of various signal restoration and scaling techniques (Chen et al., 2009a; Landerer and Swenson, 2012). More recent analysis approaches have represented the temporal gravity field using different basis functions by dividing the surface of the Earth into regular regions (e.g. Rowlands et al., 2005; Watkins et al., 2015). These basis functions are called mass concentration elements (mascons). The estimated mass change is the change in the height of water across the mascon required to cause the observed orbit perturbation.

The use of mascons in temporal gravity field estimation from GRACE observations has demonstrably improved signal recovery and reduced north-south striping errors compared to spherical harmonic solutions (e.g. Rowlands et al., 2010; Save et al., 2016). Mascons can better localise the spatial fluctuations in the temporal gravity field. However, leakage of signal across hydrological boundaries and coastlines, referred to as "intra-mascon leakage", remains problematic (Loomis et al., 2021). In addition, regularisation is utilised to improve the misappropriation of signals and reduce estimation errors by constraining the mascon parameter adjustments (e.g. Save et al., 2016; Loomis et al., 2019a). Inappropriate regularisation constraints result in signal attenuation or increased noise in the mascon estimates; thus, developing a regularisation strategy that manages these trade-offs presents a significant challenge.

The GRACE and GRACE-FO inter-satellite ranging measurements contain information on the subtle variations in Earth's gravity field caused by the redistribution of mass on Earth. Traditionally, temporal gravity field models from GRACE and GRACE-FO

measurements use range rate as the inter-satellite observation (e.g. Tapley et al., 2004; Bruinsma et al., 2010; Watkins et al., 2015; Loomis et al., 2019a). Numerical differentiation of the range rate creates the range acceleration inter-satellite observation, which amplifies the short-wavelength signals. Consequently, compared to range rate, the range acceleration contains amplified high-frequency noise and decreased power in the long-wavelength signals, which may degrade the quality of the temporal gravity field estimates. A potential advantage of using the range acceleration as the inter-satellite observation is the improved localisation of the mass variation signal compared to the range rate (Save et al., 2012). Thus, the choice of the inter-satellite observation, the temporal gravity field parameterisation and regularisation can improve the recovery of the gravity field.

Both GRACE and GRACE-FO missions were launched to an altitude of ∼490 km. As the geometry of the orbits of the GRACE twin spacecraft varied throughout the mission, so too did the ability of the observations to recover high-frequency spatial signals. The GRACE satellites descended to an altitude of ∼320 km by the end of the mission. Because gravitational signal fluctuations attenuate with distance from the source, the potential spatial resolution of the GRACE data should increase as the altitude of the satellites decreases. However, instrument noise due to internal thermal variations was also highest towards the end of the GRACE mission. As the satellites descended, they passed through periods of orbit resonance (Wagner et al., 2006; Visser et al., 2012; Klokočník et al., 2015). During orbit resonance, the satellites repeatedly observed the same strips of Earth's gravity field, reducing the spatial resolution of the temporal gravity field model that can be accurately estimated (Wagner et al., 2006). Consequently, the spatial resolution that can be achieved month-to-month using GRACE data is impacted by satellite altitude, instrument noise and orbit resonance.

Estimates of the Earth's temporal gravity field computed from GRACE and GRACE-FO measurements have provided the observations necessary to make significant scientific advances in our understanding of many aspects of Earth's dynamic systems. In particular, GRACE and GRACE-FO observations have tracked changes in ice sheets and glaciers (e.g. Velicogna and Wahr, 2006; Tapley et al., 2019), terrestrial water storage (TWS) (e.g. Chen et al., 2010a; Rodell et al., 2018), sea level and ocean dynamics (e.g. Landerer et al., 2015; Chambers et al., 2017), GIA (e.g. Riva et al., 2009; Tregoning et al., 2009a) and large-scale earthquake deformation near-continuously since 2002 at a global scale (e.g. Han et al., 2006; Panet et al., 2018). In the following sections, I provide an overview of some of the most

significant contributions of GRACE and GRACE-FO observations to the advancements of each of these scientific fields.

1.1 Monitoring Earth's water using GRACE and GRACE-FO data

1.1.1 Ice sheets and glaciers

Modern-day ocean and atmospheric warming driven by anthropogenic climate change has led to a sharp decrease in the size and extent of Earth's ice sheets and glaciers globally (Tapley et al., 2019). The resultant increase in meltwater and ice discharge from continental ice masses is one of the primary drivers of recent global mean sea level rise (Tapley et al., 2019). The GRACE mission achieved the first direct ice sheet and glacier mass balance measurements. Before GRACE, ice sheet and glacier variability measurements were limited to observations of ice height from radar (ERS-1/2, Envisat and CryoSat) and laser (ICESat 1/2) satellite altimetry. Estimates of meltwater and ice discharge contributions to global mean sea level from altimetry require assumptions about GIA and variable surface layer densities (i.e. snow, firn compaction). Alternatively, the components of ice sheet mass change (i.e. ice discharge, snow accumulation and surface ablation) can be computed using the input-output method, which utilises information from interferometric synthetic aperture radar (InSAR) and regional atmospheric climate models (e.g. Rignot et al., 2008, 2011, 2019). Recent studies have used a combination of these three independent techniques to produce an ensemble estimate of ice sheet and glacier mass balance (e.g. Shepherd et al., 2012, 2018b, 2020).

GRACE and GRACE-FO observations of the Earth's temporal gravity field have led to significant advancements in understanding modern ice sheet and glacier mass balance. One of the advantages of satellite gravimetry for deriving ice sheet and glacier mass change estimates is that, unlike other methods, the mass estimates are not reliant on the accuracy of regional atmospheric climate models (e.g. Fettweis et al., 2013; Van Wessem et al., 2014). Uncertainties are introduced into GRACE/GRACE-FO-derived estimates when accounting for poorly constrained GIA-induced mass change, which is the primary reason for large errors, particularly in Antarctica (Velicogna and Wahr, 2006; Argus et al., 2014b). The reliability of ice sheet and glacier mass balance estimates continues to increase with more accurate GIA and climate models, improved data processing and analysis techniques,

including by the combined analysis of various mass balance estimates (Shepherd et al., 2018b; Tapley et al., 2019).

1.1.1.1 Antarctic Ice Sheet

The Antarctic Ice Sheet (AIS) is the largest reservoir of fresh water on Earth. Within the first three years of the GRACE mission, significant mass loss trends were detected in West Antarctica in the Amundsen Sea Sector, which contains the Pine Island and Thwaites glaciers (Velicogna and Wahr, 2006; Chen et al., 2006) (Figure 1.2). West Antarctic mass loss trends dominated AIS mass balance throughout the entire GRACE/GRACE-FO record, becoming more robust with time and with improved processing and analysis techniques (Tapley et al., 2019). The mass imbalance in West Antarctica is driven by a decrease in the thickness and extent of ice shelves caused by rising sea surface temperatures in the Amundsen Sea, triggering increased land ice velocity discharge and retreat of marine grounding lines (Shepherd et al., 2018a). Inter-annual mass accumulation fluctuations in West Antarctica over the GRACE period have been shown to correlate well with El Niño Southern Oscillation (ENSO) related precipitation anomalies (Sasgen et al., 2010). Over the GRACE period (April 2002 to June 2017) Tapley et al. (2019) estimated that the West AIS experienced a mass change of -120 $\pm$ 14 Gt/yr with an acceleration of -7 $\pm$ 2 Gt/yr^2. During this period, West Antarctic mass loss accounted for almost 90% of the -136 $\pm$ 41 Gt/yr total AIS mass loss (Tapley et al., 2019).

Other significant mass loss trends from GRACE and GRACE-FO appear along the Antarctic Peninsula and in the Totten glacier in the Wilkes land sector of East Antarctica (e.g. Ivins et al., 2011; Shepherd et al., 2018b; Velicogna et al., 2020) (Figure 1.2). The Antarctic Peninsula region experienced persistent mass loss throughout the GRACE period until 2016 when anomalously large snowfall caused an increase in mass of 100 Gt, followed by a resumption to mass loss during 2017 which continued into the GRACE-FO period (Van Wessem et al., 2016; Velicogna et al., 2020). In Wilkes Land, GRACE and GRACE-FO observations have recorded a significant mass loss trend from 2010 due to the retreat of the Totten and other nearby glaciers. Observations from GRACE and GRACE-FO mass balance of the wider East AIS suggest that mass gains have offset the mass loss associated with the Totten glacier due to the accumulation of snow in Queen Maud Land (Velicogna et al., 2020) (Figure 1.2). However, estimates of mass balance change in East Antarctica are of relatively low confidence compared to the rest of Antarctica due to inaccuracies in

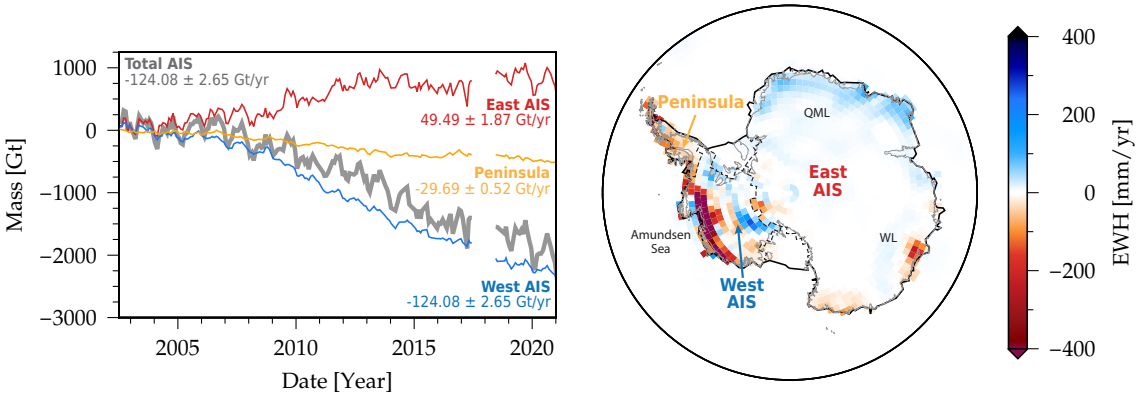

Figure 1.2: Model of Antarctic Ice Sheet (AIS) mass change. (left) Time series of anomalous West AIS (blue), East AIS (red) Antarctic Peninsula (yellow) and total AIS (grey) mass from GRACE and GRACE-FO mascon solutions (Loomis et al., 2019a) and (right) GRACE mascon trend solution (Loomis et al., 2021). Queen Maud Land (QML); Wilkes Land (WL).

the GIA models (Shepherd et al., 2018b).

A discernible trend of mass accumulation appeared in Queen Maud Land between 2009 and 2010 in the GRACE time series (Boening et al., 2012a; Velicogna et al., 2020) (Figure 1.2). From 2009 to 2020, Queen Maud Land has seen a cumulative mass increase of ∼89 Gt/yr (Velicogna et al., 2020), this trend was initiated by a large snowfall event of 300 Gt in 2009 and again in 2011 (Boening et al., 2012a). Evidence from ice core data and global atmospheric models indicated that snowfall has increased in Queen Maud Land by 25% since 1980 compared to the pre-industrial mean (Medley et al., 2018), which has been linked to the last decade of significant mass accumulation (Velicogna et al., 2020). The GRACE record of mass change in Queen Maud Land prior to 2009 has a mean mass change statistically indistinguishable from zero, despite significantly increased snowfall occurring since 1980 (Velicogna et al., 2020). The upward trending snowfall in East Antarctica is predicted to continue and has been linked to rapid atmospheric warming (Medley et al., 2018). A deceleration of Antarctic mass loss occurred after 2016 due to increased snowfall in parts of East Antarctica and the Antarctic Peninsula, which partly compensated for the continued rapid mass loss in West Antarctica (Velicogna et al., 2020).

Accelerated mass loss in Antarctica was seen in the GRACE-FO data analysis, following the decelerated mass loss towards the end of the GRACE period (Velicogna et al., 2020) (Figure 1.2). GRACE-FO Antarctic mass balance observations were found to be consistent with external mass change estimates, providing high confidence that the GRACE and GRACE-FO time series are consistent, despite the almost year-long data gap (Velicogna et al., 2020; Landerer et al., 2020; Sasgen et al., 2020). Although mass accumulation

in Queen Maud Land is substantial, the GRACE and GRACE-FO records of integrated Antarctic mass balance are dominated by rapid mass loss.

1.1.1.2 Greenland Ice Sheet

The second largest freshwater reservoir on Earth, the Greenland Ice Sheet (GIS), is highly dynamic due to its seasonal cycles of mass loss (meltwater runoff and ice discharge) and accumulation (Figure 1.3). However, thinning along the periphery of the Greenland ice sheet has been observed for many decades (Kjeldsen et al., 2015) (Figure 1.3). Before GRACE, Greenland mass balance could be estimated indirectly using a variety of measurements and models by converting changes in airborne radar and satellite laser altimeter-measured surface elevations into mass change rates (e.g. Krabill et al., 2004; Thomas et al., 2006; Kjeldsen et al., 2015). A clear mass loss trend was observed early in the GRACE mission (Figure 1.3). Less than two years of monthly GRACE spherical harmonic solutions revealed that the GIS was losing mass at a rate of -82 $\pm$ 28 Gt/yr (Velicogna and Wahr, 2005), consistent with estimates from alternate methods (e.g. Krabill et al., 2004).

During the GRACE record (April 2002 to June 2017), the GIS has lost mass at a rate of -258 $\pm$ 26 Gt/yr and contributed $\sim$1 cm to global mean sea-level rise, more than twice that of the AIS (Tapley et al., 2019) (Figure 1.3). GIS mass loss is concentrated along the Southeast and West coasts, with the highest magnitude of mass loss centred on the Jacobshavn Glacier in the Southwest (Luthcke et al., 2006b; Tapley et al., 2019). Accumulation of mass in the centre of the ice sheet has been observed over the GRACE record, which has been attributed to the millennial-scale deceleration of ice flow at the interior of the ice sheet (MacGregor et al., 2016) (Figure 1.3).

Accelerated Greenland mass loss between 2003 to 2012 was seen in GRACE analysis, while the remainder of the GRACE period was characterised by decelerated mass loss (Sasgen et al., 2020). Alternative methods (i.e. altimetry and input-output) estimated that the mass loss trend was significantly reduced relative to the GRACE-derived rate during the gap between GRACE and GRACE-FO missions, with a return to high melt rates recorded by GRACE-FO from mid-2019 (Velicogna et al., 2020; Landerer et al., 2020; Sasgen et al., 2020). Using a combination of mass balance estimates derived from GRACE and GRACE-FO, satellite altimetry and the input-output method, most GIS mass loss was attributed to increased surface melt ($\sim$66%). The remaining portion ($\sim$33%) was attributed to increased ice discharge (Van den Broeke et al., 2009; Rignot et al., 2011;

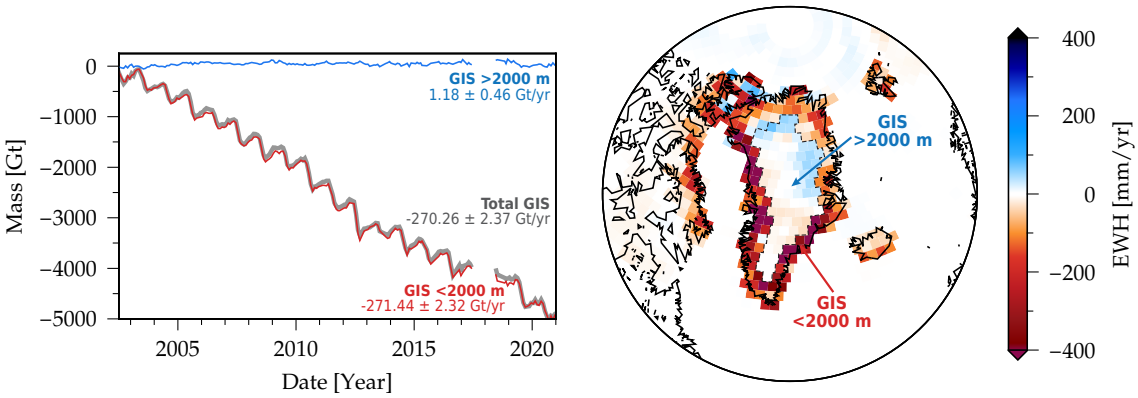

Figure 1.3: Model of Greenland Ice Sheet (GIS) mass change. (left) Time series of of total GIS (grey) mass change and at elevations <2000 m (red) and >2000 m (blue) from GRACE and GRACE-FO mascon solutions (Loomis et al., 2019a) and (right) GRACE mascon trend solution (Loomis et al., 2021).

Sasgen et al., 2020).

Several anomalous GIS melt events have occurred over the GRACE and GRACE-FO record, most notably in 2010, 2012 and 2019, during the Northern Hemisphere summer. Each event set a new record for annual GIS mass loss (Sasgen et al., 2020). The anomalous melt events measured by GRACE in 2010 and 2012, -462 ± 60 Gt/yr and -464 ± 62 Gt/yr, respectively (Sasgen et al., 2020), saw twice the mass loss compared to the annual average of the first half of the GRACE mission (Tapley et al., 2019). Both events have been linked to "Greenland blocking", circumstances which describe a high-pressure feature associated with negative North Atlantic oscillation conditions causing the advection of warm air from mid-latitudes along the west coast of the GIS (Hanna et al., 2014; Sasgen et al., 2020). Anomalously high temperatures along with decreased summer cloud cover led to increased melt production, further amplified by the reduced surface albedo of the GIS (Hanna et al., 2014; Sasgen et al., 2020). During 2019, observations from GRACE-FO indicated an annual mass loss of -532 ± 58 Gt/yr, 15% more negative than the previous record year of 2012 (Sasgen et al., 2020). Similar atmospheric conditions to 2010 and 2012 were linked to the anomalous 2019 melt (Sasgen et al., 2020).

1.1.1.3 Other glaciers and ice caps

Given their global coverage, the GRACE and GRACE-FO satellites have also successfully monitored the mass balance of many other major glaciers and ice caps. Although spatially small relative to the Antarctic and Greenland ice sheets, these glaciers and ice caps produce mass change signals readily observable by GRACE and GRACE-FO due to their high-

magnitude seasonal dynamics and, in many cases, rapid mass loss (Tapley et al., 2019). In fact, despite their size, glaciers were the most significant contributors to increased sea level mass during the twentieth century (Church et al., 2013). Over the GRACE era (April 2002 to August 2016), glaciers lost mass at a rate of 199 ± 32 Gt/yr globally, accounting for a total 8 mm sea level rise over 14 years (Wouters et al., 2019). Before GRACE, some larger regions such as glaciers in the Gulf of Alaska coast and Ellesmere and Baffin Islands in the Canadian Arctic Archipelago were monitored by satellite radar and airborne laser altimetry (e.g. Arendt et al., 2002). For these regions, mass balance estimates derived from altimetry were verified by GRACE-based estimates soon after mission launch (e.g. Tamisiea et al., 2005).

Outside of Greenland and Antarctica, the most notable mass loss trends have been quantified using GRACE observations in the Canadian Arctic Archipelago (Wouters et al., 2008; Gardner et al., 2011), the Gulf of Alaska coast (Tamisiea et al., 2005; Luthcke et al., 2006b) and the Patagonian ice fields (Ivins et al., 2011; Chen et al., 2007; Willis et al., 2012). GRACE-derived mass trends of these regions have been verified against estimates from satellite altimetry and surface mass balance models, amongst other methods (e.g. Gardner et al., 2011; Willis et al., 2012; Arendt et al., 2013; Lenaerts et al., 2013). Over the GRACE record, ice mass loss driven by continued warming of the climate in the Canadian Arctic Archipelago and the Gulf of Alaska coast appears most severe. In these regions, GRACE data has revealed mass loss trends of -74.6 ± 4.1 Gt/yr and -62.6 ± 8.2 Gt/yr, respectively, over 14 years (April 2002 to March 2016) (Rodell et al., 2018). Over the same period, a significant mass loss trend of -25.7 ±5.1 Gt/yr was observed in the Patagonian ice fields, which, with increased atmospheric warming, is likely to continue until these ice fields completely disappear (Rodell et al., 2018).

Before GRACE, mass balance trends for smaller ice-covered regions were more challenging to obtain due to their relatively small size and complicated topography and, therefore, lack of observations with adequate spatial and temporal coverage (Jacob et al., 2012; Gardner et al., 2013). Most estimates of mass balance trends for many of these smaller glaciers and ice caps were derived from the extrapolation and aggregation of in situ geodetic and glaciological measurements (e.g. Cogley, 2009). This method produced inaccurate estimates that suggested increased mass loss of many glaciers, a significant bias that was only made apparent once GRACE observations of mass change (supported by altimetry estimates) became available (Gardner et al., 2013). More than ten additional glaciated

regions, apart from those already mentioned in this section, have seen significant mass loss trends derived from GRACE measurements, including Svalbard, Iceland (Wouters et al., 2008) and others (Jacob et al., 2012; Gardner et al., 2013).

1.1.2 Sea level and ocean dynamics

Multiple physical processes influence sea level rise. Ocean warming and freshening cause thermosteric (thermal) and halosteric (salinity) volumetric expansion, respectively, while the transfer of continental water and ice discharge into the ocean causes mass increase. Before satellites, measurements of global sea level could only be estimated from the global network of tide gauges, which are unevenly distributed around the globe and need to be corrected for vertical land motion (e.g. Chambers et al., 2002). Measurements of global sea level have become significantly more reliable with the inception of satellite radar altimetry. Altimeter observations of global sea-surface height date back to 1992 with the TOPEX/Poseidon mission launch and have continued to the present-day with observations from three generations of the Jason mission series. Over the altimeter era, global sea-level has risen $\sim$2.9 $\pm$ 0.4 mm/yr and accelerating at 0.084 $\pm$ 0.025 mm/yr^2 (1993 to 2017) (Nerem et al., 2018). The individual components that contribute to this rise are observed by GRACE/GRACE-FO (ocean mass change) and the global array of Argo profiling floats (steric expansion), which achieved near-global coverage in late 2007 (Riser et al., 2016). The steric component of sea level is driven by density variations, primarily due to temperature and salinity, the latter of which is only a small contributor to modern changes in global mean sea level (GMSL) (Llovel et al., 2019). Only when the time series of all three global observation systems overlap can the individual contributing components to global sea level be reliably assessed.

1.1.2.1 The global sea level budget

The closure of the global sea level budget is achieved when observations of ocean mass, thermosteric and halosteric sea level sum to equal measurements of total sea level. Budget closure indicates that the individual components that contribute to sea level accurately represent the source of sea level change (Figure 1.4). Before GRACE, the ocean mass component of sea level could only be inferred indirectly by subtracting Argo-measured steric expansion from the total sea level measured by altimetry (Willis et al., 2004). Chambers et al. (2004) was the first to estimate ocean mass change using early iterations of GRACE

spherical harmonic data products. Their estimates of GRACE-derived ocean mass seasonal variations were consistent with estimates from steric-corrected altimetry, despite available GRACE solutions of the Earth's gravity field containing significant error at the time (Tapley et al., 2019). GRACE-derived ocean mass estimates, along with hydrographic profiles from Argo, are now routinely used to assess the contribution of individual components to changes in global sea level (e.g. Cazenave et al., 2018).

The ocean is one of the Earth's largest carbon sinks and, therefore, one of the main reservoirs for heat uptake due to rising CO_2 emissions. The availability of GRACE measurements has improved the analysis of some in situ measurements of thermosteric sea level. Before the availability of ocean mass observations from GRACE, biases in thermosteric measurements from Argo floats had been interpreted as actual trends (e.g. Lyman et al., 2006; Domingues et al., 2008; Wijffels et al., 2008). Systematic biases in a subset of Argo floats and some eXpendable BathyThermograph (XBT) data were identified (Willis et al., 2007) when discrepancies were found to exist between in situ measurements of steric sea level change and altimetry measurements corrected for GRACE estimates of ocean mass change (Lombard et al., 2007). These in situ measurements of ocean heat content had previously been interpreted to indicate rapid global cooling of the upper ocean between 2003 and 2005 (Lyman et al., 2006). This correction further perpetuated the importance of GRACE data for closing the global sea level budget.

While hydrographic profiles from Argo provide reliable observations of ocean temperatures, some issues remain due to a lack of sampling in some regions. Argo observations are scarce in shallow seas, beneath ice-covered areas, at latitudes $> 60^\circ$ and $< -60^\circ$ and only sample oceans to depths of 2000 m. GRACE observations of ocean mass, along with altimetry and available in situ measurements, can be used to indirectly measure steric sea level in areas that are not sampled by the Argo network (e.g. Chambers, 2006b; Lombard et al., 2007). For example, using an indirect approach indicated that wind-driven convergence likely caused sustained heat accumulation in the subtropical South Pacific at depths >2000 m, consistent with observations from independent hydrographic transects (Volkov et al., 2017). On a global scale, steric trends at depths >2000 m (i.e. the residual GMSL after correcting altimetry for Argo and GRACE observations) appear to be small and statistically insignificant (Llovel et al., 2014; Volkov et al., 2017). This method of inferring deep ocean steric trends and regional sea level budget closure, while less reliable, is only possible with the availability of ocean mass measurements from GRACE and GRACE-FO.

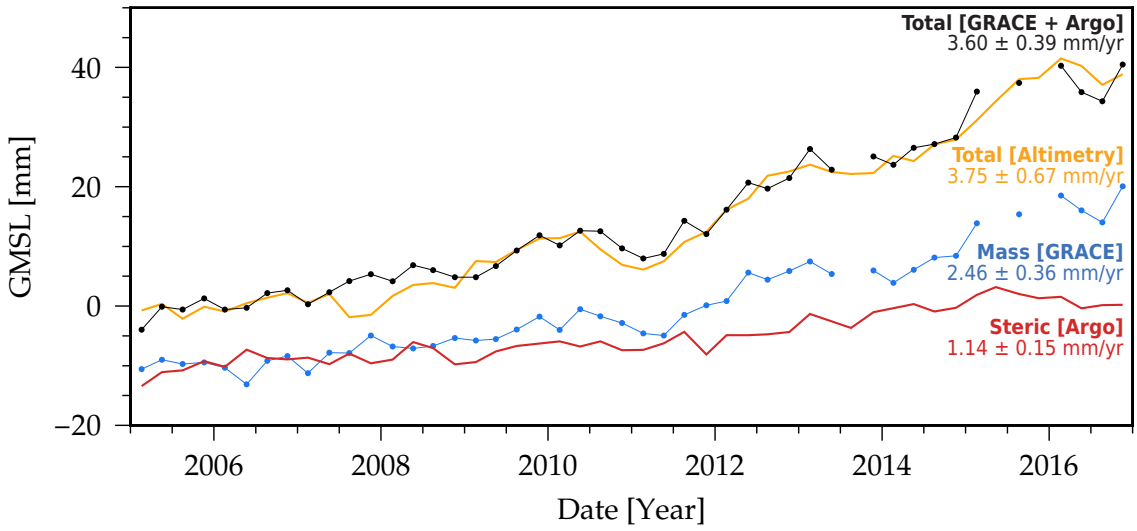

Figure 1.4: Components of the global mean sea level (GMSL) budget. Total observed by satellite altimetry (yellow), ocean mass observed by GRACE (blue) thermosteric from Argo floats (red) and sum of ocean mass (GRACE) and thermosteric (Argo) components (black) from 2005 to 2017. Values represent seasonal (i.e. three-month) means from Chambers et al. (2017) and updated by Tapley et al. (2019).

Over the period 2005 to 2017, global mean sea level increased at a rate of 3.75 ± 0.67 mm/yr according to measurements from satellite altimetry (Figure 1.4) (Chambers et al., 2017; Tapley et al., 2019). GRACE observations of ocean mass indicated that 2.46 ± 0.36 mm/yr of the observed sea level rise was due to mass inflow (Figure 1.4), while hydrographic profiles from Argo indicated that 1.14 ± 0.15 mm/yr was due to thermosteric expansion (Figure 1.4) (Chambers et al., 2017; Tapley et al., 2019). Global mean sea level almost consistently increased over the entire GRACE era; one exception occurred following the transition from El Niño to La Niña conditions from 2010 to 2011, which caused increased precipitation and terrestrial water storage, particularly in regions that had experienced recent intense drought (i.e. Australia, South America and Southeast Asia) (Boening et al., 2012b). The transition from El Niño to La Niña conditions resulted in a ∼5 mm decrease in global mean sea level (Figure 1.4), despite a background level of sea level rise of >3 mm/yr (Boening et al., 2012b). During this period, thermosteric evidence from Argo showed that temperatures remained steady, while observations from GRACE confirmed that the decrease was primarily due to the transfer of mass from oceans onto continents (Boening et al., 2012b).

1.1.2.2 Ocean bottom pressure and ocean circulation

GRACE and GRACE-FO have been used to infer monthly variations in large scale oceanic transport on a near-continuous, global scale (e.g. Chambers et al., 2004; Chambers and Bonin, 2012; Johnson and Chambers, 2013). Changes in ocean circulation can be inferred from Ocean Bottom Pressure (OBP) gradients, being the change in pressure exerted on the seafloor, from which geostrophic bottom currents can be estimated. GRACE-derived OBP gradients have been particularly useful for understanding ocean transport variability in remote locations, where few in situ measurements exist. For example, ocean bottom currents derived from GRACE gravity products have been used to estimate annual and inter-annual variations in barotropic transport of the Antarctic Circumpolar Current (ACC), highly correlated with in situ measurements (Zlotnicki et al., 2007; Bergmann and Dobslaw, 2012). Similarly, annual and inter-annual variations in Arctic Ocean mass have been measured using GRACE-derived OBP which, combined with ocean modelling, made evident that seasonal geostrophic current anomalies and non-seasonal mass variations are largely wind-driven (Peralta-Ferriz et al., 2014).

GRACE and GRACE-FO have provided an opportunity to monitor the changing dynamics of the Atlantic Meridional Overturning Current (AMOC), a significant component of Earth's climate system. In the Northern Hemisphere, the AMOC facilitates surface current heat transfer from the equator, poleward and deep return flow of North Atlantic Deep Water (NADW) via a strong bottom current. Landerer et al. (2015) were able to provide the first measurements of Lower NADW transport from OBP anomalies inferred from GRACE temporal gravity fields using mascons, which have significantly improved signal localisation and separation compared to spherical harmonic gravity products (Watkins et al., 2015). They found that GRACE-derived inter-annual fluctuations are in good agreement with in situ measurements (Landerer et al., 2015). Continued observation of long-term AMOC evolution and its response to climate change will be achievable with observations obtained from GRACE-FO and future space gravity missions (Tapley et al., 2019).

High-frequency components of ocean mass transport are aliased in the monthly GRACE and GRACE-FO temporal gravity field solutions. High temporal resolution (i.e. 10-day) gravity field solutions contain some of these non-seasonal and sub-monthly ocean mass variations, for example, in the south Atlantic Ocean's Argentine Gyre (e.g. Bruinsma et al., 2010; Yu et al., 2018). Using traditional methods, monitoring ocean gyres in polar

regions may be challenging due to the lack of altimetry measurements at high latitudes and sparse in situ records. With increased resolution towards the poles, the GRACE and GRACE-FO temporal gravity field data provide an additional method for monitoring high-frequency ocean circulation. This is evidenced by Yu et al. (2018) who found good agreement between GRACE-derived models of Argentine Gyre circulation and estimates derived from ocean altimetry and numerical models of ocean circulation.

1.1.3 Terrestrial water storage

GRACE and GRACE-FO measure the vertical integration of surface and sub-surface water masses stored as groundwater, soil moisture, surface water, snow and ice. Seasonal and inter-annual variations in terrestrial water storage (TWS) and its separate components have emerged in the GRACE and GRACE-FO temporal gravity field data (Rodell et al., 2018; Landerer et al., 2020). These TWS variations are driven by natural climate and seasonal variability, climate change and direct anthropogenic intervention (Rodell et al., 2018). Global GRACE-derived trends have indicated that water storage is increasing at high and low latitudes due to wetting and decreasing at mid-latitudes due to drying. Drying trends are commonly compounded by an increased reliance on groundwater resources which has led to their over-extraction (e.g. Scanlon et al., 2012).

GRACE and GRACE-FO observations combined with in situ records, remote sensing observations and numerical model output can be disaggregated to quantify the contribution of each component of TWS (i.e. surface water, soil moisture and groundwater storage) to the observed seasonal and inter-annual mass change trends. This has led to better quantification and classification of drought and improved predictions of drought severity and longevity (e.g. Houborg et al., 2012; Thomas et al., 2014). GRACE and GRACE-FO data, combined with auxiliary information, has indicated that groundwater consumption is occurring at an unsustainable rate (e.g. Rodell et al., 2009; Faunt et al., 2016) which is essential knowledge for influencing policy changes and improving water management strategies (Rodell et al., 2018).

1.1.3.1 Drought monitoring

TWS deficits are detected by the GRACE and GRACE-FO satellites, which measure the integrated mass variations in surface water, soil moisture and groundwater storage at a sub-basin scale. GRACE and GRACE-FO observations of TWS, combined with exter-

nal observations and hydrological models, can be disaggregated to quantify characteristics such as severity, extent and duration of hydrological (i.e. surface water), agricultural (i.e. soil moisture) and groundwater droughts. Previous studies have analysed basin-scale drought conditions using GRACE observations of TWS in Southeast Australia (Figure 1.5a) (Leblanc et al., 2009), the Amazon Basin (Chen et al., 2009b, 2010b), Texas (Long et al., 2013), Southern California (Figure 1.5b) (Famiglietti et al., 2011), Southwest China (Long et al., 2014) and the Canadian Prairies (Yirdaw et al., 2008). More recently, GRACE-FO measurements recorded the most severe drought conditions in Central and Western Europe observed over the GRACE and GRACE-FO records (Boergens et al., 2020; Landerer et al., 2020).

Other applications of GRACE-measured TWS have included the development of GRACE-based drought indices (e.g. Thomas et al., 2014) and the integration of disaggregated TWS data (e.g. Houborg et al., 2012) into drought-monitoring tools, which previously included little to no measurements of the subsurface components of TWS (Svoboda et al., 2002). The availability of GRACE TWS observations have greatly improved predictions of drought severity and longevity compared to methods that rely on precipitation data, streamflow data and sparse groundwater and soil moisture observations (Houborg et al., 2012).

The GRACE data recorded the Millennium Drought, one of Australia's most severe and long-lasting droughts, which predominantly impacted the Murray-Darling Basin in Southeast Australia for the better part of a decade (2001 to 2009; Figure 1.5a) (Van Dijk et al., 2013). The Millennium Drought was driven by rainfall deficits and record high temperatures, which led to increased groundwater consumption and depletion (Leblanc et al., 2009). Using GRACE-derived TWS, in situ and modelled hydrological data Leblanc et al. (2009) traced the propagation of the Millennium Drought through the hydrological cycle. They found that the depletion of surface water and soil moisture was rapid, stabilising within the first two years of drought onset, followed by a steady decline in groundwater storage over the remainder of the decade (Leblanc et al., 2009; Van Dijk et al., 2013).

In 2010 the Millennium Drought was broken by heavy rain, followed by severe flooding in 2011 coincident with the onset of La Niña conditions which led to a temporary decline in GMSL (Boening et al., 2012b). A global analysis of GRACE TWS misleadingly indicated that the Murray-Darling Basin in Southeastern Australia is trending wetter due to the transition from severe drought conditions during the first half of the mission into strong La

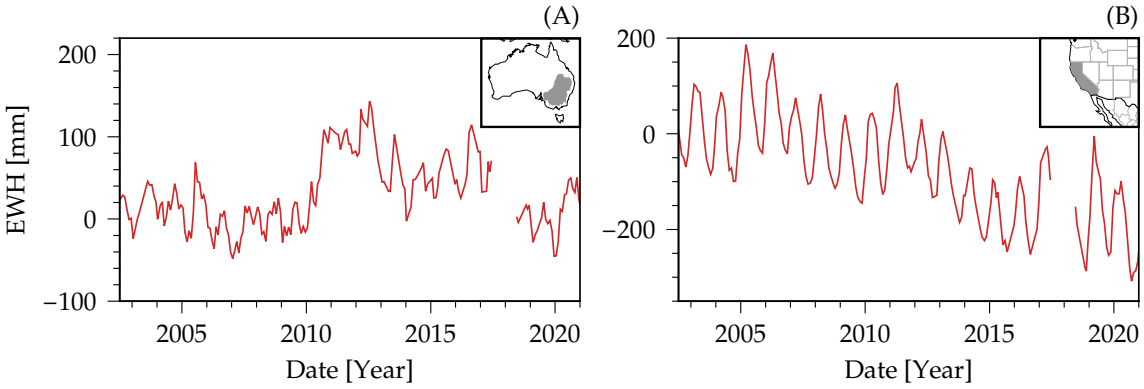

Figure 1.5: Time series of TWS anomalies from GRACE and GRACE-FO mascon solutions (Loomis et al., 2019a) in terms of equivalent water height (EWH), integrated across the (a) Murray Darling Basin, Australia and (b) California.

Niña related precipitation events in 2010 and 2011 (Figure 1.5a) (Rodell et al., 2018). The majority of excess TWS was shed by the end of the GRACE mission as eastern Australia once again entered record-breaking drought conditions during the gap between GRACE and GRACE-FO, culminating in extensive bushfires during Australia's "Black Summer" in 2019-2020 (Wang and Cai, 2020). These extreme drought conditions are reflected in the low TWS values observed during the first two years of GRACE-FO observations, reaching a minimum during the Black Summer, equivalent to the 2007 minimum during the Millennium Drought in the Murray Darling Basin (Fig. 1.5a) (Landerer et al., 2020).

Significant TWS deficits due to severe drought conditions were recorded in GRACE observations in California from 2007 through to the end of the mission (except for a wet 2010 and 2011) (Figure 1.5a) (Famiglietti et al., 2011; Scanlon et al., 2012). Precipitation and surface water deficits, predominantly due to reduced snowfall in the adjacent Sierra Nevada ranges, were compounded by increased groundwater extraction to meet water demands for irrigation in the Central Valley, one of the most productive agricultural regions globally (Faunt et al., 2016). This led to significant TWS deficits, which were quantified using GRACE data and disaggregated using additional observations of snow, surface water and soil moisture (Famiglietti et al., 2011). Thomas et al. (2017) developed a method to quantitatively assess the propagation of drought through the hydrological cycle in California's Central Valley via a GRACE-derived groundwater drought index (Thomas et al., 2014). Surface water storage was replenished towards the end of the GRACE mission; however, Central Valley groundwater storage remained in deficit (Figure 1.5b) (Faunt et al., 2016).

1.1.3.2 Groundwater depletion

In many regions of the world, groundwater is relied upon as a water source to meet domestic, agricultural and industrial needs. Despite this, there is a lack of groundwater management due to the difficulties associated with monitoring vast underground water resources (Famiglietti, 2014). Agreement between GRACE-derived TWS, numerical model output and sparse in situ measurements of subsurface water storage has validated the use of space gravity measurements for monitoring seasonal TWS variability and long-term trends of expansive aquifer systems globally (e.g. Strassberg et al., 2009; Döll et al., 2014). The unsustainable consumption of non-renewable groundwater (i.e. fossil water) and renewable groundwater resources, due to extraction outpacing recharge rates, has become an issue that is synonymous with regions in mid-latitudes with semi-arid to arid climates that lack reliable access to surface water resources (Rodell et al., 2018). Rainfall deficits and drought conditions tend to increase reliance on groundwater, further exacerbating groundwater depletion. GRACE data has been used to measure the depletion of groundwater resources in Southeastern Australia (Leblanc et al., 2009), the US High Plains region (Scanlon et al., 2012) and the Californian Central Valley (Famiglietti et al., 2011; Scanlon et al., 2012), the Ukraine and Western Russia (Rodell et al., 2018) and in regions of the Middle East (Voss et al., 2013).

The GRACE and GRACE-FO data have recorded significant groundwater depletion coupled with sporadic to severe drought conditions in the Californian Central Valley (Figure 1.5) (Famiglietti et al., 2011) and in the southern portion of the High Plains aquifer, Texas (Strassberg et al., 2009). Groundwater withdrawal has consistently outpaced recharge for decades in both regions due to reliance on groundwater resources for irrigation to sustain productive agriculture (Faunt et al., 2016; Haacker et al., 2016). In the Southern High Plains region, soils are characterised by high clay content and low hydraulic conductivity, which has led to the periphery of the aquifer having already been depleted (Strassberg et al., 2009; Haacker et al., 2016). In the Californian Central Valley, sediment compaction and land subsidence due to sustained groundwater over-extraction have permanently reduced the capacity of the Central Valley aquifer (Faunt et al., 2016). In these areas, groundwater storage is likely to remain in deficit and is unlikely to completely recover despite improved water resource management (Faunt et al., 2016).

Despite normal or above-average rainfall, alarming groundwater depletion rates have been recorded in GRACE data in some regions. For example, in arid regions of Northern

Africa (Scanlon et al., 2022), North China (Feng et al., 2013) and Northern India (Rodell et al., 2009). The negative mass trend in Northern India is due to unsustainable extraction for irrigated agriculture and was one of the first TWS trends identified by GRACE (Rodell et al., 2009; Tiwari et al., 2009). Previous studies have shown that the greatest rate of groundwater depletion globally occurs in Northern India (Döll et al., 2014), although Long et al. (2016) argued that groundwater anomalies quantified in this region using GRACE-based techniques are potentially over-estimated. The negative TWS trend has been partially offset by increased rates of precipitation observed across India. This shift is consistent with predicted responses to climate change in the region (Rodell et al., 2018). That the rate of groundwater extraction already exceeds recharge during periods of above-average rainfall suggests that groundwater depletion will likely be exacerbated during future droughts (Rodell et al., 2018).

1.1.3.3 Seasonal variations

Climate change and natural climate variability have driven recent increased seasonal TWS variability, which has led to the intensification of wet and dry conditions in the Amazon Basin (Barichivich et al., 2018). Anomalous seasonal TWS variations in the Amazon Basin have led to several extreme droughts and floods, which have been recorded by GRACE and GRACE-FO data (Figure 1.6a). Chen et al. (2010a) demonstrated the applicability of GRACE observations for measuring large-scale TWS mass change in the Amazon Basin with a focus on the inter-annual variability and the 2009 flood that impacted the Central and Northern basins. Meanwhile, hydrological drought afflicted the Southern Amazon Basin (Chen et al., 2010b; Thomas et al., 2014). Scanlon et al. (2019) underscored the importance of satellite gravity data for recording TWS variations, finding that many hydrological and land surface models underestimated seasonal TWS anomalies in the Amazon and other tropical basins when compared to GRACE-derived TWS anomaly estimates.

GRACE-derived TWS anomalies and altimetry-derived sea level height observations have revealed significant seasonal variation (∼82 mm) and long-term decline (∼-64 mm/yr) of the Caspian Sea (Figure 1.6b) (e.g. Van Dijk et al., 2014; Chen et al., 2017; Rodell et al., 2018). The seasonal variations of the Caspian Sea are predominantly attributed to the seasonality of Volga River discharge at the Russian border, which recharges the Caspian Sea from the Northwest (Van Dijk et al., 2014; Rodell et al., 2018). Inflows

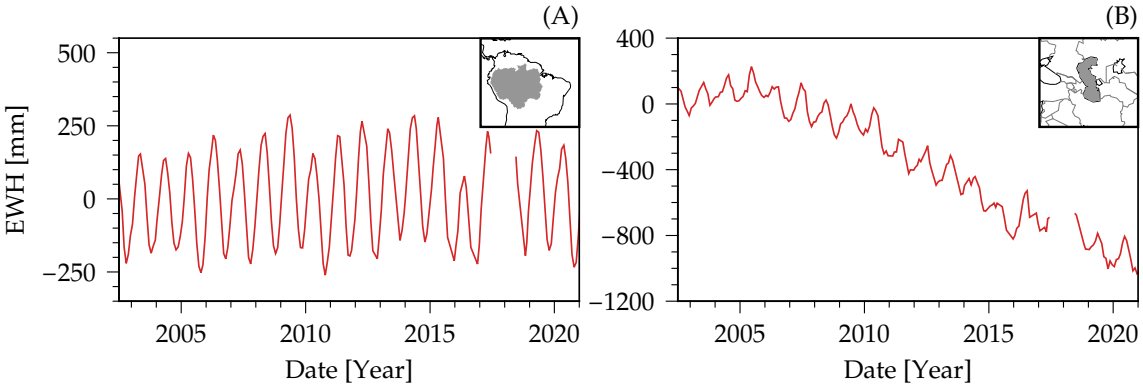

Figure 1.6: Time series of TWS anomalies from GRACE and GRACE-FO mascon solutions (Loomis et al., 2019a) in terms of equivalent water height (EWH), integrated across the (a) Amazon Basin and (b) Caspian Sea.

into the Caspian Sea are controlled by inter-annual variations in agricultural irrigation demands and precipitation fluctuations in the broader basin (Rodell et al., 2018). Seasonal variations in evaporation play a significant but secondary role in the seasonal fluctuation of Caspian Sea TWS (Chen et al., 2017; Rodell et al., 2018). Only a small component of the Caspian Sea's large seasonal signal is attributed to steric variations (Chen et al., 2017).

Direct withdrawal from the Caspian Sea and diversion of water from recharge sources are responsible for significant TWS decline, particularly from 2005 to the end of the currently available GRACE/GRACE-FO record (∼-72 mm/yr) (Figure 1.6b) (Rodell et al., 2018). Several countries surrounding the Caspian Sea, including the Southwestern region of Russia and countries in Central and Western Asia, rely on the Caspian Sea water resource for agricultural purposes. In the face of current and future climate change driving decreased precipitation and increased evaporation in the region, reliance on the Caspian Sea to provide sufficient water resources to maintain irrigation cropping will only increase (Chen et al., 2017; Rodell et al., 2018). Without the appropriate governance and at the current rate of TWS decline, the Caspian Sea will eventually be depleted (Rodell et al., 2018).

1.1.3.4 Elastic deformation

The Earth's lithosphere deforms elastically in response to changes in atmospheric and hydrologic (i.e. water, snow and ice) surface loading. Therefore, the distribution of TWS can be inferred from elastic deformation measurements extracted from GPS displacement data. At the same time, GRACE-derived TWS mass anomalies can be used to estimate

the displacement of Earth's lithosphere due to changes in hydrologic surface loads (e.g. Tregoning et al., 2009b; Argus et al., 2014b; Han, 2017). That surface deformation can be extracted from GRACE observations provides a method for validating GRACE-derived TWS against observations of elastic deformation from GPS displacement, and vice versa (Tregoning et al., 2009b). Where GPS stations are scarce, GRACE and GRACE-FO mass anomaly models provide a means for estimating elastic deformation due to hydrologic loading.

Global and regional analyses of elastic deformation have assessed the compatibility of GPS data and monthly spherical harmonic GRACE gravity estimates for inferring hydrologic loads. For example, Tregoning et al. (2009b) found broad global agreement between non-linear signals in GPS displacement data and GRACE-derived elastic deformation, suggesting that non-linear GPS anomalies are primarily due to geophysical processes (i.e. hydrologic loading) rather than analysis error. Their comparison showed better agreement between GRACE and GPS compared to previous studies (i.e. King et al., 2006; Van Dam et al., 2007) which was credited to the use of improved GPS processing techniques (Tregoning and Watson, 2009). Argus et al. (2014a) used a similar method to compare GRACE and GPS-derived estimates of TWS loading in the Californian Sierra Nevada Mountain Range. Elastic deformation of the Sierra Nevada is measured by a dense network of GPS stations with 50 km spatial resolution. GPS-measured uplift peaks at ∼12 mm annually at the end of Summer due to snowmelt, runoff and evapotranspiration. Monthly GRACE spherical harmonic models, at a comparatively lower spatial resolution, were unable to capture the distribution of seasonal water storage due to significant signal leakage, which biased the GRACE-derived estimates of TWS in the region (Argus et al., 2014a).

Using GPS displacement data and GRACE spherical harmonic gravity estimates, Han (2017) analysed inter-annual and seasonal variations of elastic deformation of the Australian continent due to the 2010-2011 La Niña. GRACE-derived elastic deformation was in agreement with GPS at the available site locations, estimating that the 2010-2011 La Niña produced >10 mm of widespread subsidence. The excess load was shed over 3-4 years, predominantly by evapotranspiration, which resulted in gradual uplift (Han, 2017). This trend continued, leading to widespread drought conditions that culminated in the "Black Summer" bushfire season of 2019-2020. Over a week in March 2021, a large portion of East Australia experienced extensive drought-breaking precipitation and flooding, which caused ∼5 mm of land subsidence observed by a network of GPS stations (Han

et al., 2021). Using a novel approach, they generated instantaneous line-of-sight gravity differences using GRACE-FO LRI inter-satellite ranging measurements (Ghobadi-Far et al., 2018). As the GRACE-FO satellites flew over Eastern Australia, during a single week, they observed subsidence consistent with the GPS data and ∼70 trillion litres of hydrologic loading, compatible with land surface model estimates (Han et al., 2021).

1.1.3.5 Integration and data assimilation

At present, satellite gravity is the only method capable of remotely measuring water storage change within each component of TWS on a global scale. However, that GRACE and GRACE-FO measure the vertical integration of each contributing component of TWS simultaneously presents its own challenges. Data assimilation and integration techniques utilise external information (i.e. in situ measurements, remote sensing data and numerical model output) to separate the components of the measured TWS anomaly (e.g. Rodell et al., 2007; Houborg et al., 2012; Tian et al., 2017). Data assimilation has been utilised to combine this information to optimise the spatial resolution and temporal resolution of GRACE TWS estimates, traditionally resolved at monthly, sub-basin scales. The spatial and temporal disaggregation of GRACE and GRACE-FO measured TWS anomalies lends to increased application of satellite gravity observations for hydrological purposes, for example, to analyse and predict extreme events (i.e. flood and drought) (e.g. Houborg et al., 2012; Kumar et al., 2016), monitor groundwater extraction over large areas (e.g. Rodell et al., 2009; Long et al., 2016) and assess water availability (e.g. Tian et al., 2017, 2019).

The validity of estimating groundwater storage anomalies via the vertical disaggregation of GRACE total TWS was tested in pre-launch simulation studies (Rodell and Famiglietti, 2002) and achieved using actual GRACE observations early in the mission. Yeh et al. (2006) was the first to utilise ground-based soil moisture measurements to isolate groundwater storage from GRACE-derived TWS anomalies, validated against a network of in situ data. Using a similar method, Rodell et al. (2007) isolated groundwater storage anomalies from GRACE-derived TWS in the Mississippi River Basin using modelled estimates of soil moisture and snow storage validated against in situ data. Their method utilised the Global Land Data Assimilation System (GLDAS). GLDAS uses ground-based and satellite observations as input and generates land surface model output, such as snow and soil moisture. GLDAS (and other data assimilation systems) is commonly utilised to

vertically disaggregate GRACE total TWS anomalies (e.g. Zaitchik et al., 2008; Houborg et al., 2012; Kumar et al., 2016).

The spatial and temporal resolution of GRACE- and GRACE-FO-derived TWS anomalies is arguably coarse compared to other methods that monitor individual components of TWS. Data assimilation of modelled or in situ soil moisture and GRACE observations into hydrological models enhances the spatial and temporal resolution of GRACE and GRACE-FO TWS observations (Zaitchik et al., 2008; Houborg et al., 2012; Kumar et al., 2016). Such studies have proven the functionality of GRACE data for improving drought forecasting and characterisation (Houborg et al., 2012; Kumar et al., 2016). More recently, GRACE and soil moisture observations from the Soil Moisture Ocean Salinity (SMOS) mission were assimilated for the first time into a water balance model to estimate sub-surface water storage variation in Australia (Tian et al., 2017). Later, Tian et al. (2019) assimilated GRACE and SMOS observations into a global hydrological model to estimate variations in dryland vegetation-accessible water storage and predicted vegetation responses months in advance.

1.2 Monitoring solid Earth dynamics using GRACE and GRACE-FO data

1.2.1 Glacial isostatic adjustment

GRACE and GRACE-FO measurements include the mass change associated with the isostatic adjustment of the Earth's lithosphere as a response to ice sheet unloading since the Last Glacial Maximum (LGM). The continuous viscoelastic response of the Earth to past variations in glacial loading is known as Glacial isostatic adjustment (GIA) (Peltier, 1982). Over decadal scales, GIA causes quasi-linear changes in the Earth's geopotential. During the LGM, large portions of North America and Eurasia were covered by ice sheets; today, these regions are dominated by seasonal hydrology signals. In these regions, GRACE-derived GIA rates can be validated against GPS uplift rates; for example, Tregoning et al. (2009a) found that GRACE data corrected for hydrology using GLDAS model output produced improved estimates of GIA-induced uplift compared to GRACE-only estimates in North America. Trends in the GRACE and GRACE-FO data can be used in conjunction with other observations that indicate past ice-sheet extent, relative sea level change and present-day uplift to constrain numerical models of GIA, which model both ice-load history

and Earth's rheology (e.g. Riva et al., 2009; Peltier et al., 2015).

The gravitational effects of GIA overlap spatially with signals induced by present-day mass change, with similar magnitudes in some presently glaciated regions (i.e. Greenland and Antarctica). The interpretation of GRACE and GRACE-FO observations requires that ice sheet mass change and GIA-induced signals be separated. One method to achieve this involves subtracting from the total temporal gravity field signal the GIA component represented by a numerical model. However, the quality and quantity of in situ observations that constrain GIA models are limited in glaciated regions, resulting in significant uncertainties (e.g. Gunter et al., 2009). Any GIA model errors are then propagated into mass balance estimates and, therefore, into the estimates of ice sheet contribution to modern sea level rise (Shepherd et al., 2018b). The most significant uncertainties are associated with the AIS, where in situ observations of past ice sheet extent are sparse (e.g. Ivins and James, 2005). Separating load history from mantle rheology is difficult, particularly in Antarctica, and accurate observations with broad temporal and spatial coverage are not readily available.

Many studies treat the rheological structure of the Earth as globally uniform, varying only in the radial direction and known a priori (e.g. Argus et al., 2014b; Peltier et al., 2015). However, significant evidence supports lateral variability and non-uniformity of the Earth's rheological structure (Morelli and Danesi, 2004). Several attempts have been made to develop models that instead solve for the Earth's rheological parameters. For example, Ivins and James (2005) and Whitehouse et al. (2012) reconstructed the AIS history using glaciological constraints and forward modelling to identify mantle rheology models consistent with the ice sheet model. The resulting GIA models were unable to close the Holocene global sea level budget and under-estimated the mass of the AIS before 12 Ka (Lambeck et al., 2014). Purcell et al. (2016) demonstrated that some GIA models (i.e. Argus et al., 2014b; Peltier et al., 2015) contained excessive uplift in the Antarctic Peninsula, which led to the release of a corrected GIA model using an alternate Antarctic bathymetry model (Peltier et al., 2018)

Attempts have been made to separate current ice mass loss rates from GIA trends based on a combination of GRACE measurements with additional data sets. For example, Riva et al. (2009) relied on the density differences of rock and ice to estimate GIA from GRACE and laser altimetry data. GIA estimates have also been computed in East Antarctica by removing the hydrological component of the GRACE signal, leaving only the GIA

component, validated through comparison to GPS-derived uplift rates (Tregoning et al., 2009a). Wahr et al. (2000) devised a methodology to use measurements from GRACE and ICESat to separate surface and sub-surface geophysical signals and accurately estimated changes in the AIS. Recovery of accurate Antarctic mass balance using this method was inhibited by a lack of robust sampling by ICESat (Ivins et al., 2013). Additionally, rheological parameters constrained by GPS uplift measurements are challenging to obtain due to the sparse GPS sites located on bedrock in Antarctica. As a result, the uncertainty of these GIA models is significant (50-150 Gt/yr) and of a similar magnitude to the mass balance signal (Gunter et al., 2009).

With improved modelling strategies and increased availability of in situ and satellite observations, GIA models in glaciated regions have improved over time (e.g. Riva et al., 2009; Purcell et al., 2016; Peltier et al., 2018). Alternative estimation and validation techniques (i.e. GPS-derived and GRACE minus GLDAS) have also improved knowledge of regional GIA rates as GLDAS has become more sophisticated and the number of GPS stations has increased in remote locations (e.g. Tregoning et al., 2009a; Ivins et al., 2013). Despite these improvements, GIA model uncertainties are still the primary source of uncertainties in GRACE ice sheet mass balance and GRACE-derived ocean mass change estimates (Shepherd et al., 2018b). Continuing the record of satellite gravity mass change observations may provide the observations to derive better or further constrain GIA models.

1.2.2 Earthquake deformation

Earthquakes result from stress build-up at a fault leading to an abrupt release of stress in the seconds to minutes following initial rupture. Co-seismic deformation produces a sudden change in the Earth's gravity field by vertical displacement of the crust and internal density structure. post-seismic deformation (i.e. afterslip and viscoelastic relaxation) occurs in the years to decades following an earthquake, causing mass redistribution to continue. The mass redistribution caused by co-seismic and post-seismic gravity changes perturbs the orbits of satellites around Earth. These perturbations can be detected by GRACE and GRACE-FO for high magnitude earthquakes (i.e. $M_w > 8.0$) and are interpreted as the spatial signature of co-seismic and post-seismic mass change (Han et al., 2013).

GRACE observed the mass redistribution caused by the greatest earthquakes to occur this century to date, for example, the December 2004 Sumatra-Andaman earthquake (M_w

9.3) (e.g. Han et al., 2006; Panet et al., 2007; De Linage et al., 2009), the February 2010 Maule, Chile earthquake (M_w 8.8) (e.g. Han et al., 2010; Heki and Matsuo, 2010), the March 2011 Tohoku-Oki earthquake (M_w 9.0) (e.g. Panet et al., 2018) and the April 2012 Indian Ocean strike-slip earthquakes (M_w 8.6, 8.2) (e.g. Han et al., 2015). Han et al. (2019) developed models of regional co-seismic and post-seismic deformation so that mass change related to each of the large earthquakes could be removed from the hydrology signals that dominate the GRACE and GRACE-FO temporal gravity field estimates.

Evidence of earthquake deformation has been extracted from both the GRACE spherical harmonic gravity field solutions and the high-resolution inter-satellite ranging data measured by the microwave system. For example, Han et al. (2006) observed the co-seismic gravity decrease in the Andaman Sea caused by a change in density structures during the December 2004 Sumatra-Andaman earthquake (M_w 9.3) using regional inversions generated from GRACE range rate data. A later study performed a continuous wavelet analysis on global GRACE 10-day geoid products, which allowed Panet et al. (2007) to successfully observe both co-seismic and post-seismic signatures in the Andaman Sea. Han et al. (2010) isolated co-seismic gravity signatures after the February 2010 Maule, Chile earthquake (M_w 8.8) by calculating the time derivative of the GRACE range rate to generate accelerations and compared those to predicted gravity changes from finite fault models. A study published at a similar time demonstrated that a co-seismic gravitational signal was observed in global GRACE gravity spherical harmonic solutions corrected for hydrology (Heki and Matsuo, 2010). Despite their different approaches, both Han et al. (2010) and Heki and Matsuo (2010) were able to isolate a gravity anomaly of -5 μGal east of the epicentre after the earthquake, consistent with external fault models.

Not only have co-seismic and post-seismic mass change signals been observed by GRACE, but some months-long large-scale signals were observed before the 2011 Tohoku-Oki earthquake. Panet et al. (2018) performed a regional analysis of monthly GRACE spherical harmonic solutions of the gravity field (Bruinsma et al., 2010) in the months surrounding the 2011 Tohoku-Oki earthquake, finding that large-scale precursor mass variations are observable three months before fault rupture. They argued that the observed pre-seismic signals are significantly larger than ordinary ocean mass variations or noise in the region. Such findings, if accurate, could have significant implications for improving seismic hazard assessment; however, others have challenged the statistical significance of the observed preseismic signals (Wang and Burgmann, 2019). Instead, Wang and Burgmann

(2019) argue that these transient mass changes are more likely representative of temporally correlated observation errors or other unnamed geophysical signals. Support for precursory mass variations was provided by a recent analysis of secular tectonic motions extracted from daily GNSS time series, which showed "wobbling" that spanned thousands of kilometres several months before the Tohoku-Oki earthquake (Bedford et al., 2020), consistent with the findings of Panet et al. (2018). Bedford et al. (2020) also managed to extract a similar signature of precursory motion months before the 2010 Maule earthquake from daily GNSS, which has yet to be observed in GRACE derived mass variations.

The high temporal resolution of the inter-satellite ranging data measured by the GRACE microwave ranging system has been utilised to observe more transient earthquake-related phenomena that can otherwise not be represented in the monthly or 10-day GRACE spherical harmonic solutions. In a recent study, Ghobadi-Far et al. (2019a) analysed GRACE inter-satellite range rate residuals for December 2004, finding the existence of a significant transient signal after the 2004 Sumatra earthquake. They speculated that this signal could be the manifestation of global-scale gravity changes due to the excitation of Earth's free oscillation, which lasted for a few days following the 2004 Sumatra earthquake (Rosat et al., 2005). These signals were of a similar magnitude to instrumental noise so could not be attributed to this phenomenon with any certainty, citing a need for more precise instrumentation in future missions (Ghobadi-Far et al., 2019a). A similar methodology was applied in a later study to analyse the transient ocean mass redistribution caused by earthquake-triggered tsunamis (Ghobadi-Far et al., 2020a). The three large subduction thrust fault earthquakes detected by GRACE (i.e. 2004 Sumatra-Andaman, 2010 Maule and 2011 Tohoku-Oki earthquakes) all triggered tsunamis causing an associated transient ocean mass redistribution which perturbed the GRACE orbits. Ghobadi-Far et al. (2020a) found that these tsunami-triggered perturbations caused 1-4 nm/s^2 anomalies in the inter-satellite accelerations for less than a day, consistent with tsunami models and independent measurements from buoys, OBP sensors and satellite altimeters.

1.3 Objectives

Accurate knowledge of the Earth's temporal gravity field is critical for monitoring the movement of water masses through the hydrological cycle within the Earth and across its surface. Of particular importance is the accurate estimation of modern ice sheet mass

balance to infer current and projected rates of sea level rise, recording the number and severity of extreme weather events driven by climate change and monitoring the availability and extraction of water resources. This study aims to improve GRACE-based estimates of the time-variable gravity field for the analysis of these mass variations by mitigating measurement errors and optimising the choices of processing strategies. The objectives of this study are as follows:

1. Develop strategies to account for thermally-induced errors in the non-gravitational acceleration measurements and high-frequency noise in the ranging observations to enable accurate temporal gravity models to be estimated from GRACE data even in the presence of significant instrument noise.

2. Identify an optimised parameterisation using mascons that effectively reduces signal leakage and the impacts of intra-mascon variability (the variations of mass change signals within a mascon) in the temporal gravity field estimates from simulated GRACE observations.

3. Assess the spatial resolution of GRACE observations throughout the mission using regularised mascons and quantify how the accurate recovery of the temporal gravity field is affected by satellite altitude, ground track coverage and observation noise.

1.4 Thesis outline

Chapter 2 provides an overview of the GRACE and GRACE-FO mission and the methods used to generate models of the temporal gravity field from GRACE and GRACE-FO data products.

Chapters 3 to 5 are based on three published first-authored and co-authored papers. Each of these papers details a different aspect of GRACE data processing.

Chapter 3 describes the characteristics of long-wavelength noise contained in the GRACE accelerometer measurements. The proposed method for thermal correction of the accelerometer measurements demonstrably reduces striping errors in the gravity field inversions and stabilises the accelerometer calibration parameters. This chapter is based on the manuscript published in Advances in Space Research:

McGirr, R., *Tregoning, P., Allgeyer, S., McQueen, H., and Purcell, A. P. (2022) Mitigation of thermal noise in GRACE accelerometer observations. Advances in Space Research, 69(1), 386-401.*

Chapter 4 describes the process of estimating mass anomalies observed by GRACE using irregularly shaped mass concentration elements (mascons) as the basis functions. The benefits of parameterising the temporal gravity field using mascons are evidenced in a detailed simulation study that utilises various mascon shapes and sizes. This chapter is based on the manuscript published in the Journal of Geophysical Research - Solid Earth:

Tregoning, P., ***McGirr, R.,*** *Pfeffer, J., Purcell, A. P., McQueen, H., Allgeyer, S., and McClusky, S.C. (2022) ANU GRACE data analysis: Characteristics and benefits of using irregularly shaped mascons. Journal of Geophysical Research: Solid Earth, 127(2), e2021JB022412.*

Chapter 5 describes the approach used for modelling GRACE and GRACE-FO orbits, the method and benefits of using range acceleration as the inter-satellite observation and the regularisation strategy used to generate the ANU GRACE mascon time series. The time series of mass variations derived from the temporal gravity field estimates are analysed and compared to results from other GRACE processing centres. This chapter is based on the manuscript published in the Journal of Geophysical Research - Solid Earth:

Allgeyer, S., Tregoning, P., McQueen, H., McClusky, S.C., Potter, E.-K., Pfeffer, J., ***McGirr, R.,*** *Purcell, A. P., and Montillet, J.-P.(2022) ANU GRACE data analysis: Orbit modelling, regularisation and inter-satellite range acceleration observations. Journal of Geophysical Research: Solid Earth, 127(2), e2021JB022489.*

Chapter 6 describes the variation in spatial resolution of GRACE-derived models of the temporal gravity field as a function of satellite altitude and ground track coverage. A detailed simulation study investigates the trade-offs between observation noise, mascon size, and mascon regularisation. This chapter is based on the manuscript submitted to the Journal of Geophysical Research - Solid Earth:

McGirr, R., *Tregoning, P., Allgeyer, S., McQueen, H., and Purcell, A. P. (2022) Interplay of altitude, ground track coverage, noise and regularisation on the spatial resolution of GRACE gravity field models. Journal of Geophysical Research: Solid Earth, submitted March 5, 2022.*

Chapter 7 summarises the key findings of this study, including suggestions for future work.

Chapter 2

Space gravity missions and data analysis

The Earth's gravity field reflects the distribution of mass around and within the globe, including mass distribution within the solid Earth along with all the components that make up Earth's hydrosphere. The Earth's gravity field is often discussed in the context of its static and time-variable components. Earth's topographic and bathymetric features largely determine the gravity anomalies of the static gravity field along with the internal density structure of the Earth. The temporal or time-variable component of the gravity field is mainly influenced by the Earth's hydrosphere, including the atmosphere, cryosphere, oceans, surface and subsurface land hydrology (i.e. lakes and rivers, soil moisture, groundwater). The time-variable gravity field also includes influences from the solid Earth, such as seismic deformation, solid Earth tides and glacial isostatic adjustment (GIA). In fact, all of the Earth's gravity field components are temporal, given that the dynamics that influence the gravity field vary over some timescale, from instantaneous (e.g. co-seismic deformation) to many millennia (e.g. tectonics and mantle convection).

Satellite gravimetry is the remote sensing of the Earth's static and time-variable gravity field from space. This method for observing the Earth's mass variations is a relatively new remote sensing technique that was not utilised before this century. Modern satellite gravimetry missions began with the launch of the single satellite mission, CHAMP (CHAllenging Minisatellite Payload), followed by the launch of the Gravity Recovery and Climate Experiment (GRACE) mission in 2002 and GOCE (Gravity and steady-state Ocean Circulation Explorer) in 2009. The components of the Earth's static and time-variable gravity field are currently observed by GRACE Follow-On (GRACE-FO). Collectively, GRACE and GRACE-FO have provided these observations at an unprecedented temporal and spatial resolution for two decades.

The GRACE satellite gravity mission observed the Earth's gravity field variations at an improved spatial and temporal resolution relative to previous space gravity missions, using a unique satellite-to-satellite tracking design. In the remainder of this chapter, I provide an overview of the GRACE mission and its successor, GRACE-FO. In Section 2.2, I review the methods used for analysing GRACE and GRACE-FO data, the limitations of these methods and sources of error.

2.1 GRACE and GRACE-FO mission overview

In the following section, I describe the GRACE and GRACE-FO satellite gravity mission within the context of their scientific payloads, the principal measurements, the quality of these measurements and the condition of the instrumentation over the course of the respective missions. In Section 2.1.3 I describe the various levels of GRACE and GRACE-FO data processing and the main products necessary for temporal gravity field estimation.

2.1.1 GRACE

The GRACE mission (Tapley et al., 2004) was a low altitude satellite-to-satellite tracking mission launched in March 2002 in a collaborative effort between the U.S. National Aeronautics and Space Administration (NASA) and the German Aerospace Centre (DLR). Two nearly-identical twin satellites were launched in a tandem circular low-Earth orbit with a separation of 220 $\pm$ 50 km. The satellites maintained a near-polar orbit with an inclination of 89° in order to sample the entire Earth. The spacecraft were launched into an orbit with an altitude of $\sim$490 km, eventually decaying to $\sim$320 km by the mission's end in October 2017. Initially anticipated to have a lifespan of just five years, GRACE operated in an extended mission phase for an additional ten years before finally being decommissioned due to battery failure. Over 15 years, the twin GRACE satellites mapped the Earth's static and time-variable gravity field with unprecedented accuracy.

Solutions of the temporal gravity field produced using GRACE observations by various processing centres (e.g. Luthcke et al., 2013; Mayer-Gürr et al., 2016; Save et al., 2016; Watkins et al., 2015; Dahle et al., 2014) have mapped the trends and fluctuations in the mass balance of terrestrial water storage (TWS), glaciers and ice sheets, sea level and ocean dynamics and provided insights into GIA and earthquake-associated mass redistribution. The success of the GRACE mission has been instrumental in advancing scientific understanding of both natural and anthropogenically induced variations in the hydrolog-

ical cycle, ice sheet mass balance, ocean dynamics and sea level change (e.g. Chambers, 2006a; Chen et al., 2010a; Tregoning et al., 2009a; Velicogna and Wahr, 2006).

Throughout its duration, the GRACE mission provided a near-continuous time series of all the inputs necessary to generate estimates of the Earth's gravity field within the publicly available suite of "Level-1B" data. The gravitationally induced accelerations and decelerations of the twin spacecraft recorded the distribution of mass on Earth near their ground track (the projection of the satellite's orbit onto the surface of the Earth) (Tapley et al., 2004) (Figure 2.1). Each satellite experienced these effects, one after the other and, thus, caused variations in the along-track range and velocity of the satellites, which are proportional to the gravitational potential energy of the mass below (Figure 2.1). These highly accurate inter-satellite measurements are used to estimate the Earth's gravity field at an unprecedented spatial and temporal resolution.

The GRACE satellites were launched to an average altitude of 490 km in a near-circular orbit. A near-circular orbit is a common choice for geodetic satellites because it allows for the uniform influence of the Earth's gravitational field on the satellites. However, because the Earth is not perfectly spherical, the altitude of the satellites still varied significantly within a day (∼40 km). By the end of the mission, the average altitude of the satellites had decayed to 320 km, with 80% of decay occurring in the second half of the GRACE mission (red, Figure 2.2).

The orbital period of the GRACE satellites was ∼94 minutes, meaning that the satellites would achieve a minimum of 15 complete revolutions around the Earth each day. A percentage of each satellite orbit would typically be spent partially in direct sunlight and partially in Earth's shadow. The percentage of time spent in direct sunlight was determined by the β' angle, which is defined as the angle between the orbital plane of the satellite and the vector pointing from the Earth to the Sun. When the Sun was in the orbital plane (i.e. β' angle of zero), the satellites spent the most time (∼37 minutes) in Earth's shadow. Conversely, when the orbital plane was near-perpendicular to the Earth-Sun vector (i.e. $|\beta'|$ angle $>70°$), the satellite's side panel was in direct sunlight for the entire duration of a revolution. The β' angle had a precessional period of ∼322 days, meaning that for ∼161 days, the Sun was on one side of the satellite, then on the other side for the next ∼161 days (grey, Figure 2.2).

The GRACE satellites' near-polar orbit (89°) caused the ground track coverage to be much denser at the poles compared to mid-to-low latitudes. The latitudinal variation

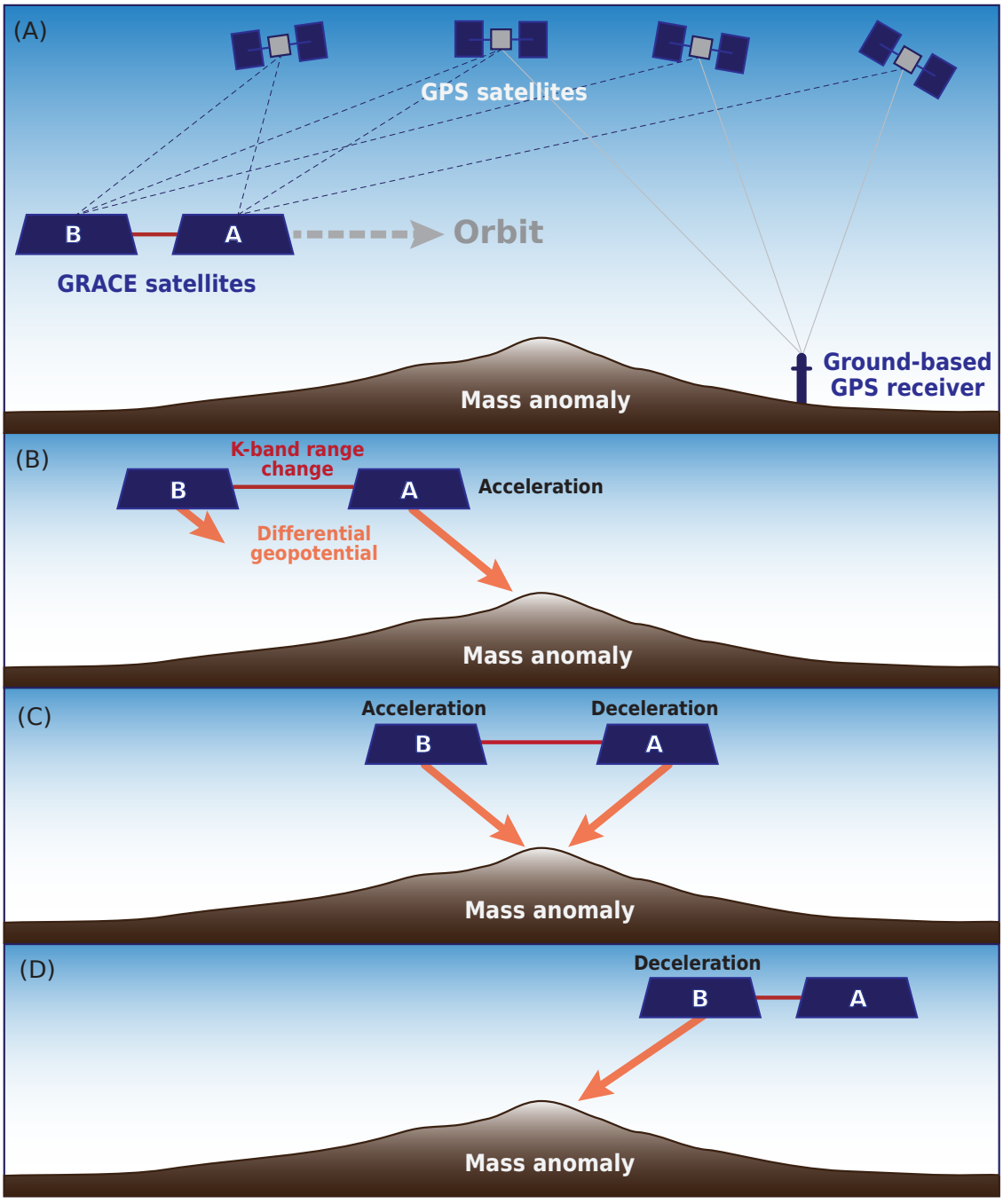

Figure 2.1: The GRACE mission concept utilises satellite-to-satellite tracking of the twin spacecraft (GRACE-A and GRACE-B) to measure via the K-band system the inter-satellite range change which contains the effects of the gravitationally induced perturbations of the satellites due to the Earth's spatially varying gravity field.

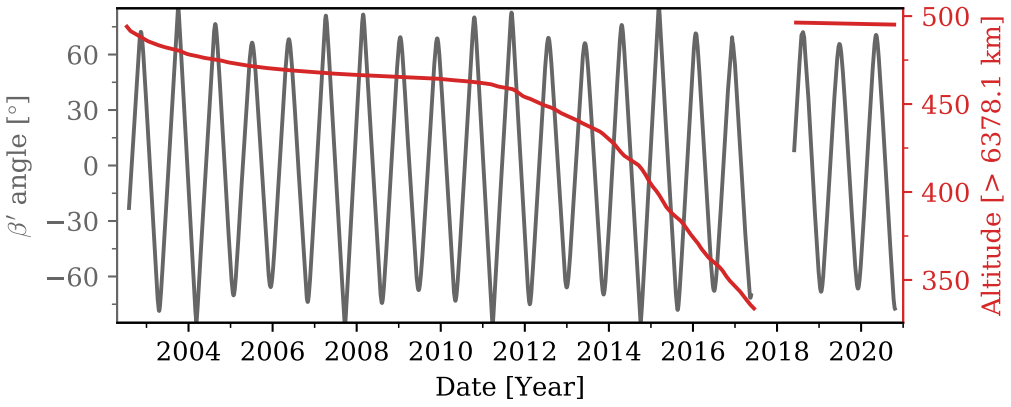

Figure 2.2: GRACE and GRACE-FO orbital configuration, average daily altitude (red) and average daily β' angle (grey) during the GRACE mission from mid-2002 to mid-2017 and GRACE-FO mission from mid-2018 to end of 2021.

in ground track coverage increases the observability of higher-frequency variations of the gravity field in polar regions. Ground tracks are the projection of a satellite's orbit onto the surface of the Earth. They should uniformly cover the Earth's surface so that all of the components of the gravity field are observed by the satellites, and maximum spatial resolution can be achieved. Typically, the ground track of the GRACE satellites evenly covered the majority of the Earth's surface every ∼30 days (Figure 2.3c), which permitted the generation of global gravity models at monthly temporal scales with a surface spatial resolution of ∼300 km and an accuracy of ∼2 cm (Tapley et al., 2004). Estimates of the temporal gravity field are permitted at a temporal resolution higher than monthly by using fewer days of observations and, therefore, fewer ground tracks (e.g. Figure 2.3a,b). However, the high-frequency components of the gravity field are under-sampled when fewer observations are used, which decreases the spatial resolution of the temporal gravity field models inferred from GRACE data. (e.g. Rowlands et al., 2005; Lemoine et al., 2007).

As the satellites descended throughout the GRACE mission, periods of significantly reduced ground track coverage occurred due to periods of orbit resonance (e.g. Figure 2.3d). A resonant orbit (also referred to as a repeat orbit) occurs when the Earth's rotation and the orbital period of the satellites are proportionate (Vallado, 2001). Under the conditions of orbit resonance, the GRACE satellites continually observed the same portion of the Earth's gravity field, leaving significant observational gaps, particularly at low-to-mid latitudes. During repeat orbit conditions, monthly solutions of the gravity field are not able to achieve a uniformly high spatial resolution as in other months with ideal ground tracks (Wagner et al., 2006). The reduction in resolution of the recoverable gravity

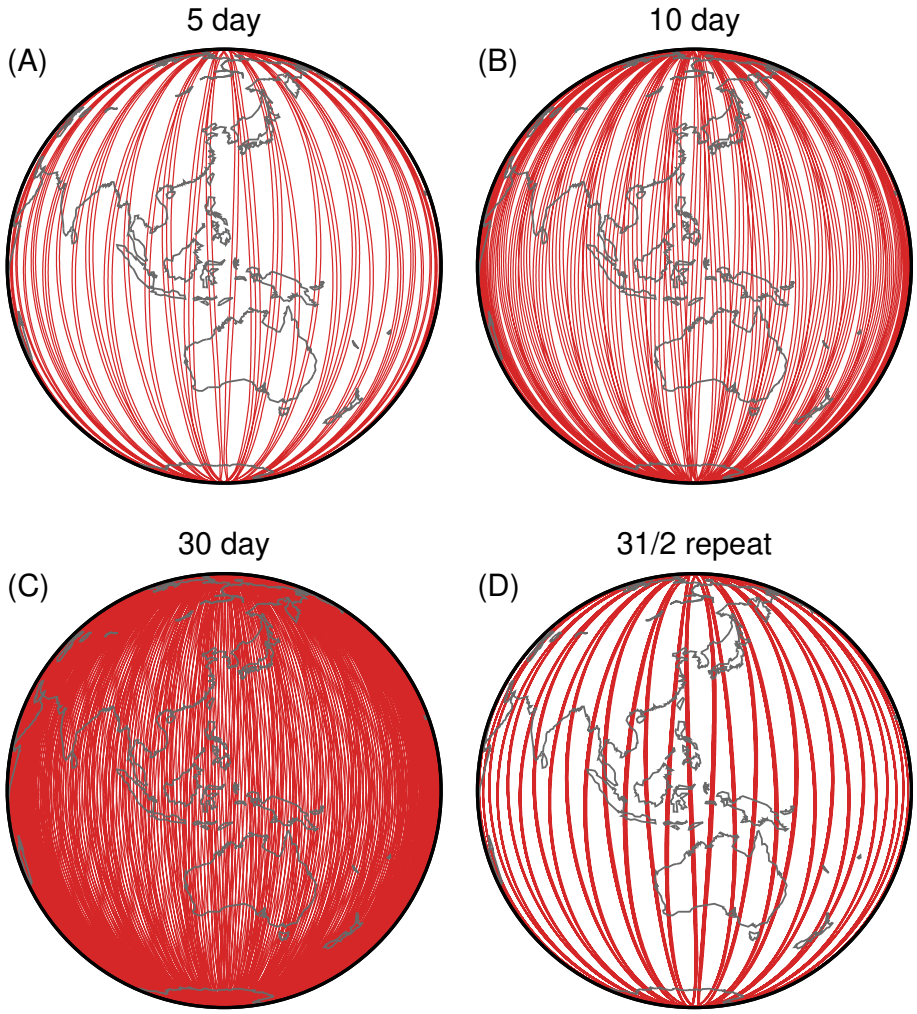

Figure 2.3: Typical GRACE ground track pattern during ideal orbit conditions producing a dense ground track pattern that evenly covers the entire Earth in April 2015 over (a) 5 days, (b) 10 days and (c) 30 days. (d) 30 days of ground tracks during the February 2015 31/2 repeat orbit, leaving large gaps between the ground tracks.

field is dependent on the repeat period of the orbit: a shorter repeat period produces a larger spatial separation between repeat ground tracks and thus a more poorly observed gravity field (Wagner et al., 2006).

The variations in the inter-satellite range between the GRACE satellites reflect the heterogeneous nature of the Earth's gravity field along the satellite's ground track. The changes in the inter-satellite distance were measured with sub-micrometre precision by the Microwave Instrument (MWI) on-board each satellite (Loomis et al., 2012). The MWI consists of the Ultra-Stable Oscillator (USO), the Instrument Processing Unit (IPU) and the K/Ka-Band Ranging (KBR) Assembly. The IPU provided onboard digital signal processing for the MWI and GPS signals along with timing references for the satellite (Dunn et al., 2003). The USO provided dual-frequency (K/Ka-band) generation of the microwave signals exchanged between the two satellites, which were transmitted and received by the KBR (Dunn et al., 2003). The inter-satellite range change measurements were generated using the dual one-way biased ranging model (Thomas, 1999), whereby the range change was derived by combining measurements of the phase of microwave (K and Ka-band) signals sent between the antenna phase centres that point between the satellites (Case et al., 2010).

In addition to the MWI, each satellite was equipped with a SuperSTAR three-axis electrostatic accelerometer, which was mounted at the centre of mass of each satellite. The accelerometers measured the non-gravitational forces acting on the spacecraft by measuring the electrostatic forces and torques necessary to maintain a proof mass motionless with respect to the sensor cage (Touboul et al., 1999, 2004). The accelerometer measurements were initially made in the Accelerometer Frame (AF), with the origin being the centre of mass of the satellite. The AF axes are parallel to the Science Reference Frame (SRF), whose axes point in the direction of the along-track (towards the antenna horn), radial (nadir pointing) and cross-track, completing the right-handed coordinate system (Figure 2.4). With respect to the SRF, the accelerometers had two high-sensitive axes, the along-track (X_{SRF}) and the radial (Z_{SRF}), while the cross-track (Y_{SRF}) component had a reduced sensitivity (Frommknecht et al., 2003). The along-track axis was dominated by atmospheric drag and solar radiation pressure, while the radial axis was influenced by both Earth albedo and solar radiation pressure. The cross-track axis was primarily affected by solar radiation pressure, the magnitude of which depends on whether the satellite was in sunlight or Earth's shadow and the elevation of the Sun with respect to the satellite orbital

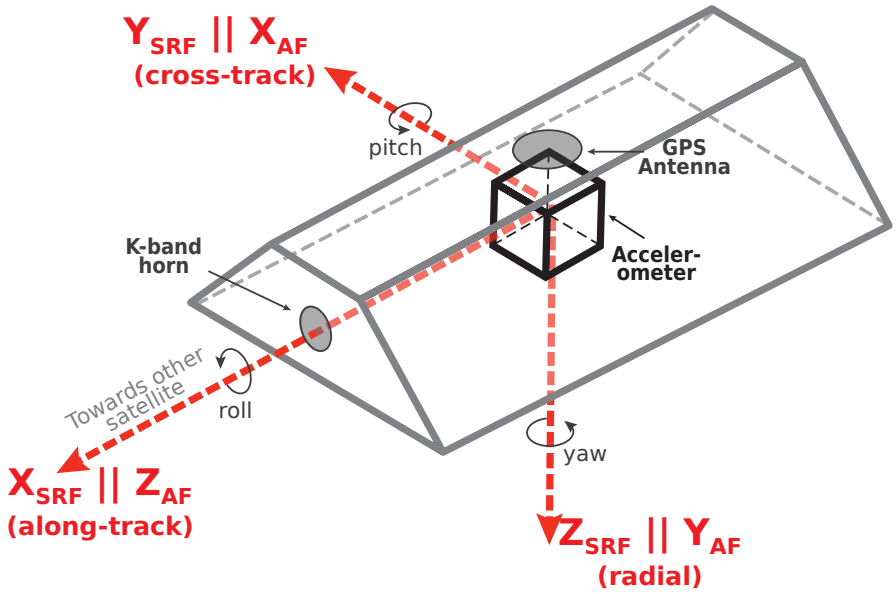

Figure 2.4: Schematic of the GRACE spacecraft, the components of the Accelerometer Frame (AF) and Science Reference Frame (SRF).

plane.

The attitude and orbital control system consisted primarily of the Global Positioning System (GPS) receivers and the dual Star Camera Assembly (SCA). The GPS receivers on each satellite recorded data used to determine spacecraft position and time synchronisation. At the same time, the SCA observed the precise orientation of the satellites in the inertial (i.e. celestial) reference frame by processing imagery captured by two star camera heads (Dunn et al., 2003).

Before the launch of the GRACE satellites, extensive simulation studies predicted the performance of the GRACE mission in the presence of instrumental noise (i.e. accelerometer noise, star camera noise and KBR system noise), which was assumed to be the dominant limitation on the accuracy of the GRACE gravity field solutions (Wahr et al., 1998; Kim, 2000; Kim and Tapley, 2002). In reality, the GRACE data produced gravity field solutions with unrealistic north-south striping due to unexpected increased error, at least a magnitude higher than the predicted baseline (Wahr et al., 2004; Han et al., 2004; Thompson et al., 2004; Ditmar et al., 2012). This discrepancy fostered the development of many post-processing methods used to suppress gravity field errors (e.g. Swenson and Wahr, 2006; Wouters and Schrama, 2007; Kusche, 2007) and led to efforts to quantify and understand the origin of such errors, which likely originated from a combination of sensor noise, data processing and temporal aliasing (Wahr et al., 2006). Temporal aliasing in this

context is the misidentification of high-frequency mass transport signals that the monthly GRACE solutions cannot resolve. To minimise temporal aliasing artifacts, appropriate dealiasing background models are used to account for the short period redistribution of mass due to ocean tides (Lyard et al., 2006, 2021) and non-tidal atmosphere and ocean signals (Flechtner, 2007; Dobslaw et al., 2017b). However, these background models contain errors that cause residual high-frequency signals to be aliased into the gravity field solutions. As a result, temporal aliasing contributes significantly to the GRACE error budget (Han et al., 2004; Thompson et al., 2004). While improvements to both background models and processing methods have substantially increased the accuracy of GRACE gravity field solutions, the accuracy of the temporal gravity field models are still limited by background model inaccuracies and instrumental noise (Ditmar et al., 2012; Dobslaw et al., 2013; Flechtner et al., 2016).

Investigations into the characteristics of instrumental noise throughout the GRACE mission has led to improved data processing which has resulted in more accurate estimates of the temporal gravity field (e.g. Bandikova and Flury, 2014; Klinger and Mayer-Gürr, 2016; Bandikova et al., 2019). The performance of various GRACE instrumentation and systems varied throughout the mission's duration and led to an increased error for some portions of the mission. Increased error is apparent during the first two years in orbit, as only one of the two star cameras per satellite were in operation, thus producing less accurate orientation observations. Errors improved and remained low from 2004 to 2010, delivering accurate, low-error gravity field solutions. During the second half of the mission, limited power supply due to the eventual degradation of the batteries led to the implementation of several strategies to reduce power usage to extend the longevity of the mission beyond 2010 (Herman et al., 2012). These power-saving strategies included disabling thermal control and switching off the accelerometers and MWI during orbit when the spacecraft were in Earth's shadow. While these strategies successfully prolonged the span of the GRACE mission, they predictably resulted in an increased error from 2011 to the end of the mission.

In addition to the non-gravitational accelerations induced by atmospheric drag, solar radiation pressure and Earth albedo, the accelerometers sensed satellite-induced disturbances due to thruster firings, heater switches, magnetic torquer spikes and so-called "twangs" (Flury et al., 2008; Peterseim et al., 2012; Peterseim, 2014). These signals occupy the high-frequency component of the accelerometer measurements, some of which are

filtered out during ground processing (i.e. twangs and heater spikes). In contrast, thruster spikes remain in the down-sampled accelerometer data. Each satellite was equipped with six pairs of thrusters that, when fired, induced angular accelerations about the ±roll, ±pitch or ±yaw axis (Figure 2.4). A pure rotation of the satellites would have resulted if the accelerometer proof mass was perfectly aligned with the satellite's centre of mass, the thruster pairs were perfectly aligned and thruster firings were executed at precisely the same time with the same force. Due to some imperfections, thruster firings caused real linear accelerations of the spacecraft that must be accounted for in orbit determination (Meyer et al., 2012; Bandikova et al., 2019). Further, the measured linear accelerations must be calibrated for an instrumental bias and scale for each satellite and accelerometer axis before use in precise orbit determination.

The accelerometers required a thermally controlled environment with variations of temperatures less than 0.1°C per revolution to achieve the desired level of performance (Flury et al., 2008). Minimal thermal variations were maintained via heaters which controlled the temperature of various instruments and sensors onboard the GRACE satellites. In a thermally stable environment, the daily variation of the accelerometer biases were insignificant and could be modelled by a quadratic fit to multiple years of observations (Bettadpur, 2009). However, thermal control of the satellites was switched off in April 2011 due to reduced battery capacity, resulting in increased complexity in the temperature variations. These variations manifested as non-linear sub-daily bias drift in the accelerometer observations, primarily observed in the less sensitive cross-track axis (Klinger and Mayer-Gürr, 2016). To further reduce battery load, both satellites' accelerometers were switched off during periods of maximum shadow time ($|\beta'|$ angle $<20°$). Non-linear sub-daily bias drift also occurred after the accelerometer were switched back on (Herman et al., 2012).

After thermal control of the GRACE spacecraft was permanently switched off in April 2011, heater switching spikes were no longer present in the data; however, temperature variations occurred frequently, increasing in frequency and magnitude. Temperature variation and bias drift became highly correlated with the β' angle during this period. When the satellites were in constant sunlight ($|\beta'| > 70°$) one of each of of the satellites' side panels was primarily illuminated at all times, causing temperature variations outside the range for optimal accelerometer operation and low-frequency cross-track and along-track bias drift (Herman et al., 2012; Klinger and Mayer-Gürr, 2016). Temperature variations outside the range for optimal accelerometer operation also occurred during thermal con-

trol due to occasional disconnections to heater lines which led to an immediate cooldown of the spacecraft. During a period of partial thermal control, modified heater tables were often uploaded to intentionally reduce the temperature of the satellites to decrease battery load. In both of these scenarios, significant temperature variations caused changes in the accelerometer bias, most noticeably in the cross-track axis (Klinger and Mayer-Gürr, 2016). Left unaddressed, this thermally-induced low-frequency accelerometer drift leads to mismodelling of the satellite orbits, which causes north-south stripes to appear in the temporal gravity field solutions (Ditmar et al., 2012).

In the seven months before the end of the GRACE mission, the GRACE-B batteries degraded further. Several measures were taken to decrease the battery load further, including the cessation of GRACE-B accelerometer operations altogether. The missing GRACE-B accelerometer data were generated using a data transplant method that uses the GRACE-A accelerometer measurements (Save et al., 2006; Bandikova et al., 2019). The transplant method is viable because the twin satellites fly in nearly the same orbit, separated by an inter-satellite distance corresponding to a ∼30 second time shift. In that time, it can be assumed that variations in atmospheric drag, solar radiation and Earth albedo are negligible. Save et al. (2006) first developed a "simple" accelerometer data transplant that accounted for an attitude and time correction to generate synthetic GRACE-B accelerometer data for a few weeks in 2002 and 2003. Later, Bandikova et al. (2019) developed the "full" transplant method, which involved an additional thruster spike correction. The use of the GRACE-B "full" transplant non-gravitational accelerations in orbit determination reduced error in the gravity field solutions compared to the "simple" transplant, however, the use of both satellites accelerometer measurements (where available) is still superior (Bandikova et al., 2019).

Each GRACE satellite was equipped with two star camera heads on the $\pm Y_{SRF}$ sides of the spacecraft to observe the absolute orientation of the satellites with respect to the inertial reference frame. The images captured by the star cameras were digitally processed on-board in real-time to generate attitude data as a set of quaternions that contain information on the spacecraft's orientation in space represented by a magnitude and axis of rotation. The attitude observations made by the star cameras were used for the realisation of in-orbit operations and for use in data post-processing. Each of the star camera heads obtained orientation information in the Star Camera Frame (SCF) where Z_{SCF} is the boresight (i.e. optical) axis, X_{SCF} is parallel to the satellites roll axis (Figure 2.3) and Y_{SCF}

completes the right-handed orthogonal system (see Bettadpur, 2012, for details). The star camera mounted on the $-\mathrm{Y}_{SRF}$ side of each of the twin satellites outperformed the other (Herman et al., 2004). However, the differences between each star camera's attitude data were mostly <1 mrad in terms of the inter-satellite pointing pitch angle (Bandikova et al., 2012). Attitude data from the primary star camera (i.e. the star camera pointed away from the Sun) was used to direct instantaneous in-orbit maneuvers to maintain the precise inter-satellite pointing between the antenna horns of the twin spacecraft. Thus, the accuracy of the inter-satellite pointing hinged on, among other things, the accuracy of the star camera measurements and the precision of the in-orbit maneuvers, actuated by the cold gas thrusters and magnetic torquers, which were part of the Attitude and Orbit Control System (AOCS).

The star cameras had an anisotropic accuracy, such that the accuracy of rotations about the X_{SCF} and Y_{SCF} axes, referred to as the cross-boresight axes, were a factor of 8 better than rotations about the weak boresight axis (Z_{SCF}) (Wu et al., 2006). The combined star camera attitude data product had increased accuracy and was therefore used in post-processing of the KBR and accelerometer observations when available. The combined star camera data product was generated by solving for the best estimate of the spacecraft attitude by a weighted least squares inversion, whereby the anisotropic noise distribution of the star cameras is introduced via a weighting matrix (Romans, 2003; Wu et al., 2006). The combined attitude product is a time series of quaternions representing the attitude of the spacecraft in the SRF (Figure 2.3) with the full accuracy for rotations about each of the roll/pitch/yaw (RPY) axes (Wu et al., 2006; Bandikova et al., 2012). The star cameras' field of view was regularly blinded by the Sun and Moon every 161 and 21 days, respectively. During these blinding events, which we call Sun and Moon intrusions, only one of the two star cameras obtained attitude data. Therefore, almost 50% of the time, the high anisotropic noise of the star cameras is propagated into the attitude product used in post-processing (Bandikova and Flury, 2014).

The K-band inter-satellite range data are generated during ground processing by compressing the combined K- and Ka-band ionosphere-corrected dual one-way biased range using a digital low-pass filter in the time domain (Thomas, 1999). The biased range measurements contain range changes introduced by the time of flight of the K-band signal, accounted for by a light-time correction, and an unknown bias. The biased range must also be corrected for geometric range changes introduced by misalignment of the space-

craft attitude variations due to imperfect line-of-sight pointing. The phase centre offset (APO) correction converts the K-band range observations to ranging measurements made between the centre of mass of the satellites instead of between the satellite's antenna phase centres. The range rate and range acceleration measurements, being the first and second time derivative of the filter used to generate the down-sampled biased range, respectively, are also provided with their respective geometric and light time corrections.

Precise attitude observations are required to compute the APO correction, which is calculated during post-processing by rotating the APO vector into the inertial frame using combined (where available) star camera attitude data and taking the dot product with the line-of-sight vector between the two satellites. Attitude data errors degrade the accuracy of the APO corrections, which, in turn, deteriorates the quality of the inter-satellite ranging observations used in temporal gravity field estimation. Attitude data may be degraded due to gaps in the star camera observations, satellite temperature variations, primary star camera head switches, reduced sensitivity to dim stars, and slight variations in the mutual orientation of the star camera heads (e.g. Bandikova et al., 2012; Harvey, 2016). These errors are a significant source of noise in the GRACE models of the temporal gravity field. They impact the accuracy of the APO corrections, the application of the non-gravitational forces during orbit integration and the precision of the inter-satellite pointing controlled by the AOCS during orbit. The variable quality of the two star camera heads further impacted the precision of the spacecraft's inter-satellite pointing, as the AOCS utilised attitude data from a single primary star camera (Bandikova et al., 2012; Inácio et al., 2015).

Investigations of the star camera observations led to improvements in data processing which reduced errors in solutions of the gravity field and the discrepancy between the observed and predicted GRACE baseline errors (e.g. Bandikova and Flury, 2014; Harvey, 2016). Errors were identified in the application of the star camera combination method whereby the noise distribution had been treated as isotropic, propagating the uncertainty of the boresight axis into the combined quaternions (Bandikova and Flury, 2014). This increased the noise in the Y_{SCF} and Z_{SCF} axes by a factor of 3-4, impacting the accuracy of the computed inter-satellite pointing angles (and, therefore, APO correction). This led to the revision of the combination method and the release of a new official combined star camera product. Later, Harvey (2016) identified that twice-per-rev signals in the star camera data were due to the wrong reference frame information being used to compute

the stellar aberration correction. This mis-modelling was also accounted for in future data releases (Harvey, 2016).

The inter-satellite ranging measurements contain significant high-frequency noise attributed to the limited accuracy of the KBR sensor at high frequencies (i.e. >10 mHz) (Flury et al., 2008; Ditmar et al., 2012). The process of compressing the observations reduced noise due to oscillator instability; however, some oscillator noise and system noise, amongst other sources, remained in the inter-satellite observations (Kim, 2000). Because differentiation amplifies short-wavelength signals, the range acceleration contained better-localised high-frequency gravity signals but also contained more noise than the range rate measurements (Save et al., 2012). Therefore, the inter-satellite range rate is traditionally used as the inter-satellite observable for GRACE gravity inversions (e.g. Tapley et al., 2004). GRACE range acceleration solutions of the temporal gravity field have also been produced but do not use the noisy range acceleration measurements generated during ground processing (Tregoning et al., 2017).

Several studies have investigated the characteristics and sources of excessive high-frequency noise in the GRACE inter-satellite measurements. For example, Ko et al. (2012) found that excessive high-frequency noise was correlated with degraded ranging system signal-to-noise ratio (SNR) measurements but did not establish the source of the SNR variations. Later, Harvey et al. (2017) analysed the SNR measurements and identified that poor SNR values of the K-band frequency of GRACE-B were correlated to variations in temperature recorded near the ranging system. They also demonstrated that SNR dips in the K- and Ka-band frequency of GRACE-B and GRACE-A, respectively, occurred during star camera Sun intrusions. Goswami et al. (2018) found that SNR dips attributed to temperature effects significantly degrade the quality of the ranging observations. Additionally, they found that there are effects in SNR values related to Moon intrusions and magnetic-torquer rod currents along the equator, in addition to the effects previously identified by Harvey et al. (2017).

Towards the end of the mission, the KBR system (often in conjunction with the accelerometers) was switched off over extended periods during low $|\beta|'$ angles to decrease the reliance on degraded batteries and fuel consumption and increase mission longevity (Figure 2.5a). From 2015, the KBR system was often intermittently switched off once per revolution for the portion of the orbit when the satellites were in shadow, leaving large sections of the Earth's gravity field unobserved. This occurred at intermediate values of

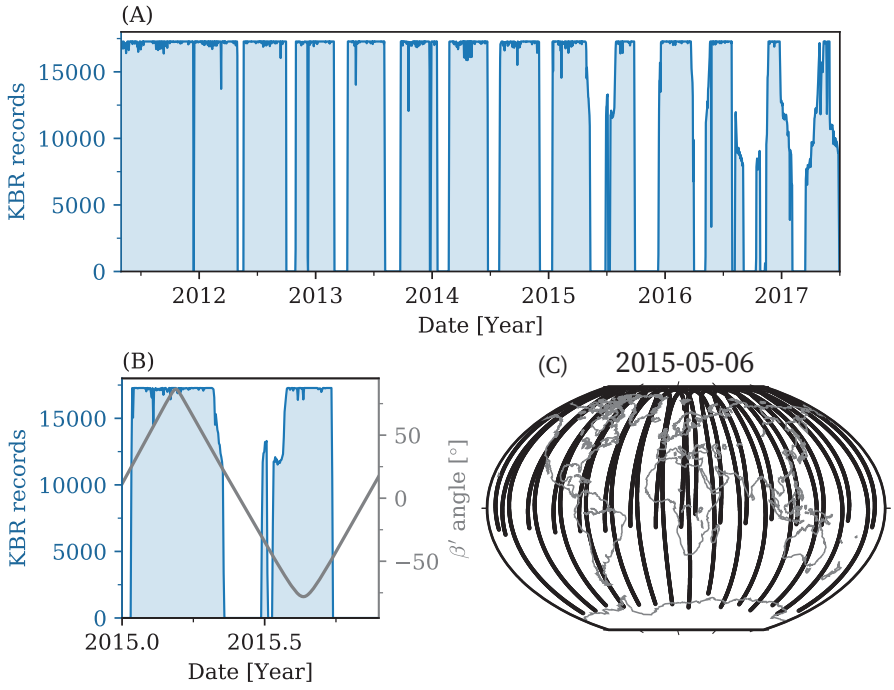

Figure 2.5: Daily KBR records provided in the Level-1B GRACE data product after battery capacity was reduced (a) from April 2011 until the missions end, (b) daily KBR records over a β' cycle in 2015 showing missing data during periods of extended shadow time, (c) spatial plot of KBR records over a 24-hour period of observations on 2015-05-06 where periods of extended shadow time.

$|\beta|'$ before and after the KBR system was switched off entirely during periods of maximum shadow time (Figure 2.5b). From 2015, inter-satellite observations are often either unavailable or significantly reduced over large portions of the Earth. For example, during the 24-hour arc of observations obtained on 2015-05-06, almost no inter-satellite records are available over the Antarctic ice sheet. At the same time, only half of the ground tracks are available South of -10° latitude when the satellites' descending pass was in eclipse (Figure 2.5c).

The measures adopted to reduce reliance on failing batteries during the second half of the GRACE mission resulted in observations only being available during periods of high $|\beta|'$ angles. Once the satellites' thermal control systems were disengaged, high $|\beta|'$ angles became the cause of internal temperature variations outside the range for optimal operation of instrumentation. These thermal variations degraded the quality of the non-gravitational acceleration observations (Klinger and Mayer-Gürr, 2016) and increased the SNR of the KBR observations (Harvey et al., 2017). The accuracy of the attitude and orbit control system was also impacted during high $|\beta|'$ angles due to Sunlight intrusions into the star cameras field of view (Goswami et al., 2018). As a result, the portion of the

time series of mass anomaly estimates corresponding to the second half of the GRACE mission suffers from missing months and reduced accuracy due to the temporal gravity field solutions becoming particularly susceptible to error propagation (Landerer et al., 2020). Increasingly significant observational gaps and the limited accuracy of the accelerometer transplant product further degraded the quality of mass anomaly estimates during the mission's final year (Landerer et al., 2020). After years of reduced operation to extend the longevity of the GRACE mission despite power constraints, the GRACE-B batteries eventually failed, ending the GRACE mission in October 2017 after 15 years and six months of operation.

2.1.2 GRACE Follow-On (GRACE-FO)

The GRACE-FO mission (Landerer et al., 2020) was launched in May 2018, 7 months after the decommissioning (in October 2017) of its highly successful predecessor, the GRACE mission. The primary objective of the GRACE-FO mission is to provide the measurements necessary to continue the GRACE record of global surface mass changes from observations of the Earth's gravity field. As with GRACE, the GRACE-FO satellites were launched in a tandem near-circular low Earth orbit at an altitude of ∼490 km (see Figure 2.2), with a separation of 220 ± 50 km and a near-polar inclination of 89°. The GRACE-FO spacecraft are essentially duplicates of the GRACE spacecraft but with a few differences. These include enhancements to the KBR, GPS receivers and accelerometers, designed to increase the accuracy of the instruments and reliability of the measurements. Notably, the SCA was increased from two to three star camera heads per GRACE-FO satellite to increase attitude data availability and quality during Sun and Moon intrusions, which were the cause of significant attitude data degradation and gaps during the GRACE mission (Goswami et al., 2018).

The most substantial addition to the GRACE-FO satellites is the inclusion of a Laser Ranging Interferometer (LRI) for the observation of precise inter-satellite ranging using a laser link between the spacecraft (Sheard et al., 2012). The LRI operates alongside the KBR, which obtains inter-satellite ranging measurements simultaneously. The ranging measurements obtained by the KBR microwave instrument remain the primary inter-satellite observations for use in gravity field estimation from GRACE-FO. This additional LRI instrumentation aims to fulfil the secondary objective of the GRACE-FO mission: to demonstrate for the first time that inter-satellite laser ranging is a viable technology for

future space gravity missions.

Both GRACE-FO satellites were fitted with a primary and redundant IPU. In July 2018, the primary IPU on GRACE-D was powered down due to indications that the IPU was using less current than expected (Webb et al., 2018). In response, the switch was made to the redundant unit; the switchover was deemed a success in October 2018 during the in-orbit checkout phase (Webb et al., 2018). Currently, the GRACE-FO mission is in the science operations phase, having completed the in-orbit checkout phase in January 2019. The first suite of Level-1B GRACE-FO data necessary to generate estimates of the temporal gravity field was released in May 2019. Before the release of GRACE-FO data, a data validation period was conducted and indicated that mission system performance satisfied the requirements of continuing the record of GRACE-generated gravity field models. Furthermore, the GRACE-FO measurements contain comparatively less noise in the KBR inter-satellite ranging product and the combined star camera attitude data product (Landerer et al., 2020).

The superior in-orbit performance of the LRI was established early in the GRACE-FO mission, with reports of the first ranging measurements confirming that the LRI measures the biased inter-satellite range with nanometer precision and with significantly less noise compared to the range measurements simultaneously obtained by the KBR (Abich et al., 2019). Indeed, Ghobadi-Far et al. (2020a) found that the LRI is sensitive to gravity field anomalies at spatial resolutions of 100-200 km at 0.1 nm/s^2, an improvement of an order of magnitude compared to the KBR. Despite these demonstrable improvements, early results suggest that the resolution of temporal gravity models from GRACE-FO remain primarily limited by instrumental (i.e. star camera and accelerometer) noise and background model errors and not necessarily the precision of the inter-satellite ranging measurements (Peidou et al., 2021).

Early in the mission, it was discovered that the accelerometer measurements from both GRACE-FO satellites (GRACE-C and GRACE-D) were contaminated by heightened levels of spurious signals compared to GRACE, with different noise characteristics for each satellite. Both satellites' accelerometer data contain unrealistic non-gravitational accelerations as a response to thruster firings and other large spurious "phantom" accelerations that appear to be geographically or orbitally correlated. After only a month in orbit, the GRACE-D accelerometer degraded further. In addition to noise in response to thruster firings and phantom accelerations, significant and frequent bias jumps appeared on all axes,

often during thruster firings. Due to the compounding errors, the GRACE-D accelerometer measurements are better inferred from the GRACE-C accelerometer measurements for use in precise orbit determination. The synthetic GRACE-D accelerometer measurements are generated using a similar transplant approach to that used for the last seven months of the GRACE mission, whereby the time corrected and yaw-rotated GRACE-C accelerometer observations are used in place of the GRACE-D non-gravitational accelerations (Bandikova et al., 2019; Harvey et al., 2021). In addition, the GRACE-D thruster information is used to accurately insert residual thruster-induced accelerations into the GRACE-D accelerometer transplant data (Bandikova et al., 2019; Harvey et al., 2021).

As with GRACE, GRACE-FO solutions that include the accelerometer transplant data poorly recover some low degree (i.e. $C_{2,0}$ and $C_{3,0}$) components of the gravity field compared to solutions that utilise both satellites' non-gravitational accelerations when available (Loomis et al., 2020). Increased noise in estimates of the low degree coefficients that describe Earth's dynamic oblateness impacts the accuracy of Antarctic and Greenland ice sheet mass change estimates (Loomis et al., 2019b, 2020). Improved recovery of both high and low degree components has been achieved using an alternative approach to generating the GRACE-D non-gravitational accelerations (Behzadpour et al., 2021). This approach involved a pitch correction, the incorporation of non-gravitational force models and the application of a drag model correction into the transplant procedure, which showed the most significant improvements to gravity recovery during periods of full-Sun orbit (Behzadpour et al., 2021). An alternative optimal calibration approach is presently being developed that will partially utilise the real non-gravitational accelerations measured by the GRACE-D accelerometer to further reduce accelerometer related errors (Landerer et al., 2020). In the meantime, both low-degree zonal components of the gravity field need to be replaced with estimates derived from SLR measurements.

Analysis of GRACE and GRACE-FO global gravity field models has demonstrated that GRACE-FO achieves a similar to slightly improved spatial resolution and accuracy compared to GRACE (Landerer et al., 2020). Furthermore, the GRACE and GRACE-FO time-series of surface mass change match well with independent mass change estimates from surface mass balance methods (Velicogna et al., 2020; Ciracì et al., 2020) and TWS reconstructions (Landerer et al., 2020). Independent mass change estimates conveniently bridge the 11-month gap between the missions, demonstrating that no inter-mission biases exist. Thus, GRACE-FO continues to successfully extend the original GRACE record,

satisfying the primary objective of the mission (Landerer et al., 2020).

Like the GRACE mission, the GRACE-FO mission lifespan is expected to be five years. Additional operation lifetime is anticipated but is dependent on instrument behaviour, battery longevity, fuel consumption and the influence of solar activity on the atmospheric-induced decay of the satellites (Tapley et al., 2019). The extended lifespan of the GRACE mission was primarily due to particularly low levels of solar radiation, which slowed the altitudinal decay of the satellites; however, the GRACE-FO mission may not benefit from the same conditions (Tapley et al., 2019). Presently, reduced fuel consumption compared to GRACE provides confidence that the GRACE-FO mission lifespan will be extended beyond five years (Landerer et al., 2020). GRACE-FO Level-1B observational data are available from a week after the launch date. They are updated on an approximately weekly basis, with an approximate 3-week lag, meaning that estimates of the Earth's temporal gravity field can be computed in near real-time.

2.1.3 Data products

The GRACE and GRACE-FO missions provide the observations necessary for temporal gravity field estimation primarily via the inter-satellite measurements, which capture the perturbation effects of the static and temporal gravity field. The GPS receivers, star cameras and accelerometers onboard each spacecraft also provide measurements essential for accurate orbit modelling. The GRACE and GRACE-FO data products are organised into sequential "levels", processed and archived in a shared Science Data System (SDS) between the German Research Centre for Geosciences (GFZ), the Jet Propulsion Laboratory (JPL), NASA, and Center for Space Research (CSR) at the University of Texas. The scientific community can access Level-1B to Level-3 data products (described below) via the Physical Oceanography Distributed Active Archive Center (PO.DAAC) operated by JPL and at the Integrated System and Data Center (ISDC) operated by GFZ, along with data product documentation, release notes, user handbooks and monthly newsletters. The newsletters include (amongst other things) updated mission status, orbit configuration and Level-1 data processing notes. These documents are cited throughout this thesis.

2.1.3.1 Science instrument and housekeeping data

Level-0

The science instrument and housekeeping data are provided in Level-0 and Level-1. The

Level-0 data products include two data files (science and housekeeping) per satellite which contain information on telemetry data from each downlink pass received and archived by the Raw Data Center of the Mission Operation System located in Germany.

Level-1A

Level-1 instrument data processing is a two-step procedure developed and operated by JPL. The first step involves the non-destructive processing from Level-0 to Level-1A. The Level-1A processing includes converting binary encoded measurements to engineering units, time-tagging, editing, reformatting and quality control. The Level-1A data are available to the scientific community for GRACE-FO but not for GRACE.

Level-1B

The second step is the possibly irreversible processing from Level-1A to Level-1B. The Level-1B processing produces resampled, downsampled, filtered data in the SRF that has been correctly time-tagged. The GRACE and GRACE-FO Level-1B data products contain all the necessary inputs for the precise orbit determination of the GRACE and GRACE-FO satellites and gravity field inversion. The Level-1B data suite also includes additional "housekeeping" data that contain information on the status of some instrumentation and calibration data and ancillary data products needed for further processing. The available Level-1B suite of data products relevant to this study are described below.

KBR1B

The KBR precisely measures the changes in the line-of-sight distance between the satellite pairs by measuring the phase change of microwave (K and Ka-band) signals sent between the respective antenna phase centres that point to the other satellite. The K-Band Ranging data product (KBR1B) reports this measurement via the dual one-way biased ranges (i.e. the true range plus an unknown bias), which have been compressed using a digital filter, where the filter is N self-Convolutions of a Rectangular time-domain window function (CRN) (in this case, N = 7) and the time window is 70.7 seconds, downsampling the signal from 10 Hz to 5-second measurements (see Thomas, 1999; Case et al., 2010, for details). The KBR1B also provides the range rate (KBRR) and range acceleration (KBRA) generated from the 10 Hz biased ranges, the first time derivative and the second time derivative of the CRN filter used to create the 5-second ranges, respectively. However, the KBRA contains significant high-frequency noise.

The KBR1B also provides a range, range rate and range acceleration light-time correction, which accounts for the distance travelled by both satellites during the transmission

and reception of the K-band signal, which is necessary for converting the observed biased range into an instantaneous range, range-rate or range-acceleration. Range, range-rate and range-acceleration geometric corrections (i.e. antenna phase offset) are also provided to reduce the K-band ranging data to the centres of mass of the satellites.

LRI1B

In addition to the KBR, the LRI also provides information on the distance between the GRACE-FO satellites. The Laser Ranging Interferometer data product (LRI1B) contains the LRI measured biased range, which has been downsampled to 2-second intervals using the CRN filter, which also outputs the first two time derivatives being the range rate and range accelerations. As with the KBR1B data product, the light time and geometric corrections are also provided.

SCA1B

The star camera assembly provides the information required for precise attitude referencing of each satellite. The Star Camera data product (SCA1B) includes the combined (when available) quaternions from each available star camera (up to two and three for GRACE and GRACE-FO, respectively) at 5-second intervals per satellite. The star cameras were subject to blinding by the Moon and the Sun at times; however, data is always available for at least one (two) star camera(s) at most times during the GRACE (GRACE-FO) mission.

ACC1B

The Accelerometer data product (ACC1B) provide the non-gravitational accelerations of the proof mass located at the centre of mass of each satellite. The linear and angular accelerations about the along-track, cross-track and radial axes of each spacecraft are included in the ACC1B data product. The ACC1A data are processed to produce the ACC1B product, which includes time corrections and CRN filtering, producing the corrected 1-second linear accelerations in the SRF (see Wu et al., 2006, for details). The ACC1B data product is only available for the GRACE mission.

ACT1B

For the seven months of unavailable GRACE-B accelerometer measurements, a synthetic Accelerometer Transplant (ACT1B) data product is available for GRACE-B that is based on the "full" accelerometer transplant of Bandikova et al. (2019). The transplant is created by removing the thrust spikes from the GRACE-A Level-1A non-gravitational accelerations (ACC1A), correcting for the variable position and orientation (about the pitch and

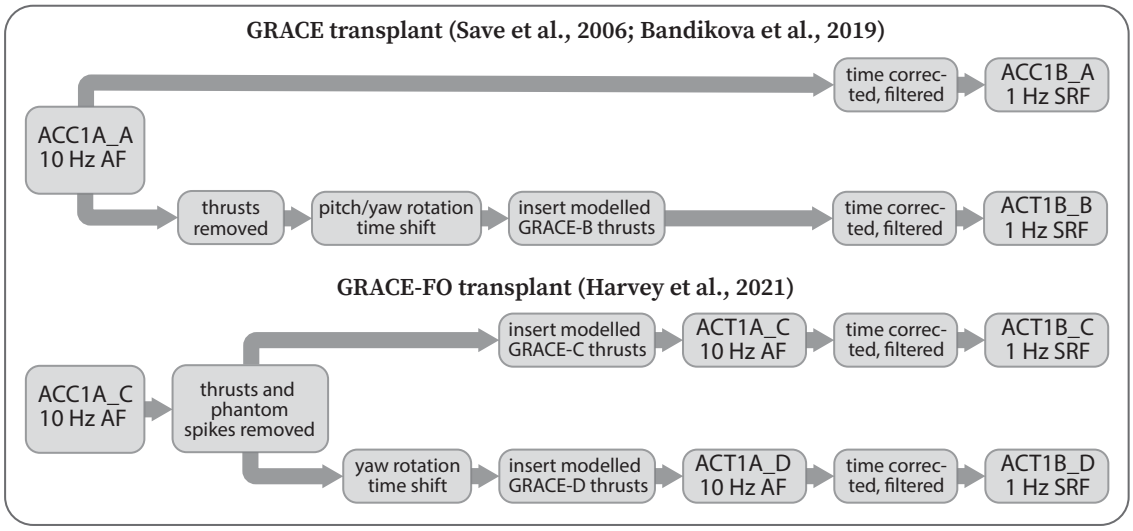

Figure 2.6: Level-1 processing procedure for the GRACE and GRACE-FO the Accelerometer Transplant (ACT1B) data product

yaw axes) of the satellites then inserting a model of GRACE-B thrust spikes (Save et al., 2006; Bandikova and Flury, 2014). These synthetic GRACE-B accelerations are then filtered and time corrected as per Wu et al. (2006), producing the GRACE-B ACT1B data product (Figure 2.6).

For the GRACE-FO mission, the ACT1B data product is available for both satellites and is the only available Level-1B accelerometer data product. A specific calibration procedure was developed for each GRACE-FO satellite accelerometer by the SDS team (McCullough et al., 2019; Harvey et al., 2021). The GRACE-FO ACT1B data product aims to enable more optimal gravity field recovery by mitigating the additional noise contained in the non-gravitational accelerations of both GRACE-FO satellites, which were not apparent in the GRACE mission. The specific noise characteristics of the GRACE-FO accelerometer observations are detailed in Section 2.1.2.

The GRACE-C and GRACE-D accelerometers contain different noise characteristics, with GRACE-D having significantly more noise. The GRACE-D observations include high-frequency error and bias jumps related to thruster firings, rendering the GRACE-D accelerometer measurements too inaccurate for use in precise orbit determination (McCullough et al., 2019). Therefore, the GRACE-D ACT1B has been synthetically created by transplanting the accelerometer data from GRACE-C to produce the Level 1A non-gravitational acceleration data (Figure 2.6). The creation of the ACT1A data product for both satellites begins with removing outlier "phantom" accelerations and accelerations that occur at or near thruster firings from the GRACE-C ACC1A data. To create the

GRACE-D ACT1B, these edited GRACE-C accelerations are then rotated 180° about the radial axis and time-shifted to account for differences in satellite position; a pitch correction is not applied (Harvey et al., 2021). A time series of modelled thruster firings are created for each satellite individually using their respective thruster housekeeping data. These accelerations are then inserted into the time series, the final step of ACT1A generation.

The ACT1A for both satellites are then processed to produce an ACT1B data product which includes time corrections and CRN filtering, producing the corrected 1-second linear accelerations of the ACC proof mass. The ACT1B data contains the same information as the GRACE ACC1B data product but without angular accelerations. The full GRACE-D transplant was only performed after the accelerometer error increased in June 2018. Before that, the GRACE-D ACT1B were produced as per the GRACE-C ACT1B.

GNV1B

The GPS Navigation format record (GNV1B) provides the Earth-fixed location (i.e. position, velocity and formal errors) of the satellites in the International Terrestrial Reference Frame (ITRF).

AOD1B

The Atmosphere Ocean and De-aliasing (AOD1B) product is an ancillary product generated by GFZ. The AOD1B contains spherical harmonic coefficients that represent the pressure and mass variations induced by transient weather systems at high spatial (up to degree and order 180) and temporal (3 hour) resolutions (Dobslaw et al., 2017b). These non-tidal atmosphere and ocean mass variations need to be included as a background model for precise orbit determination to avoid artefacts from temporal aliasing of these signals into the estimates of the temporal gravity field (Dobslaw et al., 2013).

Housekeeping data

The suite of housekeeping data includes several ancillary data products that provide instrument health and calibration information. Notably, the Accelerometer Housekeeping data (AHK1B) includes information on accelerometer temperature and proof mass voltage which can be used for accelerometer calibration. Other useful housekeeping products include the THR1B data, which provides thruster activation data. The Cold Gas Tank data (TNK1B) provides pressure and temperature measurements and some auxiliary data for the centre of mass management. The Magnetometer and Magnettorquer data (MAG1B) includes magnetic torque rod activation data. Spacecraft Mass data (MAS1B), IPU House-

keeping data (IHK1B), and information on the On-Board Data Handling (OBDH) time to GPS receiver time (TIM1B) are also available.

2.1.3.2 Gravity field products

Level-2

Level-2 data products are produced by several processing centres that have each independently developed in-house processing software to generate precise orbit and gravity field models from the Level-1B data and background models. Level-2 data products are routinely provided by the members of the SDS team (i.e. JPL, GFZ and CSR) and are publicly available. The SDS Level-2 data include the monthly estimates of the Earth's temporal gravity field in the form of dimensionless Stoke's coefficients at least up to spherical harmonic degree and order 60, which require some post-processing before analysis. The Level-2 products also include ancillary data sets of the average atmospheric and oceanic mass variations derived from AOD1B.

Level-3

The SDS also provides an additional Level-3 gridded surface mass anomalies data product derived from their Level-2 spherical harmonic solutions. These monthly temporal gravity field grids are in units of equivalent water height and have already been post-processed, ready for analysis by the user. The post-processing steps are standard across the SDS teams. They include the addition of ocean loads removed during processing (Dobslaw et al., 2017a), the removal of GIA effects (Peltier et al., 2018), decorrelation (Swenson and Wahr, 2006), Gaussian smoothing (Wahr et al., 1998), replacement of the poorly estimated low degree zonal harmonics (Loomis et al., 2019b), geocentre (Sun et al., 2016b) and ellipsoidal (Ghobadi-Far et al., 2019b) corrections.

Outside of the SDS, several research groups also provide GRACE and GRACE-FO gravity field products at a variety of spatial and temporal resolutions in the form of Stoke's coefficients or mass concentration (mascon) grids (e.g. Mayer-Gürr et al., 2016; Lemoine et al., 2018; Loomis et al., 2019a). The SDS also provides monthly mascon solutions of the temporal gravity field (Save et al., 2016; Wiese et al., 2016) as an addition to the official publicly available GRACE Level-2 and Level-3 products.

2.2 GRACE and GRACE-FO data analysis

The generation of GRACE and GRACE-FO temporal gravity field products is a multi-step process that begins with modelling the satellite orbits by integrating the various external forces acting on the spacecraft. This process is often referred to as precise orbit determination and utilises information from external forcing models and GRACE or GRACE-FO Level-1B data. Theoretical inter-satellite measurements are derived from the position and velocity of the modelled satellite orbits, which, compared to the observed inter-satellite measurements, do not contain the accelerations induced by components of the temporal gravity field. The observed minus computed residuals contain the unmodelled components of the temporal gravity field, which can be recovered by solving for adjustments to satellite orbit and gravity field parameters.

The temporal gravity field is typically parameterised by spherical harmonic coefficients or mascons as the basis functions. Post-processing methods are applied to spherical harmonics and mascon gravity field solutions to reduce noise and correct specific signals or model deficiencies. When using mascons, the inversion is stabilised by applying constraints to the mascon parameters using a regularisation strategy. Regularisation can be customised to best suit specific spatial and temporal characteristics of the expected temporal gravity field signal and is necessary for mitigating high-frequency noise and parameter correlations. The following sections summarise the general process for precise orbit determination and accurate temporal gravity field estimation from GRACE and GRACE-FO data.

2.2.1 Orbit determination

2.2.1.1 Equations of motion

The measurement of GRACE and GRACE-FO inter-satellite ranging is directly related to the spacecraft's trajectory (i.e. position and velocity). The orbits of the satellites are influenced by the various accelerations acting on them, which can be modelled numerically using dynamical equations of motion. The equations of motion are identical for each pair of GRACE and GRACE-FO twin satellites. They include the accelerations due to gravitational, non-gravitational and empirically modelled forces acting on the satellites:

$$\ddot{\vec{r}} = f_g + f_{ng} + f_{emp} \tag{2.1}$$

where $\ddot{\vec{r}}$ is the second derivative of the position vector, f_g contains the gravitational forces, f_{ng} contains the non-gravitational forces and f_{emp} are empirically modelled forces. The gravitational accelerations include direct planetary perturbations (e.g. Folkner et al., 2009) and geopotential perturbations derived from a suite of background forcing models. Here, 'geopotential' refers to the gravitational potential of the solid Earth and its surface fluid and gaseous envelopes. The geopotential perturbations include the mean and static gravity field (e.g. Tapley et al., 2007; Bruinsma et al., 2013), non-tidal atmosphere and ocean (e.g. Dobslaw et al., 2017b), atmospheric (e.g. Ray and Ponte, 2003), oceanic (e.g. Carrere et al., 2015; Lyard et al., 2021) and solid Earth tides (e.g. McCarthy, 1992; Wahr et al., 2015) and indirect planetary perturbations. General relativistic perturbations are also included in the forcing model (e.g. Petit and Luzum, 2010).

The geopotential perturbations, having been evaluated in the terrestrial reference frame, need to be rotated into the inertial (i.e. celestial) reference frame. The International Terrestrial Reference Frame (ITRF) is defined by a rotating Earth-centred, Earth-fixed coordinate system with the origin of the terrestrial reference system at Earth's centre of mass (Figure 2.7) (Petit and Luzum, 2010). Earth's axis of rotation defines the Z-axis, and the X-axis is determined by the intersection between the Greenwich (i.e. prime) meridian and the equatorial plane. The Y-axis completes the right-handed coordinate system. The International Celestial Reference Frame (ICRF) is also geocentric but fixed with respect to the stars (i.e. non-rotating) (Petit and Luzum, 2010). The vernal equinox at epoch J2000.0 defines the X-axis and the Z-axis is normal to the mean equatorial plane at epoch J2000.0 (Figure 2.7) (Petit and Luzum, 2010).

Transformation of the geopotential accelerations from the terrestrial reference frame to the inertial reference frame requires knowledge of Earth's precession, nutation, rotation and polar motion. This accounts for periodic variations in the orientation of Earth's rotation axis due to the gravitational attraction of celestial bodies and Earth's mass distribution. The information needed to perform these rotations, including the contributions of general relativity (i.e. lense-thirring effect and de Sitter precession), are provided by the International Earth System and Rotation Service (IERS) (e.g. McCarthy, 1992; Petit and Luzum, 2010).

The non-gravitational forces (i.e. solar radiation pressure, atmospheric drag and Earth albedo) are measured by the accelerometers onboard the GRACE and GRACE-FO satellites and must be accounted for during orbit integration. These forces must be rotated from

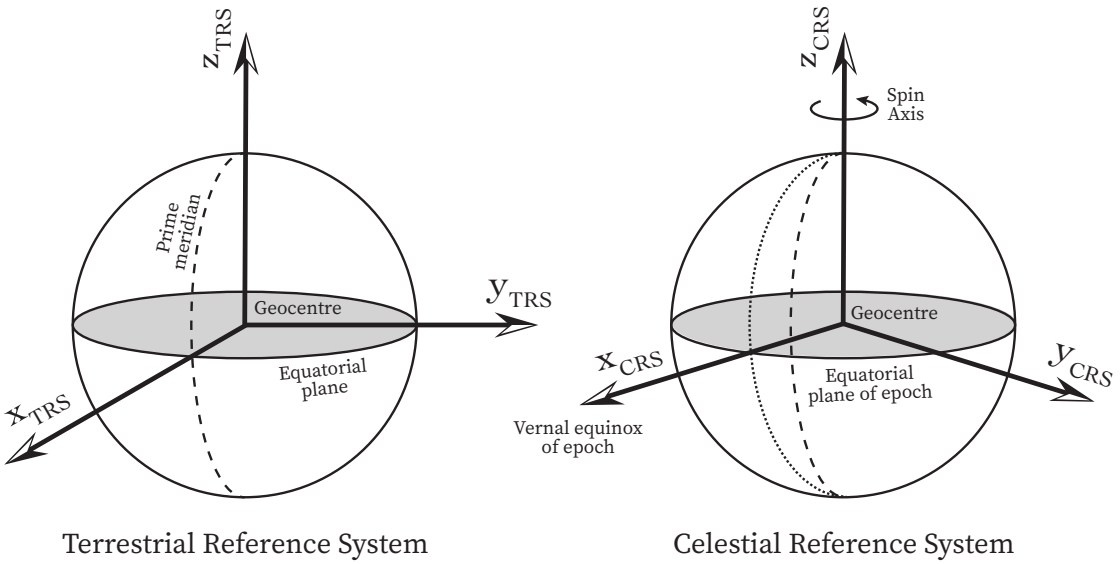

Figure 2.7: Coordinates of the (left) rotating terrestrial reference system and (right) inertial celestial reference system.

a body-fixed (i.e. satellite) reference frame (Figure 2.4) to the inertial frame of reference, which is achieved using the combined attitude quaternions contained in the star camera Level-1B data product. The integration of the equations of motion is then performed on the sum of the time-variable non-gravitational, gravitational and empirical accelerations in the inertial reference frame.

2.2.1.2 Gravitational accelerations

The background gravity model includes the gravitational forces, f_g, acting on the satellites and differs from the actual gravity field primarily because of the omission of the temporal signals. The background gravity model includes the static gravity field and some temporally varying components. Using a comprehensive background gravity model improves the prediction of the parameter values by reducing the adjustments required to the a priori values to account for the observed inter-satellite range changes during least squares inversion.

Spherical harmonic expansion is a mathematically convenient and computationally efficient method (to represent functions defined on the surface of a sphere) that has been widely utilised in many satellite geodesy studies for many decades. The background gravity model at time t can be represented using a spherical harmonic expansion with time-variable coefficients. If GM is the gravitational constant and R is the mean equatorial radius of the Earth, the geopotential acceleration U_s, at an exterior field point with geocentric radius

r, geographic latitude ϕ, and longitude, λ is:

$$U_s(r,\phi,\lambda,t) = \frac{GM}{r} + \frac{GM}{r}\sum_{l=2}^{L_{MAX}}\left(\frac{R}{r}\right)^l \sum_{m=0}^{l} \overline{P}_{lm}(\sin\phi)[\overline{C}_{lm}(t)\cos m\lambda + \overline{S}_{lm}(t)\sin m\lambda] \tag{2.2}$$

where $\overline{P}_{lm}(sin\theta)$ are the fully normalised Legendre Polynomials, $\overline{C}_{lm}$ and $\overline{S}_{lm}$ are the fully normalised cosine and sine dimensionless Stoke's coefficients of degree l and order m. The degree and order of a spherical harmonic expansion represent the zonal (latitude dependent) and sectoral (longitude dependent) harmonics. As the degree and order increase to a maximum (L_{MAX}), the coefficients capture the higher frequency spatial variations of the background gravity model.

Most of the non-spherical geopotential accelerations acting on the satellites are due to the Earth's static gravity field. The mean gravity field used in GRACE and GRACE-FO data analysis typically includes some combination of data from various modern satellite gravimetry missions (e.g. CHAMP, GOCE, GRACE) which account for components of the gravity field at various temporal and spatial resolutions (e.g. Bruinsma et al., 2013; Förste et al., 2014; Ries et al., 2011). The spherical harmonic coefficients of the mean gravity field are typically included in the background gravity model truncated to a high degree and order. In their most recent GRACE Level-2 product release (RL06), Dahle et al. (2019) included the background gravity model of Förste et al. (2014) complete to $L_{MAX} = 200$. Watkins et al. (2015) and Save et al. (2016) included the background gravity field model of Ries et al. (2011), complete to $L_{MAX} = 180$ and $L_{MAX} = 360$, respectively.

Sub-monthly atmospheric pressure variations, ocean surface currents and precipitation events are measured by the GRACE and GRACE-FO satellites (Dobslaw et al., 2013). Due to the limited ground track coverage of the GRACE and GRACE-FO satellites, short-term variations in the gravity field, such as these, cannot be accurately estimated. The contribution of these non-tidal mass variations to the gravity field are provided in the AOD1B product as dimensionless Stoke's coefficients every 3 hours, complete to $L_{MAX} = 180$ (Flechtner, 2007; Dobslaw et al., 2017b). The accelerations induced by these non-tidal atmosphere and ocean variations must be included in the background gravity model for precise orbit determination to avoid artefacts of temporal aliasing of such high-frequency signals into the temporal gravity field estimates (Dobslaw et al., 2013).

The background gravity models must also account for the accelerations induced by

semi-diurnal, diurnal and long-period solid Earth and ocean tides. Solid Earth and ocean tides occur due to the gravitational forces of the Moon and Sun, causing elastic deformation of the Earth and vertical movement of the sea surface. Solar heating of the atmosphere also causes atmospheric tides, primarily at diurnal (S_1) and semi-diurnal (S_2) frequencies. The magnitude of atmospheric tidal variations are significantly smaller than the non-tidal atmospheric variations but need to be accounted for in the background gravity model (Ray and Ponte, 2003). Atmospheric tides are provided as an additional AOD1B product (Dobslaw et al., 2017b). Pole tides are the response to variations in centrifugal force due to polar motion and affect the $C_{2,1}$ and $S_{2,1}$ spherical harmonic coefficients (Desai, 2002). Solid Earth pole tides and ocean pole tides must also be accounted for in the background gravity model (Petit and Luzum, 2010).

Indirect celestial perturbations are also accounted for in the background gravity model. These include the point mass attraction of the planets on the Earth and the interaction between the Sun and Moon on Earth's dynamic oblateness (i.e. indirect J2 effect), which impacts the $C_{2,0}$ spherical harmonic component variations (Petit and Luzum, 2010; Sun et al., 2016a). The perturbing accelerations arising from n-point masses (i.e. the Sun, Moon and planets) are computed in the inertial reference frame, unlike the geopotential perturbations. Celestial perturbations due to the direct attraction of the planets on the satellites are calculated using point mass formulations. The calculation of these direct and indirect celestial body induced accelerations requires accurate knowledge of the planetary and lunar ephemerides (e.g. Folkner et al., 2009).

2.2.1.3 Non-gravitational accelerations

Orbit perturbations are induced by non-gravitational forces acting on the satellites, such as solar radiation pressure, Earth albedo, atmospheric drag and thruster spikes due to the misalignment of the cold gas thrusters. Non-gravitational linear and angular accelerations in the along-track, cross-track and radial axes are provided in the Level-1B accelerometer data in the satellite reference frame (Figure 2.8). The accelerations induced by non-gravitational forces, f_{ng}, are modelled using the linear accelerations provided in the Level-1B accelerometer data, f_{acc}, corrected for a bias offset and instrument scale:

$$f_{ng} = q \otimes [b + S \times f_{acc}] \tag{2.3}$$

where $q\otimes$ represents the rotation from the satellite frame into the inertial frame, achieved

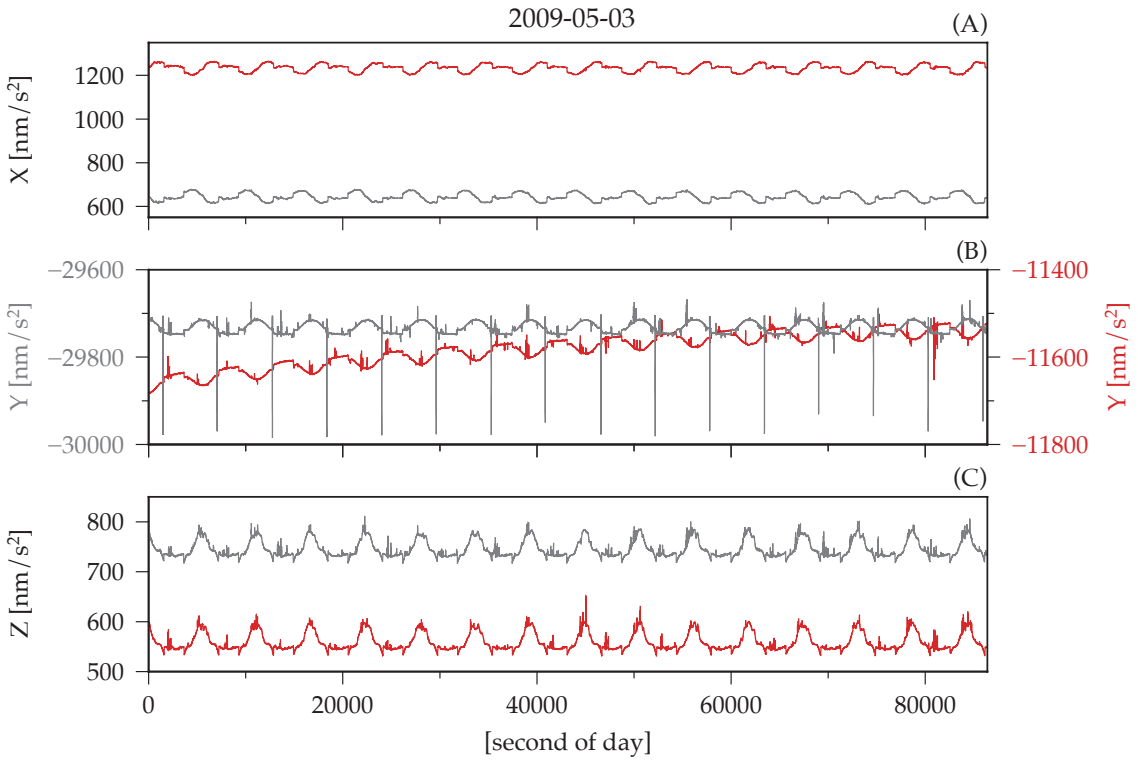

Figure 2.8: 2009-05-03 GRACE-A (red) and GRACE-B (grey) uncalibrated accelerometer observations in the (a) along-track, (b) cross-track and (c) radial directions showing the bias offset and repeating pattern of the observations per revolution.

using the attitude quaternions provided in the combined star camera Level-1B data; b is an empirical bias vector and S is a 3×3 matrix (diagonal or fully-populated) containing the scale factors. Both b and S contain estimable bias and scale factor parameters for the along-track, cross-track and radial axes of the Level-1B accelerometer observations.

The Level-1B accelerometer observations also contain noise induced by heater switches, magnetic torquer generated signals and thermal variations (Flury et al., 2008; Klinger and Mayer-Gürr, 2016; Peterseim et al., 2012) which may degrade the integration of the satellite orbits. To maintain the accuracy of the modelled orbits, the effects of temperature variations on the accelerometer observations must be accounted for. Different bias vector parameterisations have been developed to account for sub-daily low-frequency bias drift due to thermal variations, which degrade the along-track and cross-track observations (Figure 2.8). At low frequencies, temperature-induced bias drift is the dominant source of accelerometer noise (Klinger and Mayer-Gürr, 2016). Sub-daily variations in bias drift are particularly prevalent in the measurements after thermal control of the GRACE mission was deactivated in April 2011 and during periods of reduced thermal management before this date.

Most commonly, multiple bias parameters are estimated each day, particularly in the less-sensitive cross-track axis, to account for sub-daily bias variation (e.g. Dahle et al., 2014; Klinger and Mayer-Gürr, 2016; Luthcke et al., 2013). For example, Dahle et al. (2014) estimated nine accelerometer biases per axis per day. Watkins et al. (2015) estimated three-hourly accelerometer cross-track biases and once per day along-track and radial biases. They also estimate an empirical rate vector to account for thermal variations in the along-track and cross-track axes from 2010. Conversely, Luthcke et al. (2013) estimated accelerometer biases every three hours in the along-track and radial components, but only once per day in the less-sensitive and more variable cross-track axis.

Adjusting for multiple accelerometer biases within a single day could potentially introduce discontinuities in the accelerometer observations. The approach of Klinger and Mayer-Gürr (2016) ensures continuity within a single day by estimating accelerometer biases using uniform cubic basis splines with 6-hour knot intervals, requiring a total of 21 bias parameters per satellite per day. In addition, Klinger and Mayer-Gürr (2016) developed an accelerometer calibration technique to account for cross-talk (i.e. non-orthogonality of the accelerometer axes) and the misalignment of the Accelerometer Frame (AF) with the Science Reference Frame (SRF) (Figure 2.4) (Kim, 2000). Their method requires the estimation of an additional six parameters per satellite, populated in the off-diagonal elements of the scale factor matrix. This bias and scale factor parameterisation was adopted by Kvas et al. (2019) to generate their most recent GRACE gravity field time series (ITSG-Grace2018).

Estimating empirical accelerations may mitigate the effects of errors in the forcing model. Typically, constant or once-/twice-per-revolution empirical accelerations are evaluated in a specific direction. For example, Dahle et al. (2019) included estimates of a once-per-revolution along-track and cross-track periodic (sine and cosine) empirical acceleration. Empirical parameters are designed to absorb errors due to deficiencies in the background gravity model and non-gravitational observations. However, real gravitational signals may also enter these parameter estimates as the empirical accelerations are mathematically indistinguishable from real signals (Beutler et al., 2010). Watkins et al. (2015) and Save et al. (2016) integrated only the gravitational and non-gravitational accelerations acting on the satellites, suggesting that solving for empirically modelled accelerations is not required for precise orbit determination.

2.2.1.4 Orbit and gravity field estimation

The background models, including gravitational and non-gravitational accelerations, are used to predict the observed inter-satellite range changes. This is achieved by integrating the equations of motion and the variational equations (i.e. state transition matrix) in the inertial reference frame, producing estimates of the satellite trajectories and the partial derivatives of the parameters with respect to the observations, in the terrestrial reference frame (Beutler et al., 2010). The position vector $\overrightarrow{r}(t)$ of the satellite at any epoch t, is the solution to the equations of motion given some initial conditions (Beutler et al., 2010). At a minimum, the initial state vector includes the position and velocity vectors and accelerometer bias and scale of the satellite at t_0. The integration of the equations of motion and the state transition matrix is often achieved using Cowell's formulation to solve the initial values with a predictor-corrector process (e.g. Bashforth and Adams, 1883; Moulton, 1926; Krogh, 1973).

The theoretical inter-satellite range change and its derivatives can then be derived using the twin spacecrafts' differential computed positions and velocities. The least squares inversion utilises the difference between the inter-satellite observations and the theoretical values calculated from the integrated orbits. The observed minus computed values (or prefit residuals) contain variations in the inter-satellite ranging measurements caused by the unmodelled mass anomaly signal plus initial state vector parameter value errors, background model errors and instrumental noise. The adjustments to the orbit parameters (i.e. initial position/velocity, accelerometer bias and scale, empirical acceleration parameters) are solved in a weighted least squares inversion:

$$\hat{x} = (A^T W A)^{-1} A^T W b \tag{2.4}$$

where A is the design matrix containing the partial derivatives, b is the vector of prefit residuals, and W is a diagonal matrix containing the observation weights. The estimation process attempts to solve for a solution, $\hat{x}$, that minimises the weighted sum of the squares of the postfit residuals. The postfit residuals contain any noise or mass signal not absorbed by the parameters. The orbits can be re-integrated using the updated parameter values to form an improved initial state vector and converge on a solution to the parameter set that minimises the square of the residuals.

Once the 24-hour orbits have been integrated, adjustments to the background gravity model are estimated. The gravity field is parameterised and estimated, along with the

satellite parameters, in a simultaneous least squares inversion. Previous studies have parameterised the gravity field using spherical harmonics (e.g. Lemoine et al., 2007; Save et al., 2012; Dahle et al., 2019) and mascons, by relation to Stoke's coefficients (e.g. Save et al., 2012; Loomis et al., 2019b) or by explicitly relating the inter-satellite observation to mass variations (e.g. Watkins et al., 2015). The different methods for parameterising, post-processing and constraining the gravity field are described in Sections 2.2.2 and 2.2.3.

To estimate the adjustments to the background gravity field, the number of observations must far exceed the number of estimable parameters (Beutler et al., 2010). A system of normal equations is formed for each 24-hour arc of observations and stacked so that, when solved, the satellite parameters are estimated daily. The gravity field parameters are calculated as an average mass change over the period that the observations were obtained. At a minimum, 10-days of observations are used to estimate the adjustments to the background gravity model (e.g. Lemoine et al., 2007; Luthcke et al., 2013), with 30-days being the preferred period of the SDS teams (e.g. Save et al., 2012; Watkins et al., 2015; Dahle et al., 2019).

This process can be iterated until the temporal gravity field parameter adjustments are sufficiently minor such that the satellite and temporal gravity field parameters have converged (Beutler et al., 2010). The postfit residuals are an indicator of solution accuracy and should be small. However, error contained in the parameter estimates, the Level-1B measurements (i.e. inter-satellite measurements and accelerometers) and the background models appear in the residuals or can manifest as noise in the gravity field solutions (e.g. Ditmar et al., 2012).

2.2.1.5 Inter-satellite observable

The range rate observations are most often used as the inter-satellite measurement in the orbit and gravity field estimation (e.g. Tapley et al., 2004; Dahle et al., 2014; Luthcke et al., 2013; Watkins et al., 2015). However, some studies have utilised the range measurements directly (e.g. Kim, 2000; Shen et al., 2015). It is also possible to use range acceleration as the inter-satellite observation (e.g. Ivins et al., 2011; Tregoning et al., 2017; Ghobadi-Far et al., 2022). However, the KBR Level-1B range acceleration observations are dominated by excessive high-frequency noise and, therefore, cannot be used directly as the inter-satellite observation during orbit and gravity field estimation. Some studies have used a variant of the range acceleration provided in the Level-1B data files by considering

only the along-track range acceleration to estimate the temporal gravity field (e.g. Liu et al., 2010; Ditmar et al., 2012). The improved noise content of the GRACE-FO LRI ranging measurements has recently allowed for the use of the range acceleration as the inter-satellite observation (Ghobadi-Far et al., 2022).

The advantage of using range acceleration observations over range rate is that gravity anomaly signals caused by mass variations on Earth become more localised spatially, unlike the range rate observations, which contain a significant once-per-revolution signal (Save et al., 2012). As such, Save et al. (2012, 2016) and Pie et al. (2021) used postfit range acceleration residuals, derived from postfit range rate residuals, to quantify the amount of mass anomaly signal that was not absorbed by their parameterisation.

The KBR inter-satellite measurements are contaminated by microwave system noise which dominates at high frequencies, primarily sourced from thermal noise from the K/Ka-band receivers but also from the ultra-stable oscillator (USO) phase noise (Sheard et al., 2012; Thomas, 1999). The microwave ranging system noise has been shown to dominate the high-frequency component of the postfit inter-satellite residuals (Goswami et al., 2018). Ko (2008) analysed postfit range rate residuals and made a modest improvement to gravity field estimation by the application of a more aggressive digital low-pass filter during dual one-way range processing of the Level-1A data, compared to the method described by Thomas (1999). This was followed by an analysis of the signal-to-noise ratio (SNR) of the KBR measurements, which indicate system noise level, where poor SNRs were correlated to high-frequency postfit range rate residuals (Ko et al., 2012).

Ditmar et al. (2012) analysed the spectral density of theoretical range rate residuals, which were calculated by subtracting GRACE range observations from simulated range observations computed using a force model to produce GRACE dynamic orbits. Their results showed that errors from the KBR sensor dominated residuals at high frequencies (f >14 mHz), which propagated into gravity field parameters forming substantial along-track striping, particularly in mid- to low-latitudes. Behzadpour et al. (2019) echoed these findings by performing a multi-resolution wavelet analysis to decompose actual GRACE range rate residuals computed during ITSG-GRACE2016 processing (Mayer-Gürr et al., 2016), concluding that KBR ranging sensor errors dominated the short timescale details (f >12.5 mHz) of the residuals.

2.2.2 Spherical harmonics

Traditionally, GRACE and GRACE-FO models of the monthly temporal gravity field (with respect to the mean gravity field (e.g. Bruinsma et al., 2013)) have been provided in the form of numerical values for dimensionless Stoke's coefficients (e.g. Tapley et al., 2004; Lemoine et al., 2007; Dahle et al., 2014; Mayer-Gürr et al., 2016; Save et al., 2012). Thus, the time-variable dimensionless Stoke's coefficients (i.e. ΔC_{lm} and ΔS_{lm}) are parameterised and estimated in the inversion. GRACE and GRACE-FO solutions can then be evaluated in terms of temporal variations in equivalent water height (EWH; $\Delta\sigma$) by modifying the spherical harmonic expansion of Equation 2.2 (Wahr et al., 1998):

$$\Delta\sigma(\theta,\lambda,t) = \frac{R\rho_{ave}}{3\rho_w}\sum_{l=0}^{L_{MAX}}\frac{2l+1}{1+k'_l}\sum_{m=0}^{l}\overline{P}_{lm}(\cos\theta)[\Delta C_{lm}(t)\cos m\lambda + \Delta S_{lm}(t)\sin m\lambda] \quad (2.5)$$

where θ is colatitide, ρ_{ave} is the average density of the Earth (5517 kg/m^3), ρ_w is the density of water (1000 kg/m^3) and k'_l is the elastic load Love number of degree l. Given a month of observations with dense ground track coverage and nominal instrument operation, the time variable spherical harmonic coefficients that represent the temporal gravity field can usually be estimated accurately up to maximum degree and order (L_{MAX}) 60, equivalent to ∼330 km spatial resolution at the equator. The Level-2 products are also typically provided at a higher resolution, $L_{MAX} = 96$, equivalent to ∼200 km at the equator.

The spatial resolution (i.e. L_{MAX}) of GRACE and GRACE-FO spherical harmonic temporal gravity field solutions (e.g. Figure 2.9) are limited by modelling errors and instrumental noise. Signal degradation increases with spherical harmonic degree and manifests as random and correlated errors (Wahr et al., 2006; Swenson and Wahr, 2006). High degree harmonic coefficients have less impact on the Earth's potential and, therefore, on the accelerations acting on the satellites due to the faster upward attenuation compared to low degree components of the gravity field. Therefore, estimates of the poorly observed high degree Stoke's coefficients become decreasingly well observed and more susceptible to error. To produce meaningful mass anomaly estimates, spherical harmonic solutions of the temporal gravity field must be corrected for these errors using various smoothing and decorrelation filters (e.g. Wahr et al., 1998; Swenson and Wahr, 2006; Kusche, 2007; Kusche et al., 2009; Schrama and Wouters, 2011). However, these filters tend to attenuate the signal amplitudes which has led to the development of various signal restoration

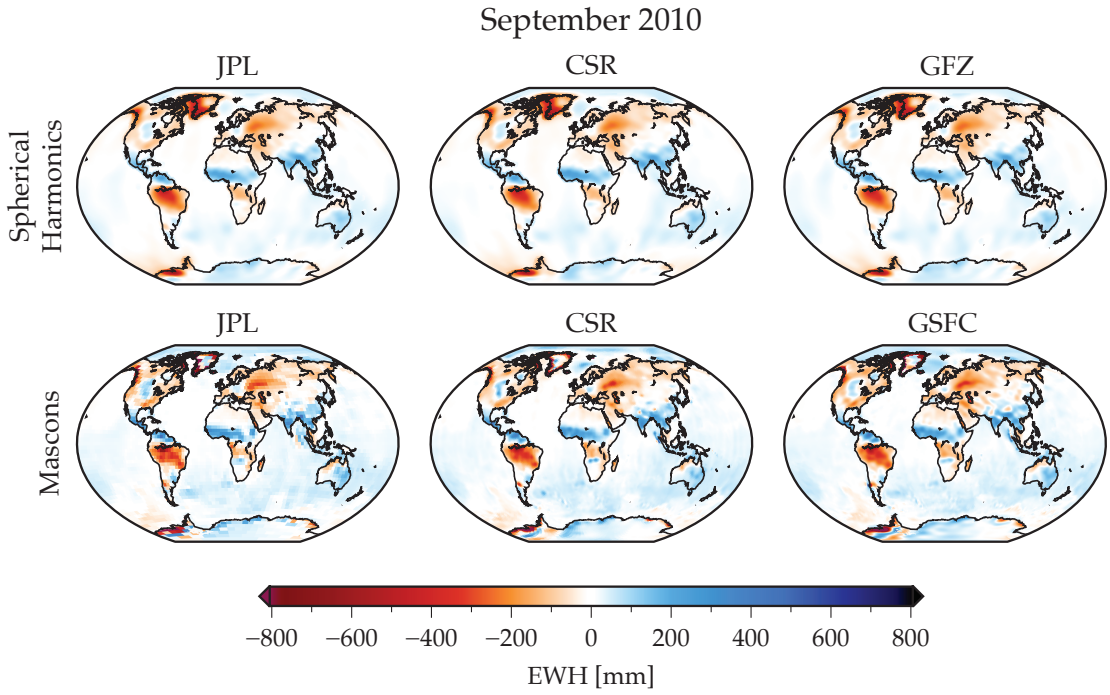

Figure 2.9: GRACE RL06 spherical harmonic and mascon solutions for September 2010. (top row) Gridded Level-3 JPL, CSR and GFZ Gaussian smoothed and decorrelated spherical harmonic solutions (Landerer and Swenson, 2012). (bottom row) JPL 3° × 3°, (Watkins et al., 2015; Wiese et al., 2016), CSR (Save et al., 2016) and GSFC (Loomis et al., 2019a) 1° × 1° mascons solutions.

techniques (e.g. Swenson and Wahr, 2002; Chen et al., 2009a; Landerer and Swenson, 2012).

2.2.2.1 Smoothing and decorrelation filters

The GRACE and GRACE-FO satellites have decreased ground track density at mid- to low-latitudes and are therefore, less sensitive to gravity changes in the east-west direction (Wahr et al., 2004). Correlated and random noise appears in the estimates of poorly observed high degree harmonic coefficients, which causes prominent north-south striping to appear in the gravity field solutions due to the polar configuration of the orbits. Correlation errors are further amplified in the presence of poor ground track coverage, as reduced observation of the higher degree components of the gravity field results in increased north-south striping (Save et al., 2012). These errors are often mitigated during post-processing by using various decorrelation filters and smoothing techniques that reduce the power in the degrees dominated by noise.

Wahr et al. (1998) were the first to propose a method for suppressing north-south striping errors typical of GRACE spherical harmonic solutions by applying a Gaussian

smoothing filter whereby a defined radius determines the spatial averaging of the solution. Gaussian smoothing is applied a posteriori by inserting the smoothing function into the spherical harmonic expansion (see Wahr et al., 1998). The spherical harmonic coefficients are essentially multiplied by a smoothing function, the value of which decreases with increasing degree, thus reducing the contribution of the poorly observed high degree coefficients (Jekeli, 1981). Gaussian smoothing is therefore degree dependent; thus, this method is definitively isotropic (Jekeli, 1981). A significantly large averaging radius (i.e. 1000 km) is required to reduce striping in the ocean (e.g. Wahr et al., 2004). As a result, there is a significant tradeoff between noise reduction and spatial resolution, which causes significant signal attenuation and leakage in continental areas (Swenson and Wahr, 2006). Sasgen et al. (2006) developed a low-pass Wiener optimal filter as an alternative to Gaussian smoothing, which requires a priori information of the degree power spectra of the desired temporal gravity signal and noise to mitigate the impacts of correlated errors. Like Gaussian smoothing, the Wiener filter treats the correlated noise as isotropic (i.e. only depending on the degree power of the signal and noise).

Because correlations exist between even and odd degree coefficients, large smoothing radii are required to remove all stripes in the GRACE models using the traditional, isotropic methods (e.g. Wahr et al., 1998). Not long into the GRACE mission, the need to develop other smoothing techniques became apparent. Many of those produced can be used either as an alternative to or in conjunction with spatial averaging by Gaussian smoothing. Such methods aim to optimise the trade-off between noise reduction and signal attenuation. Swenson and Wahr (2006) developed a decorrelation filter whereby they fitted and removed a quadratic from a moving window of even and odd degree Stoke's coefficients for a particular order, successfully reducing the uncertainty of the oceans by more than half (Chambers, 2006a). Wouters and Schrama (2007) used empirical orthogonal functions (EOFs) to decompose a time series of available GRACE Stoke's coefficients, then rebuilt the series of coefficients with the modes that passed a particular test, indicating they do not contain noise. While their method reduced striping and limited signal leakage compared to other methods, any real irregular or isolated signals were treated as noise and attenuated or removed entirely (Wouters and Schrama, 2007). The DDK filter, first proposed by Kusche (2007) for decorrelating GRACE spherical harmonic solutions, implements a non-isotropic kernel which requires a priori knowledge of the geometry of the gravity field and, thus, knowledge of the correlation-induced north-south striping. The

degree of smoothing is controllable and overall more effective and less likely to result in gravity field attenuation when compared to typical Gaussian filters (Kusche, 2007).

Often decorrelation and DDK filters are used in conjunction with Gaussian smoothing to suppress noise in GRACE spherical harmonic solutions (e.g. Save et al., 2012; Chen et al., 2021). For example, the Level-3 gridded gravity field products provided by the SDS have been smoothed using Gaussian filtering and de-striped using the decorrelation filter of Swenson and Wahr (2006) (e.g. Figure 2.9). By using the combined filter approach, a smaller averaging radius is defined for Gaussian smoothing, reducing signal attenuation and leakage while maximising the mitigation of noise. In this example Gaussian smoothing with a 300 km radius has been used to produce the land grid and a 500 km radius to produce the ocean grid (Figure 2.9). Although decorrelation filters and smoothing techniques are effective in mitigating errors caused by high degree noise, these post-processing steps still tend to attenuate the signal amplitudes, limiting the accuracy of the temporal gravity field solutions.

2.2.2.2 Signal restoration for spherical harmonic solutions

Signal restoration techniques have been developed to combat issues such as signal attenuation and leakage error introduced into the spherical harmonic solutions of the temporal gravity field due to spatial averaging induced by filtering and truncation. Truncation artefacts are caused by the inability to approximate high-frequency components of the gravity field within the limits of the well-observed harmonic degrees, leading to signal leakage in the spherical harmonic solutions of the gravity field derived from GRACE and GRACE-FO data (Swenson and Wahr, 2002; Chen et al., 2009a; Landerer and Swenson, 2012). The characteristics of leakage error are determined by both the methods used in decorrelation/smoothing and the characteristics of the signal. Truncation artefacts are prevalent in regions where sharp gravity gradients (i.e. discontinuities) occur, for example, near continental-oceanic boundaries and drainage divides. These errors are particularly pervasive in polar areas, where significant mass changes occur near continental-oceanic boundaries. For example, the high magnitude ice mass loss signals in West Antarctica and the Antarctic Peninsula is smeared across the coastline, into the Amundsen Sea Embayment where mass variation should be comparatively small (e.g. Chen et al., 2009a).

Swenson and Wahr (2002) developed several methods to restore power to GRACE temporal gravity field signals that had been attenuated by truncation and Gaussian smoothing.

One of their approaches utilised knowledge of the GRACE errors to scale the smoothed mass change estimates within a defined region (e.g. drainage basin) using an optimal averaging kernal. This method was used in several regional and basin-scale studies, for example, to estimate ice mass loss across the Antarctic ice sheet (Velicogna and Wahr, 2006), to quantify the impact of the Californian Central Valley drought (Famiglietti et al., 2011) and declining water storage in the Caspian Sea (Swenson and Wahr, 2007).

Restoration of signal attenuation was achieved at smaller scales through the definition of gain factors to restore signal on continental regions (Landerer and Swenson, 2012). The method of Landerer and Swenson (2012) is similar in concept to the optimal averaging kernel method in that the solutions of the temporal gravity field are ultimately scaled by a coefficient, in this case, a gain factor, which was calculated on a global 1° grid. The derivation of the global gain factors was achieved by assessing the impact of truncation and filtering on a synthetic model of TWS (GLDAS-NOAH; Rodell et al., 2004), truncated to $L_{MAX} = 60$ and decorrelated using a combination of the de-striping filter (Swenson and Wahr, 2006) and Gaussian smoothing with a radius of 300 km. To reduce the leakage error, the filtered TWS anomalies were compared to their unfiltered (i.e. true) counterparts, and their misfit was decreased by the estimation of a gain factor via a least squares inversion. The method, while successful in reducing the errors in simulation, is purpose-built for the specific solutions estimated to $L_{MAX} = 60$ and using the combined de-striping filter-Gaussian smoothing approach. The method also doesn't consider the possible temporal evolution of gain factors and is specifically tuned to a simulated model of TWS; thus cannot be used over oceans or ice-covered continental regions.

An alternative method for restoring signal amplitudes biased by spherical harmonic truncation and filtering uses a forward modelling procedure (e.g. Ramillien et al., 2006; Chen et al., 2007, 2009a, 2015). The forward modelling algorithm iteratively restores signal to its place of origin by constraining locations of expected mass change (Chen et al., 2015). For example, based on the forward modelling method first applied by Ramillien et al. (2006), Chen et al. (2009a) accounted for biases induced by decorrelation and Gaussian smoothing by deriving estimates of assumed mass change in nine geographic locations across Antarctica. Leakage error was minimised particularly in coastal regions adjacent to regions of high mass loss where signal had smeared into the ocean. Through simulation, Chen et al. (2015) showed that unconstrained forward modelling estimates were able to restore mass losses in West Antarctica, but not completely recover the original spatial

pattern of mass loss.

2.2.2.3 Regularisation of spherical harmonic coefficients

Regularisation is used to stabilise poorly conditioned inverse problems by constraining the parameter adjustments to the a priori values, suppressing the amount of noise that can enter the least squares solution. GRACE spherical harmonic models are traditionally unconstrained, however, several methods for regularising the spherical harmonic coefficients have been used (e.g. Bruinsma et al., 2010; Save et al., 2012; Chen et al., 2021). A successful spherical harmonic regularisation strategy mitigates correlation and truncation errors without significantly attenuating the mass change signal.

Regularised least squares is computed by constraining the normal equations, from Equation 2.4:

$$\hat{x} = (A^T W A + \alpha M)^{-1} A^T W b \tag{2.6}$$

where α is the regularisation parameter and M is the regularisation matrix. Large α constrains the parameter adjustments to the a priori values, while $\alpha = 0$ will produce an unregularised solution. The regularisation parameter should optimise the signal-to-noise ratio of the solution, balancing the noise entering the solution and signal attenuation. The regularisation matrix, M, usually contains degree and order dependent constraints, such that the high degree harmonics are most constrained, reducing correlated noise in the regularised solutions (Bruinsma et al., 2010; Save et al., 2012).

Regularised Stoke's coefficients were first computed by Lemoine et al. (2007) and Bruinsma et al. (2010) up to $L_{MAX} = 50$, for 10-day solutions of the temporal gravity field from GRACE data. They used a combination of Tikhonov regularisation with regularisation matrices constructed using the Kaula law (Kaula, 1971), which is an effective method to reduce the signal variance in the spherical harmonic degrees that contain the most error variance. Later, Save et al. (2012) designed their regularisation matrix empirically using a combination of Tikhonov regularisation and the error characteristics of the unregularised spherical harmonic coefficients. They defined the regularisation parameter, α, using L-curve approximation, a method for locating optimal α that balances signal attenuation and noise suppression. Both methods produced regularised spherical harmonic solutions that were improved significantly compared to unregularised spherical harmonic solutions (Lemoine et al., 2007; Bruinsma et al., 2010; Save et al., 2012). However, their regularised

spherical harmonic solutions still contained some correlated errors, thus a combined regularisation and Gaussian filtering was applied (Bruinsma et al., 2010; Save et al., 2012). The combination approach consistently showed the most improvement to north-south stripes while minimising signal attenuation (Save et al., 2012).

An alternative method constrains spherical harmonic solutions based on the spatial characteristics of the temporal gravity field signal. Chen et al. (2021) defined their regularisation matrix as a diagonal matrix containing spatial constraints transformed into the spectral (i.e. spherical harmonic) domain. The spatial constraints were based on the variance of monthly mass change from GRACE DDK filtered, 100 km Gaussian smoothed spherical harmonic solutions sampled onto a global grid. The regularisation parameter, α, was determined by minimising the mean square error of the preliminary regularised solution and empirically defined "true" spherical harmonic coefficients. This novel regularisation approach produced high resolution spherical harmonic solutions ($L_{MAX} = 180$) with minimal signal leakage, requiring no further smoothing or signal restoration. Mass change trends and annual amplitudes extracted from the high resolution regularised spherical harmonic solutions of Chen et al. (2021) were significantly improved compared to unconstrained filtered spherical harmonic solutions (e.g. Mayer-Gürr et al., 2016) and were comparable to mascon solutions (e.g. Watkins et al., 2015; Save et al., 2016).

2.2.3 Mascons

Mass concentration elements (mascons) are an alternative approach to spherical harmonic coefficients for parameterising the Earth's temporal gravity field. The use of mascons allows for the constrained estimation of discretised mass anomalies, reducing the leakage of signals across coastlines and hydrological basins seen in spherical harmonic solutions. The term "mascons" was first conceived by Muller and Sjogren (1968) who used them in their estimation of lunar gravity anomalies on the surface of the Moon. For use in GRACE and GRACE-FO analysis, mascons are constructed by dividing the surface of the Earth into tiles of known area. The mass change associated with each tile is then estimated as the change in the height of water across the tile required to cause the observed gravity anomaly signal.

Three categories of GRACE and GRACE-FO mascon solutions exist. The first approach involves fitting the mascon basis function parameters to spherical harmonic coefficients during postprocessing, achieving a pseudo-type mascon solution (e.g. Jacob et al.,

2012; Schrama et al., 2014; Velicogna et al., 2014). The remaining methods involve relating the mascons directly to the inter-satellite observations using explicit partial derivatives to derive the mass anomalies. This is achieved by representing each mascon as a spherical harmonic expansion (e.g. Rowlands et al., 2005; Luthcke et al., 2006b; Sabaka et al., 2010; Rowlands et al., 2010; Luthcke et al., 2013; Save et al., 2016; Loomis et al., 2019b). An alternate approach that does not require the calculation of spherical harmonic coefficients relates the inter-satellite observations to each mascon using an analytical formulation (e.g. Watkins et al., 2005; Ivins et al., 2011; Watkins et al., 2015).

2.2.3.1 Spherical harmonic representation of mascons

The NASA Goddard Space Flight Center (GSFC) developed a method for relating mascons directly to GRACE inter-satellite observations via a truncated spherical harmonic expansion using explicit partial derivatives. This method was first implemented to estimate regional gravity field anomalies using GRACE inter-satellite range rate observations. For example, Rowlands et al. (2005) utilised the short arc analysis technique of Rowlands et al. (2002) (i.e. using only data as the satellites overflew the region of interest) to estimate Amazon Basin mass anomalies by relating the mass change of $4^\circ \times 4^\circ$ mascons at 10-day intervals to the inter-satellite range rate observations via spherical harmonic coefficients. Using a similar approach, Luthcke et al. (2006b, 2008) derived regional mascon solutions of the Greenland ice sheet using $3^\circ \times 3^\circ$ mascons and the Gulf of Alaska using $2^\circ \times 2^\circ$ mascons, respectively.

The approach of relating mascons to inter-satellite range rate observations via spherical harmonic expansion was later expanded to estimate global mascon temporal gravity anomalies. Sabaka et al. (2010) and Rowlands et al. (2010) estimated $2^\circ \times 2^\circ$ equal-area mascons at 10-day and monthly intervals, respectively, followed by Luthcke et al. (2013) who decreased the size of their mascons to $1^\circ \times 1^\circ$. The most recent global GSFC mascon solution uses the mascon geometry of Luthcke et al. (2013), evaluated at a monthly temporal resolution (Loomis et al., 2019a). CSR has since adopted the mascon formulation developed by GSFC; Save et al. (2016) utilised a geometry of 1° equal-area geodesic shapes to estimate the global gravity anomalies at a monthly temporal resolution.

Each of the studies mentioned above used a mascon formulation to estimate an update to the background gravity model via the calculation of scaled differential Stoke's coefficients. From Equation 2.5, the change in the potential coefficients ($\Delta\overline{C}_{jlm}(t)$ and

$\Delta\overline{S}_{jlm}(t)$) due to the addition of a uniform layer of mass over a mascon j at time t is (Chao et al., 1987):

$$\begin{aligned}\Delta\overline{C}_{jlm}(t) &= \left[\frac{\sigma_j(t)(1+k'_l)R^2}{(2l+1)M}\int \overline{P}_{lm}(\cos\theta)\cos m\lambda d\Omega\right]H(t)\\ \Delta\overline{S}_{jlm}(t) &= \left[\frac{\sigma_j(t)(1+k'_l)R^2}{(2l+1)M}\int \overline{P}_{lm}(\cos\theta)\sin m\lambda d\Omega\right]H(t)\end{aligned} \tag{2.7}$$

where M is the Earth's mass; σ_j represents the mass of the uniform layer; and Ω is the solid angle surface area of the mascon ($d\Omega = \cos d\theta d\lambda$). The estimable parameter is $H(t)$, the change in equivalent water height over each mascon needed to induce the observed perturbation. Thus, for mascon j, the set of differential Stoke's coefficients are scaled by $H_j(t)$, representing a surface mass change relative to the background gravity model.

Recently, a computationally efficient approach was developed to estimate mascons from GRACE Level-2 spherical harmonic coefficients by reformulating the typical mascon estimation system (Croteau et al., 2021). By applying the equations from Sabaka et al. (2010) in a novel way, Croteau et al. (2021) related the monthly spherical harmonic coefficients and their full error covariances to a global grid of mascons. This method is, therefore, unlike the pseudo-mascon solutions generated as a post-processing step by fitting mascons directly to the spherical harmonic coefficients (e.g. Jacob et al., 2012; Schrama et al., 2014; Velicogna et al., 2014). These "fast mascons" are mathematically equivalent to the traditional approach (e.g. Watkins et al., 2015; Save et al., 2016) for computing mascon solutions directly from the Level-1B data. However, these solutions are limited by the truncation of the spherical harmonic solutions and the parameterisation used to generate the Level-2 solution.

The mascon solutions described in this section use spatial regularisation strategies during the inversion of the normal equations to mitigate noise and signal leakage. Therefore, unlike spherical harmonic models of the temporal gravity field, mascons do not need to be filtered or smoothed during post-processing (e.g. Figure 2.9). Using a regular global grid to define the mascon pattern will inevitably result in mascon geometries that cross coastlines such that mascons contain ocean and continental components. Coastline-crossing mascons may be a source of error when parameterising the temporal gravity field with large mascons (Figure 2.10). Small (i.e. 1°) mascon geometries are advantageous for mitigating the problem of leakage errors across coastlines (Figure 2.10b). However, computing 1° mascons is computationally intensive and not reflective of the spatial resolution of the mass anomaly estimates (Luthcke et al., 2013; Save et al., 2016; Loomis et al., 2019b).

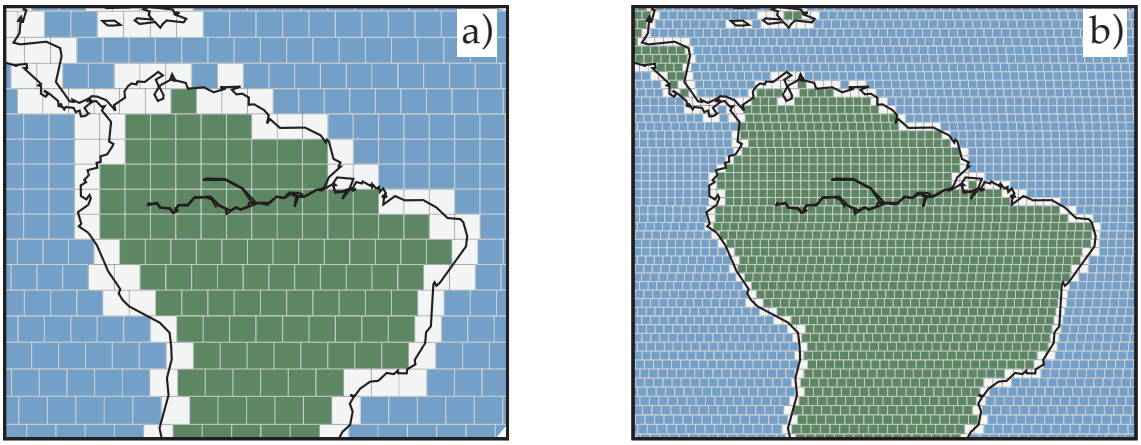

Figure 2.10: Impact of mascon size on coastline resolution. (left) 3° × 3° regular gridded mascons (right) and 1° × 1° gridded mascons showing the ocean mascons (blue), land mascons (green) and coastline-crossing mixed land/ocean mascons mascons (grey).

The processes used to improve the resolution of coastlines and the various regularisation strategies utilised in these studies are discussed in Sections 2.2.3.2 and 2.2.3.3, respectively.

2.2.3.2 Analytic formulation for mascon estimation

An alternative method for analysing GRACE data using mascons was developed at JPL that does not necessitate intermediate spherical harmonic expansion of the mascons. This method uses an analytical mascon formulation and explicit partial derivatives to relate mascons directly to the inter-satellite ranging observations to derive the mass anomalies (Watkins et al., 2015). Based on the approach outlined in Watkins et al. (2005), Ivins et al. (2011) estimated 2° spherical cap mascons globally using partial derivatives of mascon parameters related to the inter-satellite range acceleration observations. Using a similar method, Watkins et al. (2015) estimated the global temporal gravity field represented with 3° spherical cap mascons by relating the mascons to the inter-satellite range rate observations via direct partial derivatives.

Errors are introduced into the temporal gravity field solutions where mascons contain a mix of land and ocean areas, resulting in signal leakage across coastlines. Leakage errors are particularly problematic where large mass anomalies occur near coastlines (e.g. around the margin of the Greenland ice sheet). These errors are not as significant as the signal leakage errors inherent to spherical harmonic solutions due to truncation and smoothing (Landerer and Swenson, 2012; Watkins et al., 2015). However, if left unaccounted for, potentially significant errors propagate into basin-integrated mass anomaly estimates (Watkins et al., 2015). Mascon leakage errors are particularly problematic when

the gravity field is parameterised using relatively large mascons, increasing the percentage of mixed land and ocean mascons (Figure 2.10).

The identification of this problem in the mascon solutions prompted the development of techniques to relocate leaked signals to their places of origin (i.e. Watkins et al., 2015; Wiese et al., 2016). Watkins et al. (2015) developed an algorithm to relocate mass within coastline-crossing mascons to their land and ocean counterparts, effectively splitting each of the mixed mascons into two smaller mascons (i.e. one land and one ocean) delimited by the coastline. To redistribute the mass anomalies of the mixed mascons via weighted least squares, Watkins et al. (2015) estimated a priori values of the redistributed land (ocean) mass anomalies based on estimates of nearby unmixed land (ocean) mascons and solved for adjustments to these parameters by a weighted least squares inversion. This procedure effectively reduced leakage errors by 50% globally.

Wiese et al. (2016) extended the method of Watkins et al. (2015), defining their a priori estimate uncertainties using the difference of external hydrology and ocean model output averaged onto the 3° mascons and the a priori mascon estimates. This procedure for reducing leakage errors across coastlines is least accurate in ice-covered regions, where solid Earth mass changes occur and in areas where few adjacent mascons can be used to estimate an accurate a priori value (Watkins et al., 2015; Wiese et al., 2016). Wiese et al. (2016) also derived gridded gain factors for down-scaling the mass anomalies to sub-mascon (0.5°) resolution using an extension of the technique developed by Landerer and Swenson (2012). The combined application of the coastline resolution correction and the gridded gain factors reduced leakage errors in large drainage basins globally by 11%-30% (Wiese et al., 2016).

2.2.3.3 Mascon regularisation

Introducing spatial and/or temporal constraints into the mascon estimation procedure is a convenient method to improve significantly signal recovery and mitigate signal leakage. Mascon solutions are stabilised numerically by applying regularisation constraints on the least squares inversion (Equation 2.6), effectively mitigating or damping the noise that would otherwise be present in the gravity fields. Mascon regularisation has the advantage that geographic boundaries (e.g. coastlines, drainage basins) can be conveniently built into the regularisation strategy, mitigating signal leakage and improving the spatial resolution along such boundaries (c.f. top row and bottom row of Figure 2.9). Regularisation

strategies vary significantly between the three centres that produce the most widely used GRACE mascon solutions (i.e. CSR, GSFC and JPL). Specifically, they differ in their choice of how to impose temporal constraints, force correlations between nearby mascons and utilise information from external models to inform their choice of constraints.

The suite of GSFC regional and global mascon solutions available at 10-day intervals utilised spatial and temporal constraints to stabilise their high-temporal resolution mascon solutions (Rowlands et al., 2005; Luthcke et al., 2006b, 2008; Sabaka et al., 2010; Luthcke et al., 2013). Region-specific regularisation allows for constraints tailored to the location of each mascon. For example, Luthcke et al. (2013) applied the Sabaka et al. (2010) signal auto-covariance matrix to their mascon solutions. Their constraint equations are applied to location-based regions, and mascons are correlated as a function of the distance between the mascons and the time between solutions. Therefore, a mass signal estimated at one mascon influences the estimated mass change of neighbouring mascons within the same geographical region, and mass anomaly estimates are influenced by previous and future solution values. The constraints w_{ij} assigned to any pair of mascons, i and j, that reside in the same constraint region is an exponential function of correlation distance and time (Sabaka et al., 2010):

$$w_{ij} = exp\left(2 - \frac{d_{ij}}{D} - \frac{t_{ij}}{T}\right) \tag{2.8}$$

where d_{ij} is the distance between the mascon pair, t_{ij} is the positive time difference between solutions, D and T are the correlation distance (e.g. 250 km) and time difference (e.g. 10 days) (Sabaka et al., 2010). A pair of mascons that reside in different constraint regions are assigned zero correlation constraints (i.e. $w_{ij} = 0$).

Temporal correlations are not imposed on mascon estimates evaluated at a monthly temporal resolution (e.g. Rowlands et al., 2010; Loomis et al., 2019b; Croteau et al., 2021). For example, Loomis et al. (2019b) applied only spatial constraints, meaning that each monthly temporal gravity field was estimated independently:

$$w_{ij} = exp\left(1 - \frac{d_{ij}}{D}\right) \tag{2.9}$$

Previous studies, such as Watkins et al. (2015), have similarly used region-specific constraints to regularise their mascon solutions; however, they used geophysical models to design their regularisation matrices, deriving the constraint for each mascon based on

the root mean square (RMS) of monthly averaged modelled mass change values (GLDAS-NOAH (Rodell et al., 2004) and ECCO2-OMCT (Menemenlis et al., 2008)). Therefore their method relies heavily on the accuracy of the geophysical models, which, if in error, could either attenuate signal if the derived constraint is too tight or permit the absorption of noise by the mascon parameters if the constraint is too loose. Further, the regularisation scheme developed by Watkins et al. (2015) was partly motivated by improving the estimates of ocean mass variations which are small in amplitude compared to continental signals.

Other strategies are strictly based on information contained in the GRACE observations (e.g. Save et al., 2016). Save et al. (2016) used a time-variable Tikhonov regularisation on their regularised spherical harmonic solutions to inform their choice of mascon regularisation constraints. Their mascon solutions were generated using an iterative two-step approach. First, an intermediate solution was developed using a regularisation scheme whereby spatial mascon constraints were formed based on the RMS of the spherical harmonic solutions (Save et al., 2012), but with tightly constrained ocean and dryland areas. Second, they used these intermediate solutions to design regularisation matrices that vary month-to-month for the estimation of their final mascon mass anomaly time series (Save et al., 2016).

The chosen mascon regularisation scheme should use sufficiently loose spatial constraints such that the geophysical signals can be accurately estimated but sufficiently tight such that the effect of instrumental noise and background model errors are mitigated. The damping effect induced by the chosen regularisation scheme can be evaluated before inverting for the temporal gravity field by the calculation of the resolution operator, R (Loomis et al., 2019a):

$$\hat{x} = Rx \tag{2.10}$$

$$R = (A^T W A + M)^{-1} A^T W A \tag{2.11}$$

where x is the known solution vector (i.e. the "truth" temporal gravity field) and $\hat{x}$ is the estimated solution vector. Given enough observations and $M = 0$, then $R = I$ and, therefore, the regularisation induced error (i.e. bias) E is zero (Loomis et al., 2019a):

$$E = (R - I)\hat{x} \tag{2.12}$$

Because the resolution operator takes into account the regularisation and the partial derivatives of the parameters with respect to the observations (contained in A), the regularisation error is impacted by both the regularisation strategy, the shape and size of the mascons, the number of observations and the geometry of the satellite orbits.

A comparison of regularised mascon and filtered/smoothed spherical harmonic solutions using observations from September 2010 shows the improved spatial resolution that can be achieved by using mascons as the basis functions (Figure 2.9). Spatial constraints effectively decrease the correlations between constraint regions, reducing signal leakage across coastlines and drainage boundaries. The spatial resolution along these boundaries can be further increased by applying a coastline resolution improvement filter to the coastline mascon estimates (e.g. Watkins et al., 2005; Wiese et al., 2016) or by parameterising the temporal gravity field with sufficiently small mascons (e.g. Save et al., 2016; Loomis et al., 2019b). Unlike mascons, and except when spatial constraints are applied to the spherical harmonic solutions as per Chen et al. (2021), monthly spherical harmonic gravity field solutions tend not to reflect the spatial resolution that could be achieved given the highly-accurate inter-satellite range measurements contained in the GRACE and GRACE-FO observations (Luthcke et al., 2006a).

2.3 Summary

This chapter provided an overview of the GRACE and GRACE-FO missions, including their data products and sources of solution error, including instrumental noise and background model errors. I also reviewed the methods used for analysing GRACE and GRACE-FO data, including orbit and gravity field determinations and the limitations of the various techniques. The remainder of this thesis focuses on mitigating thermally-induced noise in the non-gravitational measurements and the impact of these errors on precise orbit determination. I also explore methods for improving estimates of the temporal gravity field using mascons as the basis functions and range acceleration as the inter-satellite observation. Finally, I explore the impact of orbit geometry, regularisation, and noise on the temporal gravity field's spatial resolution of mascon solutions using GRACE data.

Chapter 3

Mitigation of thermal noise in GRACE accelerometer observations

The quality of GRACE and GRACE-FO estimates of the temporal gravity field estimates is highly dependent on the availability of accurate measurements of the non-gravitational accelerations acting on the satellites. Unfortunately, the on-board accelerometers are extremely sensitive to internal temperature variations which manifests as sub-daily bias variations. While others have proposed calibration strategies to mitigate these bias variations, many approaches require the estimation of several parameters per axis per day which could absorb real geophysical signal during gravity field inversion and lead to discontinuities in the calibrated accelerometer measurements. This chapter explores the causes and characteristics of thermally induced accelerometer noise and proposes a new method to mitigate it a priori. My approach is shown to maintain the continuity of the calibrated accelerometer measurements and to significantly reduce noise in estimates of the temporal gravity field, all while keeping parameterisation to a minimum. This chapter is based on the manuscript published in Advances in Space Research:

McGirr, R., *Tregoning, P., Allgeyer, S., McQueen, H., and Purcell, A. P. (2022) Mitigation of thermal noise in GRACE accelerometer observations. Advances in Space Research, 69(1), 386-401.*

I made the following contributions to this paper:

- Characterised the behaviour of noise contained in the accelerometer measurements in the presence of thermal variations caused by heating problems and the orbital

configuration of the satellites (Section 3.2)

- Developed a protocol to remove low-frequency signal from the cross-track observations. These are correlated to temperature variations, based on the frequency characteristics of the accelerometer noise (Sections 3.3.1 and 3.3.2)
- Verified the validity of the filter protocol against noise-free observations (Section 3.3.3)
- Developed a method for identifying whether other accelerometer axes were influenced by thermal variations (Section 3.4)
- Implemented a thermally-based correction via a transfer factor to mitigate low-frequency noise in the along-track measurements while maintaining real non-gravitational low-frequency signal (Section 3.4)
- Analysed real GRACE data to show that the various methods for reducing thermal noise in the accelerometer measurements actually improved GRACE mascon solutions of the temporal gravity field using the uncorrected accelerometer observations as a control (Section 3.6)
- Wrote the text and created all of the figures for this manuscript

Abstract

The precise calculation of GRACE and GRACE-FO satellite orbits is reliant on knowledge of accurate non-gravitational accelerations acting on the spacecraft. These are measured by the on-board accelerometers that require a thermal environment stabilised to $\sim \pm 0.1$°C per revolution. However, during periods of the GRACE mission with reduced thermal control, internal temperature variations reached up to 10°C within a revolution, causing low-frequency and non-linear drifts in the accelerometer observations. Additionally, accelerometer bias drifts occurred throughout the GRACE mission as changes in the orientation of the orbital plane with respect to the Earth-to-Sun vector caused the satellites to absorb more or less solar energy. These temperature-induced drifts degrade the quality of mass change estimates, particularly during the latter half of the GRACE mission after thermal control of the satellites was terminated. We filter (in the frequency domain) the accelerometer observations to remove these low-frequency components ($f < 0.045$ mHz). The bias drift removed from the cross-track is then scaled to derive a thermally-based correction for the highly sensitive along-track observations. We then estimate temporal gravity fields using the ANU GRACE software, our filtered accelerometer observations and the range acceleration as the inter-satellite observation. The use of our thermally-corrected accelerometer measurements significantly improves the accuracy of both orbit modelling and gravity field estimation.

3.1 Introduction

Over a period of 15 years, the Gravity Recovery And Climate Experiment (GRACE) satellite mission (Tapley et al., 2004) mapped the Earth's mean and time-variable gravity field with unprecedented spatial resolution and accuracy, making GRACE one of the most successful missions in space geodesy. Temporal gravity field solutions produced by several processing centres using GRACE observations (e.g. Dahle et al., 2014; Luthcke et al., 2013; Save et al., 2016; Watkins et al., 2015) have been used to study mass balance variations and continue to lead to advances in several scientific fields, including solid Earth science (e.g. Riva et al., 2009), glaciology (e.g. Velicogna and Wahr, 2006; Tapley et al., 2019), hydrology (e.g. Chen et al., 2010a; Thomas et al., 2014) and oceanography (e.g. Chambers et al., 2010; Landerer et al., 2015).

For precise orbit and temporal gravity field determination, one must account for accelerations acting on the GRACE/GRACE-FO satellites from non-gravitational forces (i.e. atmospheric drag, solar radiation pressure and Earth albedo) along with other gravitational forces (i.e. ocean tides, atmosphere and planetary bodies). The non-gravitational forces acting on a GRACE/GRACE-FO spacecraft are measured with a three-axis electrostatic accelerometer which requires a thermally stable environment for optimal performance (Touboul et al., 1999). In addition, the accelerometers are highly sensitive to disturbances from thruster firings, heater switches and magnetic torquer activity (Flury et al., 2008; Klinger and Mayer-Gürr, 2016; Peterseim et al., 2012).

Thermal variations cause low-frequency and non-linear drifts to appear in the GRACE accelerometer observations. Throughout the GRACE mission, recurrent temperature-induced drifts are observed in the cross-track accelerations which correlate to the β' angle (Figure 3.1), defined as the angle between the orbital plane of the satellite and the vector pointing from the Earth to the Sun. The β' angle is an indicator of the percentage of time that a satellite spent in direct sunlight during a single revolution around Earth, absorbing solar radiation. The related temperature-induced drifts become particularly problematic during the GRACE mission from April 2011 when active thermal control was permanently disabled to increase the lifespan of the mission (Tapley et al., 2015).

The internal temperature of the satellites was also affected by the deliberate modification of heater settings and the occasional disabling of on-board heaters during periods of reduced thermal control prior to April 2011 (Tapley et al., 2015) (Figure 3.1). Additionally, temperature-induced drift is observed post April 2011 as the accelerometers

were switched on following extended periods of minimal direct sunlight per orbit (Figure 3.1). Both scenarios caused significant temperature-induced drift across multiple days of accelerometer observations (Klinger and Mayer-Gürr, 2016).

Temperature-induced drift in the accelerometer measurements causes mismodelling of the satellite orbits, creating error in the mass change estimates which contributes to increased unrealistic north-south striping (Ditmar et al., 2012). Therefore, to maintain the accuracy of temporal gravity field solutions, the effects of thermal variations on the accelerometer observations must be accounted for. This has been achieved in previous studies via various approaches of accelerometer bias and scale factor parameterisation during orbit estimation. Most commonly, multiple bias parameters are estimated per day, particularly in the less-sensitive cross-track axis, to account for sub-daily bias variation (i.e. drift) not related to non-gravitational forces during orbit estimation (e.g. Dahle et al., 2014; Klinger and Mayer-Gürr, 2016; Luthcke et al., 2013; Teixeira da Encarnação et al., 2020; Watkins et al., 2015). Increasing the quantity of orbital parameters could absorb geophysical signals and attenuate the gravity field; thus, limiting the number of estimated parameters is preferred.

Dahle et al. (2014) estimated nine accelerometer biases per axis per day to account for sub-daily bias variation. Similarly, Watkins et al. (2015) estimated accelerometer biases every three hours in the cross-axis and once per day in the more-sensitive along-track and radial directions. Conversely, Luthcke et al. (2013) estimated accelerometer biases every three hours in the along-track and radial components, but only once per day in the less-sensitive and more variable cross-track axis. Clearly, simply estimating multiple accelerometer biases per axis per day to account for sub-daily bias variation will introduce discontinuities in the calibrated accelerometer observations.

Teixeira da Encarnação et al. (2020) provided a comprehensive overview of accelerometer parameterisation and their impact on the quality of GRACE spherical harmonic solutions of the temporal gravity field. They found that estimating a bias plus a linear drift per axis per day, which would partially mitigate sub-daily bias variations, produced the most improvements to their gravity inversions and $C_{2,0}$ coefficient estimates (Teixeira da Encarnação et al., 2020). A more complex accelerometer calibration approach was adopted by Klinger and Mayer-Gürr (2016) to ensure that the continuity of the accelerometer observations was maintained. They developed a two-step accelerometer calibration approach which involves reducing the differences between biased accelerometer observa-

tions and modeled non-gravitational accelerations in a least squares adjustment, followed by a further adjustment of the parameters during gravity field recovery (Klinger and Mayer-Gürr, 2016). Both steps of their calibration utilise the same bias parameterisation, using uniform cubic basis splines (De Boor, 2001) they estimate a bias vector with 6 hour knot intervals, which requires the estimation of a total 7 bias parameters per axis per day (Klinger and Mayer-Gürr, 2016).

In this study, we develop a method to remove thermally-induced low-frequency bias drift from the accelerometer measurements for use in temporal gravity field estimation by filtering the cross-track accelerometer observations. We do this using a Hann window and high-pass frequency domain filter. The cross-track bias drift is then scaled and applied as a correction to the along-track measurements. We quantify the impact of our filtering technique on temporal gravity field estimation of mass concentration elements (mascons) and orbit parameters, including accelerometer biases and scales, in a least squares inversion, using range acceleration as the inter-satellite observable (Allgeyer et al., 2022; Tregoning et al., 2022). We found that it is possible to both maintain continuity and accurately represent accelerometer biases with a single parameter per axis per day, even in the presence of thermal variations.

The remainder of this paper is structured as follows: the next section deals with the causes and characteristics of thermally induced noise contained in the accelerometer observations throughout the GRACE mission and for three specific case studies. Sections three and four provide details on our methodology and validation of reducing long wavelength bias drift in GRACE cross-track and along-track accelerations, respectively. In Section five we outline the method used for GRACE orbit and gravity field determination. In Section six we provide 10-day GRACE solutions of the temporal gravity field for each case study detailed in Section 2 and demonstrate the improvement to estimates of the temporal gravity field when accelerometer bias drift is removed prior to orbit integration using the methodology outlined in Sections four and five. Finally, concluding remarks are found in Section seven.

3.2 Thermal noise contained in the GRACE accelerometer observations

In this section we explore the causes and characteristics of temperature-induced bias drift contained in the accelerometer observations generally, and for several specific scenarios.

3.2.1 Temperature-induced non-linear variations

Both the GRACE and GRACE-FO satellites were equipped with three-axis electrostatic accelerometers mounted at the centre of mass of each spacecraft, manufactured by the French national research laboratory, Office National d'Études et de Recherches Aérospatiales (ONERA) (Touboul et al., 1999). The accelerometers measure the non-gravitational forces acting on the spacecraft by measuring the electrostatic forces and torques necessary to maintain a proof mass motionless with respect to a sensor cage (Touboul et al., 2004). The accelerometers have two high-sensitive axes, the along-track and the radial, while the cross-track component has a reduced sensitivity by a factor of 10 (Flury et al., 2008). The measurements in the along-track axis are dominated by atmospheric drag, while the radial axis is influenced by Earth albedo and solar radiation pressure and, to a much lesser extent, atmospheric drag. The cross-track axis is primarily affected by solar radiation pressure, the magnitude of which depends on the β' angle.

To achieve the desired level of performance, the GRACE accelerometers were kept in a thermally controlled environment to restrict temperature variations to less than 0.1°C per revolution (Flury et al., 2008). This level of thermal control was maintained via the use of heaters which controlled the temperature of various instruments and sensors on-board the GRACE satellites. In this environment, the daily variation of the accelerometer biases has been represented by a second-order polynomial model fit to multiple years of observations (Bettadpur, 2009).

Prior to the permanent cessation of thermal control, temperature variations outside the range for optimal accelerometer operation mostly occurred due to one of two reasons. First, on several occasions one or both satellites experienced disconnections to supplemental heater lines, consequently disabling the accelerometer heaters and resulting in a cool down of the spacecraft followed by a period of reheating (Klinger and Mayer-Gürr, 2016). Second, during periods of reduced thermal control, there were a number of instances where modified heater tables were uploaded to reduce the internal temperature of the satellites in

a deliberate attempt to decrease battery load (Herman et al., 2012). On these occasions, internal temperatures decayed to new, lower temperatures. These temperature variations caused changes in the accelerometer bias of >50 nm/s^2/day in the cross-track axis (i.e. greater than the normal magnitude of non-gravitational signal variation within an orbit), which we term 'severe' bias drift. The along-track biases were also impacted by these temperature variations, but to a lesser extent.

From April 2011, active thermal control was permanently disabled on the GRACE satellites to increase the lifespan of the mission (Tapley et al., 2015). In the absence of thermal control, absorption and re-radiation of solar energy predictably became the primary influence on the internal temperature of the GRACE satellites. Thus, from April 2011 onward, accelerometer temperature variation and bias drift are highly correlated with the β' angle.

The $|\beta'|$ angle oscillated between minimum and maximum values, with a frequency of one cycle per ∼325 days (Figure 3.1a). When the $|\beta'|$ angle was high (>68°) the satellites spent no time in the Earth's shadow and received a relatively constant flux of solar radiation. At the other extreme, when the $|\beta'|$ angle was low (<20°), the satellites spent considerable time (up to 36 minutes per ∼90 minute orbit) in the shadow of the Earth. From April 2011, the accelerometers were switched off to reduce battery loads during periods when the satellites received the least amount of direct sunlight as a consequence of low $|\beta'|$ angle.

To investigate the relationship between the β' angle and thermally-induced accelerometer bias drift, we compared the daily mean of the uncalibrated GRACE-A cross-track accelerations (thrusts removed) and the daily mean β' angle from 2003 to mid-2016 (Figure 3.1a). In the early parts of the mission, the mean cross-track accelerations are smoothly varying and predictable, with the exception of large magnitude bias variations caused by temporary disabling of the accelerometer heaters and subsequent rapid decreases in the internal temperature of the spacecraft. These latter periods are characterised by a sharp decrease (>400 nm/s^2) in the uncalibrated cross-track accelerations followed by an asymptotic recovery of the bias to nominal values once the heaters have been reconnected (Figure 3.1a,b). These events tend to affect accelerometer measurements over 4-5 days.

Recurrent low-magnitude variation in the mean uncalibrated cross-track accelerations is also observed prior to April 2011 even during periods of thermal control (Figure 3.1a,c). These events occurred periodically as the $|\beta'|$ angle approached and exceeded 68° and

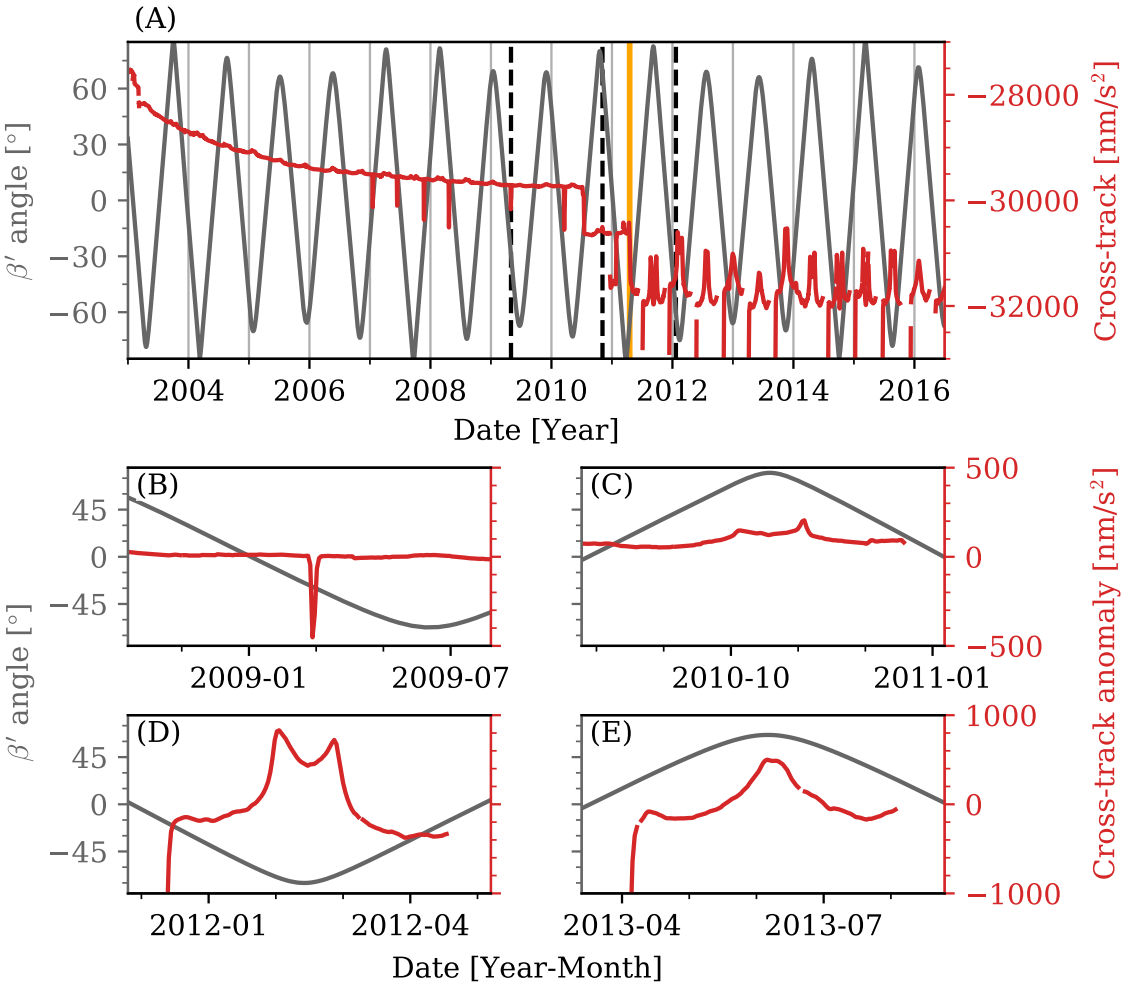

Figure 3.1: Average daily uncalibrated GRACE-A cross-track accelerations (red) compared to the average daily β' angle (grey). (a) From 2003 to mid-2016, prior to the switch-off of satellite thermal control (orange solid line) the mean accelerations contain only low-magnitude variations (with few exceptions), compared to the high-magnitude variations contained in the observations post April 2011. Periods of thermally-induced bias drift explored in this study (black dashed lines) described in Section 2.2: (b) November 2008 to July 2009, (c) August to January 2011, (d) December 2011 to May 2012 and (e) March to August 2013.

again as the satellites passed through the Earth's shadow (Figure 3.1c). These events are characterised by a steady, quasi-linear increase (>100 nm/s^2) over ∼30 days in the cross-track bias, peaking as the satellites approached full-Sun orbit, followed by a steady decrease as the satellites reached a maximum $|\beta'|$ angle. This signature is mirrored as the satellites transitioned back into orbit partially in shadow, creating a double-peaked pattern in the cross-track bias (Figure 3.1c).

The distinctive double-peaked pattern in the cross-track bias (and accelerometer temperature) occurs because sunlight would have illuminated primarily one of the side panels once the $|\beta'|$ angle exceeded 68° and the satellites remained in full-Sun orbit. Despite the satellites not entering the Earth's shadow for an extended period of time, less solar radiation was absorbed as the side panels are angled and so not normal to the incoming solar radiation and have a smaller surface area (Fulcher, 2016).

After thermal control of the GRACE spacecraft was switched off in April 2011, significant internal temperature variations increased in both frequency and magnitude (Figure 3.1a,d) (Herman et al., 2012; Klinger and Mayer-Gürr, 2016). Significant bias change (>600 nm/s^2 over ∼30 days) occurred as the satellites approached, maintained and exited full-Sun orbit, producing a relatively high magnitude double-peaked pattern in the cross-track bias (Figure 3.1d).

Occasionally the value of the $|\beta'|$ angle did not exceed 68° in a year (Figure 3.1e) and, consequently, the satellites never entered full-Sun orbits. This was caused by the resonance of the $|\beta'|$ angle signal with the precession of the right ascension of the ascending node of the orbital plane (the longitude at which the ascending node crosses the equator) which has a frequency of one cycle per ∼3.5 years. During these years the double peak in cross-track bias and accelerometer temperature during full-Sun orbit did not occur, instead a single peak in temperature and cross-track bias is observed (Figure 3.1e).

The largest-magnitude cross-track bias variations (>900 nm/s^2) over the GRACE period occurred immediately after the accelerometers had been switched on following periods of maximum shadow time ($|\beta'|$ angle <20°; Figure 3.1a,d,e). In this scenario, the cross-track bias stabilised ∼4-5 days after power was restored, similarly to the return to nominal bias values following the reconnection of heater lines during thermal control (i.e. Figure 3.1b). Both types of events caused severe bias drift, particularly in the cross-track accelerations.

Simply adjusting for multiple accelerometer biases within a single day to account for

these thermally-induced sub-daily variations in the accelerometer biases will introduce discontinuities in the accelerometer observations. The approach of Klinger and Mayer-Gürr (2016) ensures continuity of the estimated accelerometer biases within a single day by estimating accelerometer biases using uniform cubic basis splines for each orthogonal axis with 6-hour knot intervals, requiring a total 21 bias parameters per satellite per day. Alternatively, non-linear long wavelength noise could be removed from the accelerometer observations a priori before using them in the orbit integration. For example, Lemoine et al. (2018) developed an empirical approach to model accelerometer biases as a function of measured internal satellite temperature, which yields calibrated non-gravitational accelerations accurate to ± 100 nm/s^2 on the cross-track axis. However, due to the generalised nature of their model, Lemoine et al. (2018) still needed to estimate multiple bias corrections in the cross-track axis after a priori calibration for temperature effects (J-M Lemoine, personal communication, 10 October, 2019).

That the accelerometers are highly sensitive to internal temperature variations, particularly in the cross-track axis, highlights the need to develop a method that adequately removes these effects before using the observations in precise gravity field determination. This is especially true for the latter half of the GRACE mission in the post thermal control period.

3.2.2 Scenarios of thermal-induced bias drift explored in this study

We analysed three 10-day periods of GRACE accelerometer observations that are coincident with significant temperature variations: 2009-04-28 to 2009-05-07, 2010-11-01 to 2010-11-10 and 2012-01-17 to 2012-01-26. The temperature and accelerometer measurements are obtained from the Level-1B accelerometer housekeeping data product (AHK1B), and the ACC1B, respectively. We corrected the ACC1B observations (Figures 3.2-3.4) a priori for a bias offset following the recommendations of Bettadpur (2009).

3.2.2.1 Intermittent disabling of accelerometer heaters

GRACE-A experienced an onboard computer reboot on 2009-04-30 (Flechtner et al., 2009). Consequently, the accelerometer heaters were disabled, resulting in a 3.3°C temperature decrease measured in the internal core of the accelerometer, followed by a period of re-heating and thermal re-stabilisation (Figure 3.2). A bias drift was introduced into the along-track and cross-track accelerations, coincident with and proportional to the magni-

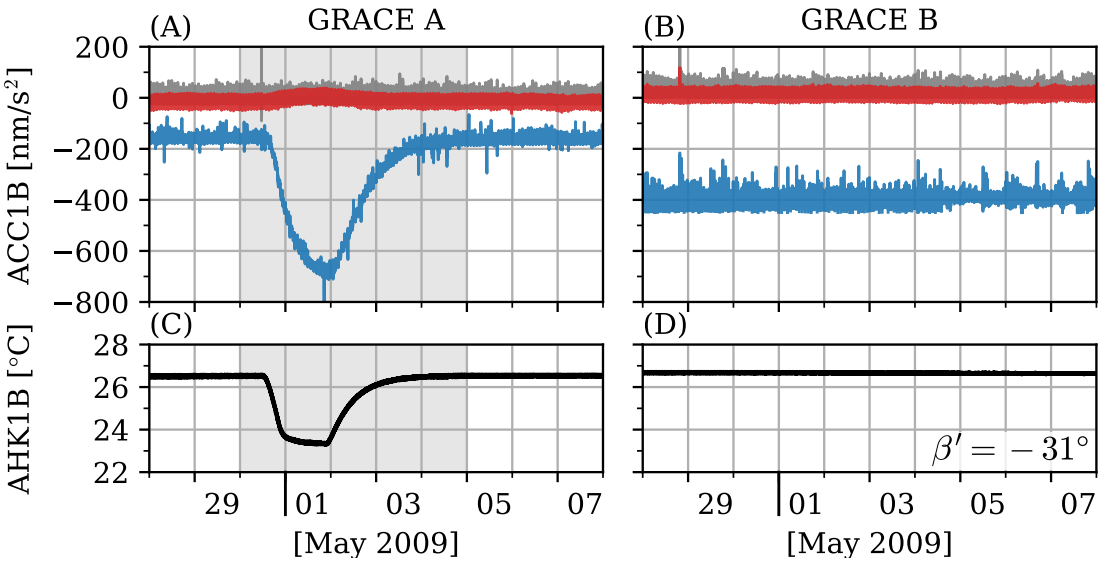

Figure 3.2: (a) GRACE-A and (b) GRACE-B ACC1B accelerometer observations in along-track (red), cross-track (blue) and radial (grey) directions calibrated to the recommendations of Bettadpur (2009) and (c) GRACE-A and (d) GRACE-B AHK1B accelerometer temperature observations for the internal core from 2009-04-28 to 2009-05-07. GRACE-A observations during a period of severe internal thermal variations (light grey) caused bias-drift to appear in the cross-track and along-track measurements while GRACE-B concurrently observed a thermally controlled environment. Many large outliers occur in the GRACE-B cross-track accelerations during this period which have been removed from this figure.

tude of the temperature variation but with a time-lagged behaviour, as shown by Klinger and Mayer-Gürr (2016). The initial temperature decrease resulted in a gradual change in the bias over a 36 hour period of 500 nm/s^2 in the less sensitive cross-track axis, and 20 nm/s^2 in the along-track axis (Figure 3.2). Once the heaters were re-enabled both the along-track and cross-track biases returned gradually over 3 days to their nominal values prior to the reboot event (Figure 3.2). A total of 5 days of ACC1B observations were impacted by the event, highlighted in grey in Figure 3.2. Flechtner et al. (2009) stated that these days should not be used in nominal gravity field determination. The GRACE-B observations were not affected during this period.

3.2.2.2 High $|\beta'|$ during period of partial thermal control

As part of a new battery management strategy, the GRACE-B accelerometer sensor unit (SU) was no longer under thermal regulation due to setting a lower temperature on the heater from 2010-10-03 (Flechtner et al., 2009). As the satellites approached a full-Sun orbit, the temperature of the internal core of the GRACE-B accelerometer started to rise (by 2.3°C) and the SU temperature started to drift in an uncontrolled manner, causing

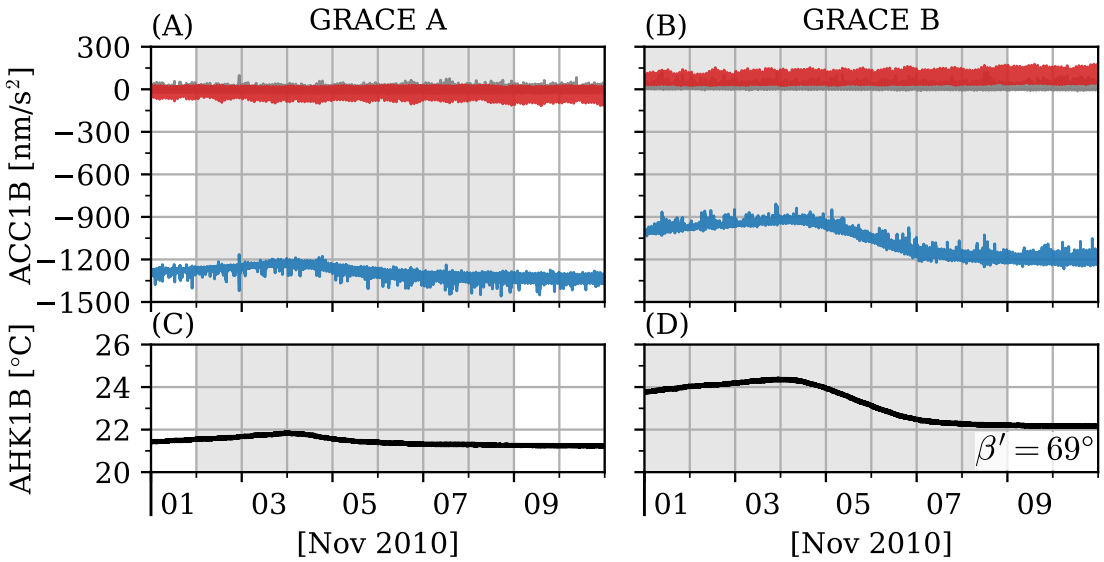

Figure 3.3: (a) GRACE-A and (b) GRACE-B ACC1B accelerometer observations in along-track (red), cross-track (blue) and radial (grey) directions calibrated to the recommendations of Bettadpur (2009) and (c) GRACE-A and (d) GRACE-B AHK1B accelerometer temperature observations for the internal core from 2010-11-01 to 2010-11-10. GRACE-A and GRACE-B both observed thermally variable environments which caused low-magnitude bias drift to appear in the cross-track accelerations coincident with high $|\beta'|$ angles during a period of partial thermal control.

the cross-track bias to drift by 300 nm/s^2 (Figure 3.3). The GRACE-B accelerometer SU returned to thermal regulation on 2010-11-08. The GRACE-A accelerometer SU was under thermal control during this period; however, on 2010-11-02 the GRACE-A cross-track bias started to drift (150 nm/s^2) due to a small increase in temperature (0.7°C) as the satellite entered a full-Sun orbit (Figure 3.3). The cross-track biases on both GRACE-A and -B stabilised on 2010-11-08, highlighted in grey in Figure 3.3. The cross-track bias drifted for both satellites but the GRACE-B bias drift is of significantly higher magnitude during the period of full-Sun orbit because it is also affected by a lack of accelerometer SU thermal control. The along-track and radial biases don't appear to be affected during this period.

3.2.2.3 High $|\beta'|$ after thermal control was disabled

During the 10-day period from 2012-01-20 to 2012-01-29, gradual temperature increases are observed on both GRACE-A (3.2°C) and -B (2.9°C) satellites as the spacecraft began to enter full-Sun orbit (Figure 3.4). As a result the GRACE-A and -B cross-track biases drifted by a total 450 nm/s^2 and 350 nm/s^2, respectively (Figure 3.4). This 10-day period occurred after permanent disabling of the satellite thermal control and, therefore, the accelerometer temperature and bias drift were highly correlated with the $|\beta'|$ angle.

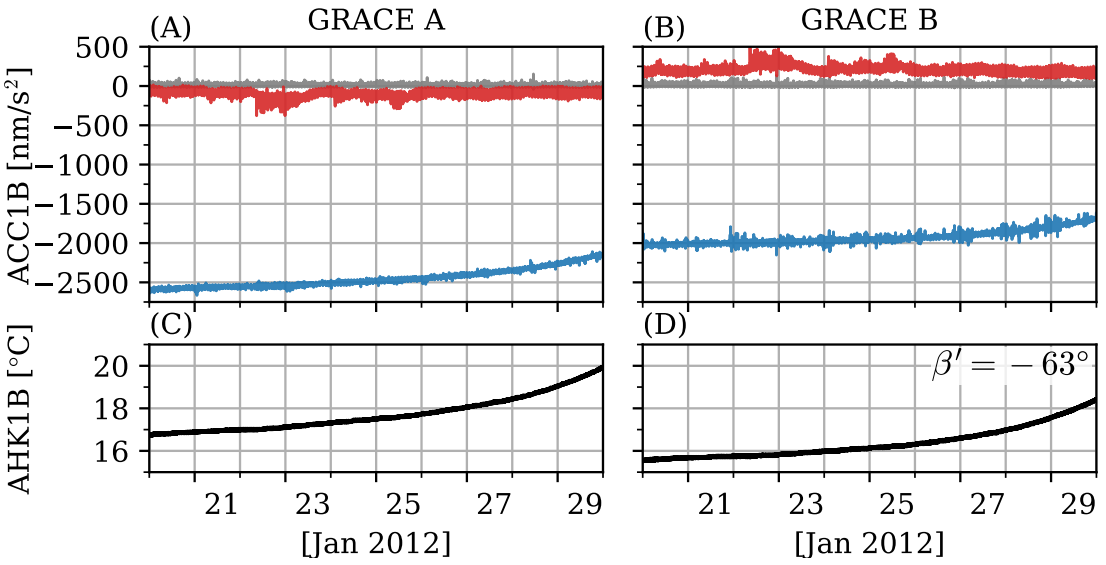

Figure 3.4: (a) GRACE-A and (b) GRACE-B ACC1B accelerometer observations in along-track (red), cross-track (blue) and radial (grey) directions calibrated to the recommendations of Bettadpur (2009) and (c) GRACE-A and (d) GRACE-B AHK1B accelerometer temperature observations for the internal core from 2012-01-20 to 2012-01-29. (left) GRACE-A and (right) GRACE-B both observed thermally variable environments which caused high-magnitude bias drift to appear in the cross-track accelerations coincident with high $|\beta'|$ angles during a period after thermal control was disabled.

3.3 Removing thermal noise from the cross-track accelerations

The characteristics that define the noise and the non-gravitational signal components contained in the cross-track accelerometer observations can be analysed in the frequency domain. Here, we compute the discrete Fourier Transform on the cross-track accelerometer observations, then filter the Fourier coefficients in the frequency domain to remove the long wavelength components of the signal, assumed to correspond to the thermal noise. We use the FORTRAN90 subroutines for real periodic 1D data from the publicly available FFTPACK5.1 (Swarztrauber, 1982) for performing fast Fourier transforms (FFT).

3.3.1 Windowing and data padding

The mathematics of the discrete Fourier Transform implicitly assume that the input discrete time-signal is a section of an infinitely long periodic sequence. This assumption suggests that if the input signal is known to be periodic it should contain an integer number of fundamental wavelengths. In the ANU GRACE software (Allgeyer et al., 2022) we process the GRACE data in 24-hour arcs, which inevitably describe a non-integer number

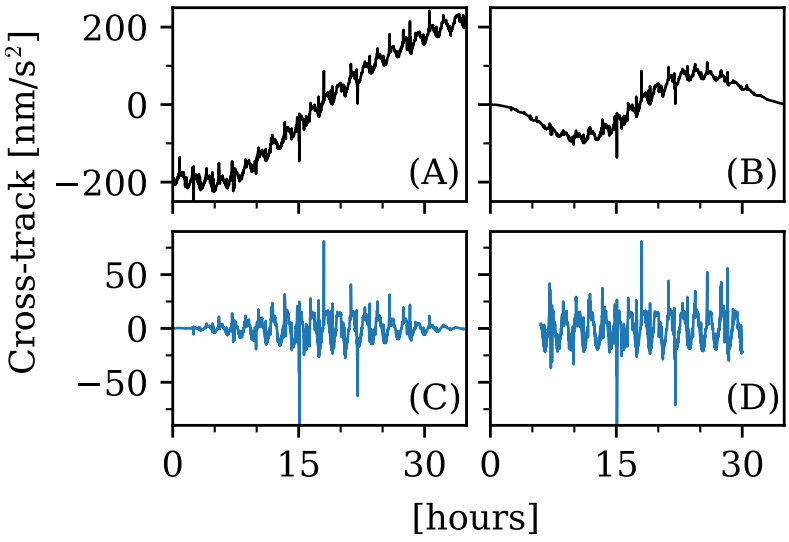

Figure 3.5: Digital filter approach applied to the (A) de-meaned and padded 2009-05-02 cross track accelerations, (B) tapered, (C) transformation of the filtered Fourier coefficients to the time domain, (D) rescaled and de-padded filtered observations used in orbit integration of the unfiltered (black) and filtered (blue) Fourier coefficients.

of orbital revolutions about the Earth. This can be mitigated by applying a tapering function to the observations to remove any discontinuities at the ends of the data. If the observations are not tapered prior to performing Fourier analysis, significant spectral leakage occurs causing additional lobes to appear in the frequency domain, preventing adequate filtering of the Fourier coefficients due to biased frequency estimates.

Prior to tapering the accelerometer observations, each end of a 24-hour period of ACC1B observations was extended by 6 hours so that the edges of each day of the filtered observations are recovered when the window function is removed once the signal is transformed back into the time domain. We removed a mean value from the observations then used the Hann window function (a raised cosine) (Blackman and Tukey, 1958) to taper the extended observations (Figure 3.5a,b). The window coefficients, $w(n)$, are calculated using:

$$w(n) = 0.5 - 0.5\cos\left(\frac{2\pi n}{N-1}\right) \qquad 0 \leq n \leq N-1 \tag{3.1}$$

We performed a forward FFT on the windowed observations (black; Figure 3.6) using a value greater than the number of observations to the next power of 2, effectively increasing the frequency resolution of the Fourier analysis and the efficiency of the computations.

3.3.2 Filter specifications

Once the windowed observations were transformed into the frequency domain (black; Figure 3.6), we filtered the frequencies using a raised cosine high-pass filter (blue; Figure 3.6). Amplitudes are attenuated between the lower, f_{lo}, and upper, f_{hi}, edge frequencies. The filter coefficients, $H(f)$, within this range were calculated using:

$$H(f) = \begin{cases} 0, & f < f_{lo} \\ 0.5(-1\cos\left(\frac{\pi(f-f_{lo})}{f_{lo}-f_{hi}}\right)+1), & f_{lo} < f < f_{hi} \\ 1, & f > f_{hi} \end{cases} \tag{3.2}$$

The values of the edge frequencies are critical to ensure that we adequately removed low-frequency noise, without affecting non-gravitational signal. We selected values of f_{lo} and f_{hi} after analysing many days of cross-track accelerations in the frequency domain and by testing a range of frequency cutoffs. The frequency components of the accelerometer observations were passed through the raised cosine high-pass filter, where f_{lo} and f_{hi} are set to 0.045 mHz and 0.055 mHz, respectively. This assumes that all frequency components less than 0.045 mHz are related to bias drift, effectively removing all signal with a period of more than ∼6 hours or one cycle per four orbital revolutions. Additionally, we assumed that all frequency components more than 0.055 mHz, (with a period of ∼5 hours) are non-gravitational signals in the accelerometer measurements.

To reconstruct the discrete time-signal back in the time domain we performed Fourier synthesis on the filtered Fourier coefficients using the inverse FFT algorithm (Figure 3.5c). The effects of the taper function and padding were then removed (Figure 3.5d) and the mean restored, forming the noise-reduced observations for use in orbit and gravity field determination.

3.3.3 Validation of the digital filter approach

Can our windowed raised cosine high-pass filter remove temperature-induced, low-frequency noise from GRACE cross-track accelerations without attenuating any non-gravitational signal? To assess this, we compared the filtered and unfiltered accelerometer observations in the time domain from 2009-04-28 to 2009-05-07 (Figure 3.2). During this 10-day period, the GRACE-A cross-track accelerometer biases varied from nominal to significantly drift-affected while the GRACE-B accelerometer biases maintained nominal

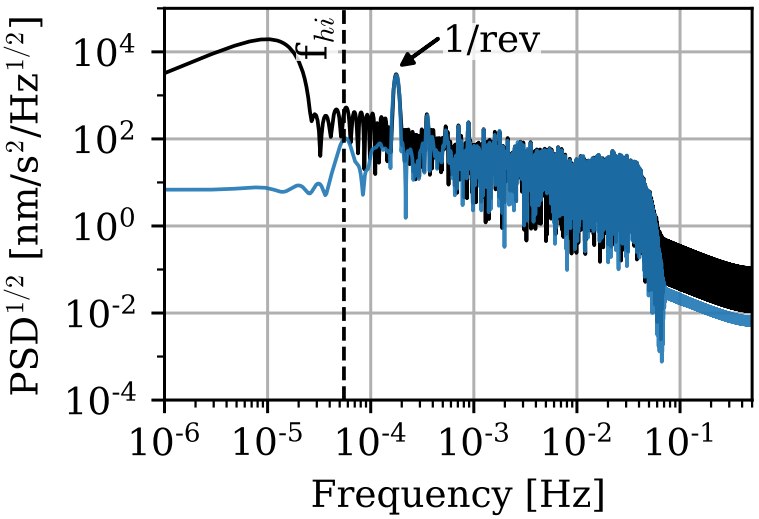

Figure 3.6: $PSD^{1/2}$ of the unfiltered (black) and filtered (blue) 2009-05-02 cross track accelerations which contained severe bias-drift in the low frequencies, removed in the filtering process which retains the non-gravitational signals of frequencies near 1 cycle-per-revolution (black arrow) and higher.

values. Hence, the filtered GRACE-A accelerations can be verified against the unfiltered GRACE-B accelerations throughout this 10-day period. We analysed two 6-hour periods of filtered GRACE-A cross-track acceleration observations, one containing negligible bias drift (2009-04-29) and another significant ($\sim$10 nm/s^2) bias drift (2009-05-04). For each 6-hour period, we compared the filtered GRACE-A cross-track accelerations to the unfiltered GRACE-A and GRACE-B observations (Figure 3.7).

Prior to the rapid decrease of the GRACE-A cross-track bias caused by the disabled accelerometer heaters on 2009-04-30, the GRACE-A accelerometer observations were unaffected by temperature-induced bias drift (Figure 3.2). The differences between the filtered and unfiltered GRACE-A cross-track accelerations should be minimal over this span assuming that our high-pass filter only removes sub-daily bias variation and not real sub-daily signal changes. As expected, the difference between the unfiltered and filtered accelerations over $\sim$4 orbital revolutions (6 hours) on 2009-04-29 is small ($<$1.2 nm/s^2 or $\sim$3% of the 1 cycle-per-revolution signal) and likely contains some low-magnitude, long-wavelength bias drift unrelated to thermal variations (Figure 3.7a). When bias drift is present in the accelerometer observations as a result of internal temperature changes, the high-pass filter removes the long-wavelength variations, an example of which is shown for 2009-05-04 (Figure 3.7B). The reconnection of the accelerometer heaters caused a 10.5 nm/s^2 bias drift over $\sim$4 orbital revolutions which brought the cross-track biases back to nominal values.

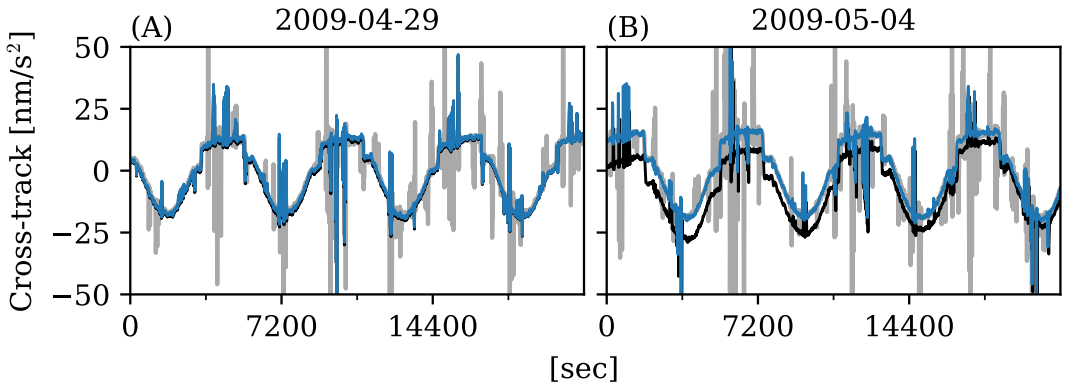

Figure 3.7: GRACE-A unfiltered (black) and filtered (blue) cross-track accelerations illustrating the effect of filtering for a 6-hour period of cross-track accelerations (a) that contain negligible bias drift and (b) some low-magnitude bias drift removed during the filtering process. Both periods are compared to the unifiltered GRACE-B observations (grey) which was not impacted by thermal variations during 2009-04-29 and 2009-05-04.

This non-linear change was appropriately removed by the high-pass filter (Figure 3.7b).

We compared the filtered GRACE-A and unfiltered GRACE-B cross-track accelerations, after having reversed the sign and applying a 35-second time offset of the GRACE-B measurements to align the observations. The dominant orbital period is consistent between filtered GRACE-A and unfiltered GRACE-B throughout the 10-day period (Figure 3.7), suggesting that the high-pass filter retains non-gravitational signal (i.e. frequency 1 cycle-per-revolution and higher) in the cross-track accelerations.

3.4 Removing thermal noise from the along-track accelerations

The along-track accelerations contain bias drift in the presence of severe internal thermal variations (e.g. Figure 3.2). In contrast to the cross-track, using the cosine high-pass filter to remove along-track bias drift tends to attenuate non-gravitational accelerations. Here, we demonstrate that there is common mode bias drift between the along-track and cross-track axes in the presence of internal thermal variations. We describe a method for transferring the derived cross-track bias drift to the along-track observations to correct for temperature-induced noise.

We compared a 24-hour arc of GRACE-A and GRACE-B accelerometer observations, wherein one satellite (i.e. GRACE-A) experienced significant thermal variations and, therefore, significant cross-track bias drift (Figure 3.8a). To try to identify the bias drift

contained in the GRACE-A along-track accelerations (Figure 3.8a), we filtered the along-track accelerations on both satellites using a raised cosine low-pass filter with a low frequency cutoff of 0.2 mHz to extract signal with a frequency of ∼1 cycle-per-revolution or less (Figure 3.8b). We then subtracted the (sign reversed and offset) GRACE-B low-passed accelerations from the GRACE-A low-passed accelerations (red; Figure 3.8c). Assuming that GRACE-B is unaffected by bias drift, the resultant signal contains the GRACE-A temperature-induced variations and a 1 cycle-per-revolution oscillation which may represent a slight difference in the GRACE-A and GRACE-B along-track accelerometer scale or pitch difference (Bandikova et al., 2019).

We derived the GRACE-A along-track bias drift (orange; Figure 3.8c) by estimating a transfer factor to scale the cross-track bias drift (grey; Figure 3.8c) to the difference in the low-passed along-track accelerations (red; Figure 3.8c). We then removed the temperature-induced long-wavelength noise by subtracting the along-track bias drift from the GRACE-A along-track observations (red; Figure 3.8d). The dominant orbital period then becomes consistent between thermally-corrected GRACE-A and unfiltered GRACE-B accelerations (Figure 3.8d), confirming that the transfer function method does not remove non-gravitational signal from the along-track observations.

To find an appropriate GRACE-A along-track bias drift transfer factor for use in a priori accelerometer calibration for the entire GRACE mission we identified days that contained a magnitude of cross-track bias drift in the GRACE-A observations (>25 nm/s^2) and negligible bias drift in the GRACE-B observations (<5 nm/s^2) prior to permanent thermal control cessation (April 2011). We calculated GRACE-A along-track transfer factors for 33 days that satisfied the test case conditions. The mean GRACE-A along-track transfer factor was -0.041 with a Root Mean Square Error (RMSE) of 3.4E−3 (blue; Figure 3.9). We repeated this process for 15 GRACE-B test cases and calculated a mean along-track transfer factor of -0.017 with a RMSE of 4.4E−3 (red; Figure 3.9). Curiously, it appears that the GRACE-A along track axis is more than twice as sensitive to thermal variations than the GRACE-B along track axis. We do not have an explanation for this.

We repeated this process for the radial accelerations for each of the GRACE-A and GRACE-B test cases. Unlike the along-track, the mean estimated radial transfer factors (-0.0037 and -0.0042 for GRACE-A and GRACE-B, respectively) were not significantly different from zero (F-test with 95% confidence interval) and produced comparatively large RMSE (2E−2 and 3.1E−2 for GRACE-A and GRACE-B, respectively) (Figure 3.9). This

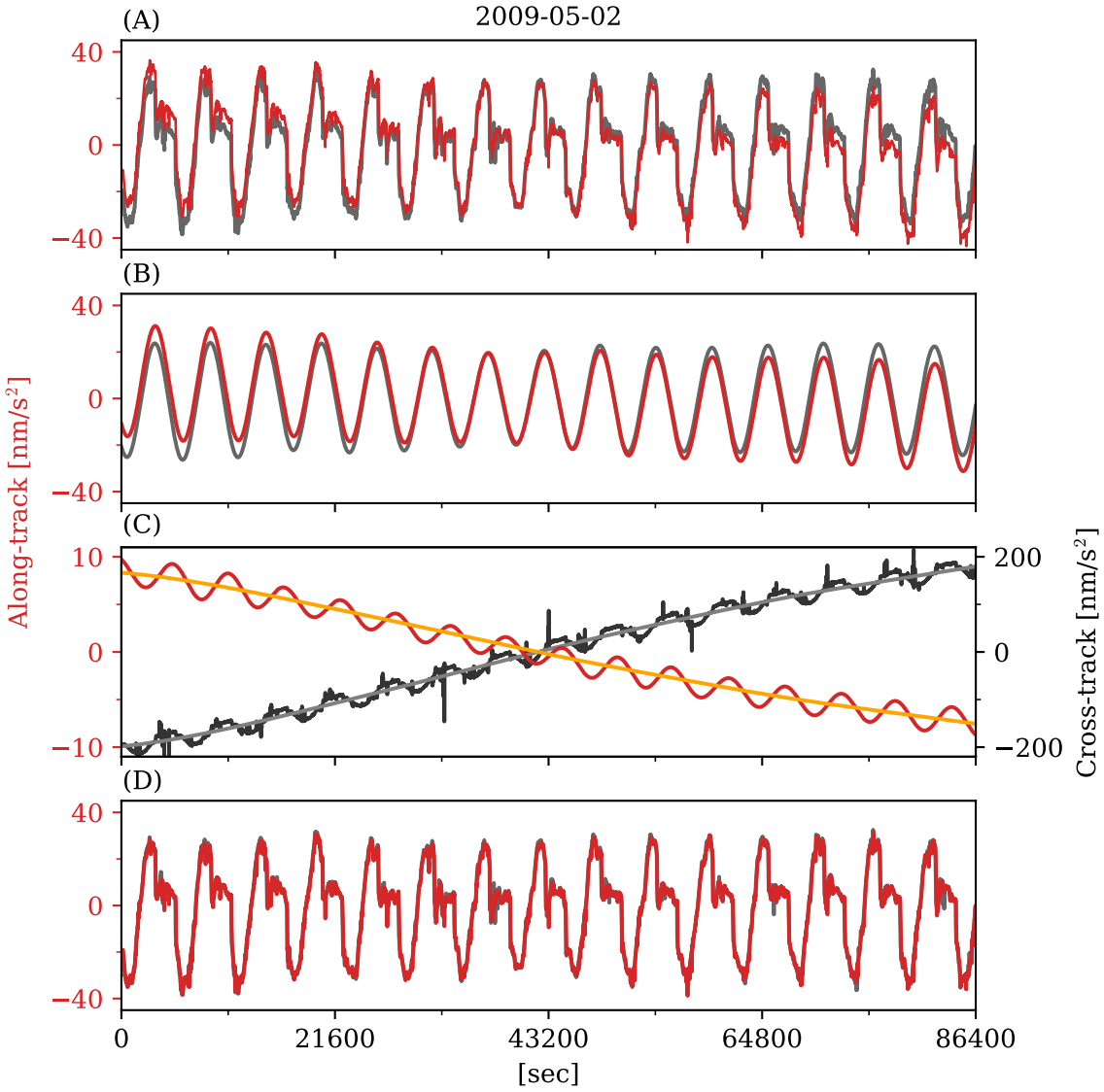

Figure 3.8: Along-track accelerations for 2009-05-02 during a period of severe internal thermal variations on GRACE-A only. The difference in (a) GRACE-B (grey) and GRACE-A (red) along-track accelerations is due to the long-wavelength bias drift contained in the GRACE-A measurements. (b) Low-pass filtered GRACE-B (grey) and GRACE-A (red) along-track accelerations. (c) GRACE-A cross-track accelerations (black), GRACE-A cross-track bias drift (grey), differenced GRACE-A and GRACE-B low-pass filtered along-track accelerations (red) and GRACE-A along-track bias drift (orange) show a common mode bias-drift in the along-track and cross-track observations. (d) GRACE-B (grey) and thermally-corrected GRACE-A (red).

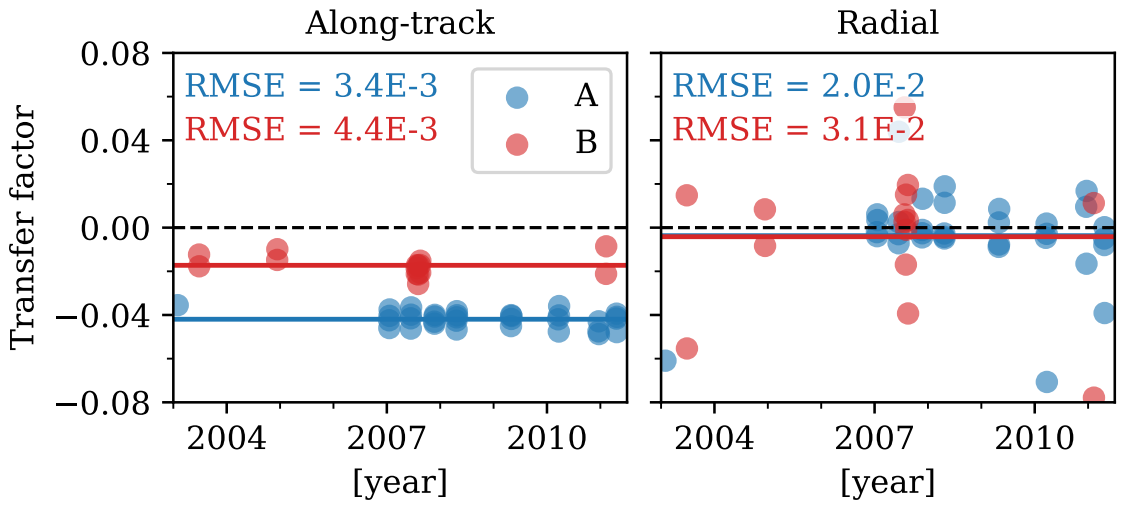

Figure 3.9: (Left) along-track (right) and radial estimated and mean transfer factors for GRACE-A (blue) and GRACE-B (red). The mean along-track transfer factor is statistically significant, which is further evidence for a common mode bias-drift between the along-track and cross-track axes. In contrast, the radial axis does not have a statistically significant transfer factor, and therefore does not appear to be impacted by internal thermal variations.

indicates that the radial accelerations do not contain detectable thermally-induced bias drift or variations correlated to the accelerometer temperature akin to the along-track and cross-track axes and, therefore, we do not apply a thermally based correction to the radial accelerometer observations.

3.5 Orbit and gravity field estimation

We estimated the temporal gravity field using the 10-days of GRACE observations for periods shown in each of Figs. 3.2-3.4, applying the filtering method described in Section 3 and the transfer function method described in Section 3.2 to the cross-track and along-track accelerations, respectively. The temporal gravity field solutions using integrated orbits calculated using uncorrected accelerometer observations and using the thermally-corrected observations were then compared (Figs. 3.10-3.12).

We computed orbits for GRACE-A and GRACE-B by integrating the accelerations calculated from the background forcing models and observations, including the static gravity field (Bruinsma et al., 2013), non-tidal atmosphere and ocean dealiasing product and atmospheric tides (Dobslaw et al., 2017a), ocean tides (Carrere et al., 2015; Lyard et al., 2021), celestial body perturbations (Folkner et al., 2009), solid Earth tides (McCarthy, 1992; Wahr et al., 2015), general relativity (Petit and Luzum, 2010) and non-gravitational accelerations (see Table 1 of (Allgeyer et al., 2022)). Following Allgeyer et al. (2022), we

use range acceleration as our inter-satellite observation, computed by numerically differentiating the range rate, which has been shown to reduce north-south striping in estimates of the temporal gravity field.

The temporal gravity field (i.e. mass anomalies with respect to a static gravity field (Bruinsma et al., 2013)) is represented using mascons as the basis functions. The change in mass of each mascon (in terms of equivalent water height), whose coordinates were calculated on the topographic surface, are explicitly related to the accelerations acting on the satellites (Tregoning et al., 2022). We formed irregularly shaped mascons with an area of 40,000 km^2 that follow continental/ocean boundaries (Tregoning et al., 2022). Densities of mass changes of 1029 g/cm^3 and 1000 g/cm^3 were assigned to oceanic and continental mascons, respectively.

We formed normal equations for each day of observations, then stacked 10 days of normal equations for each case study outlined in Section 3.2.2. Adjustments to the satellite orbital parameters and mascons in terms of equivalent water height of the appropriate density were estimated using as few parameters as possible (initial position and velocity of each satellite, one accelerometer bias and scale parameter per satellite per orthogonal axis per day and mascons) in a least squares inversion (Allgeyer et al., 2022):

$$\hat{x} = (A^T W A + C_{mass} + \lambda C_M)^{-1} A^T W b \tag{3.3}$$

where $\hat{x}$ are the adjustments to the satellite orbital parameters and mascon values, A contains the partial derivatives relating the observations to the parameters, W is an observation weight matrix, b contains the prefit residuals and C_{mass} is a constraint matrix for conservation of mass. C_M is a diagonal regularisation matrix with elements $1/\sigma_m^2$, where σ_m is a location-based constraint defined for each mascon and zero off-diagonal elements, scaled by λ. Weights were assigned to the observations of 70 mm, 70 um/s and 1 nm/s^2 for position, velocity and range acceleration, respectively. We also applied constraints of 0.1 m, 0.25 m and 0.025 m to non-glaciated continental, glaciated continental and oceanic mascons, respectively, scaled by 10, the number of stacked daily normal equations (Tregoning et al., 2022). We converged on a set of orbital parameters and mascon values that best fit the Level-1B GPS positions and velocities and inter-satellite range acceleration observations using an iterative process Allgeyer et al. (2022).

Two solutions for the temporal gravity field were created for each of the case studies described in Section 3.2.2. First, we used orbits that included the unfiltered Level-1B ac-

celerations as the non-gravitational acceleration observations. Second, we used orbits that included the filtered Level-1B accelerations as the non-gravitational acceleration observations. In the second case, we applied the raised cosine high-pass filter to the cross-track accelerations according to the method outlined in Section 3.3 and the transfer function method to the along-track accelerations according to Section 3.4. We stacked 10 days of normal equations for each case study created with the uncorrected/thermally-corrected non-gravitational accelerations and inverted to simultaneously solve for the adjustments to all satellite parameters for each 24-hour orbit. 10-day mean values were estimated for each mascon in terms of equivalent water height.

3.6 Case studies

In this section we compare the estimates of the temporal gravity field using the estimated orbits which integrated the uncorrected and thermally-corrected non-gravitational accelerations for each scenario of temperature-induced bias drift explored in Section 3.2.2.

3.6.1 Intermittent disabling of accelerometer heaters

Internal thermal variations are caused by the intermittent disabling of GRACE-A accelerometer heaters for the most severe case of temperature-induced bias drift analysed in this study (2009-04-28 to 2009-05-07; Figure 3.2). We used the uncorrected level-1B accelerometer (ACC1B) observations (black; Figure 3.10a,b) in the integrated GRACE orbits which were inverted to solve for the temporal gravity field using the parameterisation outlined in Section 3.5. As a result of low-frequency thermal contaminations in these observations, the solutions contained significantly high range acceleration postfit residuals (e.g. Figure 3.10c). The 10-day solution of the temporal gravity field containing the uncorrected non-gravitational accelerations produced significant and unrealistic north-south striping (Figure 3.10f), particularly in continental and oceanic regions in the mid-to-low latitudes. As expected, the estimates of the accelerometer scale factors are unstable on all axes, particularly for the days containing significant bias drift (black; Figure 3.10i-k).

We produced a second estimate of the temporal gravity field for this 10-day period after having re-integrated the orbits using the high-pass filtered cross-track (blue; Figure 3.10b) and the uncorrected along-track (black; Figure 3.10a) non-gravitational accelerations. The resulting range acceleration postfit residuals were slightly improved (e.g. Figure 3.10d) and the 10-day solution of temporal gravity field contained less noise. However, north-

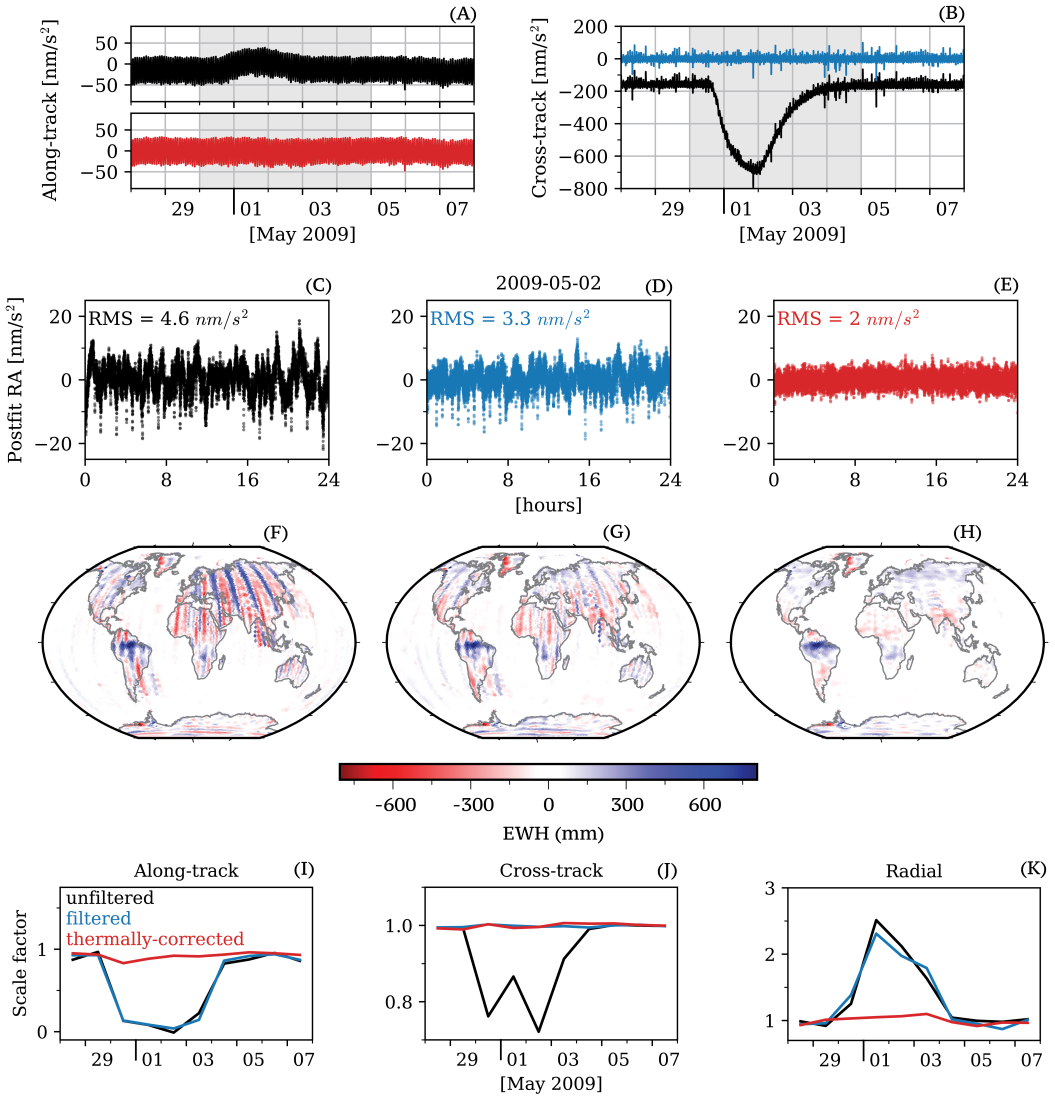

Figure 3.10: *First row*: (a) Uncorrected (black) and thermally-corrected (red) ACC1B along-track observations, (b) uncorrected (black) and filtered (blue) ACC1B cross-track observations for GRACE-A from 2009-04-28 to 2009-05-07. *Second row*: (c) 24 hours of range acceleration postfit residuals in 2009-05-02 from each 10-day temporal gravity field solution using uncorrected ACC1B, (d) filtered ACC1B cross-track and (e) thermally-corrected along-track and filtered cross-track ACC1B observations. *Third row*: stacked 10-day temporal gravity field solutions in terms of equivalent water height (EWH) using (f) uncorrected ACC1B observations, (g) filtered ACC1B cross-track observations, (h) filtered and thermally-corrected ACC1B cross-track and along-track observations. *Fourth row*:Daily scale factor parameter estimates in the (i) along-track, (j) cross-track and (k) radial axes for the uncorrected (black), filtered cross-track (blue) and filtered cross-track and thermally-corrected along-track (red) inversions.

south striping is still observed in the low to mid-latitude oceans and continents (Figure 3.10g). The scale factor estimates produced by this inversion are stabilised near 1 in the cross-track axis, but remain unstable in the along-track and radial axes (black; Figure 3.10i-k).

In our third solution, we re-integrated the orbits using the high-pass filtered cross-track (Figure 10B; blue) and the thermally-corrected along-track (red; Figure 3.10a) non-gravitational accelerations. The range acceleration postfit residuals were improved further (e.g. Figure 3.10e). Striping in the 10-day solution of the temporal gravity field is no longer evident (Figure 3.10h) and scale factor estimates in all axes are stabilised near 1 (Figure 3.10i-k), indicating that our model corrections to the cross-track and along-track accelerometer observations have removed, or significantly mitigated, the thermal noise in the accelerometer observations. The scale factor estimates in the radial axis are significantly improved (Figure 3.10k) despite not applying a thermally based correction to the radial accelerometer observations, supporting our conclusion that the radial axis is unaffected by thermal-induced bias drift. Mitigating bias drift in accelerometer observations degraded by bias drift caused by accelerometer switch-on after full-Sun orbit during the thermally uncontrolled portion of the GRACE mission also improved estimates of the temporal gravity field (results not shown).

3.6.2 High $|\beta'|$ angle

Significant cross-track bias drift is present in the cross-track accelerations during thermally controlled (2010-11-01 to 2010-11-10; Figure 3.3) and uncontrolled portions of the mission (2012-01-20 to 2012-01-29; Figure 3.4) during periods of high $|\beta'|$ angles. We used the uncorrected ACC1B (black; Figure 3.11a,b) as the non-gravitational accelerations to integrate orbits which were inverted to solve for the temporal gravity field. In both cases, unrealistic north-south striping is visible in the 10-day mascon solutions. Again, this error is particularly noticeable in low to mid-latitudinal continental and oceanic regions (Figure 3.11c,d).

The north-south striping in the 10-day 2010 estimated temporal gravity field is mitigated when the filtered cross-track and thermally-corrected along-track accelerations are used as the observation in the integrated orbits (Figure 3.11e). Some north-south striping remains in the thermally corrected 10-day 2012 estimated temporal gravity field (Figure 3.11f) due to large gaps in the ground track pattern at low to mid-latitudes, these errors

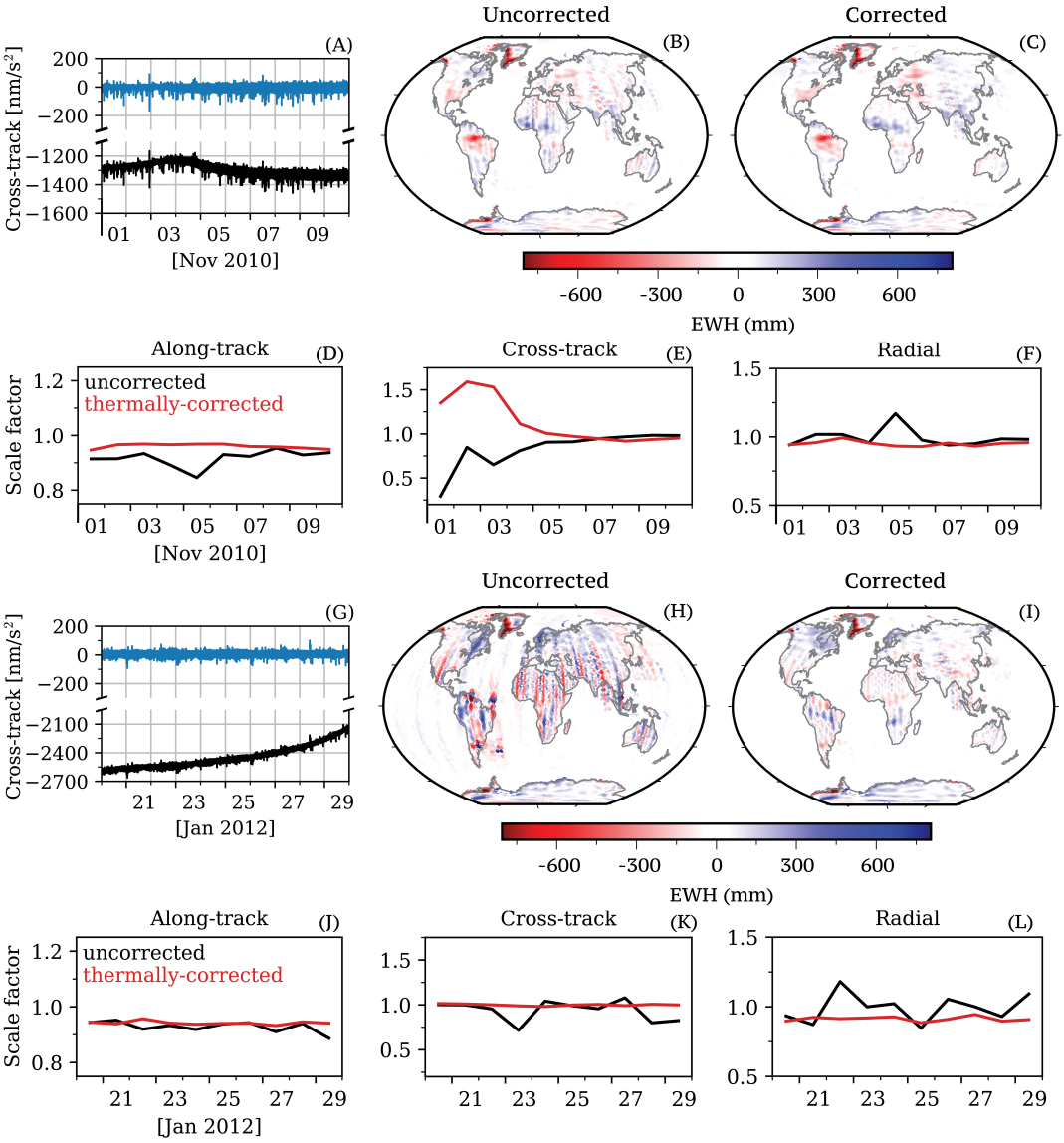

Figure 3.11: (A-F) 2010-11-01 to 2010-11-10 (a) Uncorrected (black) and filtered (blue) GRACE-A ACC1B cross-track observations. Stacked 10-day temporal gravity field solutions in terms of equivalent water height (EWH) using (b) uncorrected and (c) filtered and thermally-corrected ACC1B cross-track and along-track observations show a significant reduction in north-south striping error. Daily scale factor parameter estimates in the (d) along-track, (e) cross-track and (f) radial axes for the uncorrected (black) and filtered cross-track and thermally-corrected along-track (red) inversions. (g-l) as per (a-f) for 2012-01-20 to 2012-01-29.

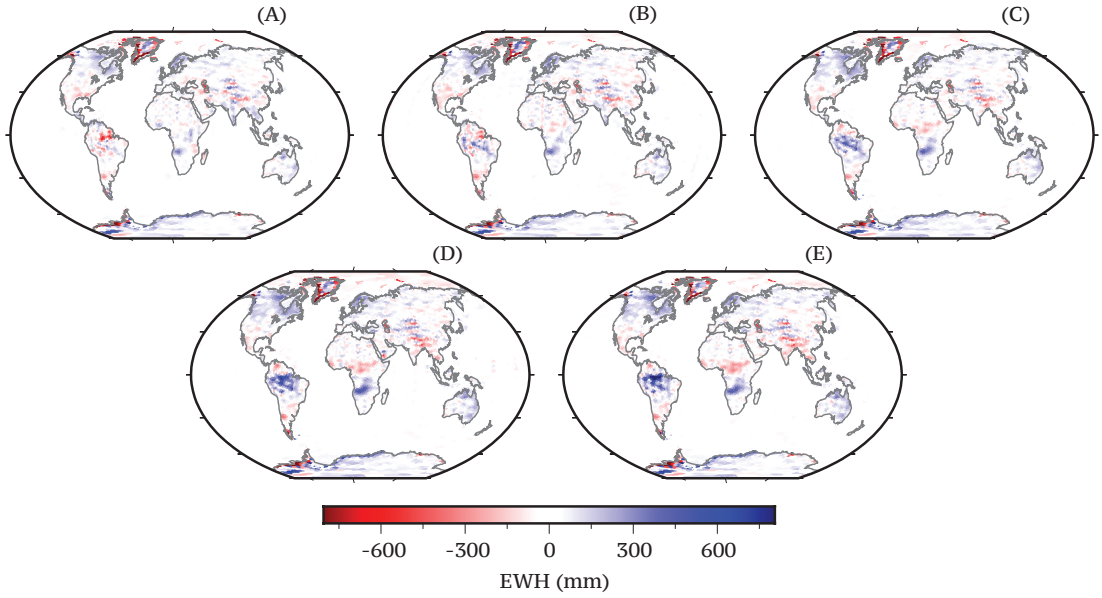

Figure 3.12: Estimates of the temporal gravity field in terms of equivalent water height (EWH) from Allgeyer et al. (2021) during the latter half of the GRACE mission in the absence of thermal control for (a) December 2011, (b) January 2012, (c) February 2012, (d) March 2012 and (e) April 2012. Across the five months, the $|\beta'|$ angle changed from a minimum in December 2011 to a maximum in February 2012 and the non-gravitational accelerations contained bias-drift of varying magnitude throughout (see Figure 3.1C).

are eliminated with the addition of more days in the stacking of the normal equations (not shown). In the correction of the along-track accelerations, small but significant bias drift is removed, a total of 5 nm/s^2 and ∼12 nm/s^2 from 2010-11-01 to 2010-11-10 and 19 nm/s^2 and 14 nm/s^2 from 2012-01-20 to 2012-01-29 from GRACE-A and GRACE-B, respectively.

The scale factor estimates are much more stable when the filtered cross-track and thermally-corrected along-track accelerations are used as the observations in the integrated orbits (Figure 3.11d-f,j-l). For all axes, the scale factor parameter estimates remain near 1, with the exception of the cross-track axis for the November 2010 inversion (Figure 3.11e). Indeed, the Level-1B cross-track accelerations from 2010-11-01 to 2010-11-04 appear to be impacted by a reduced scale, as evidenced by a reduced range and peak-to-peak magnitude of the cross-track accelerations when compared to other observations in the 10-day period. This issue is resolved by our improved scale factor estimates when the filtered cross-track and thermally-corrected along-track accelerations are used as the observation in the integrated orbits.

We analysed monthly solutions of Allgeyer et al. (2022) which include the filtered and thermally-corrected cross-track and along-track accelerations described in Section 3.3 and

3.4, from December 2011 to April 2012 (Figs. 3.1C, 3.12). These five consecutive months include orbital configurations from a minimum $|\beta'|$ angle of 18° to a maximum of 74°. That is, these months include the observations as the accelerometer temperature increased as the satellites entered then exited full-Sun orbit in early-February and early-March, respectively. The majority of each of the months from January to March were impacted by highly variable accelerometer temperatures as a result of solar radiation absorption and, therefore, the cross-track accelerations contained significant bias drift (Figure 3.1c). Despite this, the January to March solutions do not contain more noise than the December 2011 or April 2012 solutions which maintained stable bias values. This provides confidence that our method for removing bias drift effectively removes temperature-induced variations from the ACC1B along-track and cross-track observations.

3.7 Conclusion

Temperature-induced bias drifts in the accelerometer observations degrade the quality of mass change estimates from GRACE. These temperature effects are present throughout the GRACE mission, both during periods of thermal control and once thermal control of the satellites was disabled in April 2011. Prior to April 2011, low-magnitude bias drift in the along-track and cross-track accelerometer observations is highly correlated to variations in the $|\beta'|$ angle which describes the orientation of the satellite's orbital plane with respect to the Earth to Sun vector. Specifically, as the satellites approach full-Sun orbit (i.e. $|\beta'|$ angle $>68°$) solar radiation absorption increased to a maximum which is reflected in measurements of higher than average accelerometer temperatures. Although bias drift during periods of thermal control is relatively small, the errors contribute to unrealistic north-south stripes in estimates of mass change. Once thermal control was disabled, bias drift of a significantly greater magnitude began to degrade the GRACE accelerometer measurements as the internal temperature of the satellites varied freely, impacting the majority of measurements.

Throughout the GRACE mission there have been instances of sudden and significant internal temperature variations caused by operational decisions and instrument behaviours. These events, although infrequent and short-lived, tend to account for the most severe cases of accelerometer bias drift. Whenever temperature changes affected the accelerometer observations, the inclusion of drift-affected measurements in orbit integration with minimal parameterisation (a single bias and scale factor per accelerometer axis per satellite per

day) introduced large, north-south stripes in estimates of mass change, unrepresentative of the Earths temporal gravity field.

The temporal and spectral characteristics of thermally-induced bias drift have here been assessed and thus can be removed (or significantly mitigated) from the accelerometer observations. Our new method removes the long-wavelength along-track and cross-track bias changes prior to orbit integration, without attenuating non-gravitational signals, using a raised-cosine high-pass filter and transfer function. The resulting temporal gravity field solutions show significant improvements in the mass change estimates when the thermal-correction method is applied to the along-track and cross-track accelerations. Specifically, noise in the estimates of the temporal gravity field visible as north-south striping is significantly reduced by filtering out signals on wavelengths characteristic of thermally-induced biases. Our method for removing bias drift from the along-track and cross-track accelerations prior to orbit integration does not require additional parameters, thus it limits the possibility for parameter trade-offs or the attenuation of the gravity field.

Chapter 4

Characteristics and benefits of using irregularly shaped mascons

Producing mass anomaly estimates from GRACE and GRACE-FO observations requires parameterising the temporal gravity field with basis functions. The use of mascons as the basis functions involves the creation of a global (regular or irregular) grid of mascon tiles which can be constructed using any number of shapes and sizes. In this chapter, I demonstrate how the construction of the mascon pattern impacts intra-mascon variability (being the variations of mass change signals within a mascon), the misappropriation of signals caused by coastline-crossing mascons and the impact of regularisation on the recovery of a realistic synthetic temporal gravity field. We present a number of simulation studies that aim to recover a realistic, high-resolution synthetic temporal gravity field using a variety of mascon grids of different shapes and sizes. We find that 200 $\times$ 200 km irregularly shaped mascons that follow coastlines recover the synthetic temporal gravity field with the least error due to intra-mascon variability. These results serve as justification for the mascon parameterisation used to generate the GRACE mass anomaly time series presented in Chapter 5. This chapter is based on the manuscript published in the Journal of Geophysical Research - Solid Earth:

Tregoning, P., ***McGirr, R.,*** *Pfeffer, J., Purcell, A. P., McQueen, H., Allgeyer, S., and McClusky, S.C. (2022) ANU GRACE data analysis: Characteristics and benefits of using irregularly shaped mascons. Journal of Geophysical Research: Solid Earth, 127(2), e2021JB022412.*

I made the following contributions to this paper:

- Created a number of different mascon fields (Section 4.5) used in the simulation

studies which included
  - 2° and 3° coastline-crossing regular-shaped mascons (M1, M2; Table 4.1)
  - 90,000 km^2 and 40,000 km^2 irregular-shaped mascons that follow coastlines and drainage basin boundaries (M3, M4; Table 4.1)
  - 90,000 km^2 and 40,000 km^2 irregular-shaped mascons that follow coastlines and only the Amazon basin (M5, M6; Table 4.1)
- Reconfigured each of the mascon fields to reduce the impacts of problematic mascon geometries that degrade the gravity field estimates
- Created a synthetic temporal gravity field based on Dobslaw et al. (2015) which was used to simulate satellite position/velocity observations (Section 4.6, Figure 4.5)
- Produced and interpreted the results for all simulation studies (Figs. 4.6 to 4.9, Table 4.2) and wrote the text explaining these result (Section 4.8)
- Produced the iterated solutions using real GRACE Level-1B observations (Section 4.8.2; Figure 4.10)

My approximate contribution to this manuscript was 45%.

Re-configuring the mascon field

In this section, I describe the process I developed to mitigate temporal gravity field estimation errors that use as the basis function irregular-shaped mascons that follow coastlines and drainage basins. This information, which was not included in the Tregoning et al. (2022) manuscript upon which this chapter is based, is detailed in this section. To explain the process of re-configuring the mascon field to mitigate estimation errors it is necessary to outline some terms and concepts here that are further explained in depth in subsequent sections (i.e. Sections 4.2 to 4.5).

The mascon fields are defined by a pattern of small, regular $10' \times 10'$ (roughly 18 km×18 km, or 325 km^2) mascons that cover the surface of the Earth (see Section 4.2). These small mascons, which we call ternary mascons, are much smaller than the spatial resolution of the gravity anomaly fields that can be accurately estimated from GRACE data. We group these ternary mascons together to form larger mascons that have an area more compatible with the spatial resolution of the GRACE data (see Section 4.3). These larger mascons, which we call primary mascons, can be composed of any number of ternary mascons to form any regular or irregular shape (see Section 4.4). We make use of these irregularly-shaped primary mascons to create a global pattern of coastline-delimited primary mascons

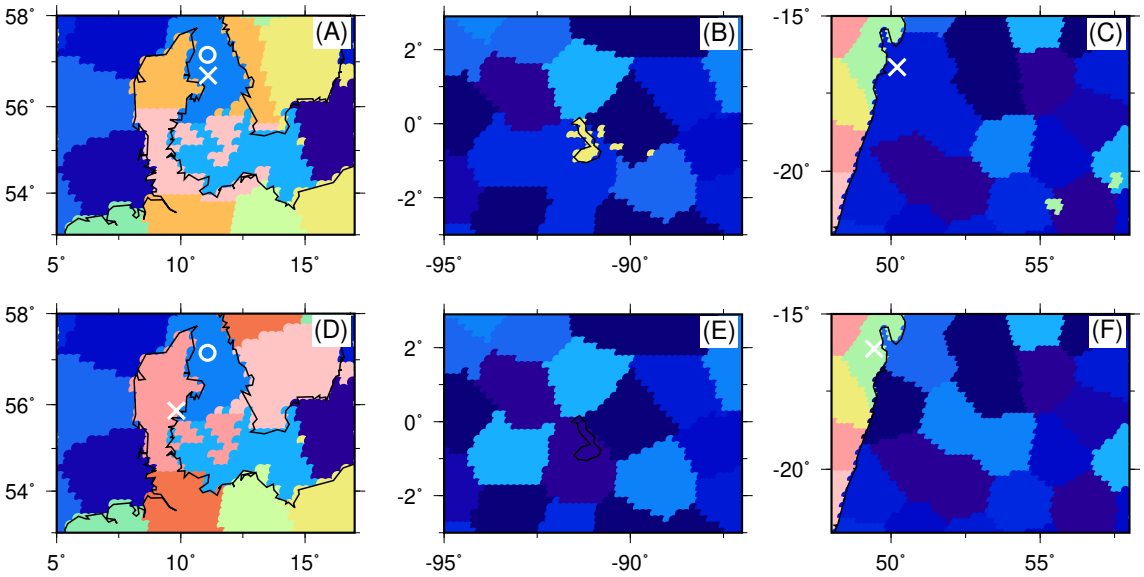

Figure 4.1: Examples of problematic and reconfigured primary mascons in the 40,000 km^2 irregular, coastline-delimited mascon grid. (a) Denmark continental (X) and ocean (O) primary mascons with co-located centres of mass (50.8 km), (b) Galapagos small island primary mascon (7,500 km^2), (c) Madagascar continental primary mascon (green, X) that includes distant ($> 6°$) ternary mascons (Mauritius and Réunion islands), (d) Denmark reshaped to repair co-located primary mascons, (e) Galapagos island primary mascon merged into surrounding ocean mascons, (f) Mauritius and Réunion island ternary mascons merged into surrounding ocean mascons to repair primary mascon with distant ternaries.

that are almost exclusively continental or exclusively oceanic. Using coastline-delimited mascons to estimate mass variations has the advantage of mitigating the misappropriation of signals caused by coastline-crossing mascons. The creation of the irregular, coastline-delimited primary mascon pattern from the regular grid of 10' × 10' ternary mascons is described in detail in Section 4.5.

The ternary mascons are aggregated to form an irregular grid of coastline-delimited primary mascons via a constrained k-means clustering and Minimum Cost Flow (MCF) algorithm (see Section 4.5 for details). Because the irregular primary mascons follow complex coastlines, the clustering algorithm can create problematic mascon geometries. Mascon geometries with co-located centres of mass can induce high correlations between the mascon parameters, which can cause errors to appear in the gravity field estimates. That is, primary mascons that have co-located centres of mass (Figure 4.1a), are significantly small in area (Figure 4.1b) or are constructed from distant ternary mascons separated by many ocean primary mascons (Figure 4.1b).

Co-located mascons are defined as a pair of primary mascons whose centres of mass are so close that adjustments to these mascon parameters cannot be uniquely estimated.

In the case of co-location, the pair of mascons produce partial derivatives that relate the mass change of each mascon to the inter-satellite observations that are not significantly different and, as a result, the parameters that represent these mascons are likely to be highly correlated. This results in inaccurate mass variation estimates for one or both mascon parameters (assuming the true value of mass change is different for each mascon).

Co-located primary mascons have been defined here as being mascons with a centre of mass less than the half-width of the mean primary mascon in distance from another primary mascons centre of mass. That is, for 200 km × 200 km mascons (40,000 km^2), a primary mascon whose centre of mass is <100 km from another mascons centre of mass is co-located. Co-located mascons appear in areas with complex coastlines, often in nearly or partly enclosed seas, for example a pair of co-located primary mascons is shown in Denmark where the North Sea and the Baltic Sea meet (Figure 4.1a). To avoid highly correlated mascon parameters, the continental regions shown in Figure 4.1a must be re-configured until there are no longer any co-located mascons (Figure 4.1d). Instances of co-location are treated on a case-by-case basis, often cases of ocean/continent co-location can only be treated by merging two ocean primaries together to shift its centre of mass away from the continental primary. This is a common necessity amongst groups of islands (i.e. Indonesia, Philippines). Co-located continental/continental mascons are rare unless the irregular mascon grid is both coastline and drainage basin delimited.

The process of creating the irregular mascon pattern also permits the creation of small island primaries that exist significantly far from other continental areas (e.g. Kerguelen Islands). These mascons have an area much less than the spatial resolution of the GRACE solutions and cannot be reliably resolved. Therefore, they must be merged into the surrounding ocean primaries or tightly constrained during the least squares adjustment. For example, the Galapagos Islands primary mascon has an area of only 7,500 km^2 (4.1b). Small continental primary mascons that have an area of less than 50% of the mean primary mascon (i.e. <20,000 km^2) are separated and merged into the surrounding ocean mascons (4.1e) during re-configuration.

Some small islands distant from mainland regions are included by the algorithm in primary mascons far from their location. For example, the Mauritius and Réunion islands are included in a Madagascar primary mascon despite being located further than 6° away (green mascon, 4.1c). I defined the ternary mascons >6° from their primary mascons centre of mass as outlier ternaries. These ternary mascons are then separated and merged

into the surrounding ocean mascons (4.1f).

To test how re-configuring problematic mascon geometries improves the accuracy of the mascon parameter estimates I performed three simulations using different mascon geometries. The methodology for producing estimates of the temporal gravity field from simulated observations is detailed in Section 4.7 and outlined here. First, I generated a set of "truth" orbits that contain the accelerations acting on the satellites computed from models and observations (see Table 1 of Allgeyer et al. (2022)) and a known temporal gravity field that I sought to recover. The "truth" orbits were then used to create the simulated observations that replace the satellite positions, velocities and range rate observations supplied in the GRACE Level-1B data. I also integrated a set of "a priori" orbits that do not include the temporal gravity field. I then solved for adjustments to the satellite parameters and mascons in a least squares inversion of the noise free simulated observations, producing a model of mass variations in terms of Equivalent Water Height (EWH) that resembles the known synthetic temporal gravity field included in the modelling of the "truth" orbits.

To create the synthetic temporal gravity field, each ternary mascon was assigned a mass change signal based on the high-resolution Earth system model of Dobslaw et al. (2015). The synthetic temporal gravity field contains the static components of the monthly-averaged variations in terrestrial water storage, cryospheric variability and solid Earth deformation for December 2006, no sub-daily high frequency mass changes were modelled (see Figure 4.5 and Section 4.6 for details). I performed several simulations using different mascon geometries for a month of observations in July 2016, the adjustments to the satellite parameters and mascons were solved for in an unregularised least squares inversion of our noise free simulated observations (see Section 4.7). I assessed the accuracy of each solution by calculating the "error", being the deviation of the mascon adjustments from the known ternary mass variations. The solution error includes the effects of intra-mascon variability within a primary mascon and the leakage (or misappropriation) of signal from one mascon to another.

The accuracy of the mascon solutions is improved when the mascon geometries are reconfigured to remove co-located primary mascons. To demonstrate this, I performed two simulations using the 40,000 km^2 irregular-shaped mascons that follow coastlines, one with a pair of co-located primary mascons in Denmark (Figs. 4.3a) and one with the region re-configured to remove the co-located centres of mass (Figs. 4.3a, M6; Table 4.1).

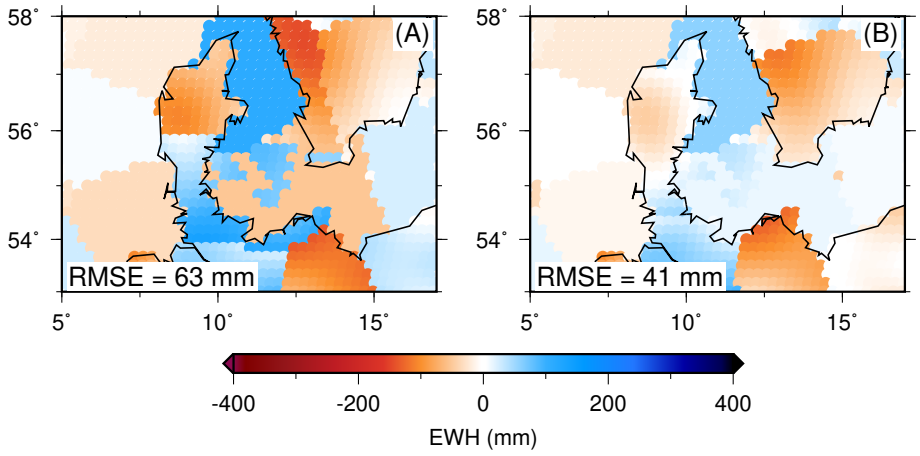

Figure 4.2: Errors in unregularised estimates of the temporal gravity field from simulations, using 40,000 km^2 mascons (a) that contain a case of primary mascon centre of mass co-location in Denmark and (b) re-configured to remove co-located centres of mass. The RMS error (RMSE; in mm) is computed on the ternary mascons over the mapped region.

By re-configuring the primary mascons that have co-located centres of mass, the accuracy of the estimates of both the re-configured mascons and surrounding mascons are improved significantly (Figure 4.4) and the Root Mean Square (RMS) of the solution error computed on the ternary mascons within the mapped region of Figure 4.4 is decreased from 63 mm (Figure 4.4a) to 40 mm (Figure 4.4b). The estimation errors of both the re-configured and surrounding mascons are significantly reduced when issues of co-located primary mascons are addressed.

A third simulation was run to demonstrate the improvements made to the mascon parameter estimates when small primary mascons and primary mascons containing distant ternary mascons are removed. In this instance, I used the 40,000 km^2 irregular-shaped mascons that follow coastlines and included a number of small island primary mascons (<20,000 km^2) and primary mascons that contain distant ternaries. As an example, the RMS error of the Galapagos ternary mascons decreased by a factor of 4.3 (from 154 mm to 36 mm) when the small island primary mascon (Figure 4.3b) was merged into the surrounding ocean primary mascons (Figure 4.3e). Similarly, the RMS error of the ternary mascons spread across the north-west Madagascan coast, Mauritaus and Réunion islands (i.e. Green mascon; Figure 4.3c) were improved by a factor of 3.3 (from 67 mm to 20 mm) when the Mauritaus and Réunion island ternary mascons were merged into the surrounding ocean primary mascons (Figure 4.3f). When all cases of small primary and distal ternary mascons were re-configured, the global RMS error decreased significantly, from 93 mm to 80 mm.

The process of re-configuring the irregular mascon grid mitigates mascon correlations by identifying and repairing problematic pairs of primary mascons whose centres of mass are co-located. In this instance, re-configuring primary mascons that are smaller than a threshold and primary mascons containing disparate ternary mascons by merging those island ternary mascons into the surround ocean primary mascons also significantly improved the mascon parameter estimates. These results depend to an extent on the magnitude of the simulated signals on the small islands, which are likely to be small in reality but cannot be known a priori. Therefore, estimating their contribution to the temporal gravity field as ocean mascons is an appropriate choice which best mitigates the error otherwise introduced by small mascons that cannot be reliably resolved.

The sections that follow are from Tregoning et al. (2022).

Abstract

The estimation of mass anomalies using Gravity Recovery and Climate Experiment (GRACE) data involves parameterising the temporal gravity field using basis functions. In this study, we show that the use of irregularly shaped mass concentration (mascon) tiles that follow land/ocean boundaries reduces the leakage of land signals into ocean regions, and vice versa. Leakage of signal from continents to oceans in mascons that cross the coastline affect the integrated mass changes at a regional scale. For example, the calculated mass loss in 2016 is ∼5% greater for Greenland when using mascons that follow coastlines. We describe efficient algorithms for computing the accelerations acting on the satellites caused by mass changes on mascons, along with the partial derivatives relating the mass changes to the inter-satellite observations. Through simulation, we quantify the impact of different mascon geometries, spatial resolution and regularisation. The variations of mass change signals within mascons, which we call "intra-mascon variability", contribute to errors in estimates of mass variation from GRACE data. While this can be mitigated through regularisation of the inversions, it cannot be removed entirely. The use of irregularly shaped mascons that follow land/ocean boundaries reduces the "intra-mascon leakage" of land signals into ocean regions, and vice versa. This approach can also be applied to hydrological basins for calculating integrated mass changes on catchment scales.

4.1 Introduction

The Gravity Recovery and Climate Experiment (GRACE) space gravity mission was one of the most successful space geodesy missions, operating for 12 years beyond the planned mission length and impacting a vast array of science disciplines including hydrology, oceanography, crustal deformation and earthquake seismology. Temporal gravity field solutions have been provided as Level-2 data products from a number of different processing centres (e.g. Lemoine et al., 2007; Bruinsma et al., 2010; Watkins et al., 2015; Save et al., 2016; Dahle et al., 2019; Kvas et al., 2019) in the form of spherical harmonic coefficients. This is a mathematical approach that has been exploited by geodetic studies for many decades and the solutions have been used to study mass balance changes in polar regions (e.g. Velicogna and Wahr, 2006; Tapley et al., 2019), floods and droughts (e.g. Leblanc et al., 2009; Reager et al., 2014; Rodell et al., 2018), glacial isostatic adjustment (e.g. Riva et al., 2009) and ocean circulation and mass increase (e.g. Chambers et al., 2010).

A significant issue with the GRACE temporal gravity fields has been the presence of north-south striped patterns in the resulting gravity fields. These have no physically plausible origin and are typically mitigated through the use of one of many different filtering processes (e.g. Swenson and Wahr, 2006; Kusche, 2007). The use of spherical harmonics also causes "leakage" of signals from continental to oceanic regions and vice-versa. This is particularly prevalent in polar regions where significant mass loss is occurring close to the continent/ocean boundary and has led to the development of various restoration techniques that seek to place the estimated mass variations in the correct spatial location (e.g. Chen et al., 2009a; Wiese et al., 2016). These leakage problems have also been mitigated by estimating scaling factors to revise estimated mass changes to more correct values, where the scale factors are a relationship between terrestrial water storage variations from land hydrology models and GRACE total water storage estimates, derived through simulation (e.g. Landerer and Swenson, 2012).

An alternate mathematical approach for representing the temporal gravity field has its roots in planetary science in the 1960s. Mass concentration elements (mascons) were first used in the estimation of gravity anomalies on the Moon (Muller and Sjogren, 1968) and Rowlands et al. (2005) were the first to transfer the approach into the analysis of GRACE observations. Essentially, the surface of the Earth is divided into a series of tiles of known area, and the mass change of each tile is then estimated as the required change in height of water across the tile to cause the observed gravity signal. Through chain rule

differentiation, Rowlands et al. (2005) and Luthcke et al. (2006a) related the mass change of a mascon (roughly $4° \times 4°$ and $3° \times 3°$, respectively) to spherical harmonic coefficients that represented the gravity field anomalies. Knowing the area of each mascon, their estimated parameters became the change in equivalent water height (EWH) over each mascon.

Watkins et al. (2015) used 3° spherical cap mascons to represent the temporal gravity field and took advantage of an analytical expression to relate directly the acceleration acting on the satellites to the change in height on each mascon. One possible limitation of this approach is that there are spatial gaps between the spherical caps, although Watkins et al. (2015) stated that the gravity signals in the gaps are included in the estimates of neighbouring mascons. Luthcke et al. (2013) reduced the size of their mascons to 1°, but stated that this is not the spatial resolution of their estimates. Save et al. (2016) used a similar approach to Luthcke et al. (2006b), although their mascon geometry was a series of 1° regular, equal-area geodesic shapes.

All of these approaches have geometries that include some mascons that contain a mix of continent and ocean regions. This becomes problematic when there are different signals in the land and ocean components and results in a smearing of the signal across the continent/ocean boundary. Essentially, the "leakage" problem that exists in spherical harmonic solutions persists in mascon solutions, although in a slightly different form. Loomis et al. (2021) call this "intra-mascon leakage". Each of the above studies has recognised the problem of signal leakage between oceans and continents. In mascons that were a mix of continent and ocean, Wiese et al. (2016) developed a technique to shift back onto the continents (or ocean) the mass loss signal in the ocean (or land) part of the mascon. Save et al. (2016) used a multi-step regularisation process to try to mitigate the leakage of signals from land to ocean, especially around polar ice sheets. Luthcke et al. (2006b, 2013); Loomis et al. (2019a) used a multi-step, multi-regularisation strategy to mitigate leakage in their mascon solutions and provided estimates of leakage error.

In this study we use a geometrical pattern of irregular-shaped mascons covering the entire surface of the Earth. We describe the topology of the connections between mascons and the algorithms used to construct the mascons that follow the continent/ocean boundaries. Through simulation, we demonstrate how spatial variability of signal within a mascon causes errors that affect the gravity field estimates and how irregularly shaped mascons reduce significantly the leakage of signals across the continent/ocean boundaries.

Finally, improvements in estimates of the temporal gravity field based on the analysis of actual GRACE observations due to the use of irregular-shaped mascons are described. A full suite of solutions of the GRACE data, including presentations and analyses of time series of oceans, polar regions etc are provided in our companion paper (Allgeyer et al., 2022). Here we focus on the construction and regularisation of our mascons and assess the leakage caused by certain assumptions and analysis choices.

4.2 Constructing the mascon pattern

A change in mass of a single mascon tile on Earth will cause a change in gravitational acceleration experienced by each GRACE satellite. If considered as a point mass, the gravitational acceleration vector, $\overrightarrow{a}_m$ acting on the satellite because of the mass of mascon m, can be computed as:

$$\overrightarrow{a}_m = \frac{GA_m\rho_m}{d^2}h_m\hat{d} \tag{4.1}$$

where G is the gravitational constant, d is the distance between the centre of mass of mascon m and the satellite, $\hat{d}$ is the unit vector between the mascon and the satellite, A_m is the surface area of the mascon, h_m is the thickness (in terms of equivalent water height) of a layer of water covering mascon m and ρ_m is the density of the water layer for mascon m. The parameter estimated is h_m, and the partial derivative relating the acceleration to the change in water height for the mascon, $\partial a_m/\partial h_m$ is found by differentiating Equation 5.1 with respect to h_m:

$$\frac{\partial \overrightarrow{a}_m}{\partial h_m} = \frac{GA_m\rho_m}{d^2}\hat{d} \tag{4.2}$$

We generated a mascon pattern that covers the Earth with mascon tiles and, assuming some a priori value for the equivalent water height, h_m, for each mascon, used the above equations to calculate the gravitational accelerations (and associated partial derivatives) acting on the GRACE satellites caused by the temporal gravity field. The approach is based on the assumption that a rectangular tile can be approximated by a point source, but the validity of this assumption depends on the size of the mascon tile and the distance between the mascon and the satellite. For satellites at typical GRACE altitudes (400-500 km), we found that the assumption is valid for a $10' \times 10'$ tile directly beneath the satellites, but errors are introduced into the acceleration calculations (and associated partial

derivatives) for larger tiles. The size of the tile can be increased without loss of accuracy if the mascons are located further away (i.e. not directly beneath the ground track of the satellites).

Thus, we chose to construct a pattern of $10' \times 10'$ (roughly 18 km×18 km, or 325 km^2) mascons over the entire Earth. We began with a spherical mascon (of radius $5'$) over the North Pole, then created latitudinal bands of mascons, each of width $10'$, and finished the pattern with a spherical mascon over the South Pole. There is an integer number of mascons in each latitudinal band, which means that they don't all have exactly the same area (<8% variation).

The number of mascons in each latitudinal band can be found by:

$$N_{lat} = [\ \frac{C_{lat}}{\alpha \times R_{lat}}] \tag{4.3}$$

where [ ] indicates the nearest integer, C_{lat} is the circumference of the centre of the latitudinal band of radius R_{lat} and α is the distance equivalent of $10'$ of latitude. At a given latitude, the mascon in which a particular longitude lies can then be found as:

$$n_{lon} = [\ N_{lat} \times \frac{\lambda}{360}] \tag{4.4}$$

where λ is the longitude of the point in decimal degrees.

The maximum number of these small mascons in a latitudinal band occurs at the equator (2160), with a total of 1,485,118 mascons required to cover the entire Earth. Given a particular point at given latitude/longitude, it is straightforward using Equations 3 and 4 to calculate in which latitude band and in which mascon around the latitude band the point resides. We compute this on the WGS84 ellipsoid but the equations are equally valid on a sphere, although the number of mascons would change.

Hydrological processes related to freshwater will cause changes in mass over continents whereas over oceans the changes will be related to seawater. We used the GEBCO-2014 topography/bathymetry model (Weatherall et al., 2015), augmented with the Bedmap-2 in the Antarctic region (Fretwell et al., 2013), to characterise whether each mascon was located predominantly over ocean or land. We then assigned a different density of water for ocean (1029 g/cm^3) and land (1000 g/cm^3) mascons. For the mascons located over marine-grounded ice sheets in Antarctica we used the freshwater density since any mass change will be due to a change in ice or snow for which a freshwater density is appropriate.

We also assigned to each mascon a mean topographic/bathymetric height and a value for the geoid-ellipsoid separation (using the EGM-2008 model of Pavlis et al. (2012)).

4.3 Mascon hierarchy

The spatial resolution of gravity anomaly fields estimated from GRACE data is much larger than the 18 km×18 km size of these small mascons. Therefore, we group them together to form larger mascons. Attributes are calculated and assigned to the larger mascons from the summation of the attributes of all smaller mascons contained within each large mascon. We can then take advantage of the fact that the point mass assumption can be used with the large mascons without loss of numerical accuracy when mascons are sufficiently distant from the satellites. In fact, once the mascons are more than 20° (about 2000 km) away from the satellite ground track the mascon size can be increased to at least 300×300 km without loss of accuracy when approximating the mascon tile as a point source. We introduced a hierarchy of mascons, with "primary" mascons used when the satellites are distant ($> 20°$ away), "secondary" mascons used for intermediate distances and "ternary" mascons (our $10' \times 10'$ mascons) for near-field cases.

A primary mascon is a collection of ternary mascons and is treated as a point source when calculating the gravitational accelerations (and partial derivatives) of the primary mascon acting on the satellites. For this calculation, we need to know the area and coordinates of the centre of mass of each primary mascon, which is derived from the attributes of all ternary mascons within the primary mascon. We summed the partial derivatives of all ternary mascons within a primary mascon to derive the partial derivatives of the primary mascon. Topological information linking ternary mascons to primary mascons (and vice versa) is read from an external file, stored in memory and accessed at various stages of the GRACE data processing, including during the orbit integration.

To make use of this mascon hierarchy when integrating the satellite orbits (and partial derivatives), we need to know where the satellites are with respect to our mascon pattern. For a given location (ϕ, λ) of a GRACE satellite, we can calculate the ternary mascon that lies directly under the satellite (using equations of Section 2) and identify the primary mascon in which the ternary mascon resides using our lookup table. This also provides information regarding coordinates of the centres of mass, area, density of water etc for that particular primary mascon and all its ternary mascons. We can then break that primary mascon into its ternary mascon components and perform the computations of acceleration

and partial derivatives by treating each ternary mascon as a point source.

Whether to treat the other primary mascons as point masses (for far-field primary mascons) or sum the computations performed on each ternary mascon depends upon the distance of the satellite from each primary mascon. There is a substantial time cost to computing the distances at each epoch between a satellite location and each mascon; therefore, we pre-compute and store the information of the distances between all primary mascons in a lookup table which is pre-read once by our orbit integrator. Having determined over which primary mascon the satellite is located, we can then use the distances from this primary mascon to all other primary mascons as the key indicator as to whether to treat each other primary mascon as a point source or as a sum of the computations on each ternary mascon contained within it.

Thus, at each time step in the orbit integration, the decision whether to perform computations on primary or ternary mascons is made by accessing the pre-computed distances between primary mascons that we store in memory. We effectively obtain the computational accuracy of 18×18 km mascons without the computational time burden of calculating values for all 1,485,118 ternary mascons. The calculation of accelerations (and associated partial derivatives) of the entire mascon field for a single epoch takes around 0.2 seconds, and 66 minutes for a 24-hour orbit integration. We parallelize these computations in our orbit integrator, since the computations for each mascon are completely independent of all other mascons.

4.4 Useful features of ternary mascons

The "building blocks" for our primary mascons are the 18 km×18 km ternary mascons. There are no mathematical restrictions as to how we might group them together and this provides a powerful tool for mitigating the leakage, or mis-appropriation, of signals between ocean mascons and land mascons, or between neighbouring mascons in different continental drainage boundaries.

Primary mascons are constructed from groups of ternary mascons which can be aggregated to form any shape. We make use of irregular primary mascon shapes to delimit the ocean/continent boundary, assigning land ternaries to "continent primary" mascons and ocean ternaries to "ocean primary" mascons. Thus, we can form a global irregular grid of primary mascons that are almost exclusively continental or exclusively oceanic (there are a few exceptions to this, typically being small remote islands that comprise $< 50\%$ of an

ocean primary mascon). With each ternary mascon being ∼18 km×18 km, we therefore limit the ocean/continent attribution error to less than half of this distance, which is no more than ∼8 km. This is a substantial improvement over the spatial smearing that occurs using spherical harmonics to represent the gravity field, where a degree-180 model would introduce spatial smearing of up to 100 km.

This feature of our ternary/primary mascon approach can also be exploited to create primary mascons that follow drainage boundaries. For example, we can define primary mascons to estimate the change in total water storage in a hydrological basin such as the Amazon Basin (Figure 4.3). Luthcke et al. (2013) also made use of drainage boundaries in this manner but their mascons sometimes cross either drainage basin boundaries or the coastlines, or both.

Another feature of our approach is that ternary mascons comprising a continental primary mascon do not necessarily need to be adjacent. Therefore, in the case of islands offshore of a continent, it is possible to sum all the hydrological signals of a region without including any of the oceanic signals that may also lie within the overall geographical region. Thus, for example, the mass change signals on the South American coast and the offshore Falkland Islands can be estimated together, while the ocean channel between them comprises part of the ocean signal (Figure 4.3d).

It is possible to define primary mascons of different spatial sizes simply by including more or fewer ternary mascons in particular primary mascons. This capability can be exploited to obtain higher spatial and/or temporal resolution in polar regions, where there is a more dense ground track pattern per day than in equatorial regions due to the near-polar orbit of the GRACE satellites. This is a particular advantage of the mascon approach to representing the temporal gravity field that cannot be achieved using spherical harmonics.

4.5 Creating the mascon field

There are a number of steps involved in creating our final pattern of mascons. First, we created the ternary mascon pattern, as described in Section 4.2. Then, using similar logic, we formed a quasi-regular primary mascon pattern (Figure 4.3a). We calculated the percentage of land ternary mascons within each primary mascon and identified all primary mascons that contain a mix of ocean and land ternary mascons. For each mixed primary mascon, we transferred the 'minority' ternary mascons to the nearest primary mascon of

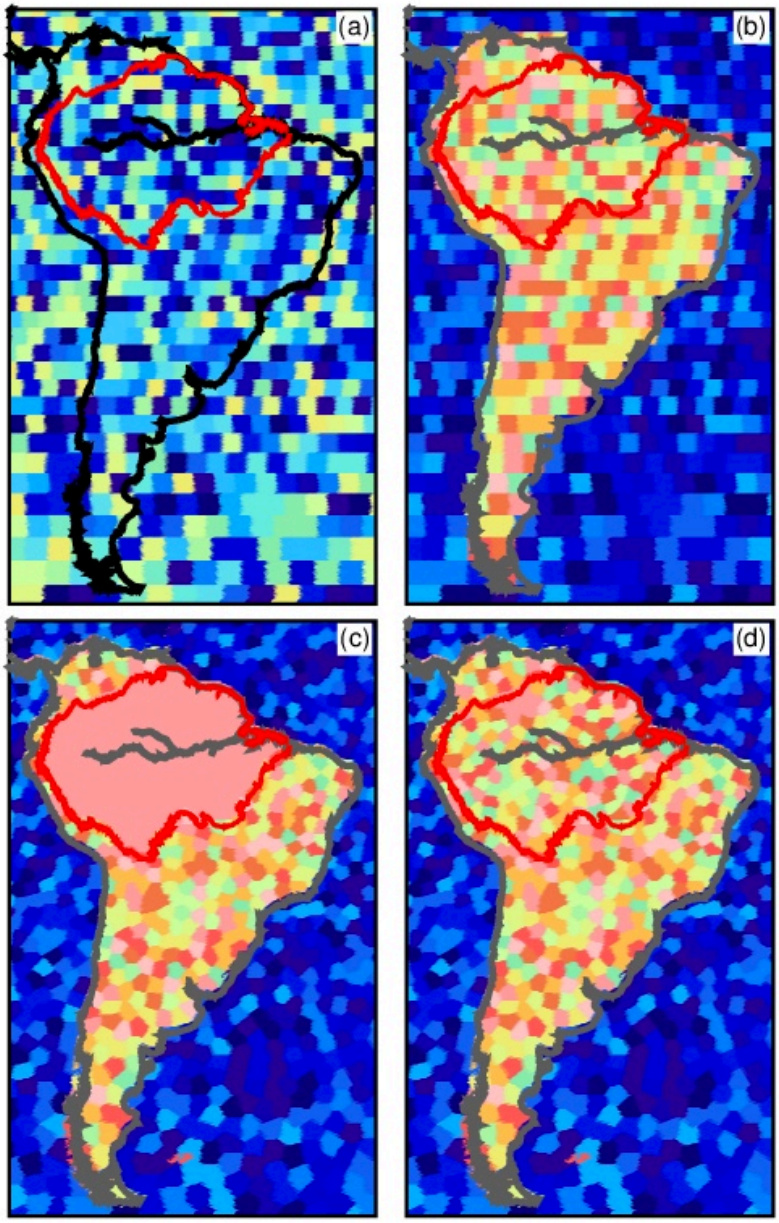

Figure 4.3: Steps of the mascon field refinement for South America. (a) Regular 2°×2° mascon pattern, (b) separated into land/ocean, (c) Irregular mascon pattern separated into land and ocean and Amazon Basin, (d) as for (c) but also including the reshaping of primary mascons within the Amazon Basin to have an area of ∼40,000 km^2.

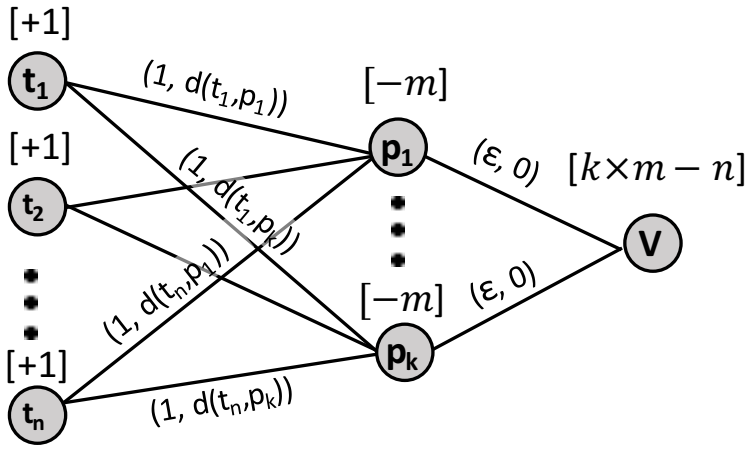

Figure 4.4: Graphical formulation of the Minimum Cost Flow Problem. There are n data nodes (t_1 to t_n) representing ternary mascons, k centre nodes (p_1 to p_k) representing primary mascons, and one virtual node (V) ensuring that the sum of supplies and demands equals zero. Supply and demand appear in brackets above each node. m is the specified minimum number of ternaries per primary. The capacity and cost appear in parentheses above arcs. The distance between t_i and p_j is noted $d(t_i, p_j)$. ϵ is the maximum difference in size (number of ternaries) allowed between two primary mascons. The size of any primary mascon will then range between m and $m + \epsilon$.

the same type (Figure 4.3b). For example, for a primary mascon that was 89% land we would transfer the 11% of oceanic ternary mascons to the nearest ocean primary mascon and for a primary mascon that was 40% land we would transfer the 40% land ternary mascons to the nearest continental primary mascon. We restricted the transfer of ternary mascons to only primary mascons located within 1500 km. If no such mascon is within this range then we left the primary mascon as a mixed mascon.

We then defined regions of interest, containing a large number of ternary mascons (either land or ocean) following coastlines, then "reshaped" the mascons by dividing a region of interest into several primary mascons of equal area. This was done using a constrained K-means clustering algorithm, based on Bradley et al. (2000). It is necessary to use constrained clusters to ensure that the size of the mascons will not change from one cluster to another to within a certain limit. The addition of a constraint on the size of the clusters will add a significant computational burden, but will allow conserving a uniform resolution for the mascon field. The algorithm consists of a regular K-means implementation where cluster assignment is done by solving a Minimum Cost Flow (MCF) problem (Kovács, 2015), as opposed to just forming clusters where each ternary is assigned to the closest centre of mass of a primary mascon. The number of clusters, k (i.e. the number of primary mascons in a region of interest), is found by dividing the area of the

region of interest by the required area of each primary mascon.

The algorithm is initiated by choosing randomly a set of a priori coordinates of centres of mass of k primary mascons from the n available ternary mascons in the region, with the objective of assigning m ternaries to each primary mascon. We permit m to $m+\epsilon$ ternary mascons to be assigned to each primary mascon and solve the MCF problem formulated in Figure 4.4, where ϵ is the maximum permitted difference in number of ternary mascons per primary mascon. This iterative process is done using the C++ MCFSimplex Solver Class from the Operations Research Group at the University of Pisa, based on the network simplex algorithm (Kovács, 2015). New cluster centres are calculated as the centre of mass of all ternaries assigned to each primary after each iteration. The assignment step is repeated until cluster centres do not move significantly (less than half the distance between ternaries).

The MCF problem can be represented graphically as a collection of nodes and arcs (Figure 4.4). Here, the nodes represent ternary and primary mascons. A pair of nodes forms an arc. Flow allows moving units from a supply node to a demand node. The supply (demand) is the amount of units that a node can send (receive). Flow is conserved at each node, implying that the total flow entering a node, must equal the total flow leaving the node. Flow is limited in an arc by a lower and an upper bound, also called capacity. Solving the MCF problem means to find the optimal flow, among all feasible flows, which minimizes the sum of the costs associated with the displacement of units along arcs.

The MCF is formulated in such a way that data nodes (ternary mascons) are nodes with unitary supplies of flow. Cluster centres (primary mascons) are nodes with a demand equal to the minimum number of ternaries needed to match the resolution defined by the user. The minimum number of ternaries per primary mascon is obtained by dividing the desired area of each primary mascon by the average area of a ternary mascon in the region of interest. One additional node allows balancing the global sum of supply and demands to zero. The latter condition is necessary to ensure that flow is conserved at each cluster centre, and therefore makes the MCF solution feasible. The data nodes are fully connected to centre nodes with costs corresponding to Euclidean distances from data points to respective cluster centres. Computations are performed with node coordinates in an azimuthal equidistant projection to preserve distances to the cluster centre on the sphere. The centre nodes are fully connected to the balance node with zero cost, and a capacity corresponding to the difference in size allowed between clusters. The MCF Solver

Table 4.1: Mascon geometry and regularisation properties used in simulations

	Mascon Geometries			
	Area (km^2)	Number of Primary mascons	Shape	Follow Coastlines (Y/N)?
M1	∼90,000	4321	regular	N
M2	∼40,000	10314	regular	N
M3	∼90,000	5654	basins	Y
M4	∼40,000	12721	basins	Y
M5	∼90,000	5647	no basins	Y
M6	∼40,000	12754	no basins	Y
	Mascon regularisation			
	Land (m)	Ocean (m)	Ice sheets	Glaciated regions (m)
loose	0.1	0.05	0.2	0.2
tight	0.015	0.01	0.05	0.05

finds the solution minimizing the sum of all costs, respecting the constraints imposed by the supply, demand, and capacity criteria.

We performed this reshaping exercise for each continent and for the global ocean as a whole. This provides a set of roughly equal-area primary mascons for a continent, where none of the primary mascons extend beyond the coastline. The required area of the primary mascons can be changed from one region to another, providing the flexibility to use smaller primary mascons in ice-covered, polar regions than in equatorial regions where the ground tracks of the GRACE satellites are further apart. In this study, we have used mascons of area ∼90,000 km^2 and ∼40,000 km^2 globally (roughly 3° and 2° mascons, respectively). A 3° primary mascon contains, on average, about 400 ternary mascons and its size varies by at most 2.5% (about 10 ternaries or 2250 km^2). Other regions of interest can be extracted using user-defined polygons, and then reshaped to the desired size. This permits us to define drainage boundaries of glaciers or hydrological basins and to force the edges of our primary mascons not to cross them. An example of this is shown for the Amazon Basin (Figure 4.3).

For the simulations described below, we created a number of different mascon patterns using a variety of sizes and shape criteria, listed as M1-M6 in Table 4.1. The process of generating our mascon geometry pattern for the mascons is thus:

- generate a set of regular mascons of the required area, including mascons that cross coastlines (M1/M2 in Table 4.1) (Figure 4.3a)
- identify primary mascons that contained a mix of oceanic and continental ternary mascons
- separate the mixed primary mascons to generate a set of ocean or continent primary

mascons (Figure 4.3b)

- reconfigure the ocean and continental mascons using the MCF algorithm to generate an irregular-shaped mascon field where each primary mascon is roughly the required area and mascon boundaries follow coastlines and either ∼33 drainage basins (M3) or just the Amazon Basin (M5) (Table 4.1, Figure 4.3c,d)

Because the mascons are permitted to be irregular in shape, in regions of complex coastlines and/or islands it is possible that the centres of mass of continent and ocean primary mascons can be co-located. This can also occur in regions where drainage boundaries cause elongated primary mascons. Both cases cause the partial derivatives of adjacent mascons to be highly correlated, which results in poor estimates for the mascon parameters. We resolve these issues by combining affected primary mascons of the same type, then reshaping the combined mascon to ensure that we maintain primary mascons of roughly the same area.

4.6 Intra-mascon variability

By estimating a single parameter per primary mascon, being the effective thickness of a plate of water over the entire primary mascon, we make the assumption that the change in mass across the entire primary mascon is the same. Of course, in reality this is very unlikely to be the case. Instead, there is likely to be some heterogeneity in the mass changes within primary mascons, especially in regions of significant mass loss around the coasts of polar ice sheets. We call the departures from a mean primary mascon value the "intra-mascon variability". The intra-mascon variability therefore represents the minimum error that can be achieved in mascon solutions, using a mascon size inherently larger than the expected geophysical signals. This error cannot be quantified, since the actual intra-mascon variability cannot ever be established from the space gravity data alone. Another source of error is the "intra-mascon leakage", defined by Loomis et al. (2021) as the misappropriation of signal within mascons. While the average mass change within each mascon is still conserved, the high-resolution mass changes are not modelled within the mascon. For example, when a single mascon with a continental mass variation signal crosses the coastline the mean value for the mascon will under-estimate the mass variation over the continental component and incorrectly assign some of the mass variation over the ocean component of the mascon. This is different from "inter-mascon leakage" (or just "leakage") which is often referred to in GRACE analysis studies, being the assignment

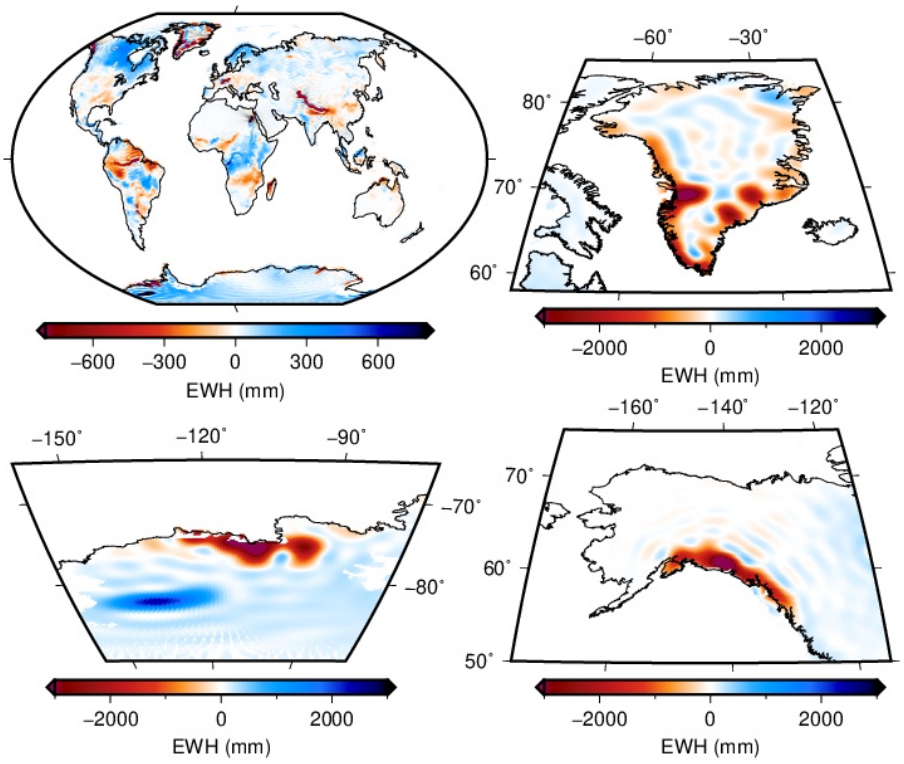

Figure 4.5: Simulated temporal gravity field signal using the model of Dobslaw et al. (2015). (a) Global, (b) Greenland, (c) West Antarctica, (d) Alaska.

of signal into the wrong mascon, or the wrong spatial location (Loomis et al., 2021). In that latter case, the average value of mass changes per primary mascon will differ from the average 'true' value.

The fact that intra-mascon variability exists means that modelling the mass change over a primary mascon using just a single value will induce errors into the orbit integrations because the spatial variability of the temporal gravity field will not be represented accurately. Thus, the intra-mascon variability will introduce perturbations into the gravity field estimation process that cannot be resolved. Even in simulation with noise-free observations, unless the spatial resolution of the primary mascons is sufficiently small as to capture all the spatial variability of the signal to be estimated with a single parameter (i.e. the intra-mascon variability is zero), it will not be possible to obtain a perfect solution. The perturbations introduced by intra-mascon variability then cause inter-mascon leakage, being error in estimates of mass changes on other primary mascons, due to the inability of the parameterisation to capture accurately the signal.

We introduced intra-mascon variability into our simulations below by modelling a different mass change signal on each of our ternary mascons, using an a priori model from Dobslaw et al. (2015). The model represents changes in mass and we included their static

components of monthly-averaged terrestrial water storage signals and monthly-averaged cryospheric variability as well as solid Earth deformation, using a spherical harmonic model to degree 180 (we do not include any sub-daily high frequency mass changes). We chose to use their values for December 2006 because it contains realistic signal magnitudes seen during the GRACE mission (i.e. about 3 m EWH mass loss in polar regions). Because of the spherical harmonic truncation of large-amplitude signals of mass loss near the coast, the model actually predicts significant and unrealistic ocean signals in a ringing pattern, most notably around Alaska, Greenland and West Antarctica. Therefore, zero values were assigned to ocean regions in our simulations below but we included all continental signals (Figure 4.5).

The magnitude of intra-mascon variability depends upon how the chosen primary mascon geometry actually overlays the signal to be recovered. Of course, in practice this can never be known accurately because the signal is not know accurately at very high spatial scales. In simulation, one can assess the impact of different choices of mascon geometry, both in terms of spatial size and shape of primary mascons. The intra-mascon variability (i.e. the difference of each modelled ternary signal from the mean primary mascon value) in Greenland, Alaska and West Antarctica is shown in Figure 4.6 for mascons of size $\sim$90,000 km^2 and $\sim$40,000 km^2, with three different primary patterns: a regular pattern that does not follow coastlines (M1, M2), a coastline following pattern that does (M3, M4) and does not (M5, M6) include definitions of continental hydrological drainage basins.

The most accurate estimate of mass change that one could obtain would be the average value of the total signal across each primary mascon. Therefore, the smallest error that can be obtained in estimates is the intra-mascon variability within each primary mascon. This is what is shown in Figure 4.6. Note, however, that this error relates only to the simulated signal that we have used from the model of Dobslaw et al. (2015). While it may be indicative of the actual intra-mascon variability in these regions, there is no guarantee of that being the case.

4.7 Temporal gravity field estimation

We performed several simulations using different mascon geometries and levels of regularisation to assess the extent of intra-mascon and inter-mascon leakage. The interplay between the signal recovery (expressed as a correction to the a priori value), the regularisation of the solution and the associated error induced in the temporal gravity field

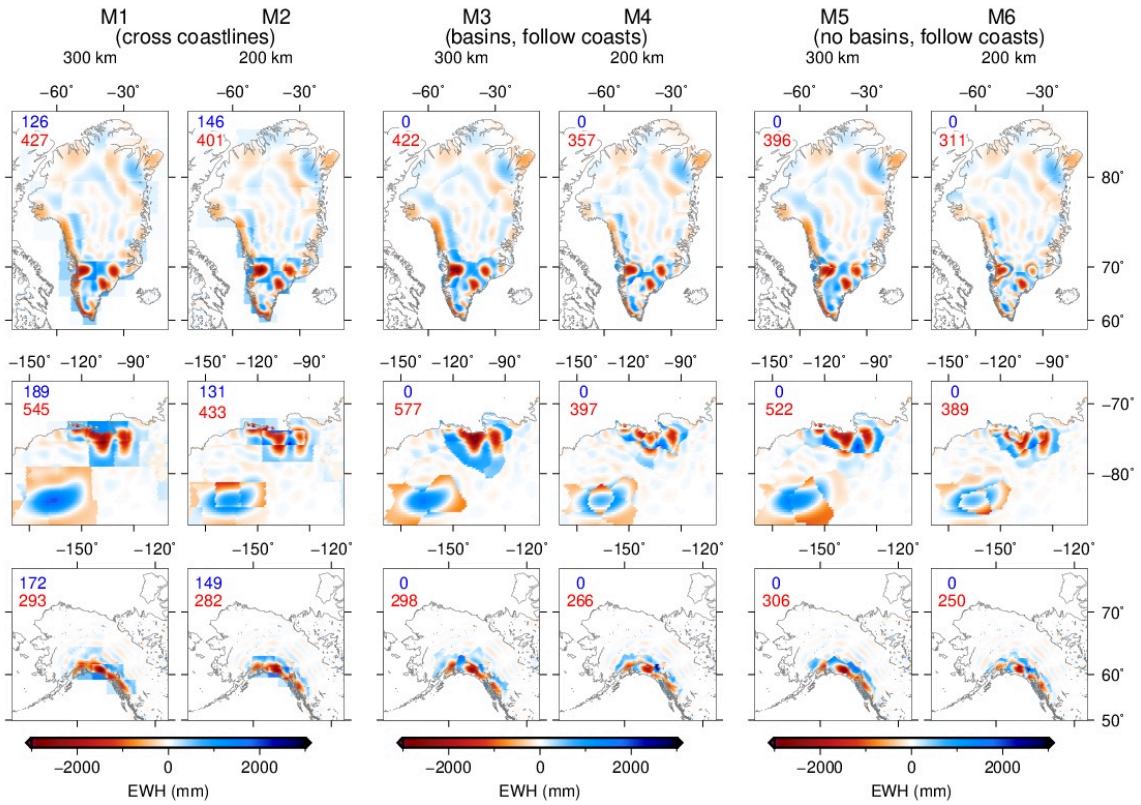

Figure 4.6: Intra-mascon variability (i.e. the ternary anomalies with respect to the mean value across each primary mascon) for mascon geometries at 300 km and 200 km spatial scales. RMS (in mm) of intra-mascon variability computed on the ternary mascons over each region is shown for ocean ternaries (blue) and land ternaries (red). There is no non-zero intra-mascon variability for the M3 - M6 ocean primary mascon configurations because the primary mascons do not cross the coastlines and there is no signal simulated in the oceans. Therefore, the ocean RMS values are zero for M3 - M6.

estimates is assessed (throughout this paper, 'error' is used in the sense of "difference from the true value". It does not refer to the formal uncertainties - often called "errors" - of parameter estimates). Each ternary mascon was assigned a mass change signal using the simulated signals for December 2006 (Dobslaw et al., 2015) then, from the ternary mascons assigned to each primary mascon we calculated the attributes of the primary mascons. This created the 'truth' temporal gravity field that was to be recovered in the simulations.

We integrated satellite orbits for GRACE A and GRACE B, using accelerations computed from models and observations listed in Table 1 of Allgeyer et al. (2022). These orbits also included the accelerations induced by the temporal gravity field as represented on our ternary mascon field. This provided us with a set of "truth" orbits for each day in July 2016, which represent realistic orbits of how the actual GRACE satellites would have flown around Earth (assuming that the modelled a priori gravity field of Dobslaw et al. (2015) is realistic). We then integrated another set of orbits for the same days but without including the accelerations caused by the temporal gravity field. Thus, these orbits differ from the "truth" orbit by only the unmodelled effects of the temporal gravity field. This set of orbits forms our "a priori" orbits.

When integrating the a priori orbits we used the mascon geometry of regular-shaped primary mascons that cross coastlines (M1, M2 in Table 4.1) as well as the irregular mascon patterns that follow coastlines (M3 - M6 in Table 4.1). We treated the position/velocity values at each epoch of our "truth" orbits as "observations", akin to using the GNV1B values of position/velocity except that our position/velocity values include the effects of the temporal gravity field whereas the GNV1B values do not. We also computed range rate "observations", $\dot{R}$, from the position and velocity values of our "truth" orbit:

$$\dot{R} = \frac{\sum \Delta p_i \sum \Delta \dot{p}_i}{R} \tag{4.5}$$

where R is the inter-satellite range and p_i, $\dot{p}_i$ are the relative cartesian position and velocity vector components between the centres of mass of the two satellites. The inertial positions and velocities of the satellites were used in Equation 5, although Earth-fixed values can be used as well since the range rate is independent of reference frame. Range rate prefit residuals were formed, being the difference in range rate computed from the "truth" and a priori orbits. We then generated range acceleration prefit residuals by numerically differentiating the prefit range rate residuals (Tregoning et al., 2017; Allgeyer et al., 2022).

It is the range acceleration prefit residuals that were used as our inter-satellite observable when estimating the temporal gravity field. In our companion paper (Allgeyer et al., 2022), we demonstrated that using range acceleration information in this manner leads to a reduction in north/south striping in estimated gravity fields while also being able to resolve spatially both the low- and high-frequency components of the temporal gravity field.

Normal equations were formed for each day of July 2016, then stacked to estimate monthly mean values for each mascon but separate satellite parameters (position, velocity, accelerometer calibration parameters) for each 24-hour orbit. No perturbations were applied to any of these satellite parameters in the simulations. We solved for adjustments to the initial satellite positions/velocities, accelerometer calibration scale factors and biases (one per axis per satellite per day) and adjustments to the mascons in terms of an equivalent height of water (of the appropriate density) in a least squares inversion of our simulated observations for each month (Allgeyer et al., 2022):

$$\hat{x} = \left(A^T W A + C_{mass} + C_M\right)^{-1} A^T W b \tag{4.6}$$

where $\hat{x}$ are the adjustments to all a priori satellite and mascon parameter values, A is the design matrix of partial derivatives, W is a diagonal weight matrix for the observations, b are the prefit residuals (the "observed minus computed" difference between observations from our "truth" and a priori orbits). We assigned weights to the observations of 70 mm, 70 um/s and 1 nm/s^2 for observations of position, velocity and range acceleration, respectively. C_{mass} is a constraint matrix to conserve mass in the Earth system. The matrix C_M is a diagonal regularisation matrix with elements $1/\sigma_m^2$ where σ_m is a parameter constraint on each mascon (all off-diagonal elements are zero). We assigned different values for different mascons, based on whether each mascon is located in a non-glaciated continental region, an ocean or a glaciated continental region (including Antarctica, Greenland, Baffin Island, Patagonian and Alaskan glaciers). Two different levels of constraints were used, as described in Table 4.1.

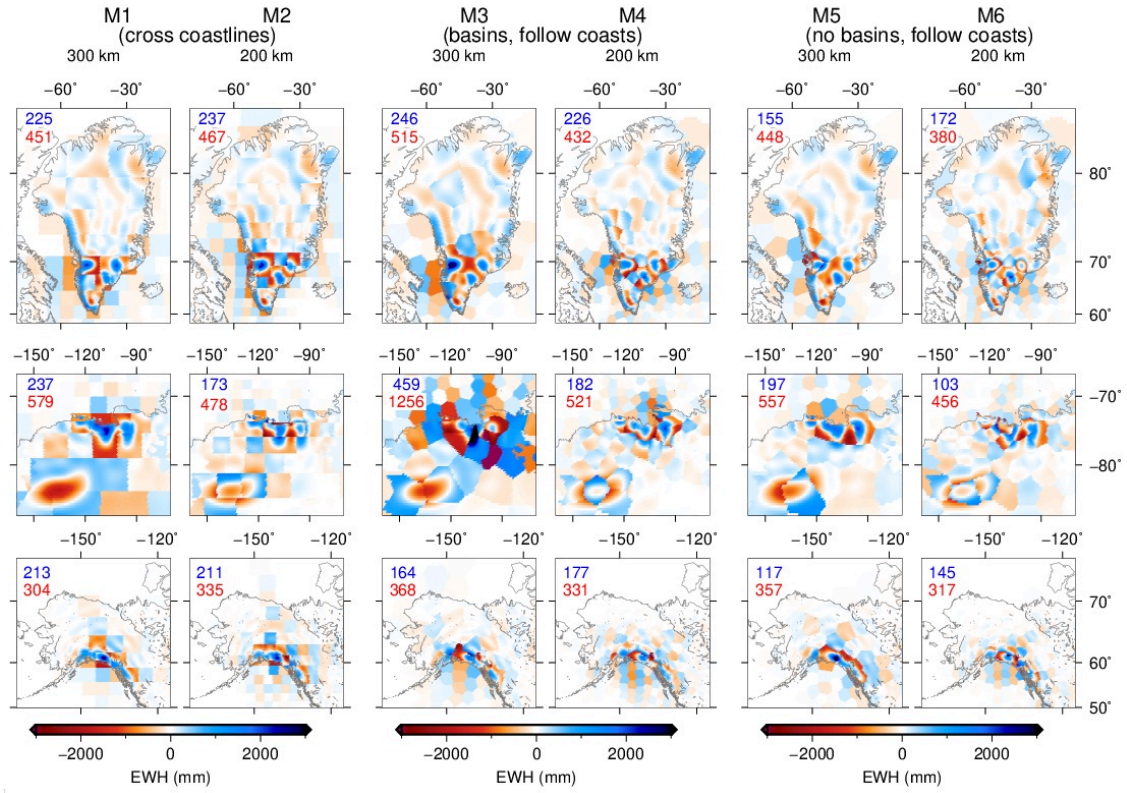

Figure 4.7: Errors in unregularised estimates of the temporal gravity field from simulations, using the mascon geometries at 300 km and 200 km spatial scales. RMS error (in mm) computed on the ternary mascons over each region is shown for ocean ternaries (blue) and land ternaries (red).

4.8 Results

4.8.1 Simulation experiments

To test how well a simulated signal can be recovered, we simulated two sets of orbits. First, we incorporated into the orbit integrations the simulated temporal gravity field of Dobslaw et al. (2015) as shown in Figure 4.5. We call these orbits "truth" orbits, since they contain the simulated (i.e. known) temporal gravity field signals that we seek to recover, and used them to create the simulated observations to replicate the GRACE Level-1B observations (satellite positions, velocities and range rate). We also integrated orbits that did not include the temporal gravity field and we call these our "a priori" orbits.

4.8.1.1 Intra-mascon variability and leakage

When intra-mascon variability (Figure 4.6) is present in the simulated temporal gravity field signal, the parameterisation no longer represents accurately the spatial pattern of mass change (Figure 4.5) and it is not possible to estimate a perfect solution from noise-

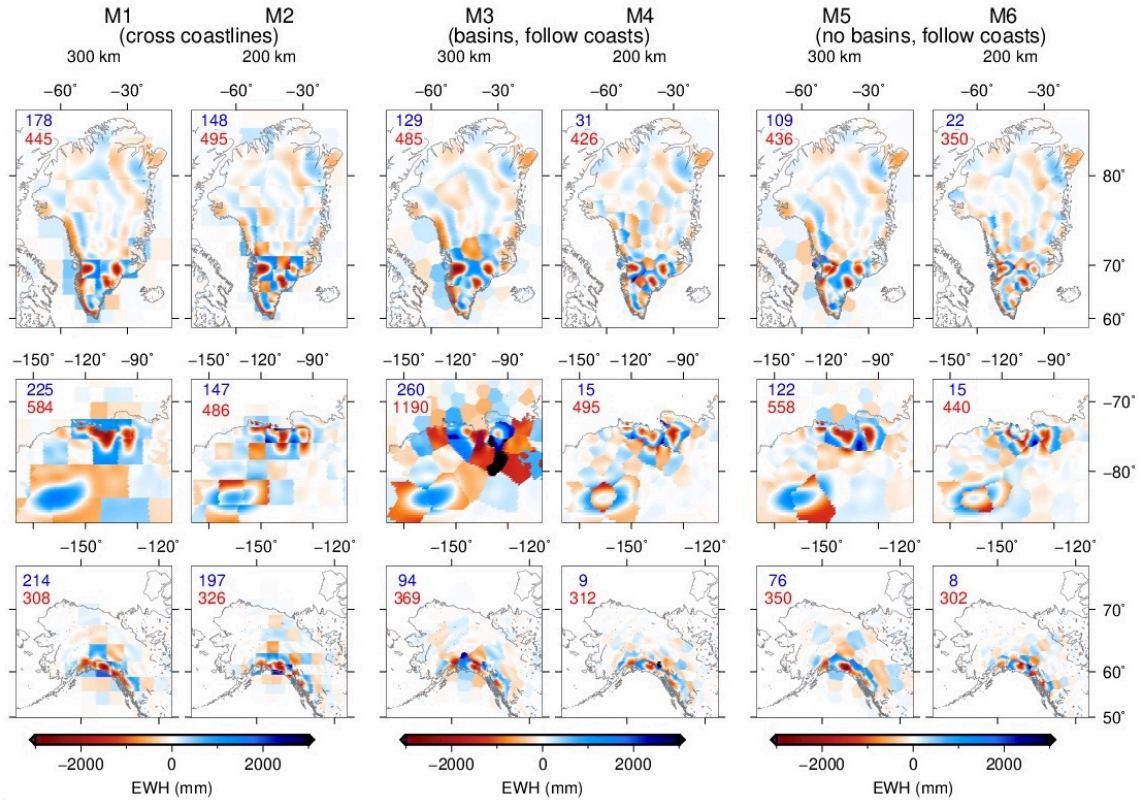

Figure 4.8: Errors in regularised estimates of the temporal gravity field from simulations, using loose regularisation (Table 4.1) and the mascon geometries at 300 km and 200 km spatial scales. RMS error (in mm) computed on the ternary mascons over each region is shown for ocean ternaries (blue) and land ternaries (red).

free, simulated data. The error in the estimated gravity fields varies depending on the size and shape of the primary mascons and to what extent the mascon pattern overlies the pattern of simulated signal (Figure 4.7). The solutions with primary mascons that cross coastlines (M1, M2) have higher land and ocean RMS errors because of intra-mascon leakage (the misappropriation of continental signal over ocean ternary mascons), which also causes inter-mascon leakage (the incorrect assignment of mass change to the wrong mascon). In addition, there is usually less intra-mascon variability when the size of the primary mascons is smaller (compare results of M2 vs M1, M4 vs M3, M6 vs M5 in Figure 4.7). If intra-mascon variability was the only source of error then the spatial patterns in Figure 4.7 should match exactly those of Figure 4.6. The differences between them therefore identifies inter-mascon leakage, induced by the presence of intra-mascon variability.

An unexpected result was that the intra-mascon variability induced significantly more inter-mascon leakage in the solutions with defined drainage basins (M3, M4) than in

either the regular-shaped mascons (M1, M2) or the irregular-shaped without complex drainage basin geometry (M5, M6). This was particularly noticeable around Pine Island and Thwaites Glaciers in West Antarctica (middle panels of Figure 4.7) but is also visible in increased error in ocean mascons offshore of Greenland and Alaska. We do not have an explanation for this but suspect that there is an adverse interaction between complex mascon geometry of the drainage basins and the orbital geometry that is causing increased correlations between partial derivatives relating the primary mascons to the range acceleration observations.

These simulation results (Figure 4.7) show significant inter-mascon leakage of simulated ice loss signals into the oceans (recall that we applied zero ocean signals in our simulation; therefore, all estimated non-zero signals in the ocean regions are errors). Applying diagonal, spatially varying regularisation to the inversions (through matrix C_m in Equation 6) is found to mitigate this continent/ocean inter-mascon leakage which is caused by intra-mascon variability. For example, applying loose regularisation (Table 4.1) the inter-mascon leakage is mitigated for the M4 and M6 mascon patterns that follow coastlines. This demonstrates the benefit of designing mascon geometry to exclude mascons with a mix of land and ocean and that inter-mascon leakage caused by intra-mascon variability is readily mitigated through regularisation of the ocean mascons. Intra-mascon leakage is still evident in the regular-shaped mascons that cross coastlines (M1, M2) and in the larger (∼300 km) mascon cases (M3, M5) (Figure 4.8).

On the basis of these results, we chose to use the M6 mascon geometry as our principal mascon pattern (∼200 km, following coastlines, no defined drainage basins). We include the geometry of only one major continental drainage basin into our mascon pattern, being the Amazon Basin, because the inclusion of this basin caused no significant inter-mascon leakage effects.

4.8.1.2 Regularisation

It is possible to estimate the temporal gravity field with errors <5 mm EWH when inverting noise-free - and intra-mascon variability-free - simulated data without applying regularisation constraints to the mascon parameters (Figure 4.9d). However, constraints must be applied when inverting real data to mitigate observation and model noise in the GRACE and GRACE-FO inversions (e.g. Save et al., 2012; Loomis et al., 2019a) and to reduce errors caused by intra-mascon variability (c.f. Figure 4.7 and Figure 4.8). Applying

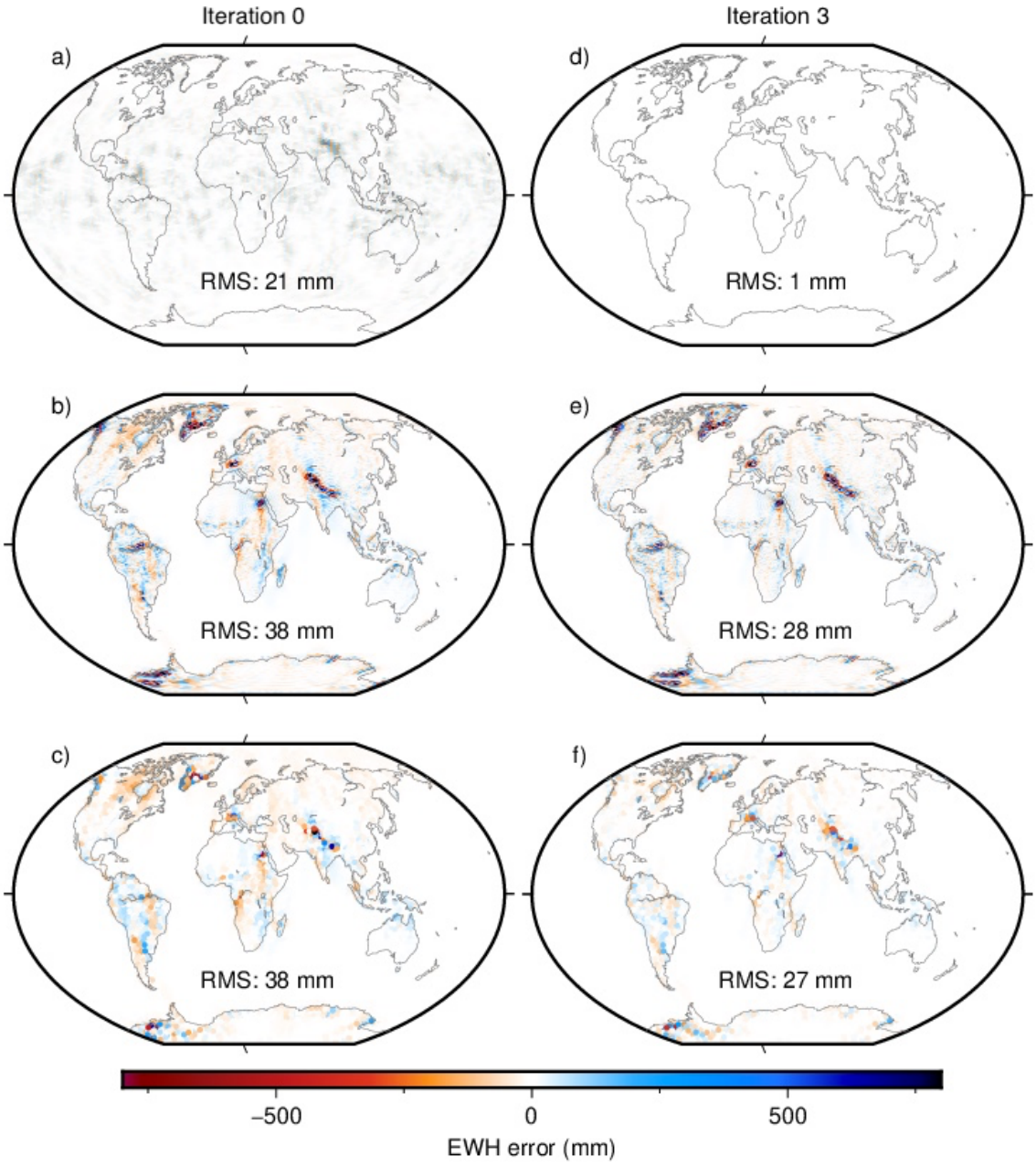

Figure 4.9: Errors in estimated average primary mascon values from noise-free simulations where the simulated signal is the average value on each primary mascon (i.e. no intra-mascon variability). Estimates are shown, using no regularisation (top row) and tight regularisation (middle row). Regularisation error caused by tight regularisation as predicted using the resolution operator (bottom row).

regularisation constraints to the mascons can have the undesirable effect of attenuating the gravity field if the parameter constraints (σ_m) are too tight, consequently preventing the mascon parameters from adjusting to recover the full magnitude of the signal (e.g. Save et al., 2016). The challenge is to minimise the trade-off between signal attenuation and noise in the mascon adjustments by applying appropriate regularisation constraints to each region. Different approaches to regularisation of mascon solutions have been employed, including distance-based constraints that impose correlations on changes in nearby mascons (e.g. Sabaka et al., 2010), constraints based on variability computed from hydrology and/or ocean models (e.g. Watkins et al., 2015) and from the GRACE data directly (Save et al., 2016; Loomis et al., 2019a).

While the application of "loose" regularisation (Table 4.1) applied to our noise-free simulations mitigated the inter-mascon leakage into the oceans caused by intra-mascon variability on ice sheets, this level of regularisation is too weak to be used in the analysis of actual GRACE data; otherwise, the estimated temporal gravity fields are dominated by noise in the form of north/south stripes. Allgeyer et al. (2022) discussed the selection of appropriate regularisation values and we use their values for our "tight" regularisation in our simulations and analysis of real data (Table 4.1). Unlike previous authors (e.g. Luthcke et al., 2006b, 2013; Watkins et al., 2015; Loomis et al., 2019b) we do not include off-diagonal terms in our regularisation matrix, which means that we do not impose spatial correlations between neighbouring mascons. While Croteau et al. (2021) showed that such off-diagonal terms are essential to stabilise inversions using 1-arc-degree mascons, we find that it is not necessary for our 40,000 km^2 mascons. This is consistent with the approach of Save et al. (2016).

We seek to separate the impacts of regularisation alone from the impacts of regularisation in a real-world situation where intra-mascon variability is present and significant. We assessed the former by performing a simulation where we averaged the perturbation signal of Dobslaw et al. (2015) onto our primary mascons, effectively setting the intra-mascon variability to zero. An unregularised inversion of the data yields a near-perfect answer, with RMS of only 1 mm and maximum error on a primary mascon of only 5 mm after three iterations updating the a priori mascon values (Figure 4.9a,d). Applying the tight regularisation introduces inter-mascon leakage (Figure 4.9b,e), which is reasonably well predicted by the resolution operator of Loomis et al. (2019a) (Figure 4.9c,f).

The addition of intra-mascon variability into the simulated signals makes the combined

Table 4.2: RMS of errors (in mm) in Greenland, Antarctica and globally, showing contributions from regularisation (R) and intra-mascon variability (IMV)

	Zero a priori mascons		*Iteration 1*	
	R only	R + IMV	R only	R + IMV
Greenland	192.3	188.4	141.6	165.6
Antarctica	36.5	37.8	32.4	36.3
Global	37.8	67.6	31.8	65.7
	Iteration 2		*Iteration 3*	
	R only	R + IMV	R only	R + IMV
Greenland	121.2	158.6	107.6	155.6
Antarctica	30.4	35.3	29.0	34.6
Global	29.6	65.0	28.1	64.6

error in mascon estimates worse, by as much as a factor of 3 (Table 4.2). A component of this increase is due to the intra-mascon variability itself (see Figure 4.6). This cannot be overcome nor can it be quantified for real data analysis since it is below the possible spatial resolution of GRACE analysis.

4.8.2 Analysis of real GRACE Level-1B data

The analysis of Level-1B data involves a multi-step process of iterating the inversions of GRACE data to estimate the orbital parameters (initial position, velocity and accelerometer calibration parameters) and the adjustments to the mascon parameters (Allgeyer et al., 2022). Non-linear thermal noise is removed from real accelerometer Level-1B observations using the high-pass filter approach of McGirr et al. (2022). The use of actual (rather than simulated) observations introduces noise into the inversions, which requires the more stringent regularisation strategy used here for simulated data and in Allgeyer et al. (2022) for real data. The details of the orbit analysis and a full assessment of our mascon time series (including the handling of geocentre and $C_{2,0}/C_{3,0}$ are provided in Allgeyer et al. (2022).

There is a difference in estimates of ice sheet mass balance change obtained from real data when using irregularly shaped, ∼200 × 200 km mascons that follow coastlines (M6, Table 4.1) instead of a regular pattern of similar-sized mascons that cross coastlines (M2, Table 4.1) (Figure 4.10). For the M2 mascons, we define 'Greenland' mascons as being any mascon that contains any ternary mascons on Greenland. The spatial patterns of the monthly estimates of the temporal gravity field in the Greenland region for April 2003, September 2010 and July 2016 are different, with the M6 estimates matching more closely the geometry of the outlet glaciers. For example, the strong mass loss signal at Jakobshavn

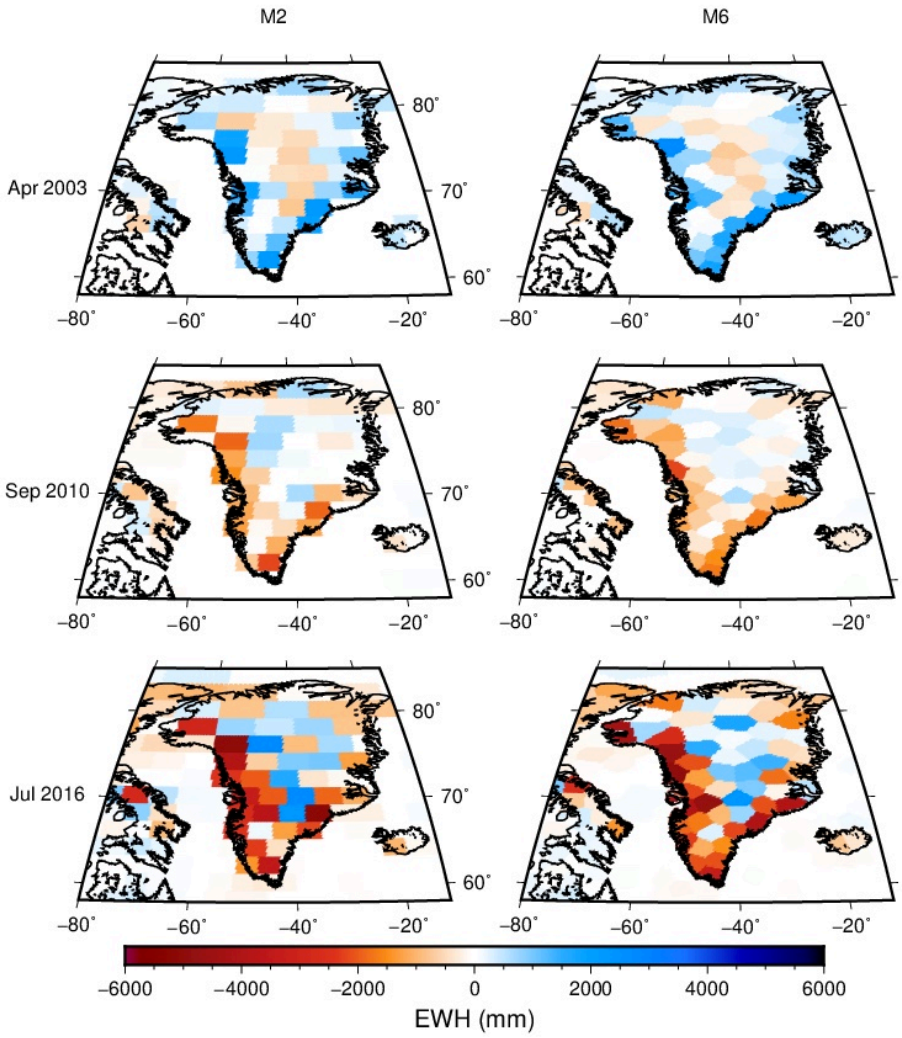

Figure 4.10: Mascon estimates after three iterations using 200 km mascon geometry that cross coastlines (M2) and follows coastlines (M6) for an analysis of real data for April 2003, September 2010 and July 2016.

Glacier (and interior region) in July 2016 is clearly evident in the M6 solution, whereas it has been smeared somewhat into neighbouring mascons in the M2 solution.

Intra-mascon leakage of signal from continents to oceans occurs when using the M2 mascon pattern but does not occur when using our M6 mascon geometry that follows coastlines. The proper assignment of greater mass loss along the edges of Greenland also accentuates the estimated mass gain signal in central Greenland. The integrated mass loss over Greenland for the M6 solutions for July 2016 is ∼5% greater than the M2 solution for the same month, equating to around 233 Gt (or 0.4 mm global sea level). This demonstrates that intra-mascon leakage in the coastline-crossing mascon solutions does impact basin-averaged computations of mass change.

Of course, the fundamental analysis choices of orbit parameterisation, accelerometer observation calibration, mascon regularisation etc can be far more influential on regional mass balance change estimates than the <10% changes shown here through different mascon geometry choices. However, assuming proper calibration of orbital parameters and accelerometer bias/scale calibrations (including the removal of thermal effects from the accelerometer observations (McGirr et al., 2022)), the selection of mascon geometry does become a significant issue in terms of the remaining error budget.

4.9 Conclusions

Our unique method for creating geometrical patterns of irregularly-shaped mascons mitigates leakage errors in estimates of the temporal gravity field from GRACE observations by delimiting oceans and continents. Through the use of algorithms and pre-computed tables, we can achieve a numerical accuracy of computed accelerations and partial derivatives of mascons equivalent to a spatial accuracy of around 18 km×18 km without a burdensome computational expense. This improves the accuracy of the mass change estimates on the mascons which have been computed at a spatial resolution of ∼200 km.

The variability of signal magnitude within a primary mascon, which we call "intra-mascon variability", affects the accuracy of the estimated temporal gravity fields and is an unavoidable problem. The use of smaller mascons mitigates the magnitude of intra-mascon variability but there is a limit on how small the mascons can be before the inversion of the normal equations will become numerically unstable. Regularisation of the inversion assists here but also induces signal attenuation, although this can then be mitigated by iteration through updating of the mascon parameter values. Our simulations show that

it is not possible to estimate a perfect mascon solution at 200 km spatial resolution from simulated, noise-free data using regularisation of sufficient strength to mitigate the noise in inversions of real data.

Our method for constructing the mascon geometry can be used to form primary mascons that follow drainage boundaries as well as to form primary mascons of different sizes in different regions of Earth. This provides significant flexibility and utility, allowing easy configuration of the mascons for a number of different applications for both GRACE and GRACE-FO data. The leakage problems are reduced in computations of integrated total water storage changes of drainage basins as well as glaciated regions, since the proper assignment of mass change to the continents or ocean mascons occurs naturally because of the geometrical construction of the mascon field. This reduces considerably the leakage of signals between ice sheets and neighbouring ocean regions. There is also no need to include off-diagonal terms in the regularisation matrices used to stabilise the inversions for mascons as small as 40,000 km^2 (200 km $\times$ 200 km) used here and in Allgeyer et al. (2022), since the matrices used to generate the solutions are full rank and can be inverted.

Chapter 5

Orbit modelling, regularisation and inter-satellite range acceleration data

The ability to generate accurate models of Earth's static and temporal mass variations from GRACE and GRACE-FO inter-satellite measurements is almost entirely contingent on the accuracy of the modelled orbits of the twin satellites. The modelled orbits are an integration of all of the accelerations acting on the satellites as they orbit around Earth, which include (but is not limited to) the non-gravitational accelerations measured by the accelerometers, the static gravity field and the ocean tides. Thus, the accuracy of the modelled orbits hinges on the quality of both the Level-1B observations and background models, but also the chosen orbit parameterisation and integration procedure. Further, the choice of the inter-satellite observation and basis functions can improve the recovery of the gravity field by better localising the mass variations. Here, we use the range acceleration as the observation and the 200 km $\times$ 200 km irregular, coastline-following mascons introduced in the previous chapter as the basis functions. This chapter details the ANU approach to orbit modelling, regularisation and gravity field inversion using range acceleration derived by numerical differentiation of the Level-1B range rate prefit residuals as the inter-satellite observation. This chapter is based on the manuscript published in the Journal of Geophysical Research - Solid Earth:

Allgeyer, S., Tregoning, P., McQueen, H., McClusky, S.C., Potter, E.-K., Pfeffer, J., ***McGirr, R.,*** *Purcell, A. P., and Montillet, J.-P.(2022) ANU GRACE data analysis: Orbit modelling, regularisation and inter-satellite range acceleration observations. Journal of Geophysical Research: Solid Earth, 127(2), e2021JB022489.*

I made the following contributions to this paper:

- Developed the accelerometer thermal correction procedure and integrated it into the ANU GRACE processing software. It is used to correct the non-gravitational accelerations for each day prior to orbit integration and accelerometer calibration (Section 5.2.2, Figure 5.5)
- Developed a method to reduce high-frequency noise in K-Band Range Acceleration (KBRa) prefit residuals by implementing a low-pass filter on the prefit range acceleration residuals (Section 5.2.5, Figure 5.8)
- Created the mascon file (as described in Chapter 4) used to estimate the gravity field from the GRACE observations
- Produced the simulations that demonstrate to what extent we can recover the low degree components of the temporal gravity field under different regularisation constraints (Section 5.3, Figure 5.10)
- Tested and developed the mascon iteration procedure used to produce unattenuated mascon estimates of the temporal gravity field

My approximate contribution to this manuscript was 25%.

Impact of accelerometer thermal correction on parameter estimates

The method described in Chapter 3 was integrated into the ANU GRACE processing software and applied to each day of available GRACE accelerometer observations used in the orbit integration. However, a detailed analysis of the impact of accelerometer thermal corrections (Figure 5.5) on the GRACE solutions was not presented in Allgeyer et al. (2022). To determine the impact of accelerometer thermal correction on the estimates of the temporal gravity field, I compared the statistics of the position and range acceleration postfit residuals for a year of GRACE solutions that included the uncorrected (black), cross-track corrected (Y; blue) and cross-track and along-track corrected (XY; orange) non-gravitational accelerations (Figure 5.1). During the chosen year (2012), thermal control of the satellites was disabled, allowing the temperature of the accelerometers (and therefore the cross-track biases) to fluctuate with the $|\beta'|$ angle (Figure 5.1).

There is a clear reduction in the daily RMS of the postfit residuals of the position

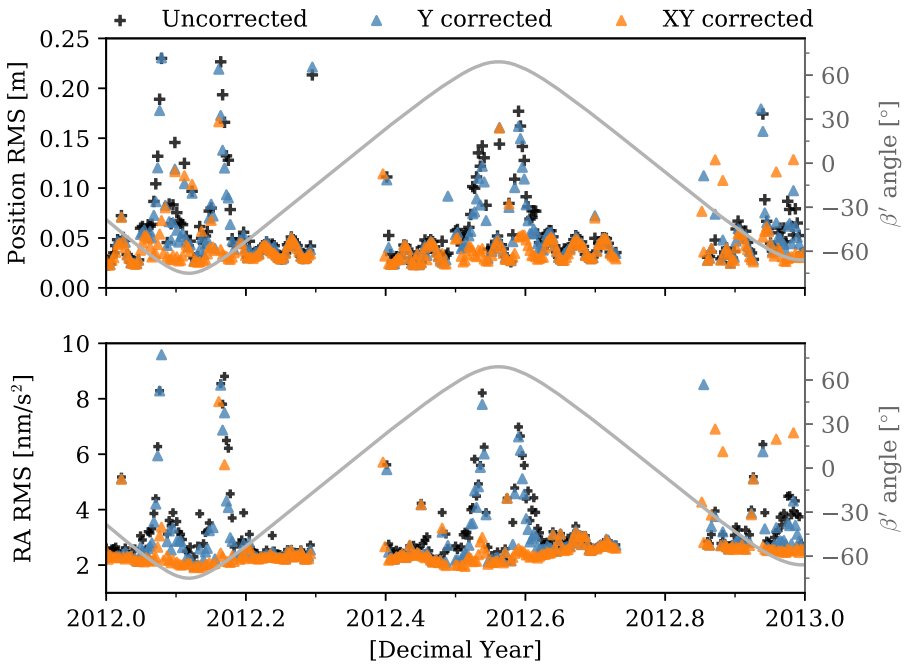

Figure 5.1: β' angle (light grey) and daily Root Mean Square (RMS) of the (top) postfit position residuals and (bottom) postfit Range Acceleration (Ra) residuals over the period 2012 to 2013 using uncorrected ACC1B (black), high-pass filtered cross-track ACC1B (Y; blue) and filtered and thermally-corrected cross-track and along-track ACC1B (XY; orange).

and range acceleration parameter estimates when the thermal correction method is applied to the Level-1B cross-track and along-track non-gravitational accelerations prior to integrating the GRACE orbits, compared to the uncorrected and cross-track filtered accelerometer solutions (Figure 5.1). For the three solutions, I calculated the Root Mean Square (RMS) of the daily position and range acceleration postfit residuals. Treating each of the daily RMS values as an observation, I then calculated the mean and standard deviation RMS postfit residuals for 2012. A modest reduction in the RMS of the position postfit residuals is made when just the cross-track axes of the ACC1B have been corrected for long-wavelength bias drift (blue; 53.21 $\pm$ 34.01 mm), compared to the unfiltered ACC1B (black; 56.23 $\pm$ 36.24 mm) (Figure 5.1). The most significant reduction in RMS occurs when both the along-track and cross-track axes are corrected for thermally induced bias variation (orange; 40.01 $\pm$ 20.05 mm) (Figure 5.1). Similarly, the daily RMS of the postfit range acceleration residuals are slightly improved when the cross-track ACC1B has been corrected (2.97 $\pm$ 1.19 nm/s^2) but significantly improved when both the along-track and cross-track ACC1B have been corrected (2.56 $\pm$ 0.8 nm/s^2), compared to the unfiltered ACC1B (3.2 $\pm$ 1.19 nm/s^2) (Figure 5.1).

The reduction in the RMS of the postfit residuals is most evident when the $|\beta'|$ angle was $> 60°$ (Figure 5.1), which coincides with the largest satellite temperature variations and, therefore, most significant along-track and cross-track accelerometer bias drift (see Figure 3.1). The reduction in the RMS of the postfit residuals is also reflected in the improvements in the gravity field solutions, specifically, the reduction in north-south stripes and the improved stability of the daily scale factor estimates as presented and discussed in Chapter 3, Section 3.6.

Mitigating high-frequency noise present in the inter-satellite observations

KBR system noise has been shown to dominate the high frequency component of the GRACE inter-satellite observations (Figure 5.8) which can degrade estimates of the temporal gravity field (Thomas, 1999; Ditmar et al., 2012). Therefore, understanding at which frequencies these errors exist and whether they are affecting the frequency band that contains the majority of the gravity field signal (0.1 to 18 mHz) is important for understanding the GRACE error budget (Thomas, 1999; Goswami et al., 2018). Previous studies mostly agreed that the KBR system noise dominates at frequencies >20 mHz (e.g. Thomas, 1999; Ko, 2008; Ko et al., 2012; Goswami et al., 2018), although others have demonstrated that these errors impact frequencies within the gravity field signal band. For example, Ditmar et al. (2012) analysed the frequency content of GRACE inter-satellite ranging measurements and found that errors originating from the KBR sensor dominated at frequencies >14 mHz, which propagated into gravity field parameters forming substantial north-south stripes, particularly in mid- to low-latitudes. In a more recent study, Behzadpour et al. (2019) performed a multi-resolution wavelet analysis to decompose actual GRACE range rate residuals, concluding that KBR ranging sensor errors dominated at frequencies >12.5 mHz.

Previous studies have attempted to mitigate the impacts of high-frequency noise contained in the KBR observations on gravity field estimation by the application of low-pass filters during dual-one-way range processing (Thomas, 1999) and have made modest improvements (Ko, 2008). I developed a method to mitigate high-frequency noise, mostly induced by the KBR sensor, by instead filtering the prefit residuals prior to performing the least squares inversion to solve for the temporal gravity field. The prefit residuals are

the difference between the observed inter-satellite measurements and the theoretical values computed from the orbits that do not contain the effects of temporal mass variations. By not modelling the temporal gravity field, the prefit residuals contain the unmodelled mass variation signals, any errors in the parameter estimates, background model errors and errors due to system noise.

I modified the filtering method developed in Chapter 3 to remove unrealistic high-frequency noise contained in the prefit KBRA residuals which are derived from the numerical differentiation of the prefit K-Band Range Rate (KBRR) residuals using the noise robust derivative filter (Section 5.2.5). Similar to the accelerometer implementation of the digital frequency filter, the observations are de-meaned and padded prior to applying the taper function and performing the Fourier analysis on the prefit residuals. To do this, I extrapolated the observations to include an additional 700 epochs on either end by fitting a periodic function to the first and last 1000 epochs of the residuals (extending the time series of range acceleration residuals prior to applying the window function is necessary to recover the edges of each day of the filtered residuals when the window function is removed once the signal is transformed back into the time domain). Prior to applying the taper function, I filled any data gaps by interpolation using the same periodic function to reduce the effects of data gaps on the Fourier analysis.

The extrapolated and interpolated prefit residuals are tapered using the Hann window as per Equation 3.1 and transformed into the frequency domain. The frequencies are then filtered using a raised cosine low-pass filter. The low-pass filter is a modification of the high-pass filter defined per Equation 3.2:

$$H(f) = \begin{cases} 1, & f < f_{lo} \\ 0.5(\cos\left(\frac{\pi(f-f_{lo})}{f_{lo}-f_{hi}}\right)+1), & f_{lo} < f < f_{hi} \\ 0.5, & f > f_{hi} \end{cases} \tag{5.1}$$

To determine the appropriate edge frequencies, I tested several implementations of the raised cosine low-pass filter on the prefit residuals. I first tested an f_{lo} and f_{hi} of 20 mHz and 21 mHz, respectively, as the cutoff frequencies. The choice of 20 mHz for f_{lo} was based on previous studies that identified postfit and prefit inter-satellite residuals to be noise dominated at frequencies higher than 20 mHz (Ko, 2008; Ko et al., 2012; Goswami et al., 2018), while avoiding the frequency band that contains the majority of the temporal gravity field signal. An f_{lo} of 20 mHz effectively removes signal with a period less than 50

seconds. Therefore, this assumes that the gravity field signal measured by the microwave ranging system on-board the GRACE and GRACE-FO satellites is not resolvable at a spatial resolution higher than ∼350 km, greater than the 300 km spatial resolution of GRACE cited in previous studies (e.g. Thomas, 1999; Tapley et al., 2004)

I also tested two end-member implementations of the low-pass filter; using a higher frequency cut-off (which allows more noise to pass through the filter) and a lower frequency cut-off (which filters out more noise, but potentially removes high-frequency temporal gravity signals). For the high frequency end member an f_{lo} and f_{hi} of 30 mHz and 31 mHz were chosen, respectively, which effectively removes signal with a period less than 35 seconds. In this case, the assumption is that the microwave ranging system on-board the GRACE and GRACE-FO satellites is not resolvable at a spatial resolution higher than ∼230 km. For the low frequency end member an f_{lo} and f_{hi} of 10 mHz and 11 mHz were chosen, respectively, which effectively removes signal with a period less than 100 seconds. This assumes that microwave ranging system is not able to resolve the gravity field at a spatial resolution higher than ∼700 km.

To test whether any coherent signals are contained in the prefit residuals at frequencies >10 mHz I performed several simulations. I simulated the GRACE Level-1B position, velocity and range rate observations for 2010-09-10 to 2010-09-20 from "truth" orbits using the spherical harmonic Earth system model of Dobslaw et al. (2015) up to degree 180, temporally-averaged over the month of December 2006 (i.e. excluding any sub-daily high frequency mass changes) as per Chapter 4. The same process was used to generate the prefit range acceleration residuals in simulation using the noise robust derivative filter alone (RA_{ND}) and low-pass filtered using an f_{lo} cutoff frequency of 30 mHz (RA_{30}), 20 mHz (RA_{20}) and 10 mHz (RA_{10}). Because the ranging observations are simulated, the prefit KBRA residuals contain none of the effects of systematic or background model errors. Therefore, the prefit KBRA residuals should only contain the unmodelled gravity field but may include minor high-frequency error introduced by the noise robust derivative filter.

The Dobslaw et al. (2015) model of the temporal gravity field represented by spherical harmonic coefficients up to degree and order (L_{MAX}) 180, contains gravitational changes up to frequencies of ∼70 mHz, significantly higher than the frequency of gravitational variation that can be detected by the GRACE satellites. In both the temporal and frequency domain, the unfiltered RA_{ND} (light grey), low-pass filtered RA_{30} (blue) and RA_{20}

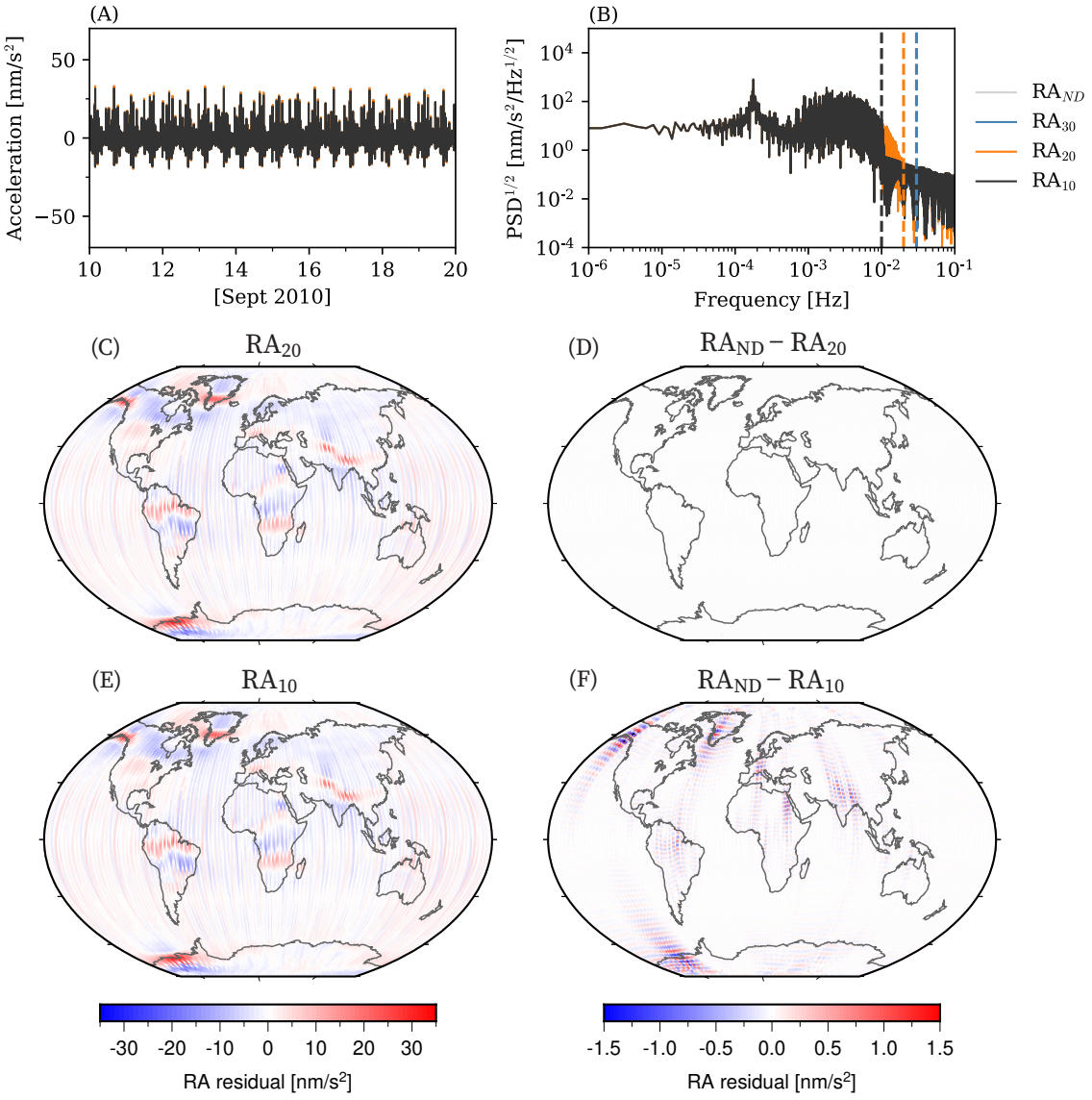

Figure 5.2: Simulated prefit range acceleration residuals derived from the ND filter (RA_{ND}; light grey), then low-pass filtered using 30 mHz (RA_{30}; blue), 20 mHz (RA_{20}; orange) and 10 mHz (RA_{10}; light grey) cutoff frequencies for 2010-09-10 to 2010-09-20 in the (a) temporal and (b) frequency domain. (c) RA_{20}, (d) RA_{ND} minus RA_{20}, (e) RA_{10} and (f) RA_{ND} minus RA_{10} in the spatial domain. Simulation uses the truth field of Dobslaw et al. (2015)

(orange) simulated prefit range acceleration residuals appear to be indistinguishable from each other (Figure 5.2a,b), suggesting that there is negligible signal contained in the 20 mHz to 30 mHz frequency band. However, for the RA_{10} filtered simulated prefit range acceleration residuals, it is noticeable that high-frequency signal has been removed from the 10 mHz to 20 mHz frequency band in the temporal and frequency domains (black; Figure 5.2a,b).

To determine the spatial characteristics of the prefit range accelerations filtered from the time series, I subtracted the filtered residuals from the unfiltered residuals (Figure 5.2d,f). The difference between the RA_{ND} and RA_{20} range acceleration residuals does not appear to contain coherent signal (at a scale of ± 1.5 nm/s^2) (Figure 5.2d) suggesting that no geophysical signal is contained in the inter-satellite observations at frequencies >20 mHz. Some geographically correlated signals are actually apparent at frequencies >20 mHz, but only in the range ± 0.15 nm/s^2 (not shown), consistent with the recent findings of Spero (2021) (see Figure 3 therein). Spatially, the RA_{10} range acceleration residuals (Figure 5.2e) do not appear attenuated compared to RA_{20} (Figure 5.2c). However, the difference between the RA_{ND} and RA_{10} range acceleration residuals clearly demonstrates that using an f_{lo} of 10 mHz removes some coherent signal, but only in the range ± 1.5 nm/s^2 (Figure 5.2f). The location of these signals are related geographically to the places that have the largest amplitude signals in the simulated field (i.e. West Antarctica, Alaska, Greenland, Amazon, Egypt and the Himalayas).

The high-frequency noise content of the prefit KBRA residuals for the period 2010-09-10 to 2010-09-20 computed from real GRACE observations can be analysed in the temporal and frequency domains. The unfiltered prefit KBRA residuals (RA_{ND}; light grey) exhibits a rapid increase in power from 10 mHz, peaking at 50 mHz (Figure 5.3b). Previous studies have demonstrated that this signature appears consistently throughout the GRACE mission and has been attributed to the limited accuracy of the KBR sensor at high frequencies (i.e. >10 mHz) (Flury et al., 2008; Ditmar et al., 2012). As expected the corresponding unfiltered time series of prefit KBRA residuals contains considerable noise (Figure 5.3a). The noise content in the temporal domain is dramatically decreased when the residuals are low-pass filtered using the highest frequency cutoff (RA_{30}; blue) (Figure 5.3a). In the frequency domain, it appears that an f_{lo} of 10 mHz is needed to mitigate the high-frequency noise (black; Figure 5.3b), while the other implementations of the filter preserve some high-frequency noise (orange and blue; Figure 5.3b).

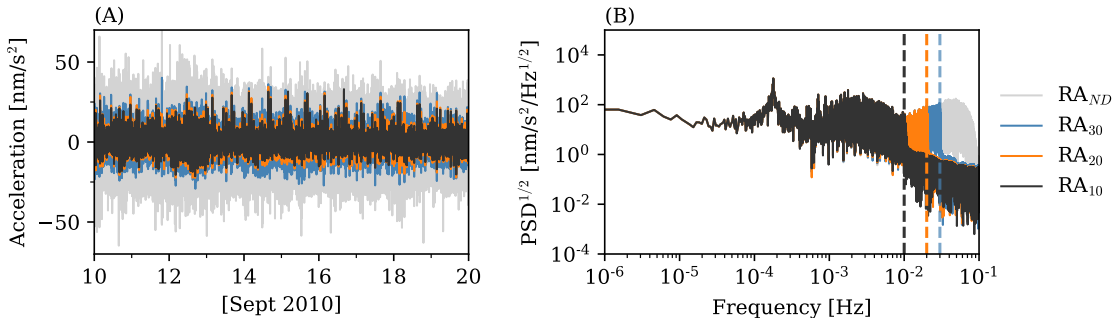

Figure 5.3: Prefit range acceleration residuals derived from the ND filter (RA_{ND}; light grey), then low-pass filtered using 30 mHz (RA_{30}; blue), 20 mHz (RA_{20}; orange) and 10 mHz (RA_{10}; black) cutoff frequencies for 2010-09-10 to 2010-09-20 in the (a) temporal and (b) frequency domain.

For all applications of the low-pass filter the mass variation signal and noise can be observed spatially, specifically, the temporal gravity field signal in the prefit KBRA residuals becomes more visible as the f_{lo} is decreased from 30 mHz to 10 mHz (Figure 5.4a,c,e). To test whether any of the applications of the low-pass filter visibly remove any geophysical signal, I subtracted the filtered RA_{30} prefit KBRA residuals from the unfiltered KBRA prefit residuals (RA_{ND}), then RA_{20} from RA_{30} and RA_{10} from RA_{20} to identify any geographically correlated geophysical signal in these frequency bands. A significant amount of noise contained in the 30 mHz to Nyquist (100 mHz) frequency band is removed from the RA_{30} residuals (Figure 5.4b). The additional noise removed from the RA_{20} residuals in the 20 mHz to 30 mHz band also appears significant (Figure 5.4d), while minimal noise appears to be contained in the 10 mHz to 20 mHz band (Figure 5.4f). In each case, no geographically correlated signals appear to be removed by the low-pass filter (e.g. Figure 5.4b,d,f).

Based on the the analysis of the prefit residuals calculated from simulation and from real GRACE inter-satellite range rate observations, I think that values of an f_{lo} and f_{hi} of 20 mHz and 21 mHz, respectively, are the most appropriate. These values were then used for GRACE (and GRACE-FO) processing in Allgeyer et al. (2022). These edge frequencies were selected to mitigate the high-frequency signals without attenuating the gravity field signal contained in the prefit KBRA residuals. Note that these filter settings are not compatible with the LRI ranging measurements as the inter-satellite observable, as the LRI is sensitive to 0.1 nm/s^2, an order of magnitude better than the KBR instrument (Ghobadi-Far et al., 2020b).

The sections that follow are from Allgeyer et al. (2022).

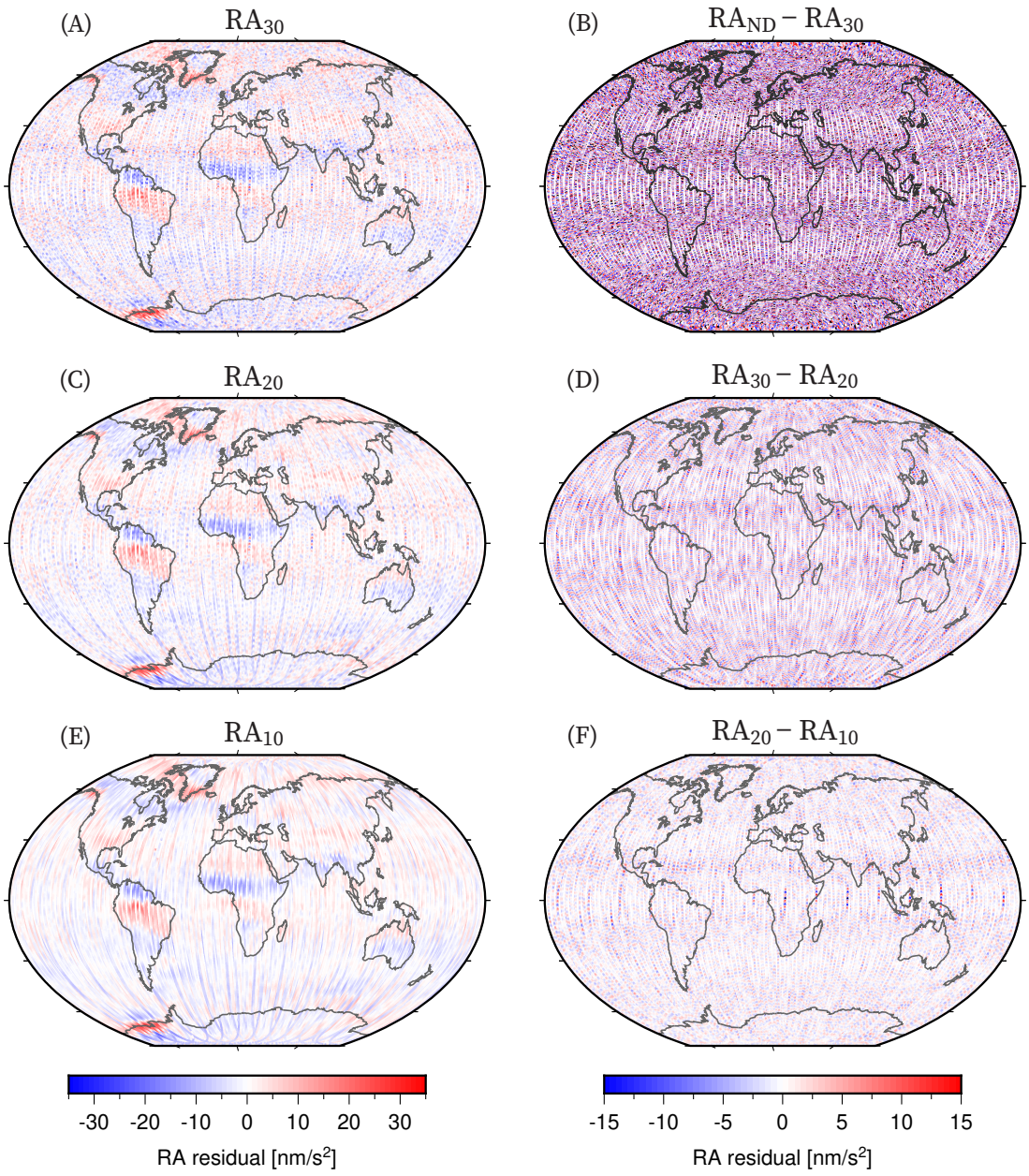

Figure 5.4: Prefit range acceleration residuals derived from GRACE inter-satellite range rate observations, then low-pass filtered using cutoff frequencies (a) 30 mHz (RA_{30}), (b) unfiltered (RA_{ND}) minus RA_{30}, (c) 20 mHz (RA_{20}), (d) RA_{30} minus RA_{20}, (e) 10 mHz (RA_{10}) and (f) RA_{20} minus RA_{10} for 2010-09-10 to 2010-09-20 in the spatial domain.

Abstract

Several different basis functions have been used to represent the Earth's gravity field in order to generate estimates of mass variations on Earth from the analysis of data of the Gravity Recovery and Climate Experiment (GRACE) and its successor GRACE Follow-On missions, including spherical harmonics, mass concentration elements (mascons) and slepian functions. Each approach depends inherently upon accurate modelling of the orbits of the pair of satellites as they revolve around the Earth, so that the observations of inter-satellite changes in range (or, more specifically, range rate) can be exploited to identify mass variations. We have developed software using a classical orbit modelling approach, mascons and 24-hour orbit integration, to estimate simultaneously corrections to orbital parameters and the temporal gravity field from GRACE data. Rather than using the range rate, we use the range acceleration as the inter-satellite observable as it aids in localising the mass variations. Level-1B range acceleration observations contain high levels of high-frequency noise that inhibits their usefulness for this purpose. Instead, we generate range acceleration observations by numerical differentiation of the Level-1B range rate prefit residuals. Simulations show that the gravity signal is not attenuated in this process. Our monthly estimates of mass anomalies from GRACE data (2003-2016) agree well with previous studies, both spatially and temporally. When converted to spherical harmonics our time series of $C_{2,0}$, derived from GRACE data alone, are close to the independent estimates from satellite laser ranging, but the overall solution is improved by substituting the SLR $C_{2,0}$.

5.1 Introduction

The Gravity Recovery and Climate Experiment (GRACE) space gravity mission (Tapley et al., 2004) operated from 2002 until it was decommissioned in 2017. Data from the mission have had major impacts in the fields of hydrology (e.g. Leblanc et al., 2009; Lo et al., 2010; Rodell et al., 2018), cryospheric science (e.g. Velicogna and Wahr, 2006; Luthcke et al., 2013), oceanography (e.g. Boening et al., 2012b; Chambers, 2006a) and glacial isostasy (e.g. Riva et al., 2009; Martín-Español et al., 2016). Small changes in the strength of the Earth's gravity field caused by the redistribution of mass on the Earth cause subtle changes in the range between the satellites. This is the fundamental observation that made the GRACE mission unique.

A number of different mathematical approaches have been used to parameterize the Earth's gravity field and the convergence of the inversions of the data. Solving for coefficients of spherical harmonic models has been the most common approach used since the start of the GRACE mission (e.g. Tapley et al., 2004; Lemoine et al., 2007). A common characteristic of the estimated temporal gravity fields is a north-south striped error pattern, in part related to the high correlations between even and odd order coefficients (Swenson and Wahr, 2006). Such errors have been mitigated through the application of their destriping filter but also through the use of a number of other filters such as Gaussian (e.g. Wahr et al., 1998) and the suite of DDK filters (e.g. Kusche, 2007). Some studies (Lemoine et al., 2007; Bruinsma et al., 2010) applied constraints to the spherical harmonic coefficients so that their change in magnitude with higher degree matched some empirical pattern, thus reducing the noise in the estimated temporal gravity fields.

Rowlands et al. (2005) and Watkins et al. (2005) introduced the use of mass concentration elements (mascons) as an alternate parameterization to represent the temporal gravity field from GRACE data. A mascon is defined as a tile or region of known area on which a change in mass is estimated. They related the change in mass of each mascon (represented by a uniform thickness of water over the surface of each mascon) to spherical harmonic coefficients representing the temporal gravity field and, hence, estimated the spatial pattern of mass variations. Luthcke et al. (2006b) showed that the use of mascons permitted more intuitive applications of spatial and temporal constraints in the inversion steps, resulting in temporal gravity field estimates that contained significantly less noise and did not require any further filtering. They used a regular $3^\circ \times 3^\circ$mascon geometry. Subsequent studies using mascons have adopted different approaches to defining the mas-

con geometry. Watkins et al. (2015) used 3° equal-area spherical caps for each mascon, while Save et al. (2016) used 1° geodesic shapes. Luthcke et al. (2013) reduced the size of their regular-shaped mascons to 1°×1°, although they state explicitly that this is not the actual spatial resolution of the solutions, since neighboring mascons are correlated.

Different approaches have been used to improve the convergence of the inversions for temporal gravity field solutions using mascons. Luthcke et al. (2013) used empirically determined constraints on each mascon along with spatial and temporal correlations between mascons. Watkins et al. (2015) used variations derived from geophysical models (and the GRACE data itself) to regularise their solutions. Save et al. (2016) constrained their inversions using only the information contained in the GRACE measurements themselves. Their regularisation matrices were time varying and did not bias their solutions towards any particular model values.

To date, all published solutions use the range rate information. Numerical differentiation of the range rate creates a range acceleration observable but amplifies short-wavelength signals while reducing the amplitude of longer-wavelength signals. The potential advantage of using the range acceleration as the primary observation (instead of the range rate) is that gravity anomaly signals caused by mass anomalies on Earth would be better localised spatially, with a spike occurring in the range acceleration observations when the satellites are approximately overhead (Save et al., 2012). However, it has not been demonstrated that the longer-wavelength signals are retained in this approach. Postfit range acceleration residuals, derived from postfit range rate residuals, have been used (Save et al., 2012, 2016) to quantify the amount of mass variation signal that was not captured by parameters when estimating the temporal gravity field. These studies did not directly use the range acceleration observations to estimate the gravity fields.

Range rate observations contain a once-per-revolution signal after passing over a disturbing mass signal. Conversely, range acceleration observations are much less affected once the satellites have passed over a mass anomaly signal. This feature can be exploited when inverting GRACE observations to estimate the spatial pattern of the temporal gravity field, provided that the long-wavelength features of the gravity field can also be sensed and estimated.

We show below that accurate mass anomalies at short and long spatial scales can be recovered from GRACE range acceleration observations, although the range acceleration observations provided in the Level-1B mission data contain a signal to noise level that

precludes their use in gravity field estimation. Through an alternate numerical differentiation process, it is possible to filter out the high-frequency noise without attenuating the short-wavelength signals of the mass anomalies. The resulting temporal gravity field estimates recover accurately both the short- and long-wavelength components of the temporal gravity field.

In this paper we describe our orbit modelling and mascon parameterisation used to estimate temporal gravity fields using data from the GRACE mission. We describe how the inter-satellite range acceleration data can be used to estimate the temporal gravity fields and how it reduces the typical north-south striped error pattern seen in solutions derived using the range rate. In our companion paper (Tregoning et al., 2022) we describe how we constructed our mascon field, and its effect on mitigating the smearing of signals between oceans and continents.

5.2 Methods

5.2.1 Orbit modeling

We have developed the ANU GRACE processing software with which we estimate the temporal gravity field of the Earth from GRACE observations. Our software uses the classical variational approach to integrate satellite orbits (e.g. Beutler et al., 2010), then estimates adjustments to a static gravity field to quantify the "temporal gravity field" (time varying mass anomalies with respect to a mean gravity field). We parameterise the temporal gravity field using mascons and derive changes in mass on each mascon in terms of an equivalent thickness of water over the area of the mascon. We explicitly relate the change in mass of each mascon directly to the inter-satellite measurements, as described in our companion paper (Tregoning et al., 2022).

We integrate the satellite orbits using an Adams-Bashforth-Moulton 3-4 integrator. It is composed of an Adams-Bashforth (order 3) explicit step (Bashforth and Adams, 1883) as a predictor phase followed by an Adams-Moulton (order 4) step (Moulton, 1926) as a corrector phase. Table 5.1 describes the forces acting on the satellites in our orbit integration. Our integrator uses a 5-second step size, performs the integrations in the inertial reference frame (defined using IERS 2010 conventions, Petit and Luzum (2010)) and outputs positions, velocities and partial derivatives in the terrestrial reference frame.

We parameterise the satellite orbits using as few parameters as possible: initial position

Table 5.1: Background force modelling used in the orbit integrations

Process	Description
Static gravity field	DIR-R4 (truncated to degree 200) (Bruinsma et al., 2013)
Dealiasing atmosphere and non-tidal ocean	AOD1B-RL06 (Dobslaw et al., 2017a)
Ocean tide model	FES2014 (Carrere et al., 2015; Lyard et al., 2021) modified Antarctica from Padman et al. (2002)
Atmospheric tides	S_1, S_2 and S_3 from the AOD1B product (Dobslaw et al., 2017a)
Non-gravitational accelerations	Level-1B data ACC1B/SCA1B
Cellestial body perturbation	JPL Ephemeris DE421 (Folkner et al., 2009)
Solid Earth tides	IERS 2010 non-elastic Earth (Petit and Luzum, 2010) including mean polar motion (Wahr et al., 2015)
General relativity	IERS 2010 standard (Petit and Luzum, 2010)

and velocity of each satellite plus one accelerometer bias and scale parameter per satellite per 24 hour period in each of the along-track, cross-track and radial directions. We iterate the orbits to converge to a set of orbital parameters that best fit the GPS positions and velocities (provided in the GNV1B data files) and intersatellite range rate measurements (provided in the KBR1B data files) before estimating simultaneously all orbital and mascon parameters. This process is described in detail in Section 3.

5.2.2 Calibration of accelerometer observations

The observations made by the accelerometers onboard the GRACE and GRACE-FO satellites require calibration. Previous studies have differed significantly in their approach to calibrating the observations, although most studies adopt a model which includes a bias and a scale factor. The temporal estimation of bias values varies from up to 28 values per day (Rowlands et al., 2010) to daily values (e.g. Bruinsma et al., 2010; Watkins et al., 2015), while scale factor values have been estimated daily (e.g. Bruinsma et al., 2010; Rowlands et al., 2010), as monthly mean values or even fixed at a value of 1 for the radial scale factor (Watkins et al., 2015). Once the thermal control within the satellites was deactivated later in the GRACE mission (from April 2011 onwards), thermally driven non-linear variations occurred in the accelerometer measurements (Klinger and Mayer-Gürr, 2016; McGirr et al., 2022), particularly in the cross-track and radial components.

The purpose of calibrating the accelerometer observations is to turn the biased measurements into "absolute" measurements of the non-gravitational accelerations acting on

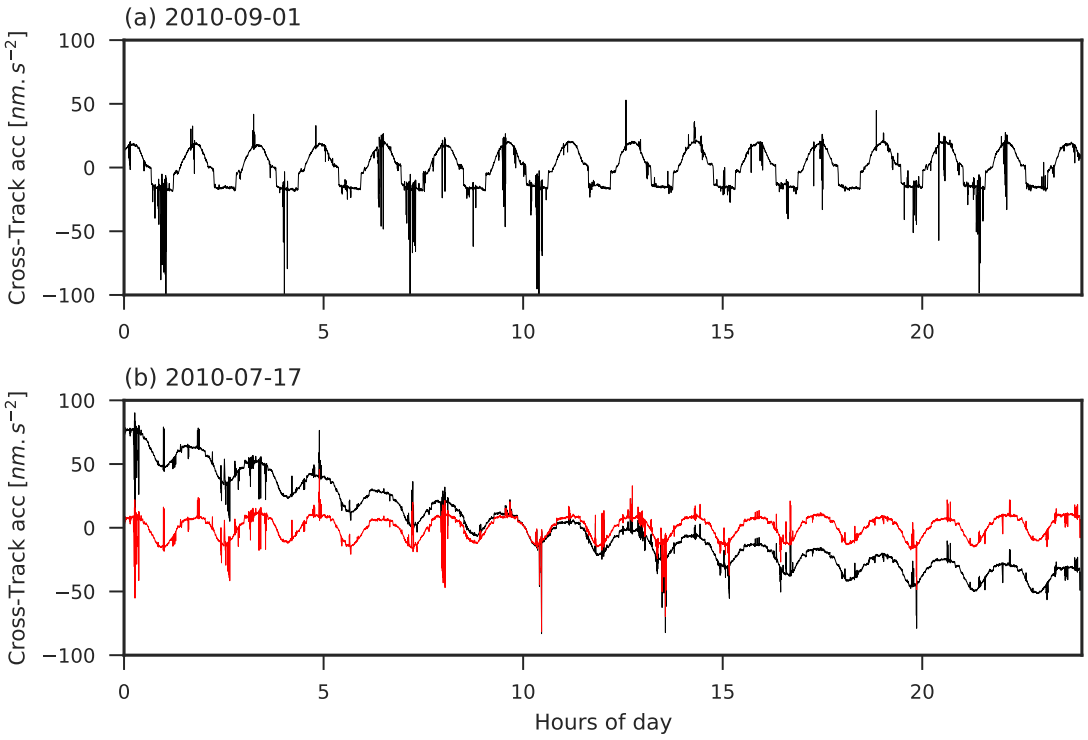

Figure 5.5: Uncalibrated cross-track accelerometer observations of GRACE-A for (a) a typical day (2010-09-01) when the satellites pass into the shadow of the Earth, showing the repeating pattern of the observations for each revolution. (b) 2010-07-17, including low-frequency thermal effects (black) and high-pass filtered values (red). Signals have been demeaned. The observed spikes are generated by thrust events.

each satellite. These calibrated measurements can then be applied directly in the integration of the satellite orbits. The measurements are a sum of the effects of atmospheric drag, solar radiation pressure, reflected energy from the Earth and linear components of the thruster firings during satellite attitude manoeuvres. The atmospheric drag dominates the along-track component while the solar radiation dominates the radial component. In most cases, each of these effects has a quasi-stable signature that repeats through each orbit cycle within a single day. Therefore, one would expect that the calibrated accelerometer observations would display a repeatable pattern throughout the ∼15 orbital revolutions within a day. We find that, in general, a single bias and scale factor parameter per orthogonal axis per day is sufficient to ensure that the calibrated accelerometer observations display the expected temporal patterns in the along-track and radial directions (Figure 5.5a).

Thermal variations within the satellites affect the accelerometer observations and we mitigate these effects by applying a raised cosine high-pass filter as described in McGirr

et al. (2022), with low- and high-edge frequencies of 0.045 and 0.055 mHz (Figure 5.5b). Once the low-frequency thermal effects are removed, the accelerometer observations can be calibrated using single bias and scale parameters per axis per day, as before.

5.2.3 Partial derivatives

The state vector parameters ($\vec{S_0} = (p_0, v_0, s_0, b_0)$), defining the initial condition of satellite orbits include the initial position ($\vec{p}_0$) and velocity ($\vec{v}_0$) at the start of the orbit and also the accelerometer calibration parameter scales ($\vec{s}_0$) and biases ($\vec{b}_0$). We derive partial derivatives that relate the observed positions and velocities ($\vec{o} = (\vec{p}, \vec{v})$) of a satellite to the initial state vector parameters by integrating additional orbits where each parameter is perturbed by a small amount at the start of the orbit. We calculate the partial derivative for a parameter at epoch t as the difference between the actual and perturbed orbit at each time t divided by the magnitude of the original perturbation.

$$\frac{\partial o}{\partial S_0^i} = \frac{\vec{o}_{\delta S_0^i} - \vec{o}}{\delta_{S_0^i}} \tag{5.2}$$

where $\vec{o}_{\delta S_0^i}$ is the instantaneous position and velocity of the satellite in the perturbed orbit, $\vec{o}$ is the instantaneous position and velocity coordinate of the satellite in the unperturbed orbit and $\delta_{S_0^i}$ is the size of the perturbation applied to the initial value of S_0 to perturb the orbit. The perturbations that we apply are 0.5 m for position parameters, 0.05 mm/s^2 for velocity parameters, 50 nm/s^2 or accelerometer bias parameters and 3% for accelerometer scale parameters. We derive partial derivatives relating our mascon parameters to the observations through an equation for the gravitational acceleration of two point sources, as described in Tregoning et al. (2022).

5.2.4 Prefit residuals

The least squares inversions to solve for the mass anomaly fields use the difference (which we call here the "prefit residuals") between the observations and the theoretical values computed from orbits integrated without disturbing masses. By not modelling a priori the mass anomaly fields, these prefit residuals contain the unmodelled mass anomaly signals, plus any errors in orbit modelling and/or forward models used in the orbit integration (e.g. ocean tides, non-tidal ocean and atmosphere, orientation errors for the GRACE satellites etc.). If the orbital parameter values used in the orbit integration are reasonably accurate then the prefit residuals are dominated by the effects of the unmodelled gravity

field anomalies.

Typically, gravity field inversions using GRACE data have been done using the rate of change of range between the satellites, known as the "range rate", as the observable. The time derivative of the range rate, called the "range acceleration", also provided in the Level-1B data has not been exploited for gravity field estimation; however, range acceleration solutions have been produced (Tregoning et al., 2017, 2018; Save et al., 2019). The Level-1B range acceleration observables, $\ddot{R}_{L1B}$, provided at 5-second sampling, are generated from 10 Hz dual one-way ranges using a digital filter, where the filter is N self-Convolutions of a Rectangular time-domain window function (CRN) (in this case, N = 7) and the time window is 70.7 seconds (see Thomas, 1999; Case et al., 2010, for details). The CRN filter for the range acceleration observations is actually the double time derivative of the CRN filter used to generate 5-second ranges from the same 10 Hz data. Thus, it is not the Level-1B range measurements themselves that are used to derive the 5-second range acceleration observations present in the Level-1B file but the 10 Hz Level-1A dual one-way ranges. Note that all of the Level-1B range, range rate or range acceleration "observations" are, in fact, derived values, not direct observations, and no covariance or correlation information between these three observables is available in Level-1B data files.

The use of the range acceleration to estimate the temporal gravity field offers distinct advantages over the use of the range rate because it localises the mass change signals; however, it contains high frequency noise, which needs to be removed from the Level-1B range accelerations in order to make the range acceleration a viable observable for estimating temporal gravity fields. In theory, this can be done by appropriate filtering techniques.

5.2.5 Derivation of range acceleration data

In this section we show how we derive prefit range acceleration residuals that do not contain the high-frequency noise of the Level-1B observations. We do this through numerical differentiation of prefit range rate residuals, employing a noise robust derivative filter which helps to mitigate the high frequency noise. We show below through simulation that our range acceleration observable retains all the gravity signal but contains significantly less noise than the Level-1B range acceleration.

To derive an analytical expression from which to calculate typical range acceleration prefit residuals using simulated data, we start with the inter-satellite range, R:

$$R^2 = \vec{r}_{AB} \cdot \vec{r}_{AB} \tag{5.3}$$

where $\vec{r}_{AB}$ is the vector of the inter-satellite relative position between GRACE-A and GRACE-B. The range rate, $\dot{R}$, is the time derivative of the range:

$$\dot{R} = \hat{e}_{AB} \cdot \dot{\vec{r}}_{AB} \tag{5.4}$$

where $\dot{\vec{r}}$ is the inter-satellite relative velocity vector and $\hat{e}$ is the unit vector of the line of sight direction between the two satellites. By differentiating Equation 3 with respect to time, one can derive an analytical expression for the range acceleration, $\ddot{R}$ (Rummel, 1979):

$$\ddot{R} = \dot{\hat{e}}_{AB} \cdot \dot{\vec{r}}_{AB} + \hat{e}_{AB} \cdot \ddot{\vec{r}}_{AB} \tag{5.5}$$

where $\ddot{\vec{r}}_{AB}$ is the inter-satellite relative acceleration vector and $\dot{\hat{e}}_{AB}$ is the time derivative of the unit vector $\hat{e}$. This has been called the "classic acceleration" approach (e.g. Rummel, 1979).

Projecting those equations in Cartesian coordinates, they become:

$$R = \sqrt{\sum p_i^2} \tag{5.6}$$

$$\dot{R} = \frac{\sqrt{\sum \dot{p}_i p_i}}{R} \tag{5.7}$$

$$\ddot{R} = -\frac{\dot{R}^2}{R} + \frac{\sum \dot{p}_i^2 + \ddot{p}_i p_i}{R} \tag{5.8}$$

where p, $\dot{p}$ and $\ddot{p}$ are the relative difference in position, velocities and acceleration between both satellites.

5.2.5.1 Prefit range acceleration residuals as a temporal gravity field proxy

We generated simulated GRACE orbits and extracted from our orbit integrator the positions, p, velocities, $\dot{p}$, and accelerations, $\ddot{p}$, for each satellite at each epoch in the inertial reference frame. We used these values in Equation 4.7 to create a set of simulated range acceleration observations. We calculated orbits for day 2010-09-01 and included in our gravity models for these orbits the temporal gravity field estimate for September 2010 of

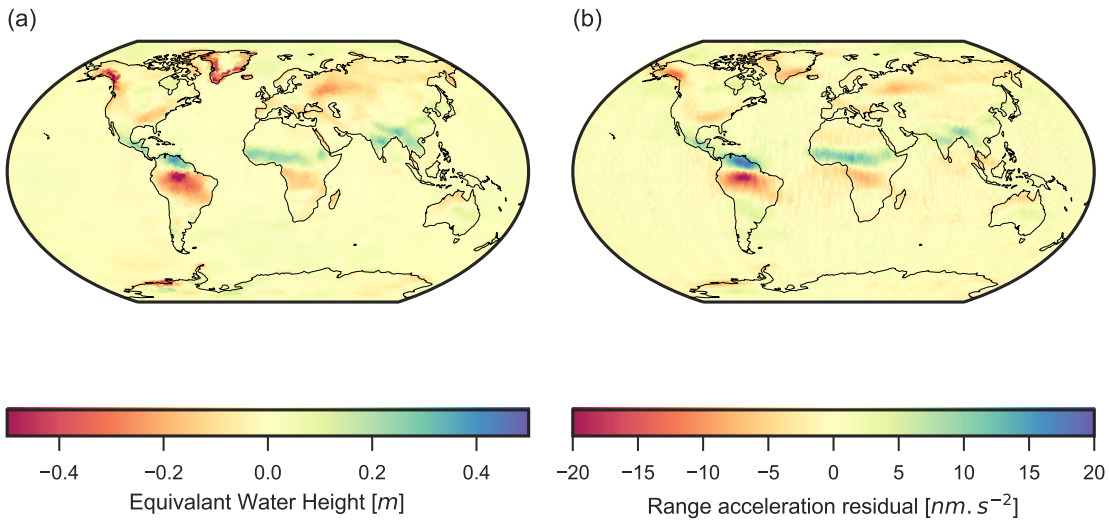

Figure 5.6: (a) Temporal gravity field of Luthcke et al. (2013) for September 2010, (b) Prefit Range acceleration residuals for the same month generated using Equation 4.7 for our "target" - "a priori" orbits.

(Luthcke et al., 2013) (Figure 5.6a) that we will call "target" orbits. Thus, these perturbed range acceleration observations, $\ddot{R}^t$ (where superscript t stands for target orbits) contain the effects of the temporal gravity field for this date. We also calculated the simulated range rate observable, $\dot{R}^t$ from Equation 4.6.

Next, we generated a second set of GRACE orbits where we did not use the temporal gravity field as part of the gravity models in the integrator (which we call our "a priori" orbits). That is, we simulated the satellites flying around just the static component of the Earth's gravity field. Once again, we extracted the positions, velocities and accelerations at each epoch for each satellite and, using Equation 4.6 and 4.7, computed the range rate and acceleration observations, $\ddot{R}^a$ (where superscript a stands for a priori orbits).

The difference between $\ddot{R}^t$ and $\dot{R}^a$ provides us with simulated prefit range acceleration residuals, $\Delta\ddot{R}^a$, computed analytically and containing only the effects of the temporal gravity field on the inter-satellite observable. Plotted spatially (Figure 5.6b), these prefit range acceleration residuals do indeed correspond to the places on Earth where there are signals in the temporal gravity field for September 2010 (compare Figure 5.6a,b).

The amplitude spectrum of the analytically derived range acceleration residuals, $\Delta\ddot{R}^a$, are shown in Figure 5.7a (blue line). The gravity signal is evident at frequencies lower than 0.01 Hz, with essentially no other power present. To some extent, this is influenced by the spatial resolution with which we simulated the temporal gravity field (∼200 km). Abich et al. (2019) and Tapley et al. (2019) estimated that the highest detected frequencies of

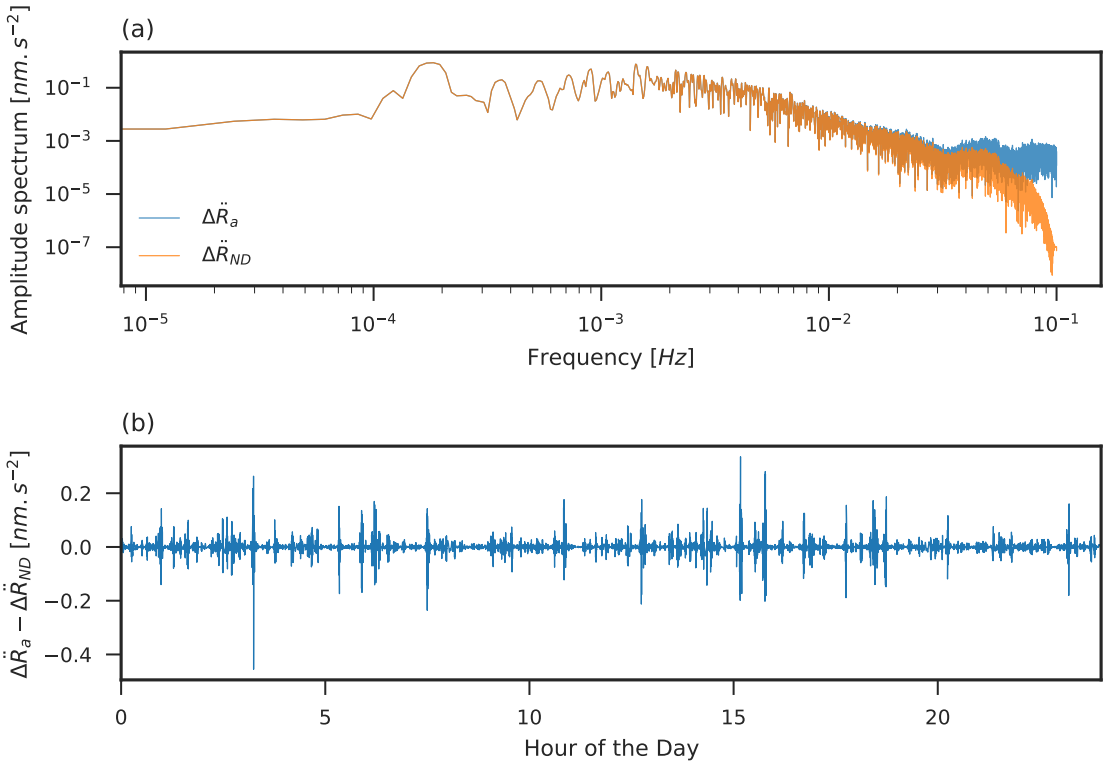

Figure 5.7: (a) Amplitude spectra of range acceleration residuals from a simulated temporal gravity field (Blue: values computed using Equation 4.7. Orange: values derived from the ND filter of the simulated range rate differences). (b) Time series for 2010-09-01 of the range acceleration difference between the analytical formula (Equation 4.7) and using the maximally flat derivative filter.

the temporal gravity field were likely to be around 30 mHz, which is consistent with our simulation.

5.2.5.2 Range acceleration obtained via numerical differentiation of Range rate

Mass changes on mascons will have a direct effect on the accelerations acting on the satellites. Hence we choose to use the acceleration in the range measurement to determine the gravity field, but to do this it is necessary to suppress short wavelength noise in the range acceleration prefit residuals.

We seek a means of deriving prefit range acceleration residuals using real data through numerical differentiation of the range rate data. It is important to verify that the numerical differentiation process does not contaminate or attenuate the gravity signal; therefore, we first performed the numerical differentiation (ND) on our simulated range rate observables, $\dot{R}^t$ and $\dot{R}^a$ using a maximally flat numerical differentiation filter:

$$\ddot{R}_{nd} = F_{ND}(\dot{R}) \tag{5.9}$$

where F_{ND} is the ND filter. The derivative routine implements a 7-point maximally flat low-pass digital differentiation filter (Selesnick, 2002; Hosseini and Plataniotis, 2017) that minimises high frequency noise in a uniform manner while producing an accurate derivative at low frequencies.

We calculated the prefit range rate residuals, $\Delta\dot{R}_a$, (being $\dot{R}^s - \dot{R}^b$) and performed the numerical differentiation on $\Delta\dot{R}_a$. This generated a second set of range accelerations, $\Delta\ddot{R}_{nd}$. Figure 5.7 shows the difference between the two methods on a single day (2010-09-01). Here, we found a good agreement between the derived prefit range rate residuals and those calculated analytically from simulated data, with an RMS differences of only 0.04 nm/s^2. The full amplitude of the temporal gravity field is retained in the amplitude spectrum (orange line; Figure 5.7a) with insignificant noise having been introduced at higher frequencies and differences less than 0.4×10^{-9} m/s^2 in the time series (Figure 5.7b).

In summary, numerically differentiating prefit range rate residuals yields prefit range acceleration residuals that are insignificantly different from those generated using the analytical expression in Equation 4.7. Our numerical differentiation of range rate prefit residuals can substitute as a means of generating prefit range acceleration residuals. We adopt our procedure to generate prefit range acceleration residuals from real observations.

5.2.5.3 Prefit range acceleration residuals derived from real data

Range acceleration observations are provided in the Level-1B data for the microwave instrument of the GRACE mission, but they contain a very high level of noise (Tregoning et al., 2017) (blue curve; Figure 5.8a). The difference between the Level-1B range acceleration observations and our range acceleration observations derived using Equation 4.7 therefore contains a very higher level of high-frequency noise above 0.2 Hz. The noise is so large that it obscures the temporal gravity field signal completely in the spatial domain (Figure 5.8c).

To create prefit range acceleration residuals using the Level-1B data, we need to create a range acceleration observation that is not dominated by short wavelength noise. Since we do not have Level-1B observations of the Cartesian accelerations required to compute the range acceleration analytically using Equation 4.7, we calculate the observations by

differencing the observed and our computed range rates, then numerically differentiating the prefit range rate residual as described in Section 5.2.5.2 (orange curve; Figure 5.8a).

We applied this method to the actual GRACE Level-1B data for September 2010. That is, we difference the Level-1B range rate observations from range rates computed from our integrated a priori orbits for this day, then numerically differentiated the difference. It is perhaps not surprising that the amplitude spectrum of these prefit range acceleration residuals contains a higher level of high frequency noise (orange curve; Figure 5.8a) than our simulated values shown in Figure 5.7; however, it is clear that the part of the spectrum that contains the gravity field signal contains similar power to the simulated gravity field for this day (i.e. no signal attenuation has occurred). However, there is a significant reduction in high frequency noise compared to using the Level-1B range acceleration observable. Furthermore, the spatial pattern of signals in our range acceleration prefit residuals (Figure 5.8d) match those created by simulation from the temporal gravity field estimated by Luthcke et al. (2013). This gives confidence that our prefit range acceleration residuals are both realistic and not dominated by noise.

Next, we applied a low-pass raised cosine filter to the prefit range acceleration residuals, using a cutoff frequency of 0.02 Hz. Tapley et al. (2019) showed that 0.03 Hz is the upper limit of the likely signals of the temporal gravity field, so we consider all power in the spectrum above this frequency to be noise. Applying the high-pass filter reduces this noise (green curve; Figure 5.8a,b), leaving a prefit range acceleration residual that can be used with confidence in inversions for the temporal gravity field (Figure 5.8e). The comparison between the different maps, as well as the first 30 minutes of the times series (Figure 5.8b), demonstrates that the noise level of the range acceleration residual after this processing is at the nm/s^2 level.

5.2.5.4 Range acceleration observable reduces north-south striping in gravity field solutions

The practical advantage of using the range acceleration observations, rather than the range rate observations, is that it causes a significant reduction in the presence of north-south stripes in the estimated temporal gravity fields. This occurs because there is a substantial reduction in cross-correlation between partial derivatives relating mascon parameters to the inter-satellite observations when using range acceleration rather than range rate observations.

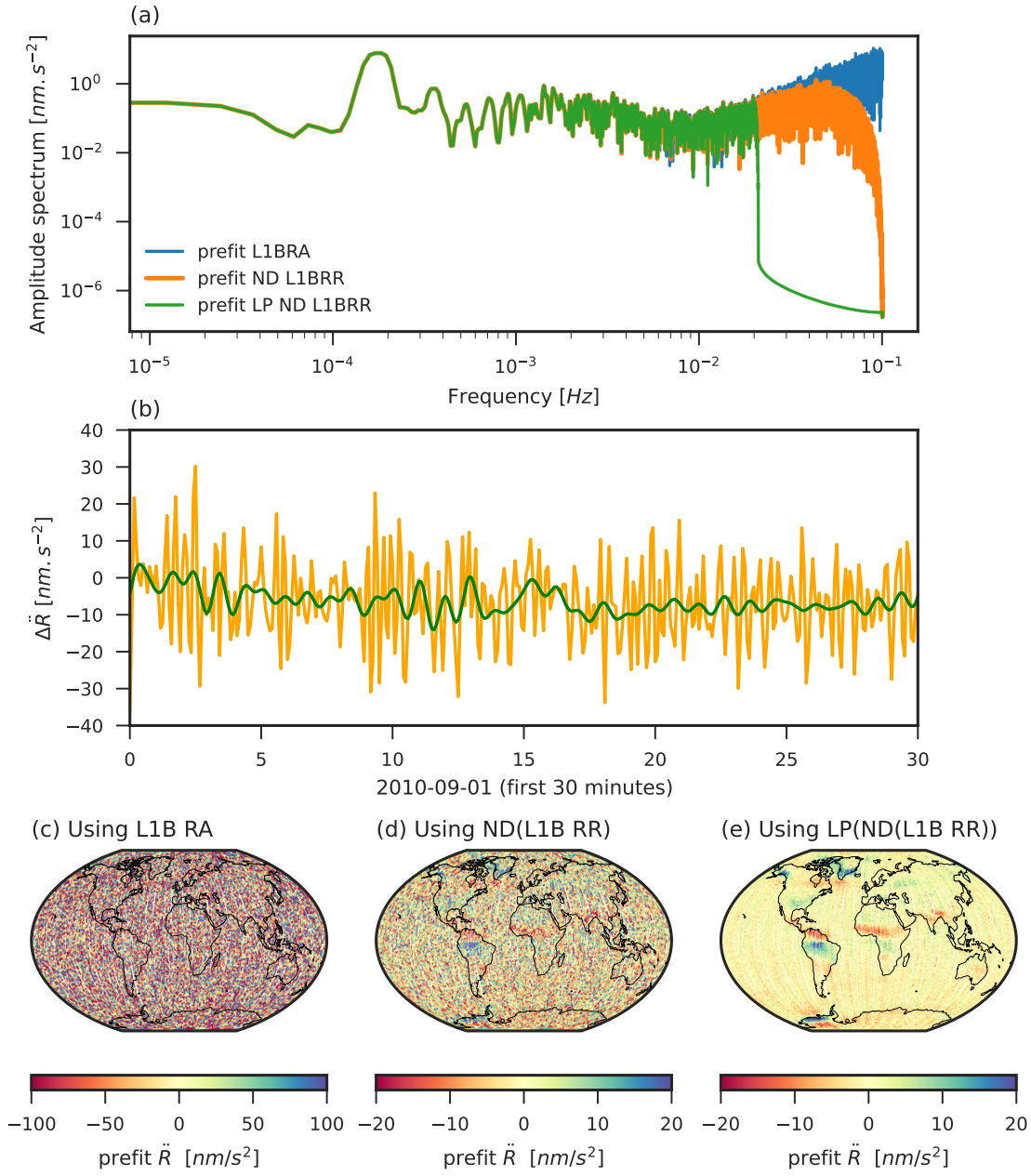

Figure 5.8: (a) Amplitude spectra of range acceleration residuals from GRACE data on 2010-09-01 using values computed using Level-1B range acceleration observations (blue), values derived from the numerical differentiation of the range rate prefit residuals (orange) and values derived from the numerical differentiation of the range rate residual, then low-pass filtering (green). (b) first 30 minutes for range-acceleration residual determined using the numerical differentiation filter (orange) and after applying the low pass filter (green). Spatial distribution of the prefit range acceleration for September 2010 using (c) Range acceleration Level-1B observations, (d) numerically differentiated prefit range rate, and (e) as for (d) but also applying a low-pass filter.

In the inversions, the partial derivatives relating each mascon to the inter-satellite measurements are required (either range rate $\partial RR/\partial mascon_i$ or range acceleration $\partial RA/\partial mascon_i$, where i is the ith mascon number). If one calculates the cross-correlations between these partial derivatives for mascon i and all other mascons then strikingly different spatial patterns are obtained for the range rate and the range acceleration partial derivatives. To illustrate, we calculated the cross-correlations between all mascons and a single randomly selected mascon located in Panama. In the case of the range rate observations (Figure 5.9a), strong north-south striping is present in the cross-correlation pattern. This means that, mathematically, a change in any mascon along the flight path of the satellites passing over mascon i (or a change of opposite sign in mascons beside the flight path) will likely yield a very similar fit to the observations. This explains some of the north-south striping patterns that have been present in GRACE temporal gravity fields since the start of the mission. In contrast, the range acceleration partial derivatives (Figure 5.9b) are much more weakly correlated along track. Indeed, if anything, there is a slight east-west cross-correlation between the partial derivatives but it is much weaker than for the north-south pattern of the range rate cross-correlations.

There is a spike in the partial derivatives of both $\partial RR/\partial mascon_i$ and $\partial RA/\partial mascon_i$ when the satellites pass close to mascon i. The high cross-correlations between range rate partial derivatives stem from the fact that the spike is $< 50\%$ larger than the subsequent once-per-revolution signal induced in the partial derivatives (Figure 5.9c).

That is, the once-per-revolution signal dominates each of the range rate partial derivative time series, which leads to high correlations (or anti-correlations) between partial derivatives of different mascons. On the other hand, the spikes in the range acceleration partial derivatives are around an order of magnitude greater than the associated once-per-revolution signals (Figure 5.9d), meaning that the mass change signals on the ith mascon dominate the partial derivatives and are, therefore, well located spatially. The dominance of the spike signals in the partial derivatives actually breaks the cross-correlations between partial derivatives of different mascons, as evidenced by the much smaller magnitudes of cross-correlations visible in Figure 5.9b.

To demonstrate the effect on a global solution, we used the temporal gravity of September 2010 from Luthcke et al. (2013) to simulate observations, then estimated the temporal gravity field using the range rate or range acceleration as the inter-satellite observable. All other analysis choices were exactly the same in the two solutions. North-South striping is

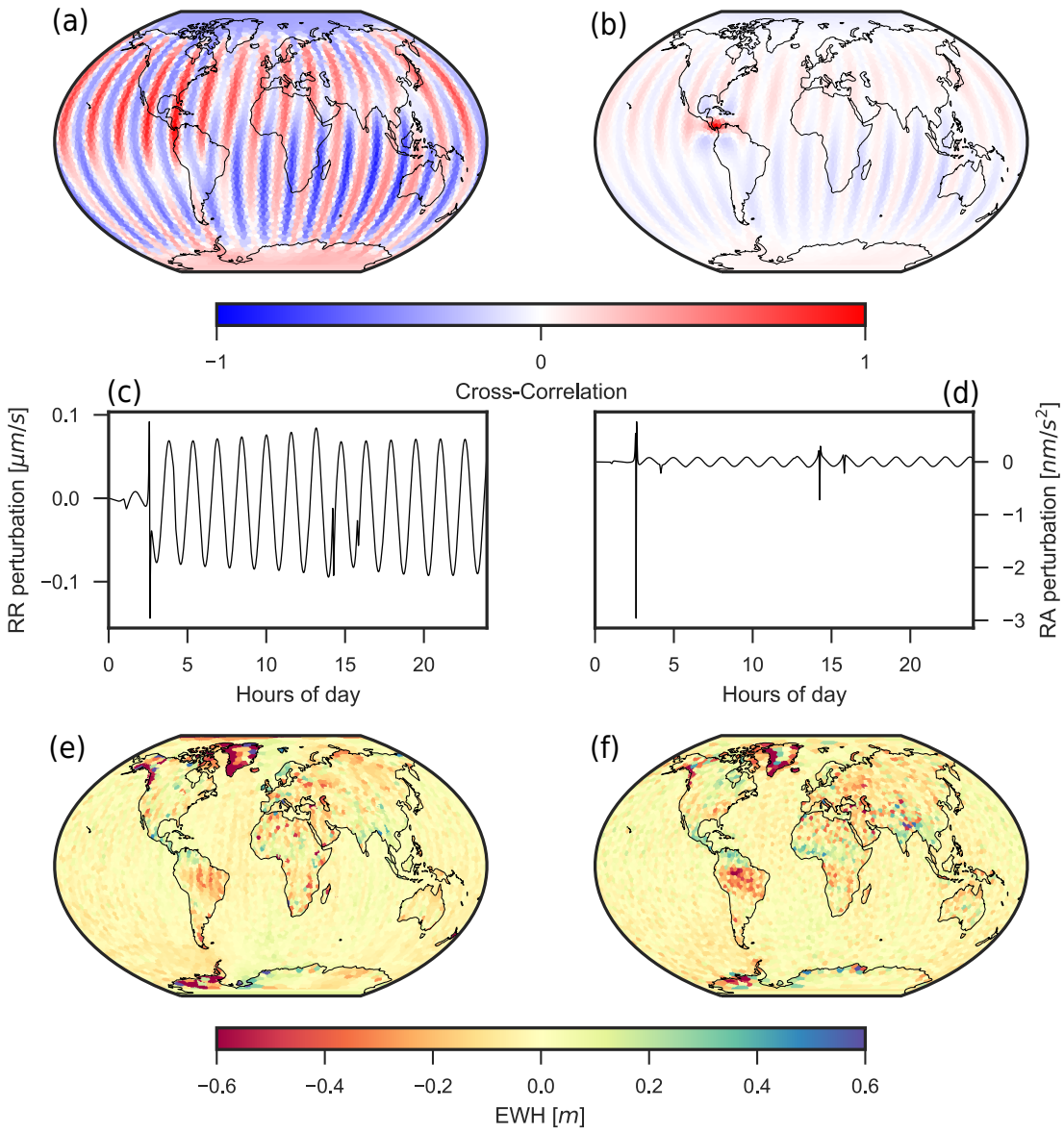

Figure 5.9: Cross-correlations between partial derivatives relating mascon parameters to (a) range rate observations, (b) range acceleration observations. Example time series of these partial derivatives for (c) range rate, (d) range acceleration Note the dominance in the range acceleration partial derivatives of the spike as the satellites pass over the mascon. Estimated temporal gravity fields for September 2010 using (e) range rate observations, (f) range acceleration observations. Note that the north/south striping visible in the range rate solution is significantly reduced in the range acceleration solution.

evident in the range rate solution (Figure 5.9e) but not when using the range acceleration observable (Figure 5.9f). Note that we have not applied any filtering to the temporal gravity field solutions, neither spatial Gaussian filters nor any filters in the frequency domain. While we acknowledge that our range rate solution might be improved by the application of such filters, it is not the focus of this study. Furthermore a "stripe-free" solution can be achieved simply by choosing to use the range acceleration as the inter-satellite observable, without the need for any additional filtering steps.

5.3 Processing workflow and constraints

We have processed the full GRACE Level-1B dataset for the period August 2002 to August 2016.

We parametrise the surface of the Earth in 12,721 mascons of about 40,000 km^2 (roughly 200 km by 200 km, located on the ellipsoid) using the methodology of Tregoning et al. (2022). For the mascon solutions we also adopt an iterative process to refine the loads using basic linear least-squares approach (Tarantola, 2005),

$$x_j = x_{j-1} + (A^T C_D^{-1} A + C_M^{-1} + C_{mass})^{-1} (A^T C_D^{-1} b) \tag{5.10}$$

where x_j are the adjustments to the a priori parameters x_{j-1} for iteration j, A is the design matrix of partial derivatives, C_D is a diagonal weight matrix of the observations, C_M is the constraint (or regularisation) matrix, C_{mass} is the conservation of mass constraint and b is the vector of prefit residuals. Monthly solutions are generated by stacking the normal equations of the daily solutions, which then creates time series of mass changes on each of our mascons.

After each iteration an a priori model of the mascon loads on land is generated by computing an annual variation of the time series of each mascon, plus characterising long-wavelength inter-annual variability as determined using a Butterworth filter with a cut-off period of 2 years. We conserve mass of the system by calculating the integrated change in mass over land and uniformly distributing any excess mass into/out of the ocean to satisfy mass conservation. The a priori model derived from iteration j is then used in iteration $j+1$. The Jacobian matrix A for each iteration is determined by re-integrating the orbits using the mascon estimates obtained from the previous iteration as a priori values. C_D is the covariance on the observation, set to 0.07 m for the positions, 0.07×10^{-3}m/s for the

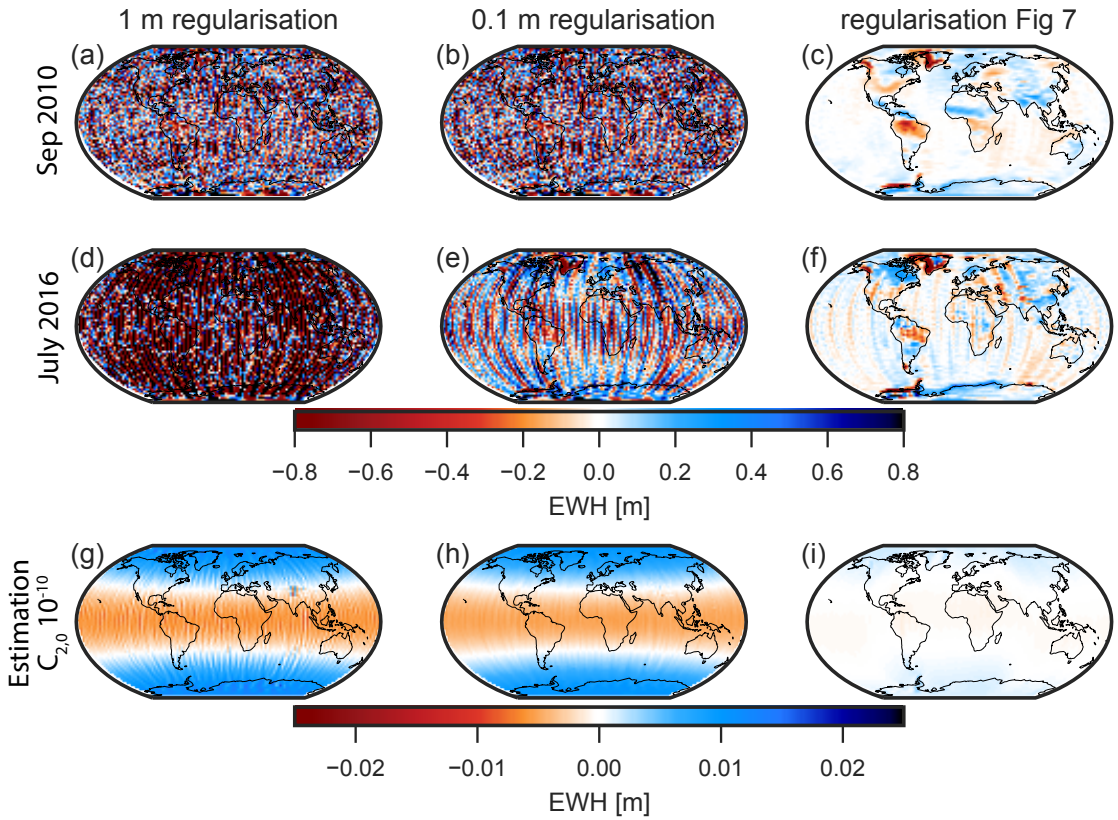

Figure 5.10: Effect of the regularisations Tikonov 1 m (first column), Tikonov 0.1 m (second column) and selected regularisation (last column) for September 2010 (first row), July 2016 (second row), and its ability to recover a $C_{2,0}$ perturbation of 10^{-10}.

velocities, 1×10^{-9} m/s^2 or the range acceleration.

As shown by Save et al. (2016), it is difficult to find and apply a model covariance (C_M) that is tight enough to suppress the noise but sufficiently loose to permit the mascons to adjust to their optimal values. Figure 5.10 shows the impact of regularisation (uniform regularisation at 1 m, 0.1m and tighter variable regularisation) on two monthly solution (September 2010 a-c, July 2016 d-f). Only the tight regularisation is able to suppress the noise in the monthly inversions and, in fact, there is still noise present in the July 2016 estimate.

We use a geographically variable C_M where different values of the uncertainties of the mascons depend on very general a priori knowledge of the hydrological processes in the region. We defined four categories of uncertainty values, 1 cm for the areas with small hydrological variations (most seas, oceans, interior Antarctica), 1.5 cm for continental mascons, 2.5 cm for the Amazon Basin and the Caspian Sea, and a 5 cm is defined for glaciated areas where large variation is expected (Greenland, Alaska, Patagonia, Antarctic

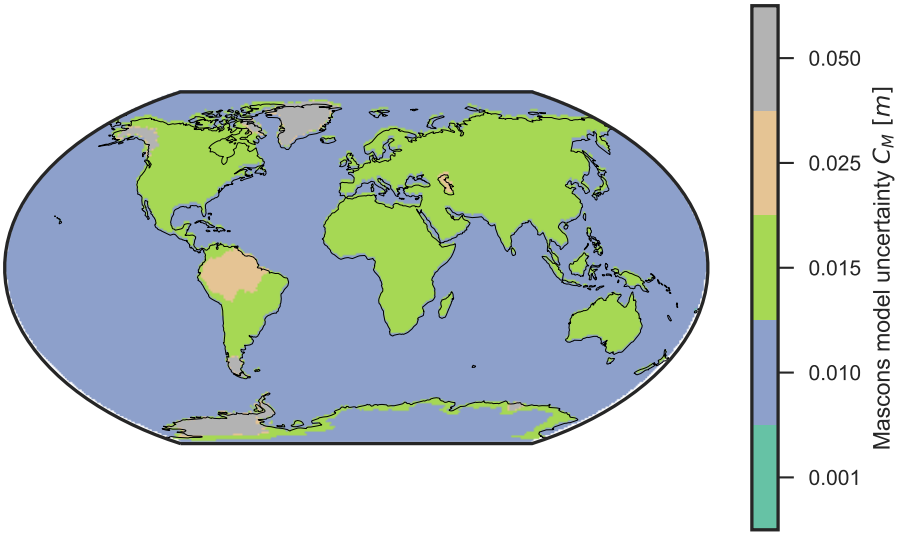

Figure 5.11: Covariance of the model (regularization) used for the mascons in the inversion procedure. The model used is purely diagonal (values in meters).

Peninsula, West Antarctica) (Figure 5.11). The C_{mass} constraint is applied to conserve the mass of the system by adding a condition that the sum of all mass adjustments is equal to zero. While these constraints are tight, as shown is the following section it is possible to estimate signal up to 8 m through this process of iteration. The selection of these values is subjective and was made based on extensive assessments of noise levels in the solutions and whether we could identify any attenuation of signals by the presence of spatial coherence in the postfit range acceleration residuals. Our chosen values suppress the noise in the inversions while not attenuating the signals (see Figure S1 in the Supplementary Material).

To assess how the regularisation might affect the estimation of long-wavelength components of the gravity field, we conducted a simulation where we perturbed the $C_{2,0}$ term of the static gravity field by $1e^{-10}$, then attempted to recover the perturbation by estimating changes using the mascon parameters, using different levels of regularisation. The estimated mass change fields were then converted to spherical harmonics and the estimated $C_{2,0}$ term compared to the perturbation. Using very loose, 1 m Tikhonov regularisation we recover ∼60% of the perturbation (Figure 5.10). However, the estimated temporal gravity field is dominated by noise using this level of regularisation, indicating that stronger regularisation is required. The amount of recovered $C_{2,0}$ signal decreases to ∼50% if the regularisation is tightened to 0.1 m (Figure 5.10) but the mascon estimates

are still dominated by noise. When the tight, spatially variable regularisation is used, we obtain our temporal gravity field estimates but $C_{2,0}$ perturbation is not well recovered at all. Thus, the estimation of $C_{2,0}$ variations from the analysis of GRACE data is strongly affected by the regularisation applied to the mascon parameters.

5.4 Results

To validate our results, we compare our estimates of integrated water changes over specific regions with the RL06 solutions of the Center for Space Research, University of Texas at Austin (CSR) (Save et al., 2016; Save, 2020) and the Goddard Space Flight Center (GSFC) (Loomis et al., 2019a). Differences between the three analysis approaches mean that one should not necessarily expect to find exact agreement between the solutions. The most significant differences are that (a) we use the range acceleration observable, which then requires less filtering/regularisation of the results, and (b) unlike the mascons in the solutions of the other centers, our variable-shaped mas484 con geometry means that our mascons don't cross coastlines or the Amazon drainage boundaries (Tregoning et al., 2022). Our solution has been corrected for $C_{2,0}$ (Loomis et al., 2020), degree 1 (TN13-1 Swenson et al., 2008; Sun et al., 2016b), GIA (Peltier et al., 2018) and AOD1B-GAD product (Dobslaw et al., 2017a). We also compare with our solution corrected only for the GIA to assess the effect of the different corrections.

5.4.1 $C_{2,0}$

Previous analyses of GRACE data have found significant and unrealistic noise in the estimated $C_{2,0}$ coefficients of the temporal gravity field (e.g. Watkins et al., 2005) This has led analysts to replace their estimated $C_{2,0}$ coefficients with values derived from Satellite Laser Ranging (SLR) observations (Watkins et al., 2015; Save et al., 2016). Mascon solutions have also been found to have inaccurate estimates of this long-wavelength component of the temporal gravity field, and Watkins et al. (2015) made a correction of the (implied) $C_{2,0}$ component of their mascon fields by converting to spherical harmonic coefficients, replacing the $C_{2,0}$ terms then converting back to mascons.

We converted our estimated monthly gravity fields to spherical harmonic models, then compared our $C_{2,0}$ coefficient time series with the values derived from SLR observations. Our GRACE-derived $C_{2,0}$ captures the general trend of the SLR observations known as TN-11 (Cheng and Ries, 2017) and TN-14 (Loomis et al., 2020). The largest discrepancy

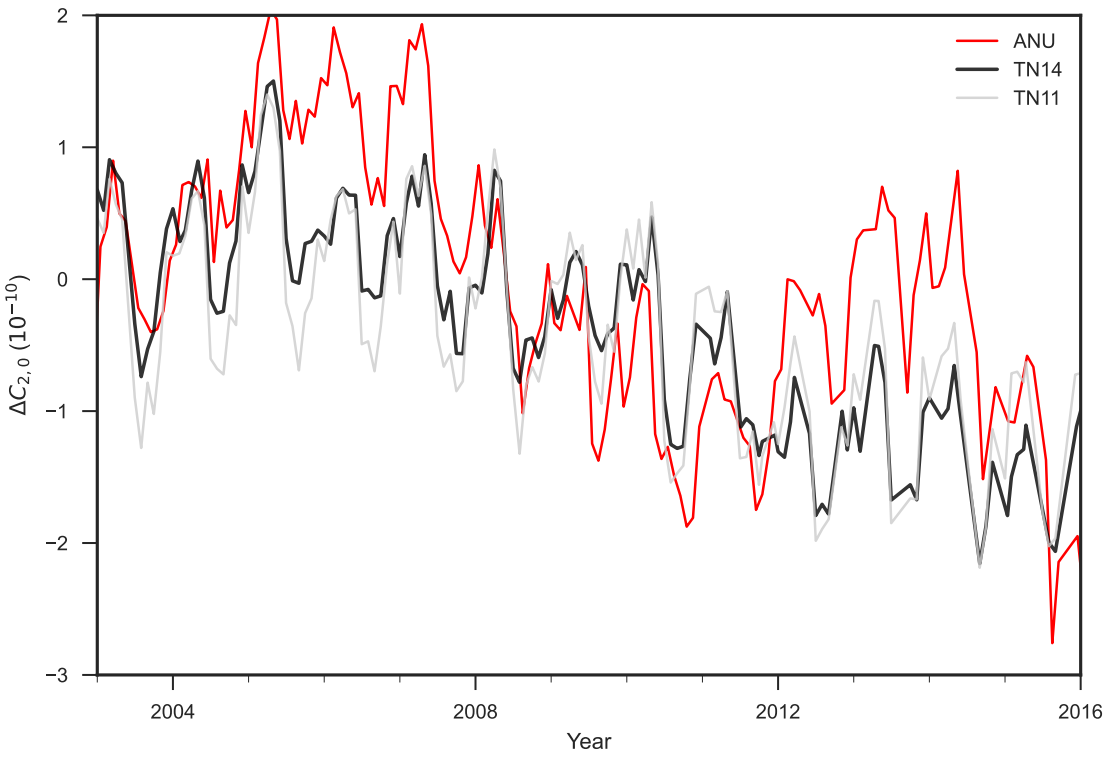

Figure 5.12: Comparison of the $C_{2,0}$ variation from the our GRACE solution with the SLR derived values TN-11 (Cheng and Ries, 2017) and TN-14 (Loomis et al., 2020) relative to their TN-14 mean value of -4.8416945732$\times 10^{-4}$.

occurs around 2006.5; converted to a spatial difference this amounts to around 5 cm of equivalent water height in the polar region. This suggests that there is a need to make a correction to our GRACE mascon solutions to remove errors in out estimated $C_{2,0}$.

5.4.2 Polar ice sheets

One of the major uses of GRACE data is in the quantification of mass loss of the polar ice sheets in Greenland and Antarctica. Our solutions for the integrated change of Greenland are in broad agreement with those of CSR and GSFC, especially in terms of annual variations (Figure 5.13a). Based on a least squares fit over this time period, the trends of mass loss of the different solutions are similar for the GRACE-era (2002.5 to 2016.5): -219.7 $\pm$ 17.4 Gt/year for this study versus -225.7.0 $\pm$ 13.8 Gt/year and -263.1 $\pm$ 14.8 Gt/year for the CSR and GSFC solutions, respectively. The RMS difference between our time series and that of CSR is 852 Gt/year which is of similar magnitude to the difference between CSR and GSFC (700 Gt/year). We see no significant difference between our solution with and without all the corrections ($C_{2,0}$, deg1, GAD) for the time series integrated over

Greenland.

In contrast, in Antarctica (Figure 5.13b) we find that our solutions with and without these corrections adjustments do differ. The corrected time series exhibits a strong seasonal variations which is related to the degree 1 correction. Our integrated Antarctic mass loss signal which include all corrections agrees broadly with the time series of CSR or GSFC (RMS = 202 Gt/year).

5.4.3 Ocean mass change

We summed the change in mass across all our ocean mascons and compare with the GRACE estimate of total mass change in the oceans of CSR and GSFC (Save et al., 2016; Loomis et al., 2019a). Here, there is potentially a significant difference in the two approaches, since our ocean mascons essentially include the entire ocean right to the shoreline around continents, whereas those of CSR and GSFC include mascons that cross the coastline. Save et al. (2016) addressed this by breaking their mascons into smaller ocean and continent components, while Loomis et al. (2019a) used a multi-iteration regularisation strategy to mitigate the leakage of signal. We do not invoke any particular strategy since our mascon geometry correctly locates the signals on continent or ocean, thereby mitigating any signal leakage issue (see Figure 4.8) Tregoning et al. (2022).

All time series (Figure 5.14) have a similar amplitude of annual variation (ANU: 12.6 ± 0.3 mm; CSR: 10.8 ± 0.3 mm; GSFC: 10.3 ± 0.2 mm) and all have a statistically significant acceleration term (ANU: 0.13 ± 0.01 mm/yr^2; CSR: 0.06 ± 0.01 mm/yr^2; GSFC: 0.12 ± 0.01 mm/yr^2), showing broad agreement between the three solutions.

5.4.4 Caspian Sea and Amazon Basin

Finally, we compare two major basins which have been observed previously to have large seasonal variations as well as multi-year, non-linear trends. Here again, one might not expect a high level of agreement between our solutions and those of CSR and GSFC because our mascons are constructed to follow the shoreline of the Caspian Sea (Figure 5.15a) and the drainage divide of the Amazon Basin (Figure 5.15b), whereas the mascons of the other two centres span these natural boundaries. Our integrated time series for the Caspian Sea agrees very closely with that of CSR, whereas that of GSFC has a larger range and slightly larger annual amplitude. In contrast, our annual amplitude for the Amazon Basin (170 ± 5 mm) is about 15% smaller than those of GSFC and CSR (200 ±

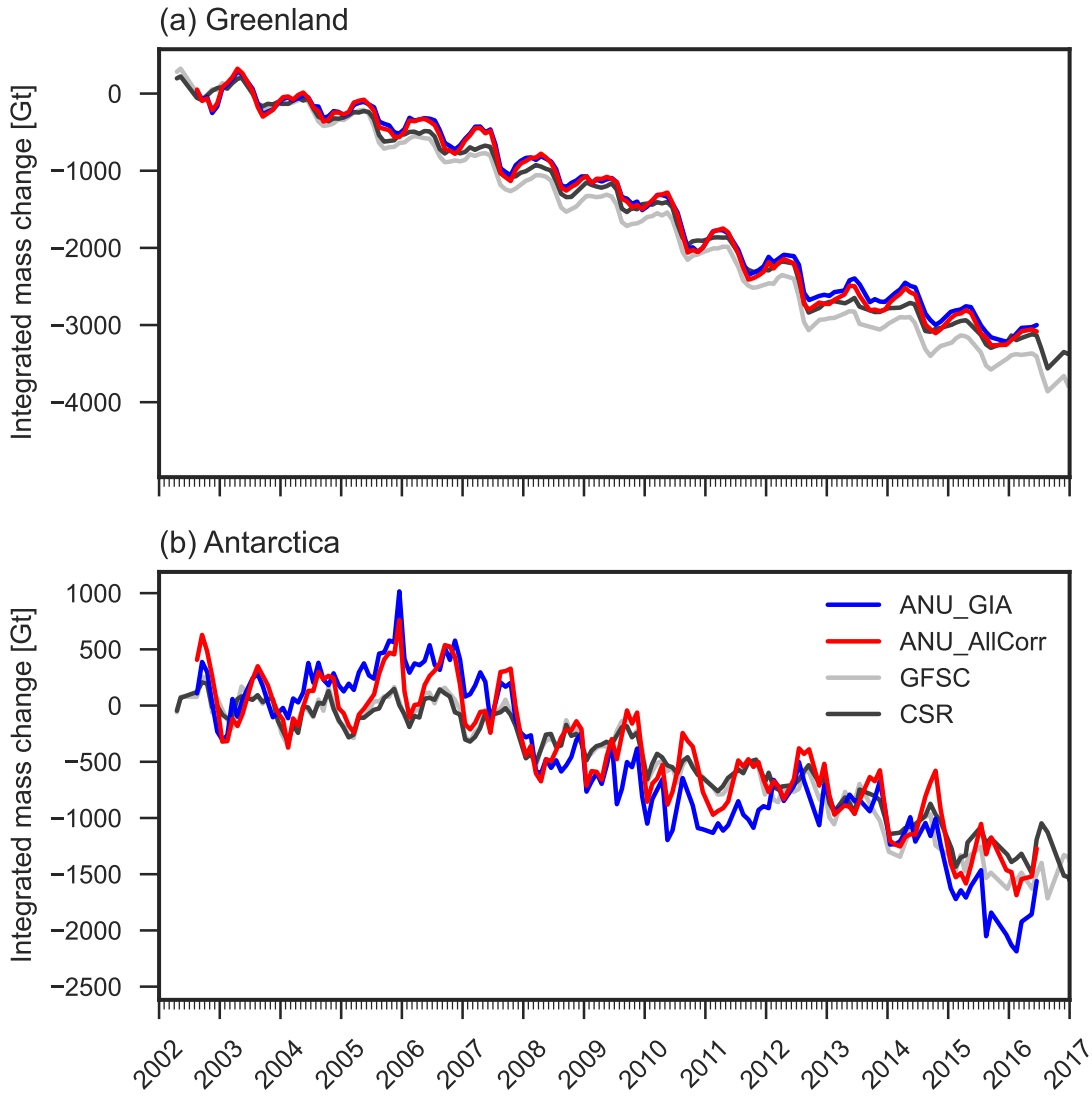

Figure 5.13: Comparison of the integrated mass in gigatons (Gt) over (a) Greenland and (b) Antarctica over the GRACE-era for the ANU time series in blue (our solution), the GSFC mascons solution (grey) and the CSR solution (black). All time series have been demeaned on their 2003 to 2004 average.

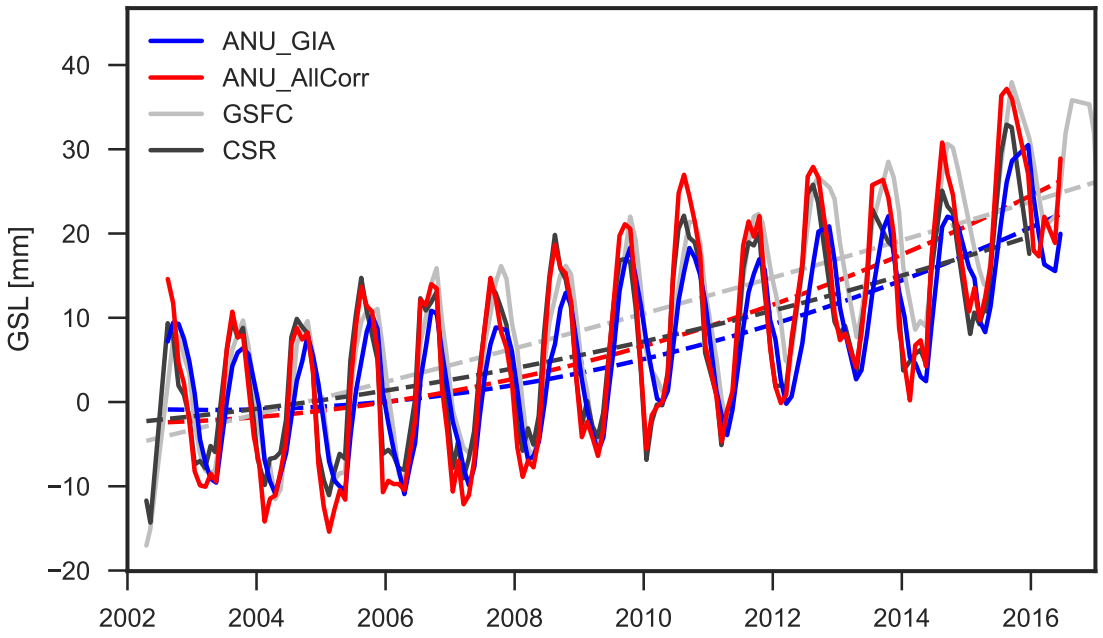

Figure 5.14: Comparison of the variation of the global sea level (GSL) over the GRACE-era from the ANU time series in blue (in red with correction applied), the GSFC mascons solution in grey and the CSR solution in black. All time series have been demeaned on the 2003 to 2004 average. The dashed lines are the polynomial to the second degree.

4 mm and 195 ± 5 mm respectively). No significant difference is seen between any of the solutions in terms of long-term trend of total water storage change in the Amazon Basin.

5.5 Conclusions

The range acceleration observable can be used to estimate accurate temporal gravity fields from GRACE data; however, the very high levels of high-frequency noise in the Level-1B range acceleration observations cause significant errors in gravity field estimates. We reduced the noise through a combination of a maximally flat derivative filter and a low-pass filter of range rate residuals, without attenuating the gravity field signals themselves. When converted to spherical harmonics, the C2,0 coefficients of our monthly mass anomaly fields agree broadly with the independent SLR estimates although the estimates are affected by the choice of regularisation. We therefore replace the $C_{2,0}$ in our mascon solution with the TN-14 SLR estimate. The resulting mass anomalies compare well with other mascon estimates, both in terms of spatial pattern and temporal evolution in both continental and oceanic environments. The observed differences can be attributed to the different processing methodology and definition of the mascons geometry (c.f. our com-

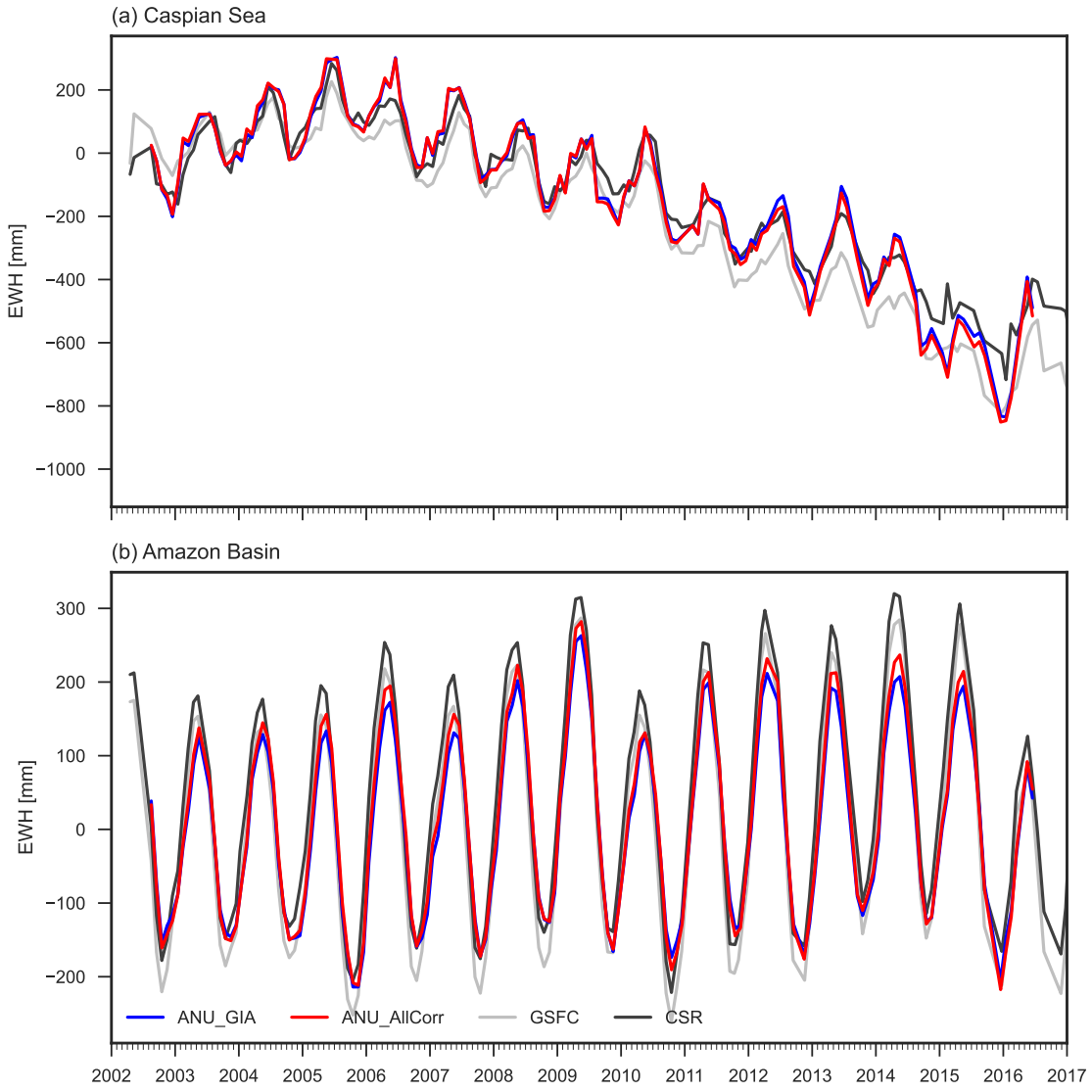

Figure 5.15: Comparison of the integrated mass in mm of equivalent water height over (a) the Caspian Sea and (b) the Amazon Basin over the GRACE-era from the ANU time series (blue, red with the $C_{2,0}$ correction), the GSFC mascons solution (grey) and the CSR solution (black). All time series have been demeaned on their 2003 to 2004 average.

panion manuscript Tregoning et al. (2022)). With the successful launch of the GRACE Follow-On mission in May 2018, including a more accurate laser to measure the inter-satellite range, the use of range acceleration observations offers the potential to improve significantly the recovery of the temporal gravity field.

Chapter 6

Interplay of altitude, ground tracks, noise and regularisation on resolution

The ability to accurately estimate the Earth's gravity field is improved when satellite measurements are made at lower altitude. Consequently, the spatial resolution of the estimated gravity field may improve as the altitude of the GRACE satellites decreased throughout the mission. However, as the satellites descended, they passed through periods of orbit resonance, during which time the GRACE satellites repeatedly observed the same strips of the Earth's gravity field, resulting in sparse ground track coverage. This decreased the ability to accurately estimate spatially small fluctuations in the temporal gravity field. This chapter explores the trade-offs between satellite altitude, ground track coverage, observation noise and regularisation on the spatial resolution of the GRACE gravity fields. Under simulation conditions using realistic noise on the observations, we find that small (i.e. $\sim$150 km $\times$ 150 km) regularised mascons produced the most accurate estimates of a known high-resolution temporal gravity field. The accuracy of the gravity field estimates are not substantially affected by resonant orbits but are significantly improved with decreased orbit altitude. This chapter is based on the manuscript submitted to the Journal of Geophysical Research - Solid Earth:

McGirr, R., *Tregoning, P., Allgeyer, S., McQueen, H., and Purcell, A. P. (2022) Interplay of altitude, ground track coverage, noise and regularisation on the spatial resolution of GRACE gravity field models. Journal of Geophysical Research: Solid Earth, submitted March 5, 2022.*

I made the following contributions to this paper:

- Developed the methodology for quantifying the numerical stability of the temporal gravity field using GRACE/GRACE-FO observations
- Generated and interpreted the time series of condition numbers from the GRACE and GRACE-FO time series
- Created four additional mascon fields (Section 6.4.1) used to test the impact of orbit altitude and ground track coverage on the accuracy of the estimated solutions in simulation
- Reconfigured each of the mascon fields to reduce the impacts of problematic mascon geometries that degrade the gravity field estimates (See Chapter 3)
- Created the synthetic temporal gravity field based on Dobslaw et al. (2015) which was then used to simulate satellite position/velocity observations
- Developed a method to add real GRACE observation noise to simulated prefit residuals which included computing unfiltered postfit residuals from GRACE temporal gravity field models (Section 6.4.3)
- Conceived the study, processed all the data and interpreted the results for all simulation studies (Section 6.5)
- Wrote the text and created all of the figures for this manuscript

Abstract

Models of the temporal gravity field derived from space gravity missions are typically produced with monthly temporal resolution and ∼300 km spatial resolution. However, variations in instrument performance and altitude of the Gravity Recovery and Climate Experiment (GRACE) mission impact the spatial resolution that can be achieved month-to-month. As the altitude of the orbits of the twin spacecraft vary throughout the mission, so does the ability of the observations to recover certain components of the temporal gravity field. Reduced altitude intensifies the gravity signals acting on the satellites, thus the potential spatial resolution of GRACE observations should increase as the altitude decreases throughout the mission. From simulations using actual GRACE altitude and ground track coverage and realistic noise levels, we found this predicted influence of the altitude of the satellites on the accuracy of the estimated solutions. However, while solutions with larger mass concentration elements (mascons) are more numerically stable as the satellite altitude decreases, they suffer from greater error caused by inability to properly represent spatial variations of signals within mascons, referred to as intra-mascon variability. Mascons as small as ∼150 km × 150 km reduce the intra-mascon variability and, with appropriate regularisation, yield the most accurate solutions, especially during the low-altitude periods in the latter years of the GRACE mission. Importantly, the use of mascon regularisation prevents degradation of solutions during resonant orbit months. This was further enhanced during the 31/2 resonance of February 2015 because of the lower altitude of the GRACE satellites.

6.1 Introduction

Over a period of 15 years, the Gravity Recovery And Climate Experiment (GRACE) satellite mission was used to observe the Earth's mean and time-variable gravity field with unprecedented spatial and temporal resolution and accuracy (Tapley et al., 2004, 2019). The success of the GRACE mission led to the launch of the GRACE Follow-On (GRACE-FO) mission in May 2018 which continues to observe the Earth's gravity field. The GRACE-FO satellites are largely replicas of their predecessors, but with the addition of a Laser-Ranging Interferometer (LRI) which measures with significantly improved precision the inter-satellite range using a laser link in parallel with the Microwave Instrument (MWI) system (Sheard et al., 2012; Abich et al., 2019). Temporal gravity field solutions produced by several processing centres using GRACE and GRACE-FO observations have mapped the trends and fluctuations of the surface and subsurface components of the Earth's hydrosphere and within the solid Earth (e.g. Luthcke et al., 2013; Dahle et al., 2014; Watkins et al., 2015; Save et al., 2016; Allgeyer et al., 2022).

The ability to accurately model the Earth's temporal gravity field from satellite gravity observations is dependent on, amongst other things, the orbital configuration of the satellites. Both GRACE and GRACE-FO missions were launched to an altitude of ∼490 km with an along-track separation of 220 km ± 50 km in near-circular polar orbits Tapley et al. (2004). Because gravitational signal fluctuations attenuate with distance from the source, the contribution of high-frequency spatial variations to the Earth's gravitational potential are better observed by satellites in low-Earth orbits. A near-circular orbit is a common choice for geodetic missions because it allows for a (roughly) uniform influence of the Earth's gravitational field on the satellites (Wagner et al., 2006). Polar orbits allow for global coverage of satellite ground tracks (being the projection of a satellite's orbit onto the surface of the Earth).

Typically, the ground tracks of the GRACE satellites evenly covered the Earth's surface every ∼30 days, permitting the generation of global gravity models with a surface spatial resolution of ∼300 km at monthly temporal scales (e.g. Tapley et al., 2004). More specifically, the spatial resolution of GRACE observations not only varies throughout the mission but also globally as a function of latitude (Wahr et al., 2006) because of the the polar orbit of the GRACE satellites. The altitude of the GRACE satellites' (in height above the surface of the Earth) decreased throughout the mission, causing the orbital elements of the satellites' to change, which affected the ground track patterns. In addi-

tion to temporal variations in instrument performance and background model accuracy, the quality of a given GRACE solution is also influenced by the geometry of the satellite orbits during that month.

To obtain temporal gravity field models that have homogeneously high spatial resolution globally, the satellite ground tracks need to be distributed uniformly over the Earth's surface so that all of the components of the gravity field may equally affect the satellites at all epochs. The increased ground track coverage at high latitudes generally improves the spatial resolution of the gravity field estimates away from the equator (Wahr et al., 2006). This increases the spatial resolution of high-frequency variations at locations where some of the most significant mass anomalies are observed (i.e. polar ice sheets), but decreases the spatial resolution at low latitudes where the largest variations in terrestrial water storage occur (i.e. the Amazon Basin).

The orbital elements of the GRACE satellites varied throughout the mission. By the mission's end, the satellite orbits had decreased by ∼160 km to an altitude of ∼330 km, at which time the satellites would have been more than twice as sensitive to high-frequency gravity field variations compared to the beginning of the mission. As the satellites descended throughout the GRACE mission, periods of significantly reduced ground track coverage occurred occasionally due to orbit resonance (Wagner et al., 2006; Visser et al., 2012; Klokočník et al., 2015). A resonant orbit (also referred to as a repeat orbit) occurs when the Earth's rotational period and the satellites orbital period become proportional and their ratio is composed of two co-prime integers (Vallado, 2001). Under such conditions and when the integers are small, the GRACE satellites repeatedly observed the same strips of the Earth's gravity field, leaving large gaps between ground tracks, particularly at low- to mid-latitudes, thus decreasing the spatial resolution of the temporal gravity field model that can be accurately estimated (Wagner et al., 2006).

The spatial resolution of gravity field models from satellite observations is also partly dependent on the processing strategies used to generate the mass anomaly estimates required to cause the observed GRACE inter-satellite range changes. GRACE and GRACE-FO temporal gravity field models are typically represented as either a spherical harmonic expansion (e.g. Lemoine et al., 2007; Save et al., 2012; Mayer-Gürr et al., 2014) or as mass anomalies on tiles of known area, known as mass concentration elements (mascons) (e.g. Rowlands et al., 2005; Luthcke et al., 2006a; Rowlands et al., 2010; Save et al., 2016; Tregoning et al., 2022). GRACE/GRACE-FO spherical harmonic and mascon estimates

of the temporal gravity field are both affected by instrument and model errors which manifest spatially as north-south stripes. These errors are mitigated through regularisation constraints and/or post-processing techniques (e.g. Wahr et al., 1998; Swenson and Wahr, 2006; Save et al., 2016). Regularisation and post-processing techniques (i.e. smoothing and decorellation filters) are effective at mitigating truncation artifacts, north-south stripe errors and high-frequency noise, but are likely to attenuate the signal amplitudes (e.g. Chen et al., 2009a; Landerer and Swenson, 2012; Wiese et al., 2016).

The use of mascons in GRACE processing has been shown to better mitigate many of the errors encountered with spherical harmonic solutions, such as north-south striping and leakage of signals across coastlines (Save et al., 2016; Loomis et al., 2019a; Tregoning et al., 2022). Monthly solutions of the temporal gravity field have been produced using mascons at a range of different shapes and sizes (e.g. Luthcke et al., 2013; Watkins et al., 2015; Save et al., 2016). However, the spatial resolution of a GRACE mascon solution of the temporal gravity field is not necessarily equivalent to the size of the individual mascons used. For example, Save et al. (2016) and Loomis et al. (2019a) used 1° mascons, but highlighted that their monthly mascon solutions are still limited by the fundamental spatial resolution of the GRACE measurements (i.e. ∼300 km).

The constraints applied to the mascons during inversion of the data must be tight enough to mitigate the impacts of model and instrument errors, but loose enough to not attenuate the estimates of the mass change signals (Save et al., 2016). Regularisation may also increase the correlations between neighboring mascons (Loomis et al., 2019a), decreasing the spatial resolution of the estimates. Some have attempted to optimise their regularisation strategy to account for latitude dependent spatial resolution due to variations in ground track density. For example, following the error analysis of GRACE spherical harmonic solutions (Wahr et al., 2006), Loomis et al. (2019a) adopted a latitudinally (and regionally) varying regularisation scheme, applying looser mascon constraints towards the poles where ground track coverage is most dense.

The impact of reduced ground track coverage due to orbit resonance throughout the GRACE mission on the spatial resolution of the spherical harmonic estimates of the derived gravity field estimates (e.g. Wagner et al., 2006; Visser et al., 2012; Klokočník et al., 2015). In contrast, while it is well known that the altitude of the GRACE satellites changed significantly throughout the mission, to our knowledge, there are not yet studies of the impact of altitude decay on the resolution of the temporal gravity field generally

throughout the GRACE mission. Many studies have, however, investigated the possible increase in spatial resolution that could be achieved in future satellite gravimetry missions with lower orbital altitudes (e.g. Loomis et al., 2012). Given that lower orbit altitudes increase orbital sensitivity to variations in the temporal gravity field, it is possible that the spatial resolution of GRACE models might be inversely correlated with satellite altitude, (assuming equivalent levels of instrumental noise and background modelling error throughout the mission).

In this study we assessed the interplay and trade-offs of five variables, being the orbit altitude, ground track coverage, mascon size, observation noise and regularisation and how it effects mascon solutions of the temporal gravity field. We analysed several months of GRACE measurements taken at a range of altitudes and ground track coverage. We quantified the numerical stability of each month of GRACE and GRACE-FO data using the singular value decomposition (SVD) of the normal equations of monthly solutions and analysed the mascon parameter uncertainties. From a simulation of noise-free observations, we estimated the temporal gravity field with various mascon resolutions and regularisation strategies using GRACE orbits at various altitudes and with different ground track patterns. We then repeated this analysis with observations containing realistic noise on the inter-satellite observations and quantified the impact of noise on the recovery of the simulated temporal gravity field. We found that the most numerically stable solutions are generated using large mascons from observations obtained at low altitudes with high ground track coverage. However, at low orbit altitudes and in the presence of intra-mascon variability, smaller regularised mascons produced the most accurate estimates regardless of observation noise level or ground track coverage.

6.2 Methods

In this study, we investigated the impacts of orbit altitude decay and ground track coverage variability on the numerical stability of the linear system throughout the GRACE and GRACE-FO records. We refer to this numerical stability measure as the "observability" of the temporal gravity field. This was achieved by solving for monthly mass anomalies via a weighted least squares inversion of GRACE and GRACE-FO observations and analysing the eigenvalues associated with each month's normal equations matrix. Below we provide information on how these approaches were applied.

6.2.1 Orbit and gravity field estimation

Following Allgeyer et al. (2022) and Tregoning et al. (2022), the temporal gravity field (i.e. departures of mass from the static gravity field) is represented on roughly equal-area 200 km × 200 km (∼40,000 km^2) irregular-shaped coastline-following mascons. The mass change of each mascon is expressed in Equivalent Water Height (EWH) as a plate across each mascon. This is directly related to the accelerations acting on the satellites via explicit partial derivatives. Our solutions were generated by first computing 24-hour orbits for each of the twin satellites via an integration of the accelerations calculated from observations and models of the gravitational and non-gravitational forces acting on the spacecraft (see Table 1 of Allgeyer et al. (2022)). We solve for the temporal gravity field by estimating adjustments ($\hat{x}$) to the initial satellite orbital parameters (i.e. position, velocity, accelerometer calibration scale factors and biases per axis) for each 24-hour orbit and a monthly mass anomaly for each mascon using a weighted least squares inversion:

$$\hat{x} = (A^T W A + C_{mass} + C_M)^{-1} A^T W b \tag{6.1}$$

where A contains the explicit partial derivatives relating the observations to the parameters, W is a diagonal observation weight matrix, b contains the prefit residuals (the difference between the inter-satellite range acceleration observations and the theoretical values computed from the integrated orbits), C_{mass} is a constraint matrix for conservation of mass and C_M is a diagonal regularisation matrix. Weights were assigned to the observations of 70 mm, 70 um/s and 1 nm/s^2 for position, velocity and range acceleration, respectively (Allgeyer et al., 2022). The regularisation constraints are geographically variable, for example, larger uncertainties were assigned to regions where more signal variation is expected (i.e. glaciated polar regions, the Amazon basin, the Caspian Sea). This is discussed further in Section 6.4.2.

6.2.2 Singular Value Decomposition

We investigate the inherent numerical stability of the least squares inversion by analysing the eigenvalues associated with the monthly weighted normal equation matrix (i.e. $A^T W A$) which contains the weighted partial derivatives of the observations with respect to the parameters. We use the properties of the Singular Value Decomposition (SVD) to determine the "observability" of the gravity field, which depends on the quality and quantity of the observations (Klema and Laub, 1980). Previous studies have used a similar

method to assess the conditioning of GRACE spherical harmonic problems, particularly during periods of orbit resonance (e.g. Wagner et al., 2006; Pini, 2012).

The SVD is a factorisation of any real $m \times n$ matrix, M, into its corresponding eigenvalues and eigenvectors:

$$M = U\Sigma V^T \tag{6.2}$$

where Σ is a diagonal matrix which contains the square root of the eigenvalues (i.e. the singular values), σ_i, of MM^T and M^TM in descending order. U and V are orthogonal matrices that contain the eigenvectors of MM^T (i.e. the left singular vectors) and M^TM (i.e. the right singular values), respectively (Klema and Laub, 1980).

M is rank deficient (i.e. singular), and therefore not invertible, if any of the singular values are zero. Practically, M is unlikely to be formally rank deficient, but rather numerically deficient. The rank, r, of M is the number of singular values greater than some tolerance (i.e. double precision floating-type machine epsilon). M is rank deficient if it contains singular values that are so close to zero that they cannot be accurately inverted. Determining how conditioned (i.e. how accurately invertible) a linear system is can be achieved through an analysis of the singular values of M via the calculation of the condition number, k (being the ratio of the largest σ and smallest σ). A low condition number (i.e. $k = 1$) is well-conditioned, while large condition numbers are associated with ill-conditioned problems.

Given the properties of the SVD (Klema and Laub, 1980), we take the square root of the singular values, contained in Σ, of the monthly weighted normal equation matrix (i.e. A^TWA) to approximate the singular values of A. This is not a perfect representation of the singular values of A, as incorporating observation weights into the normal equations alters the results, however, the relative singular values still accurately represent the changing "observability" of the temporal gravity gravity field throughout the GRACE/GRACE-FO record.

6.3 Condition numbers throughout the GRACE/GRACE-FO record

The monthly normal equations were generated using the method of Allgeyer et al. (2022), as outlined in Section 6.2.1, using the ∼200 km × 200 km irregular-shaped coastline-

following mascons as the basis functions (see Figure 4.3) (Tregoning et al., 2022). The condition number, k, is the ratio of the largest and smallest singular values of the A matrix. An ill-conditioned linear system, which corresponds to a large condition number, will experience large changes in the solution in the presence of small perturbations (i.e. noise), whereas, the solution to a well-conditioned linear system, which corresponds to a small condition number, is more numerically stable. Thus, that the temporal gravity field solution for a month with a relatively high condition number would be more sensitive to instrumental or background model errors due to the reduced "observability" of the temporal gravity field which causes the linear system to be numerically unstable.

The condition numbers vary throughout the GRACE mission due to the changing orbital elements of the twin spacecraft, which can be thought of as a function of average orbit altitude and ground track coverage (Figure 6.1). The average altitude of the GRACE satellites decayed slowly from ∼490 km at launch to ∼460 km by January 2011 at a rate of ∼0.3 km/month (Figure 6.1). During the second half of the GRACE mission, the orbits decayed at a rate of ∼1.65 km/month, reaching an average orbital altitude of 335 km by July 2017. Using the 5-second Earth-fixed positions provided in the GPS Navigation Level-1B data, we define "ground track coverage" for each month using the proxy of the number of times each mascon was flown over by the satellites within a month, then computed the percentage of mascons ($n = 12754$) that were flown over at least once.

Over the GRACE record where all mascons were overflown (i.e. 100% or "complete" ground track coverage), the condition numbers decrease logarithmically with altitude (Figure 6.1). Condition numbers were an order of magnitude higher at the beginning of the mission than at the end and remained relatively stable until 2011, when orbit decay accelerated. The GRACE-FO satellites lost altitude at a much slower rate (∼0.04 km/month) during the beginning of the mission (from launch until December 2021) compared to GRACE (Figure 6.1). Consistently high ground track coverage (i.e. >99%) led to the condition numbers remaining relatively stable throughout the available GRACE-FO record. As expected, GRACE-FO condition numbers are mostly consistent with the condition numbers of the GRACE mission at comparable altitudes with complete ground track coverage. However, the condition numbers are slightly increased from 2019 to 2021 due to an extended period of somewhat less-than-complete ground track coverage (i.e. <100%).

Visible variations in the condition number time series mostly occur during periods

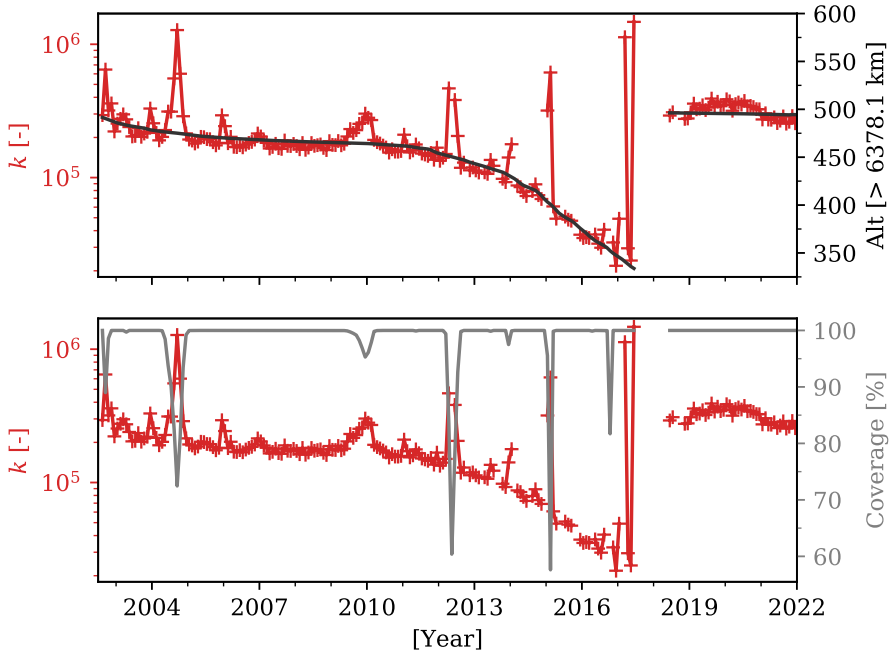

Figure 6.1: Condition numbers, k, throughout the GRACE and GRACE-FO record (red) compared to (top) GRACE-A average altitude (black) and (bottom) ground track coverage (grey) as a percentage of the 200 × 200 km mascons overflown by the GRACE-A satellite over each month.

when the GRACE satellites passed through short repeat cycle orbits. A repeat orbit is referred to as an R/D repeat where R and D are co-prime integers that denote the number of orbital revolutions that the satellites complete within the repeat period in days, respectively (Wagner et al., 2006). The smaller the values of R and D, the sparser the ground track pattern, especially at the equator.

The condition numbers peak during critical repeat orbits during September 2002 ($R/D = 76/5$), September 2004 (61/4), December 2009 (107/7), May 2012 (46/3), December 2013 (77/5) and February 2015 (31/2). The largest condition number for the entire time series is September 2004, during the 61/4 repeat orbit when orbit altitude was still near insertion levels (∼475 km). The condition number for this month is a magnitude larger than months with complete ground tracks at similar altitude (Figure 6.1). A 46/3 repeat occurred during May 2012, however too few Level-1B records are available during this period and so Allgeyer et al. (2022) did not produce a temporal gravity field solution for this month. However, condition numbers increased substantially as the orbits approached and exited resonance during April and July 2012.

The most significant orbit resonance occurred in February 2015 during a 31/2 repeat, where just over 57% of the ∼200 km × 200 km mascons were overflown. During this

period the average altitude of the orbits had already decreased to ∼400 km. The increase in condition number due to orbit resonance is more than a magnitude greater than the condition numbers for months with complete ground track coverage at similar altitudes.

Other notable condition number deviations occurred near December 2009 due to the long-lasting 107/7 repeat. Reduced ground track coverage occurred for 9 months as the satellites passed through the orbit resonance, degrading the condition numbers from July 2009 to March 2010. Condition numbers are also particularly variable between the 2002 and 2004 repeat orbits despite near-complete ground track coverage. This is due to the satellites passing through many resonant orbits with larger repeat periods. Increased condition numbers also occur intermittently between early 2006 and early 2007 for the same reason.

Towards the end of the GRACE mission, the K-Band Ranging (KBR) system was switched off multiple times per day and resulted in many days of incomplete inter-satellite observations. Consequently, the number of observations for many months, particularly during the final year of the mission, were reduced due to incomplete data records. This is reflected in the instability of the condition numbers towards the end of the GRACE record (Figure 6.1) due to the reduced "observability" of the temporal gravity field over large portions of the Earth. The "observability", using condition number as a proxy, is therefore contingent on variations in orbit altitude, ground track pattern and the number of available Level-1B records during a month of GRACE observations (Figure 6.1).

Decreased observability of the temporal gravity field has been previously noted in the GRACE spherical harmonic coefficient uncertainties and Root Mean Square (RMS) of the ocean signal (e.g. Dahle et al., 2019; Kvas et al., 2019; Chen et al., 2022). These results show that the numerical stability of the spherical harmonic solutions varies as the satellites passed through resonant orbits and periods of reduced KBR records throughout the GRACE record. These results are consistent with our GRACE and GRACE-FO condition number time series (Figure 6.1), using 200 km × 200 km mascons as the basis functions (Allgeyer et al., 2022).

6.4 Spatial resolution simulation study

The size of the mascons also impacts the "observability" of the temporal gravity field. We simulated several months of satellite observations made at varying orbit altitudes and ground track patterns and generated the normal equations. We then analysed the

mascon estimation errors and parameter uncertainties as a function of latitude, altitude and ground track coverage. The accuracy of the temporal gravity field estimates from simulated data was then analysed as a function of orbit altitude, ground track coverage, mascon size, regularisation and observation noise. The following subsections detail the simulation procedure.

6.4.1 Mascon field generation

Four irregular-shaped, coastline-following mascon fields, composed of roughly 100 km × 100 km, 150 km × 150 km, 250 km × 250 km and 300 km × 300 km primary mascons were used, in addition to the 200 km × 200 km mascon field of Allgeyer et al. (2022) (we refer to them as, for example, "200 km" mascons hereafter). We used the same procedure as Tregoning et al. (2022) to generate our mascon fields whereby small (18 × 18 km) regular-shaped ternary mascons are aggregated to create irregular-shaped primary mascons that followed coastlines. The mass change on each primary mascon (in terms of EWH) was estimated on the topographic surface for land primary mascons and at sea level for ocean primary mascons using the mascons of sizes shown in Table 6.1. Our five mascon fields span the range of mascon sizes (i.e. from 3° to 1°) that have been previously used to generate mascon solutions of the GRACE and GRACE-FO mass anomaly time series at a monthly temporal resolution (e.g. Luthcke et al., 2013; Watkins et al., 2015; Save et al., 2016; Loomis et al., 2019a; Allgeyer et al., 2022).

Table 6.1: Size, Root Mean Square (RMS) of intra-mascon variability (IMV) and equivalent spherical harmonic degree (L_{MAX}) of each mascon field and regularisation properties used in simulations.

Mascon Geometries				
Mean width (km)	Area (km^2)	Total mascons	RMS IMV (mm)	Equivalent L_{MAX}
∼300	∼90,000	5,647	69.22	60
∼250	∼62,500	8,150	61.62	72
∼200	∼40,000	12,754	56.45	90
∼150	∼22,500	22,765	47.49	120
∼100	∼10,000	51,083	34.24	180
Mascon regularisation				
	Ocean (m)	Land (m)	Ice sheets (m)	Glaciers (m)
Loose	0.05	0.1	0.2	0.2
Tight	0.01	0.015	0.05	0.05

In terms of spherical harmonics, our mascon solutions are approximately an equivalent maximum degree and order (L_{MAX}) 60 expansion for our lowest resolution (300 km) up to 180 for our highest resolution (100 km) mascon fields (Table 6.1). Spherical harmonic

solutions of the GRACE and GRACE-FO monthly temporal gravity fields are routinely provided by several processing centres at $L_{MAX} = 60$ and $L_{MAX} = 96$ as Level-2 data products as part of the shared Science Data System (SDS) (Save et al., 2012; Watkins and Yuan, 2012; Dahle et al., 2019). However, Watkins and Yuan (2012) only provided $L_{MAX} = 60$ spherical harmonic solutions as their maximum resolution for months that are impacted by reduced observability due to limited ground track coverage. Save et al. (2012) and Dahle et al. (2019) suggested that more aggressive post-processing strategies might be required to mitigate increased errors due to noise entering the estimates of the poorly observed high degree coefficients.

6.4.2 Recovering simulated signals

To perform the simulations, we created a high resolution "truth" temporal gravity field to be recovered, based on the Earth system model of Dobslaw et al. (2015). Their model represents high spatial and temporal resolution mass variations via dimensionless stokes coefficients up to degree and order 180. Mass variations due to terrestrial water storage, cryospheric variability and solid Earth deformation were included, temporally averaged over a month (i.e. we do not include sub-daily high-frequency mass changes). We chose to use their last epoch, being December 2006, which contained the highest magnitude signals (i.e. $\sim$3 m EWH mass loss in polar regions). A mass change signal was assigned to each of our land ternary mascons, setting the ocean ternary mascons to zero (see Figure 4.5) (Tregoning et al., 2022).

As per Tregoning et al. (2022) and Allgeyer et al. (2022), we integrated two sets of 24-hour orbits per satellite, which we refer to as the "a priori" and "truth" orbits. Only the "truth" orbits include the accelerations induced by the "truth" temporal gravity field represented on the ternary mascons. Therefore, the two sets of orbits for each day only differ by the accelerations induced by the "simulated truth" temporal gravity field which we aim to recover from the least squares inversion (Equation 1). Position and velocity "observations" were computed from the "truth" orbits which were used to generate the simulated inter-satellite range rate measurements that include the effects of the known temporal gravity field model Tregoning et al. (2022). We selected several months of GRACE observations obtained at a range of orbit altitudes, characterised by complete and repeat ground tracks to simulate (Table 6.2).

We calculated prefit range rate residuals (the difference between observations from

the "truth" and "a priori" orbits) then numerically differentiated them to generate the prefit range acceleration residuals, used as the inter-satellite observable (Allgeyer et al., 2022). Given that no perturbations were applied to the satellite parameters, the prefit range acceleration residuals should only contain the accelerations induced by the simulated temporal gravity field. Normal equations were formed for each day, then stacked by month (Table 6.2) and inverted to solve for the monthly mean mass anomalies in terms of EWH for each primary mascon, along with estimated adjustments to the satellite parameters per 24-hour orbit, as per Section 6.2.1.

Every month of GRACE observations used in the analysis and the average orbital altitude of the satellites' during that month are listed in Table 6.1, each of which is characterised by 100% ground track coverage over the 200 km × 200 km mascons. The months of observations were sampled at 15-30 km intervals of average altitude, from 485 km in December 2002 to 360 km in August 2016, covering the range of average orbit altitudes for the majority of the GRACE mission. Most of the months selected fall during the second half of the mission since that is when most change in altitude occurred.

Table 6.2: Months used in simulations.

Altitude decay simulations			
Month	Ground track coverage (%)		Altitude (km)
2002-12	100		485
2008-01	100		465
2012-12	100		442
2014-03	100		423
2015-04	100		395
2016-01	100		371
2016-07	100		357
Repeat orbit simulations			
Month	Ground track coverage (%)	R/D	Altitude (km)
2004-02*	100	N/A	476
2004-09	72.5	61/4	474
2015-04*	100	N/A	395
2015-02	57.6	31/2	401

*Complete ground track month compared to repeat month.

The numerical stability of the stacked normal equations were assessed for each month by analysing its singular values and rank. From the inverted unregularised normal equations (i.e. $(A^T W A)^{-1}$), we extracted the formal uncertainties of the mascon parameters, being the square root of the parameter variance. These uncertainties were then analysed as a function of mascon size, satellite altitude and mascon latitude. The performance of each simulation was determined by assessing the errors in the estimated temporal gravity

field solutions, being the difference between the estimated mascons and their "true" value.

By estimating a single mass change parameter per primary mascon, we make the assumption that the mass change is homogeneous within a primary mascon, despite the "truth" temporal gravity field including intra-mascon variability (the deviation of ternary mass anomalies from the mean primary mascon values; see Table 6.1) (Tregoning et al., 2022). Thus, when intra-mascon variability is present in the simulated temporal gravity field signal, the mascon parameterisation can no longer perfectly represent the spatial pattern of mass change. Tregoning et al. (2022) identified that the presence of intra-mascon variability induced other errors (i.e. inter-mascon leakage) in their temporal gravity field estimates from simulated observations.

Constraints must be applied to mascon parameters when inverting real GRACE and GRACE-FO observations to mitigate the effects of instrumental and model noise on the temporal gravity field estimates (e.g. Save et al., 2012; Loomis et al., 2019a). Tregoning et al. (2022) demonstrated through simulation that regularisation is also necessary to reduce errors induced by intra-mascon variability. Following Tregoning et al. (2022), we constrained the mascon parameter adjustments by applying two levels of geographically varying regularisation; "loose" and "tight" (Table 6.1). The different values used for the mascon uncertainties are based on a very general a priori knowledge of the hydrological processes in the region, such that regions characterised by large seasonal hydrology signals are less tightly constrained compared to oceans, for example. The regularisation matrix is a diagonal matrix; therefore, we do not enforce correlations between neighboring mascons.

6.4.3 Adding noise to the simulations

The GRACE and GRACE-FO measurements contain instrumental noise (i.e. accelerometer noise, star camera noise and KBR system noise), as do the background models used during orbit integration (Wahr et al., 2006). These errors are a considerable source of noise in the GRACE and GRACE-FO models of the temporal gravity field. For various reasons, the performance of GRACE instrumentation and systems varied throughout the mission, which led to increased levels of error during the first two years in orbit and during the second half of the mission (Landerer et al., 2020). To maintain optimal instrument performance, the variability of the internal temperature of the satellites was kept to a minimum via a network of sensors and heaters. However, the thermal control system was switched off in April 2011 due to power constraints (Herman et al., 2012) which increased

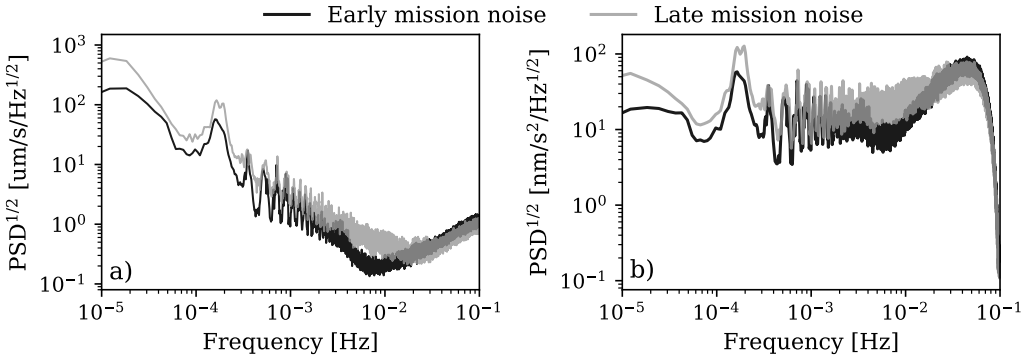

Figure 6.2: Average PSD of January 2008 (early mission noise; black) and January 2016 (late mission noise; grey) postfit (a) range rate residuals and (b) range acceleration residuals, calculated from Allgeyer et al. (2022).

the occurrence of spurious signals in many of the observations (Landerer et al., 2020). Instrumental noise was at a minimum between 2004 and 2010, producing the most accurate, low-error gravity field solutions from GRACE data (Landerer et al., 2020).

Synthetic models of GRACE/GRACE-FO instrumental noise and background model errors have previously been used to perturb the satellite parameters in simulation (e.g. Loomis et al., 2012). Because it is difficult to accurately simulate real mission errors (Croteau et al., 2020), we introduced noise into our simulations from an assessment of postfit residuals derived from an analysis of real GRACE observations. The postfit residuals contain the part of the observations that the temporal gravity field model parameterisation failed to fit. Assuming there is no attenuation of the estimated temporal gravity field signal, the postfit residuals provide a proxy for instrumental noise, background model error and errors in the parameter estimates. By inter-satellite observations using noise from analysis of real GRACE data found in the postfit residuals, we are able to make use of realistic GRACE errors while also introducing a synthetic signal to be estimated.

We calculated the daily range rate and range acceleration postfit residuals with respect to the monthly temporal gravity mascon solutions of Allgeyer et al. (2022) for two months; January 2008 and January 2016. These months were chosen to represent the noise characteristics during the thermally controlled half of the mission when errors were at a minimum (i.e. early mission noise; Figure 6.2; black) and during the final years of the GRACE mission when internal thermal variations led to increased instrument noise (i.e. late mission noise; Figure 6.2; grey). To generate the range rate and range acceleration observation noise, we averaged the spectral content of the daily unfiltered postfit residuals for each month. We preserved the magnitude of the averaged postfit residuals but

randomised the phase component of the signal then converted the magnitude and phase spectra into a time series of ranging measurements representing realistic inter-satellite observation noise. Prior to solving for the parameter adjustments, the synthetic range rate and range acceleration noise was added to the prefit residuals of the inter-satellite observations. The prefit inter-satellite observations are otherwise dominated by signals induced by the known simulated temporal gravity field.

This method makes several assumptions with regard to the signal content of the postfit residuals generated from the monthly temporal gravity field solutions of Allgeyer et al. (2022). First, we assume that the postfit residuals do not contain attenuated gravity signals, which is supported by the lack of geographically correlated signals in the range acceleration postfit residuals (Allgeyer et al., 2022). Second, that at least the majority of instrumental noise and background errors are in fact discarded as postfit residuals and not absorbed by the parameterisation. The range acceleration postfit residuals of Allgeyer et al. (2022) are within the GRACE noise level, consistent with Save et al. (2016). We therefore assume that the postfit residuals of Allgeyer et al. (2022) provide a realistic assessment of GRACE noise.

6.5 Results

6.5.1 Altitude decay and mascon resolution

To identify the impact of orbit altitude on the accuracy of temporal gravity field estimation we simulated observations at various altitudes and solved for adjustments to mascon parameters using five different resolutions of irregular-shaped mascon grids as the basis functions (Table 6.1). Our selected seven months of GRACE observations at various orbit altitudes (Table 6.2) are characterised by dense (i.e. complete) ground track coverage (e.g. Figure 6.3a) to eliminate (as much as possible) the impact of ground track pattern on the "observability" of the linear system. That is, we isolated average orbit altitude and mascon size as the two independent variables to be tested for numerical stability and accurate recovery of the high-resolution "truth" simulated temporal gravity field. In the following subsections, we present the variations in numerical stability of the normal equations and mascon parameter uncertainties as a function of mascon size, orbit altitude and latitude. This is followed by an analysis of the temporal gravity field estimates (noise-free and in the presence of instrument and model noise).

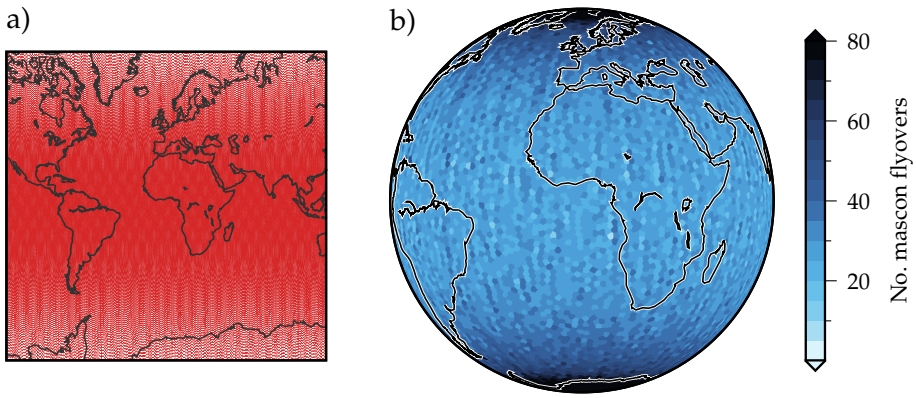

Figure 6.3: Typical non-repeat month (March 2014) of GRACE satellite orbits (a) producing complete ground tracks with complete coverage of the Earth. (b) Number of times each 200 km × 200 km primary mascon was overflown by the satellites during the month, showing increased flyovers at high latitudes.

6.5.1.1 Numerical stability of the mascon solutions

We performed SVD on the stacked weighted normal equations, which contain the weighted partial derivatives of a month of observations with respect to the parameters, and calculated the condition number of their singular values. The temporal gravity field was parameterised using each of the different resolution mascon fields (Table 6.1) as the basis functions. The condition numbers decrease with decreasing altitude and the number of mascon parameters to be estimated (Figure 6.4a). That is, the normal equations are most invertible (i.e. well-conditioned) with larger mascons, towards the end of the mission when the GRACE satellites were in a lower orbit. The normal equations using 300 km and 200 km mascons at high altitude (485 km) are as well-conditioned as those using 200 km and 150 km mascons at low altitude (357 km), respectively. This suggests that, by the end of the GRACE mission, the temporal gravity field estimates could have twice the spatial resolution compared to those at the beginning of the mission.

There is a limit on how small the mascons can be before the inversion of the normal equations will become numerically unstable. Rank deficiency of the weighted normal equations matrix occurs at different mascon resolutions for different altitudes (Figure 6.4b). All of the stacked normal equations are full rank when estimating the larger 300 km, 250 km and 200 km mascons. The 150 km mascon normal equations range from ∼80% to 100% rank (being the percentage of linearly dependent columns), becoming full rank at orbit altitudes lower than ∼400 km. All of the 100 km mascon normal equations are rank deficient, ranging from ∼35% to ∼60% at the highest and lowest orbit altitude, respectively. Regularisation can be used to help to invert a rank deficient or ill-conditioned

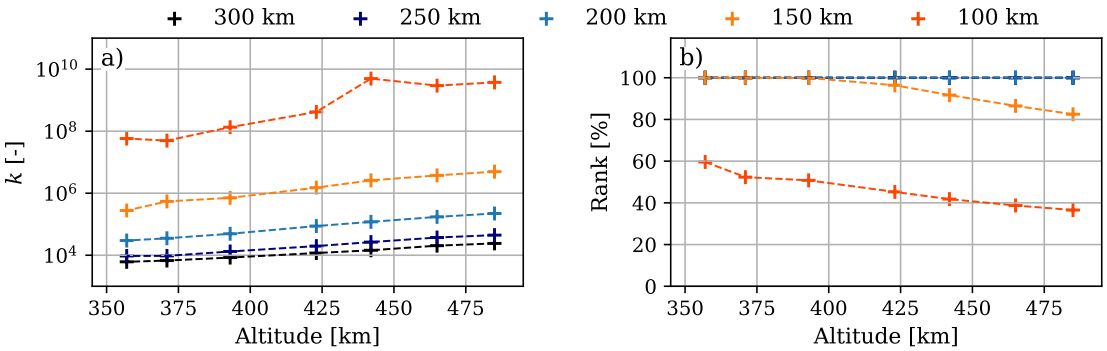

Figure 6.4: Analysis of monthly stacked weighted normal equations (Table 6.2) using five mascon resolutions (Table 6.1) (a) condition number, k, of the weighted normal equations (b) rank as the percentage of linearly dependent columns of the weighted normal equations.

problem by adding information to the normal equations to improve the numerical stability of the inversion and this is discussed in Section 6.4.2.

Polar orbits create ground track spacing that vary latitudinally, such that they have significantly decreased ground track coverage at mid- to low-latitudes and denser ground track coverage at high latitudes (Figure 6.3b). To assess the impact of ground track coverage on solution accuracy, we analysed the behaviour of unregularised mascon parameter uncertainties as a function of latitude. We calculated the RMS of the mascon parameter uncertainties (σ) within 10° latitudinal bands from the $(A^T W A)^{-1}$ (Figure 6.5). Similar to the condition numbers, the RMS uncertainty is predictably smallest for 300 km mascons and decreases with altitude for all mascon resolutions (Figure 6.5). These results indicate that, given perfect noise-free data, an inversion of fewer mascon parameters produces the most accurate estimate of the temporal gravity field, if the signal to be recovered contains no intra-mascon variability.

As expected and irrespective of mascon size, the highest error appears at mid- to low-latitudes, where ground track coverage is the least dense. The latitude-dependent mascon parameter uncertainties increase significantly with decreasing mascon size (Figure 6.5). A cross-section through the 0°-10° latitude band for each mascon field (e.g. pink dashed line; Figure 6.5a) shows that the RMS mascon uncertainty decreases with lower altitude and with larger mascons (Figure 6.5d). For example, at 485 km orbit altitude the RMS uncertainty for 100 km mascons is ∼650,000 mm RMS compared to ∼130 mm RMS for 300 km mascons (Figure 6.5d). A cross-section through 425 km orbit altitude (e.g. yellow dotted line; Figure 6.5a) demonstrates that the polar regions consistently contain the lowest RMS uncertainty. For example, the polar latitude band contains on average

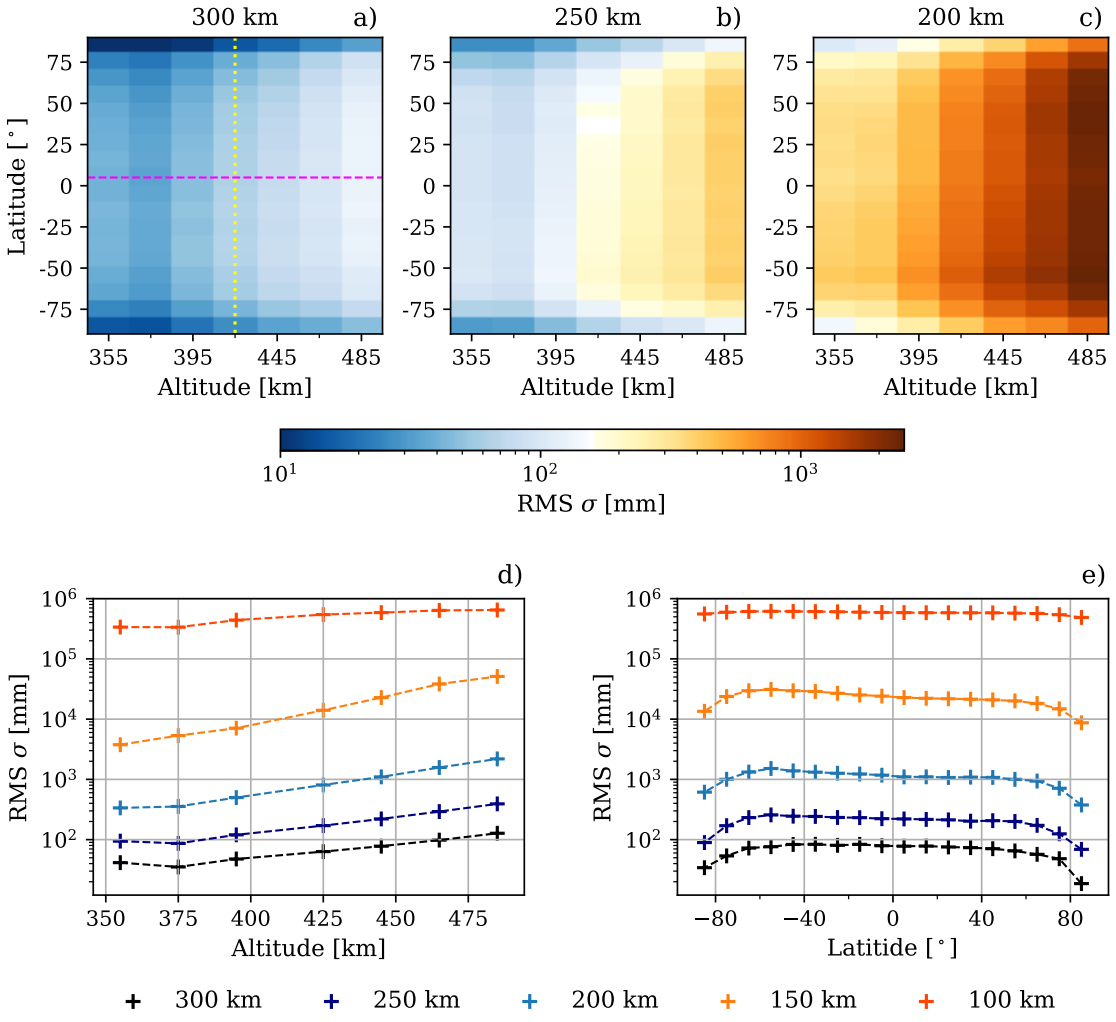

Figure 6.5: RMS of the mascon parameter uncertainties (σ) from unregularised monthly stacked weighted normal equations (Table 6.2) as a function of latitude and satellite altitude. (a) 300 km, (b) 250 km, (c) 200 km. (d) Variation of RMS σ as a function of altitude taken along a cross-section through the 0°-10° latitude band (pink dashed line) and (e) as a function of latitude taken along a cross-section through 425 km orbit altitude (yellow dotted line).

78% and 20% less RMS uncertainty compared to the mid- to low-latitude bands for the 300 km and 100 km mascons, respectively (Figure 6.5e).

Previous studies (e.g. Loomis et al., 2019a; Croteau et al., 2020) have utilised a latitudinally varying regularisation scheme under the assumption that higher spatial resolution occurs at high latitudes, as suggested by the error analysis of GRACE spherical harmonic solutions (Wahr et al., 2006). Our analysis agrees with Wahr et al. (2006), that mascon uncertainties are inversely correlated spatially with ground track density. Furthermore, we found that this holds for all of our mascon resolutions (Figure 6.5). However, the uncertainties also have a temporal component, varying significantly with changes in altitude throughout the GRACE mission.

6.5.1.2 Noise-free temporal gravity field recovery

When the signal to be recovered from simulated noise-free observations represents a realistic high-resolution temporal gravity field, the accuracy of the solution is limited by both the numerical stability of the normal equations and the intra-mascon variability of the "truth" signal (see Table 6.1) (Tregoning et al., 2022). Simply assessing the quality of a solution from an analysis of the numerical stability of the normal equations and/or the unregularised parameter uncertainties (Figure 6.4) is not an adequate approach. These methods do not account for the parameter constraints, the actual observations which contain the effects of intra-mascon variability or any post-processing procedures. Therefore, we analysed the quality of the solutions produced from simulated noise-free observations using different mascon resolutions and assessed the error content of the actual mascon parameter estimates under different levels of regularisation.

The RMS error of the unregularised 300 km and 250 km mascon solutions barely changes with altitude, the average RMS error for both is 86 mm, which is mostly accounted for by the RMS intra-mascon variability (80% and 72%, respectively, being the ratio of RMS intra-mascon variability and total RMS error) (black, navy; Figure 6.6a). The RMS errors of the 200 km solutions are more obviously impacted by altitude with RMS intra-mascon variability accounting for 70% RMS error at low altitude, decreasing to 58% at high altitude (blue; Figure 6.6a). The RMS error of the 150 km solutions vary significantly as a function of altitude with RMS intra-mascon variability accounting for 21% RMS error at low altitude, decreasing to 5% at high altitude (orange; Figure 6.6a). This is because the 150 km mascon normal equations are far more numerically stable at lower altitudes

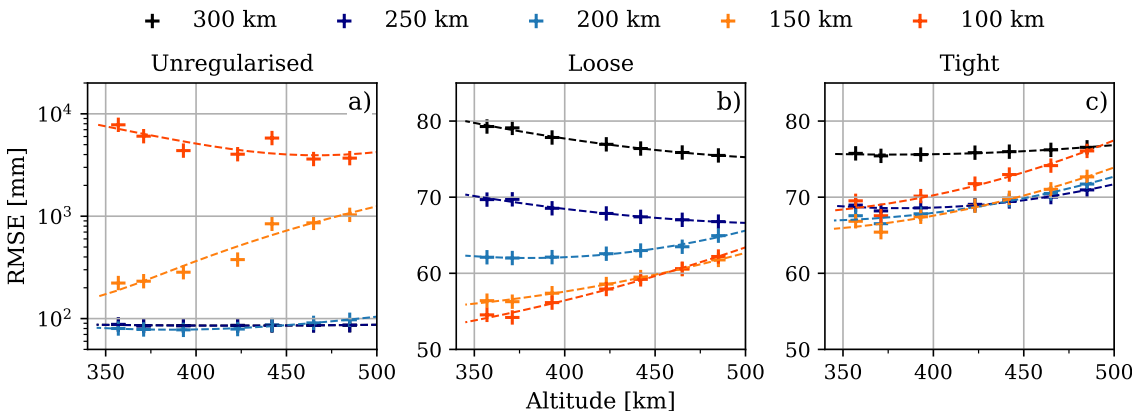

Figure 6.6: RMS Error (RMSE), being the difference from the "truth" temporal gravity field and the monthly mascon estimates from simulated noise-free observations (Table 6.2) using five mascon resolutions (Table 6.1). (a) Unregularised, (b) loosely regularised and (c) tightly regularised. Lines of best fit (quadratic) are shown as visual aids.

than at high altitudes (Figure 6.5). The RMS error of the 100 km solutions increases with decreasing altitude, unlike the other solutions (red; Figure 6.6a). The low altitude solutions contain more high-frequency errors, particularly at mid- to low-latitudes (not shown), despite the normal equations being more numerically stable (Figure 6.4), which seems counter-intuitive.

When the mascon parameters are loosely regularised, high-frequency errors due to numerical instability of the normal equations are reduced and the quality of the mascon estimates become mostly limited by the intra-mascon variability (Figure 6.6b). Therefore, smaller mascons are generally better able to represent the temporal gravity field signal compared to larger mascons because the intra-mascon variability is reduced (Table 6.1). The RMS error of the smaller mascon solutions (i.e. 200 km mascons and smaller) decreases with decreasing satellite altitude, with the 100 km showing the most altitude-dependent RMS error variance. This is because, at low altitudes, the solutions are less impacted by upward continuation of the gravity signal and are more numerically stable (Figure 6.6b). The same is true for the 250 km and 300 km mascon solutions (Figure 6.6b), however, due to increased intra-mascon variability, at low altitudes the large mascon solutions are more impacted by the leakage of large continental signals (i.e. West Antarctica and Greenland mass loss) into the adjacent ocean areas (Tregoning et al., 2022). As a result, the RMS error of the larger mascons increases with decreasing altitude (Figure 6.6b).

When the mascons are tightly regularised, the accuracy of the large mascon solutions (i.e. 250 km and 300 km) are only marginally improved by decreased altitude and are

mostly limited by the intra-mascon variability, explaining ∼90% of the RMS error (Figure 6.6c). Because the ocean mascons have been constrained so tightly (10 mm), the leakage of signal across coastlines is less limiting on the solution accuracy, although, still apparent. The accuracy of the smaller mascon solutions (i.e. 200 km mascons and smaller) again increases significantly with decreasing altitude (Figure 6.6c). When the solutions are tightly constrained, the 100 km mascon solutions are more in error than all of the other mascon resolutions (with the exception of the 300 km solution) irrespective of satellite altitude (Figure 6.6c). Similar behaviour is observed under loose regularisation where the 150 km mascon solutions outperform the 100 km mascon solutions at high altitudes (>450 km) (Figure 6.6b).

Applying tight regularisation to poorly conditioned problems (i.e. small mascons at high altitude) increases inter-mascon leakage and signal attenuation, causing the solution accuracy to no longer benefit from decreased intra-mascon variability (Figure 6.4). For example, at ∼425 km altitude, the RMS error of the tightly constrained 250 km, 200 km and 150 km mascon solutions intersect (Figure 6.6c). Below this altitude, the smaller mascon solutions benefit from the ability to represent the high-frequency spatial variations of the synthetic temporal gravity field. Whereas at altitudes above the intersection point, the smaller mascons are less well-observed and more susceptible to signal attenuation due to the upward continuation of the gravity signal. A similar behaviour is observed under the loose regularisation where, by extrapolation, the RMS error of the three mid-sized mascon solutions would have intersected at ∼525 km had the GRACE satellites orbited at higher altitudes (Figure 6.6b). Thus, the mascon resolution likely to produce the solution least in error is dependent on both the altitude of the satellites and the strength of the mascon constraints.

With noise-free observations, it is possible to tailor the regularisation to each mascon parameterisation, stabilising the inversion just enough to prevent high-frequency errors due to numerical instability, but not so tight as to cause significant signal attenuation or inter-mascon leakage. Therefore, when the temporal gravity field is known a priori and with perfect observations, the best solution (i.e. lowest RMS error) is achieved using the smallest mascons (loosely regularised, 100km mascons; Figure 6.6b). However, GRACE instruments and background models contain considerable noise; therefore, a tight regularisation scheme may be required to adequately mitigate their impact on the accuracy of the parameter estimates. For example, if the noise level required that the mascons be

constrained using our tight regularisation scheme, the 100 km mascons would likely produce one of the highest error solutions due to the susceptibility of small mascons to signal attenuation under regularisation (Figure 6.6c). So, to minimise the solution error, the chosen mascon parameterisation and regularisation strategy must also take into account measurement and background model error.

6.5.1.3 Temporal gravity field recovery in the presence of noise

Instrument and background model noise require that the mascon solutions be tightly constrained so that meaningful estimates of the temporal gravity field can be produced using real GRACE measurements (e.g. Save et al., 2016; Allgeyer et al., 2022). The conclusions outlined in Section 6.5.1.2 are not changed in any significant way with the addition of measurement and model noise to the simulations. Generally speaking, the RMS of the mascon errors are shifted higher when the observations contain late mission noise compared to early mission noise under any of the regularisation schemes tested here (Figure 6.7). The unregularised solutions contain the highest errors, followed by the "loosely" regularised solutions and the "tightly" regularised solutions (Figure 6.7). The RMS errors of the tightly regularised solutions in the presence of early mission noise (Figure 6.7c) are very similar in magnitude and altitude variance to the tightly regularised noise-free simulations (Figure 6.6c). Compared to the noise-free solutions, the increased RMS errors of the regularised solutions containing either noise level is mostly due to increased spatially incoherent errors in the mascon parameter estimates.

In simulation, if the mascon constraints are not strong enough to mitigate the impact of noise on the observations, the accuracy of the temporal gravity field estimates is increased with orbit altitude, which is counter-intuitive (Figure 6.7b,e). Under loose regularisation, the 100 km mascons (red; Figure 6.6b) produce the best solution at every altitude, however, this level of regularisation is not adequate in the presence of either early or late mission noise. In fact, almost any mascon field (except 300 km mascons in the presence of early mission noise) will produce a better solution under tight regularisation (Figure 6.6c,f). Overall, when the observations contain noise, the solutions least in error are the tightly regularised 150 km mascons (orange; Figure 6.7c,f).

Once the choice of mascon constraints is appropriate for the noise level contained in the observations, the accuracy of the temporal gravity field estimates increases with low orbit altitude (Figure 6.7c,f). Generally, the accuracy of the solutions also becomes more

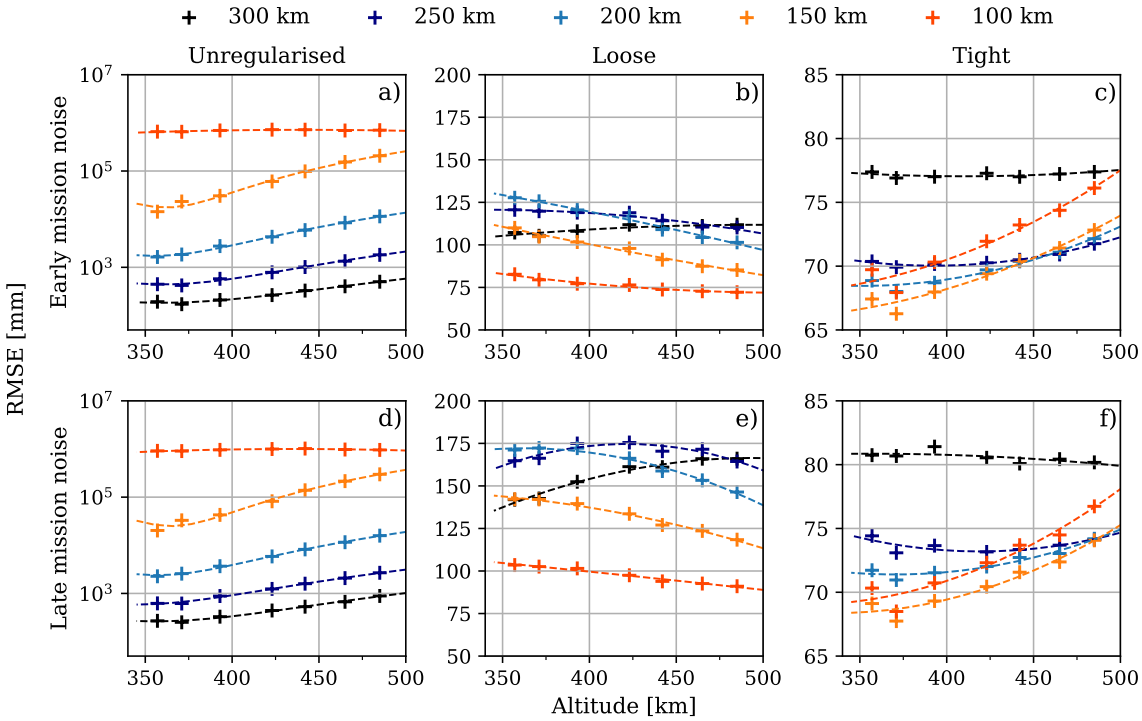

Figure 6.7: RMS Error (RMSE), being the difference from the "truth" temporal gravity field and the monthly mascon estimates from simulated observations (Table 6.2) in the presence of early mission noise (a-c) and late mission noise (d-f) using five mascon resolutions (Table 6.1). (a,d) Unregularised, (b,e) loosely regularised and (c,f) tightly regularised. Lines of best fit (quadratic) are shown as visual aids.

limited by the intra-mascon variability when the mascon constraints are strengthened (Figure 6.7c,f). Under tight regularisation, the 300 km mascons consistently contain the highest errors which are almost entirely (i.e. 85-90%) explained by the intra-mascon variability. The range of errors between the 250 km, 200 km, 150 km and 100 km mascon solutions are mostly small (Figure 6.7c,f). However, at low altitudes, when the simulated observations contain late mission noise, the accuracy of the solutions benefits significantly from the use of high-resolution (i.e. small) mascons. At high altitudes, for either noise level, the 150 km, 200 km and 250 km mascons all perform at a similar level.

Using tight regularisation, the 100 km solutions produce significantly attenuated solutions at all altitudes, causing increased RMS errors (red; Figure 6.7c,f). In any of the cases tested here, the possible gains that could be made by estimating 100 km mascons are outweighed by the difficulty in designing a regularisation scheme that adequately mitigates noise while minimising signal attenuation. Further, we find that the computational cost of estimating >50,000 mascon parameters is far too high to justify any possible benefits ($\sim$60 hours vs $\sim$240 hours for a month of observations using 150 km and 100 km mascons, respectively).

6.5.2 Repeat orbits and mascon resolution

To identify the impact of resonant obits we performed several simulations using the five different mascon grids as the basis functions and assessed the accuracy of temporal gravity field estimation under repeat and complete ground track conditions. We selected two months of observations that were obtained as the satellites passed through repeat orbits and compared the results from the SVD and temporal gravity field estimation to those obtained during months characterised by dense ground track coverage at similar altitude (Figure 6.8; Table 6.2). For the repeat orbits, we selected the months that were impacted by the most critical repeat orbits but not impacted by missing Level-1 data (Figure 6.1), being the September 2004 61/4 repeat and the February 2015 31/2 repeat (Figure 6.8).

During September 2004, the GRACE satellites orbited the Earth at $\sim$475 km average altitude, passing through a 61/4 repeat cycle. The GRACE satellites repeated the same ground track pattern from 61 orbital revolutions every 4 days, producing large ground track gaps at mid-latitudes, reaching a distance of 5.5° at ±30 latitude ($\sim$530 km) (Figure 6.8a). Ground track coverage for this month is 73% on our 200 km mascon field (Figure 6.8c). The most significant orbit resonance of the GRACE mission was encountered during

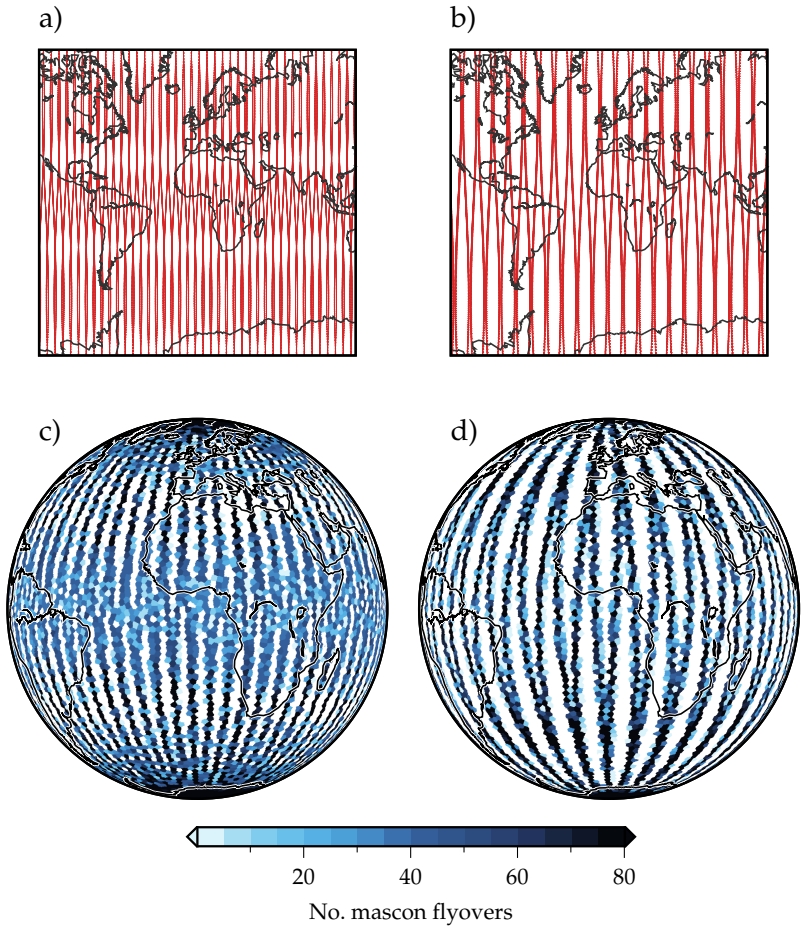

Figure 6.8: GRACE satellite resonant orbits months (a) resulting in a 61/4 repeat ground track in September 2004 and (b) 31/2 repeat ground track in February 2015. Number of times each 200 km $\times$ 200 km primary mascon was overflown by the satellites during (c) September 2004 and (d) February 2015, showing increased flyovers at high latitudes and large gaps at mid- to low-latitudes.

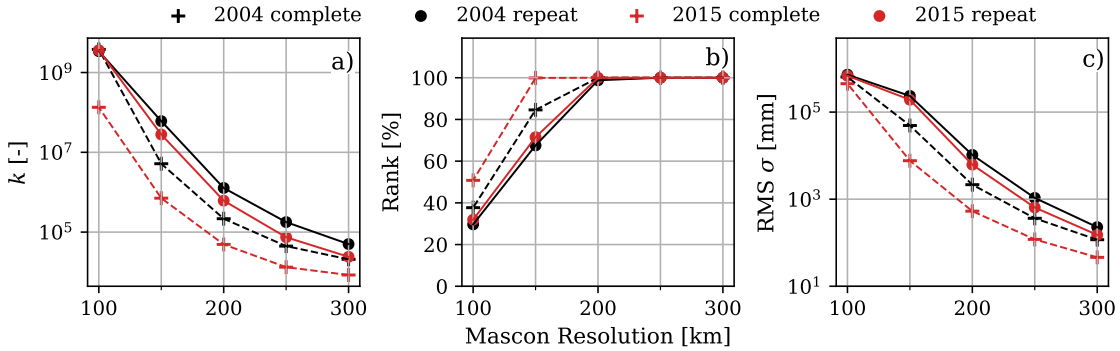

Figure 6.9: Analysis of monthly stacked unregularised weighted normal equations from repeat (solid line, circles) and complete (dashed, crosses) orbits (Table 6.2) using five mascon resolutions (Table 6.1) (a) condition number, k, of the weighted normal equations (b) rank as the percentage of linearly dependent columns of the weighted normal equations (c) RMS of the unregularised mascon parameter uncertainties, σ.

February 2015, when the satellites were orbiting at ∼400 km average altitude. The 31/2 repeat, with almost half the unique ground tracks of the 61/4 repeat, resulted in 7° gaps between ground tracks at ±20 latitude (∼730 km) (Figure 6.8b). Ground track coverage for this month is 58% on our 200 km mascon field (Figure 6.8d). In our analysis, we compared each of these repeat months to nearby months characterised by complete (i.e. 100%) ground track coverage at similar altitudes (Table 6.2).

The condition numbers and mascon parameter uncertainties of each of the repeat months are predictably higher than complete months at similar altitude (cf. dashed and solid line of the same colour; Figure 6.9a,c). As expected, the repeat months are lower rank compared to their altitude-equivalent complete ground track months using 150 km and 100 km mascons (Figure 6.9b). Perhaps less obvious is the behaviour of the repeat months compared to each other (cf. red and black solid lines; Figure 6.9). The condition number of the 2015 repeat solutions is roughly half that of the 2004 repeat solutions (with the exception of the 100 km mascon solutions) despite having almost half the number of unique ground tracks. The lower condition number for the 31/2 repeat orbit is due to the increased stability of the linear system provided by the 75 km lower orbit altitude in February 2015 compared to September 2004 (see Figs. 6.1, 6.9a). The increased numerical stability provided by the decreased orbit altitude is also reflected in the slightly improved mascon parameter uncertainties for February 2015 compared to September 2004 (Figure 6.9c). However, the improvement in condition number and mascon parameter uncertainties appears to decrease with increasingly smaller mascons. The February 2015 normal equations are also slightly less rank deficient for the smaller (i.e. 150 km and 100 km)

mascon solutions compared to the September 2004 normal equations (Figure 6.9b).

The unregularised solutions of the temporal gravity field derived from the repeat ground tracks produced poor results with increasingly higher errors as the mascon size was decreased and the noise level on the simulated observations was increased. When loose or tight regularisation was applied to the mascons, the resonant months produced solutions with only slightly increased errors compared to months with more complete ground tracks at an equivalent altitude, regardless of the mascon resolution (Figure 6.10). The September 2004 (i.e. $R/D = 61/4$) solutions were consistently outperformed by the February 2015 (i.e. $R/D = 31/2$) solutions, regardless of regularisation strength or observation noise level (Figure 6.10b,e). In fact, when using 150 km mascons, the February 2015 repeat orbit better observed the temporal gravity field than the non-repeat February 2004 orbit, which is characterised by complete ground track coverage (Figure 6.10a,e). This shows that the altitude of the satellites has a greater impact on the recovery of the "truth" temporal gravity field than does the density of the ground track coverage.

The impact of repeat ground tracks on the recovery of the gravity field is well studied in terms of spherical harmonic coefficients (Wagner et al., 2006; Klokočník et al., 2008; Pini, 2012; Visser et al., 2012; Klokočník et al., 2015). Each of these studies has shown that, during conditions of orbit resonance, a threshold is reached beyond which the high-frequency spatial variations of the gravity field are under-sampled, reducing the accuracy of the estimates beyond a particular spherical harmonic degree. Previous studies have suggested that, under repeat conditions, R is twice as large as the maximum resolvable spherical harmonic degree (i.e. $L_{MAX} = \frac{R}{2}$) (Wagner et al., 2006). More recent work has shown that this conclusion is too conservative and in most circumstances $L_{MAX} < R$ is appropriately observed (Pini, 2012; Visser et al., 2012). This would suggest that, using the least conservative estimate, the September 2004 and February 2015 ground tracks are only capable of producing accurate estimates up to spherical harmonic degree 60 and 30, respectively. This is equivalent to mascon resolutions of 3° (∼330 km) and 6° (∼660 km) for September 2004 and February 2015, respectively. Our results show that, not only is a 150 km mascon solution possible under the conditions of orbit resonance, but that the most significant repeat orbit throughout the GRACE mission, being the February 2015 31/2 repeat at 400 km, produces a better estimate of the temporal gravity field than a complete ground track at higher orbit altitudes.

We find that regularisation improves the solutions during repeat conditions remarkably

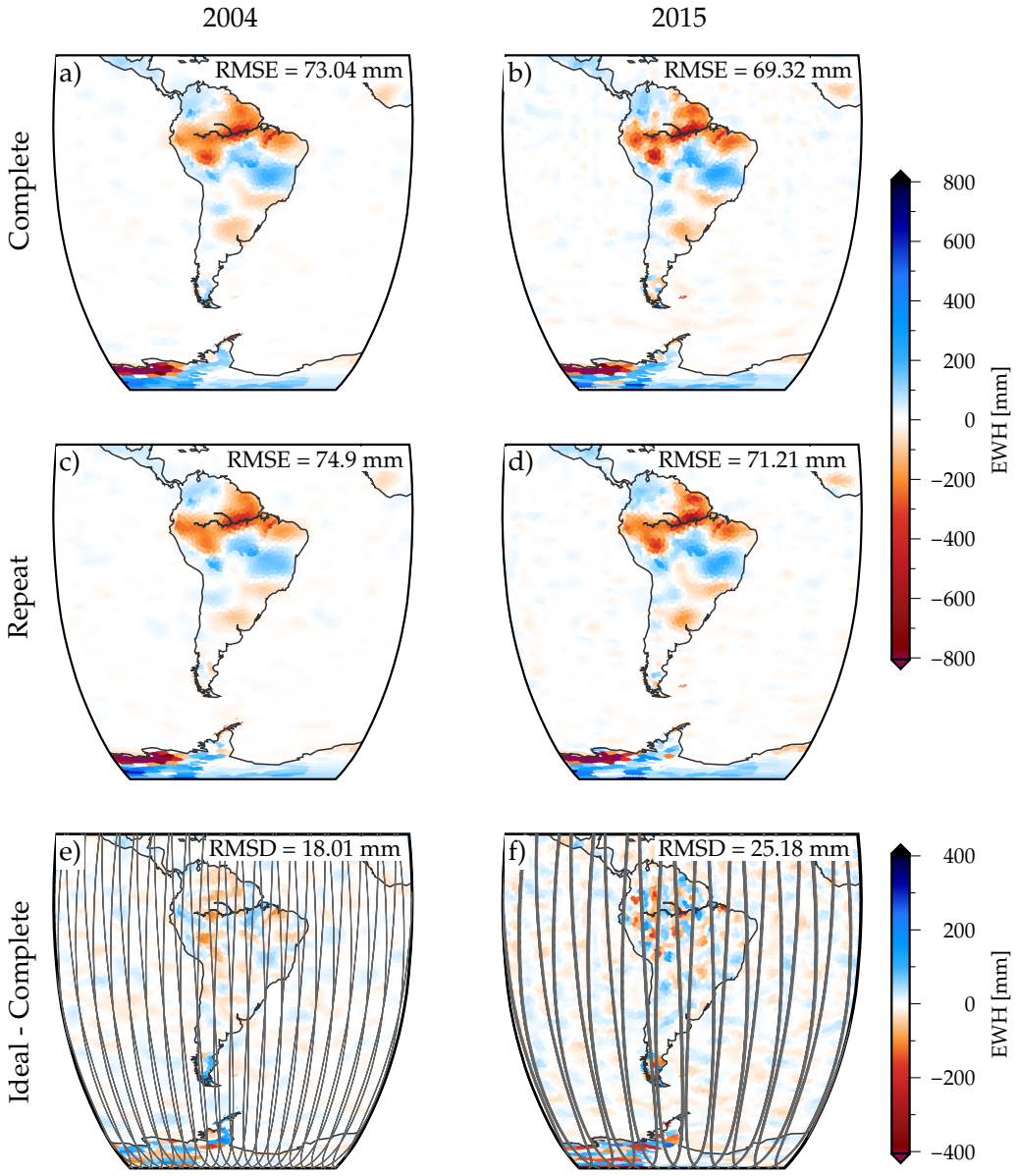

Figure 6.10: Tightly regularised 150 km mascon solutions of the temporal gravity field using simulated observations in the presence of late mission noise. Complete ground track months (a) February 2004 at ∼475 km altitude and (b) April 2015 at ∼400 km altitude compared to (c) September 2004 61/4 repeat and (d) February 2015 31/2 repeat including the RMS error (RMSE) of each solution. Difference between the complete and repeat mascon adjustments for (e) 2004 and (f) 2015, including the RMS of the difference (RMSD) and the repeat month ground track pattern (grey).

(Figure 6.10), to the point that orbit altitude has more impact than reduced ground tracks during orbit resonance on accurate recovery of the temporal gravity field. Save et al. (2012) recognised that regularisation and a priori constraints can be used to improve the temporal gravity field estimates using spherical harmonics. They used a tailored regularisation strategy for their spherical harmonic solutions to account for reduced ground track coverage during repeat orbit conditions.

Our results suggest that, when using mascons, a specifically tailored regularisation approach or extra a priori information is not necessary to produce an accurate solution of the temporal gravity field from observations obtained during orbit resonance. This has also been seen in GRACE time series of the RMS of ocean signal, where spherical harmonic solutions contained increased ocean variability during resonant orbits but ocean variability in mascon solutions remained low at that time (see Figure 2 of Landerer et al., 2020).

6.6 Conclusions

The ability to estimate accurate temporal gravity fields from space gravity data depends upon a number of factors, many of which are intricately linked and which vary with time throughout the GRACE mission. The numerical stability of the normal equation matrices to be inverted varies as a function of altitude of the satellites and the spatial resolution of the gravity field being estimated. The condition number of the matrices provides a nice proxy for identifying whether analysis choices will lead to stable solutions. We found from simulations using noise-free observations that using large, unregularised mass concentration elements (mascons) leads to the most accurate estimates of a known temporal gravity field signal.

However, GRACE and GRACE-FO models of the temporal gravity field must be regularised to mitigate the impact of instrumental noise and background model errors on accurate estimation of mascon parameters. Because temporal gravity field signals vary over smaller length scales than the mascons (i.e. intra-mascon variability), the solutions using large mascons no longer produce the most accurate estimates when regularisation is introduced. Trade-offs then need to be considered between the size of the mascons used to estimate the temporal gravity field, the altitude of the satellites making the measurements and the regularisation strategies chosen when making the analysis.

Under the conditions of orbit resonance, the estimated temporal gravity field is less

accurate compared to solutions estimated from observations obtained during nominal orbit conditions at a similar altitude. Perhaps surprisingly, the accuracy of the estimates from low-altitude repeat orbits are comparable to estimates of the temporal gravity field from observations obtained at higher altitudes, when the satellites were less sensitive to high-frequency mass variations. This result is at odds with those obtained from studies on the impact of orbit resonance on spherical harmonic solutions of the temporal gravity field. Such studies have not accounted for altitude variations and consistently concluded that the accuracy of the estimate is significantly degraded at degrees higher than the number of orbital revolutions during a repeat period. In contrast, we found that good solutions can be obtained from even a 31/2 resonant orbit.

The interplay between mascon size, orbit altitude, ground track coverage, observation noise, regularisation and intra-mascon variability is complex. Simply assessing the numerical stability of the normal equations is not an appropriate proxy for determining the quality of GRACE mascon solutions of the temporal gravity field. Under realistic simulation conditions, using the ANU GRACE processing strategy and irregular-shaped coastline following mascons, we find that using $\sim$150 km mascons produced accurate estimates throughout the entire GRACE record. Naturally, the results are most accurate when the observations are obtained at low altitudes during non-repeat orbit conditions.

Chapter 7

Summary and outlook

The ability to accurately estimate the temporal gravity field from space gravity data depends upon several factors, many of which are intricately linked and vary with time throughout the GRACE mission. In this study, I investigated the impact of thermally-induced errors and the interplay between orbital characteristics, mascon size and regularisation on the accuracy of temporal gravity field solutions using GRACE data. It was primarily motivated by improving GRACE-based estimates of the time-variable gravity field for accurately analysing the redistribution of water masses across and within Earth's surface and sub-surface. This was achieved by mitigating GRACE measurement errors and optimising the processing strategies. In this chapter, I present a summary of the conclusions made throughout this study and make suggestions for future research.

7.1 Conclusions

7.1.1 Thermally-induced accelerometer noise

Thermally-induced bias drift in the accelerometer observations is present throughout the GRACE mission and degrades the quality of mass change estimates from GRACE data. Drift-affected accelerometer measurements occurred during periods of thermal control as the orbits approached high $|\beta'|$ angles, causing the satellites to absorb increased solar energy. They also occurred during short-lived periods of intermittent accelerometer heater disconnections and with increased frequency and duration once thermal control of the satellites was permanently disabled. In Chapter 3, I assessed the temporal and spectral characteristics of thermally-induced bias drift. I developed a method to remove the long-wavelength bias changes in the along-track and cross-track accelerations prior to orbit integration without attenuating the real non-gravitational signals. I showed that the inclusion of drift-affected non-gravitational accelerations in orbit integration with minimal accelerometer parameterisation introduced significant north-south stripe errors in the

temporal gravity field estimates.

In Chapter 3, I developed a method to remove thermally-induced low-frequency bias drift from the accelerometer measurements by filtering the cross-track accelerometer observations. The cross-track bias drift is then scaled and applied as a correction to the along-track measurements. By removing (or significantly mitigating) the long-wavelength along-track and cross-track accelerometer thermal errors, the resulting temporal gravity field solutions showed significant improvements in the mass change estimates. Unrealistic north-south striping was significantly reduced and scale factor estimates on all three axes stabilised. By removing bias drift from the along-track and cross-track accelerations prior to orbit integration, minimal accelerometer parameterisation could be maintained, thus limiting the possibility for parameter trade-offs or the attenuation of the gravity field. This work was published in McGirr et al. (2022).

In Chapter 5, I showed that the application of the along-track and cross-track accelerometer thermal correction method, integrated into the ANU GRACE software, improved the temporal gravity field significantly during the second half of the GRACE mission. This was reflected in the reduction of postfit residuals given a year of temporal gravity field solutions after thermal control had been disabled.

7.1.2 Mascons and inter-satellite observations

Traditionally, GRACE mass change estimates have been generated using range rate as the inter-satellite observation and spherical harmonics to represent the temporal gravity field. The choice of inter-satellite observation, temporal gravity field parameterisation and regularisation strategy can improve the recovery of the gravity field. In Chapters 4 and 5, I demonstrated how the use of mascons can reduce signal leakage, especially between ice sheets and neighbouring oceans, and how using range acceleration as the inter-satellite observation can reduce unrealistic north-south striping.

I quantified the impact of different mascon geometries, spatial resolution and regularisation on recovering a high-resolution synthetic temporal gravity field through simulation. In Chapter 4, I showed that the use of coastline-following $\sim$200 $\times$ 200 km irregularly-shaped mascons were best able to reduce the impacts of "intra-mascon variability", including the leakage of land signals into ocean regions. Using July 2016 GRACE data, the mass loss integrated across Greenland was $\sim$5% greater when the preferred coastline-following mascons were used to parameterise the gravity field. This work was published in

Tregoning et al. (2022). The preferred mascon field was then used to generate the ANU GRACE mass anomaly time series presented in Chapter 5.

Elevated levels of high-frequency noise are contained in the GRACE range acceleration inter-satellite observations, precluding the possible benefits of estimating the temporal gravity field from more localised mass change observations. In Chapter 5, I showed that using a combination of a noise-robust derivative filter and a low-pass filter on the prefit range rate residuals creates prefit range acceleration residuals with significantly reduced high-frequency noise without attenuating the gravity field signal. My contributions meant that a simple parameterisation could be maintained. This work was published in Allgeyer et al. (2022).

The use of regularised coastline-following mascons to represent the temporal gravity field and filtered range acceleration residuals as the inter-satellite observation localised the spatial fluctuations in mass change and reduced the occurrence of unrealistic north-south stripes. The resulting time series of mass anomalies from the iterated mascon solutions were compared to other mascon estimates, matching well the mass loss signals in Antarctica and Greenland, ocean mass increase contribution to global sea level rise and seasonal signals in the Caspian Sea and Amazon Basin.

7.1.3 Altitude and ground track coverage

Temporal gravity field models derived from GRACE data are typically produced with $\sim$300 $\times$ 300 km spatial resolutions and monthly temporal resolution. However, variations in altitude and instrument performance throughout the GRACE mission impacted the accuracy that could be achieved each month. In Chapter 6, the ability of the observations to recover the temporal gravity field accurately was shown to vary as the altitude of the orbits of the twin spacecraft changed throughout the mission. This was achieved through simulation with realistic observation noise and parameterising the gravity field with a range of irregularly-shaped mascons of different sizes.

The numerical stability of the normal equation matrices is unaffected by the quality of the observations or the observed mass anomalies. It was found that the numerical stability of the solutions varied predictably, increasing with decreased orbit altitude, increased ground track coverage and increased mascon size. However, because temporal gravity field signals vary within the mascons (i.e. intra-mascon variability), the solutions using the largest mascons produced the least accurate estimates once the solutions were

regularised. The mascons must be regularised to improve the misappropriation of signals, reduce estimation errors and prevent instrument noise from entering the mascon estimates.

In Chapter 6, I showed that, under simulation conditions with realistic noise on the observations using the ANU GRACE processing strategy and irregular-shaped coastline following mascons, ∼150 × 150 km mascons produced the most accurate estimates throughout the GRACE record. The smallest mascons (i.e. ∼100 × 100 km) were too numerically unstable and became significantly attenuated once the mascons were constrained. Using ∼150 × 150 km mascons, I found that reasonable solutions could also be obtained during resonant orbit conditions. In fact, data obtained in repeat orbit conditions at low-altitude were better able to recover the mass anomaly signal than high-altitude observations with complete ground track coverage.

7.2 Future work

The accelerometer thermal correction method developed in Chapter 3 was tested only on GRACE data where both satellites' accelerometer observations were available. Thus, the process for mitigating thermally-induced bias drifts is not advised for use in GRACE-FO data analysis or on GRACE accelerometer transplant data. Therefore, future work is needed to tailor this method to pre-process the non-gravitational observations during GRACE and GRACE-FO single-accelerometer months. Such work could improve the accuracy of the temporal gravity field estimates, especially during the last seven months of the GRACE mission, once the GRACE-B accelerometer operations had ceased.

In chapter 6, I showed that numerical stability of the mascon solutions increased with denser ground track coverage. Because ground track density increases towards the poles, the numerical stability of the mascon solutions is highest over large ice-covered regions. There is sufficient flexibility to create a mascon field with different-sized mascons, which allows for a high-resolution polar solution to be produced. This might involve creating a mascon field using ∼100 × 100 km mascons in ice-covered regions and larger mascons elsewhere to generate a new spatially high-resolution time series of Antarctic and Greenland mass balance.

The treatment of mass anomalies in the ANU GRACE software allows for the gravitational effects of mass redistribution, both at depth and at the Earth's surface, to be represented simultaneously. Therefore, future work may involve generating a time series of surface mass balance change and GIA solved simultaneously. This would require

the execution of two steps: first, the construction of spatially overlapping surface and sub-surface mascons and second, the development of specific spatial and temporal regularisation constraints for mascons that will exhibit mass change caused by GIA. Of particular importance is the ability to generate accurate mass change estimates towards the end of the GRACE mission, when the altitude of the satellites was lower and the gravity field's effects were less attenuated. Therefore, the work completed in this study will contribute to the success of this future work, including the improvement of the gravity field estimates by mitigating instrument noise and identifying the mascon parameterisation that produces the most accurate temporal gravity field.

With confirmation that the GRACE-FO laser ranging interferometer measures with significantly increased accuracy the inter-satellite range compared to the microwave system, the use of range acceleration observations will further improve the recovery of the temporal gravity field. NASA recognised mass change as one of five "designated observables" essential to their overall program in their decadal survey. Extending the record of Earth's water masses has been identified as a scientific priority; therefore, the time series of mass change is likely to be continued with the launch of future space gravity missions. Spatial and temporal resolution of mass anomaly models are likely to improve with increased inter-satellite measurement accuracy, instrument performance and improved mission design.

Bibliography

Abich, K., Abramovici, A., Amparan, B., Baatzsch, A., Okihiro, B. B., Barr, D. C., Bize, M. P., Bogan, C., Braxmaier, C., Burke, M. J., et al. (2019). In-orbit performance of the GRACE Follow-On laser ranging interferometer. *Physical Review Letters*, 123(3):031101.

Allgeyer, S., Tregoning, P., McQueen, H., McClusky, S., Potter, E.-K., Pfeffer, J., McGirr, R., Purcell, A., Herring, T., and Montillet, J.-P. (2022). ANU GRACE data analysis: Orbit modeling, regularization and inter-satellite range acceleration observations. *Journal of Geophysical Research: Solid Earth*, 127(2):e2021JB022489.

Arendt, A., Luthcke, S., Gardner, A., O'neel, S., Hill, D., Moholdt, G., and Abdalati, W. (2013). Analysis of a GRACE global mascon solution for Gulf of Alaska glaciers. *Journal of Glaciology*, 59(217):913–924.

Arendt, A. A., Echelmeyer, K. A., Harrison, W. D., Lingle, C. S., and Valentine, V. B. (2002). Rapid wastage of Alaska glaciers and their contribution to rising sea level. *Science*, 297(5580):382–386.

Argus, D. F., Fu, Y., and Landerer, F. W. (2014a). Seasonal variation in total water storage in California inferred from GPS observations of vertical land motion. *Geophysical Research Letters*, 41(6):1971–1980.

Argus, D. F., Peltier, W., Drummond, R., and Moore, A. W. (2014b). The Antarctica component of postglacial rebound model ICE-6G_C (VM5a) based on GPS positioning, exposure age dating of ice thicknesses, and relative sea level histories. *Geophysical Journal International*, 198(1):537–563.

Bandikova, T. and Flury, J. (2014). Improvement of the GRACE star camera data based on the revision of the combination method. *Advances in Space Research*, 54(9):1818–1827.

Bandikova, T., Flury, J., and Ko, U.-D. (2012). Characteristics and accuracies of the GRACE inter-satellite pointing. *Advances in Space Research*, 50(1):123–135.

Bandikova, T., McCullough, C., Kruizinga, G. L., Save, H., and Christophe, B. (2019). GRACE accelerometer data transplant. *Advances in Space Research*, 64(3):623–644.

Barichivich, J., Gloor, E., Peylin, P., Brienen, R. J., Schöngart, J., Espinoza, J. C., and Pattnayak, K. C. (2018). Recent intensification of Amazon flooding extremes driven by strengthened Walker circulation. *Science Advances*, 4(9):eaat8785.

Bashforth, F. and Adams, J. C. (1883). *An attempt to test the theories of capillary action by comparing the theoretical and measured forms of drops of fluid*. University Press.

Bedford, J. R., Moreno, M., Deng, Z., Oncken, O., Schurr, B., John, T., Báez, J. C., and Bevis, M. (2020). Months-long thousand-kilometre-scale wobbling before great subduction earthquakes. *Nature*, 580(7805):628–635.

Behzadpour, S., Mayer-Gürr, T., Flury, J., Klinger, B., and Goswami, S. (2019). Multiresolution wavelet analysis applied to GRACE range-rate residuals. *Geoscientific Instrumentation, Methods and Data Systems*, 8(2):197–207.

Behzadpour, S., Mayer-Gürr, T., and Krauss, S. (2021). GRACE Follow-On Accelerometer Data Recovery. *Journal of Geophysical Research: Solid Earth*, 126(5):e2020JB021297.

Bergmann, I. and Dobslaw, H. (2012). Short-term transport variability of the Antarctic Circumpolar Current from satellite gravity observations. *Journal of Geophysical Research: Oceans*, 117(C5).

Bettadpur, S. (2009). Recommendation for a-priori bias & scale parameters for Level-1B ACC data (Version 2), GRACE TN-02. Technical report, Center for Space Research, The University of Texas at Austin.

Bettadpur, S. (2012). Level-2 Gravity Field Product User Handbook (Rev. 3.0, May 29, 2012), GRACE. Technical report, Center for Space Research, The University of Texas at Austin.

Beutler, G., Jäggi, A., Mervart, L., and Meyer, U. (2010). The celestial mechanics approach: theoretical foundations. *Journal of Geodesy*, 84(10):605–624.

Blackman, R. B. and Tukey, J. W. (1958). The measurement of power spectra from the point of view of communications engineering—Part I. *Bell System Technical Journal*, 37(1):185–282.

Boening, C., Lebsock, M., Landerer, F., and Stephens, G. (2012a). Snowfall-driven mass change on the East Antarctic ice sheet. *Geophysical Research Letters*, 39(21).

Boening, C., Willis, J. K., Landerer, F. W., Nerem, R. S., and Fasullo, J. (2012b). The 2011 La Niña: So strong, the oceans fell. *Geophysical Research Letters*, 39(19).

Boergens, E., Güntner, A., Dobslaw, H., and Dahle, C. (2020). Quantifying the Central European droughts in 2018 and 2019 with GRACE Follow-On. *Geophysical Research Letters*, 47(14):e2020GL087285.

Bradley, P. S., Bennett, K. P., and Demiriz, A. (2000). Constrained k-means clustering. *Microsoft Research, Redmond*, 20(0):0.

Bruinsma, S., Lemoine, J.-M., Biancale, R., and Valès, N. (2010). CNES/GRGS 10-day gravity field models (release 2) and their evaluation. *Advances in Space Research*, 45(4):587–601.

Bruinsma, S. L., Förste, C., Abrikosov, O., Marty, J.-C., Rio, M.-H., Mulet, S., and Bonvalot, S. (2013). The new ESA satellite-only gravity field model via the direct approach. *Geophysical Research Letters*, 40(14):3607–3612.

Carrere, L., Lyard, F., Cancet, M., and Guillot, A. (2015). FES2014, a new tidal model on the global ocean with enhanced accuracy in shallow seas and in the Arctic region. In *EGU general assembly conference abstracts*, volume 17.

Case, K., Kruizinga, G., and Wu, S.-C. (2010). GRACE Level-1B data product user handbook. Technical report, Jet Propulsion Laboratory, California Institute of Technology.

Cazenave, A., Meyssignac, B., Ablain, M., Balmaseda, M., Bamber, J., Barletta, V., Beckley, B., Benveniste, J., Berthier, E., Blazquez, A., et al. (2018). Global sea-level budget 1993-present. *Earth System Science Data*, 10(3):1551–1590.

Chambers, D. and Bonin, J. (2012). Evaluation of Release-05 GRACE time-variable gravity coefficients over the ocean. *Ocean Science*, 8(5):859–868.

Chambers, D. P. (2006a). Evaluation of new GRACE time-variable gravity data over the ocean. *Geophysical Research Letters*, 33(17).

Chambers, D. P. (2006b). Observing seasonal steric sea level variations with GRACE and satellite altimetry. *Journal of Geophysical Research: Oceans*, 111(C3).

Chambers, D. P., Cazenave, A., Champollion, N., Dieng, H., Llovel, W., Forsberg, R., von Schuckmann, K., and Wada, Y. (2017). Evaluation of the global mean sea level budget between 1993 and 2014. In Cazenave, A., Champollion, N., Paul, F., and Benveniste, J., editors, *Integrative Study of the Mean Sea Level and Its Components*, pages 315–336. Springer.

Chambers, D. P., Mehlhaff, C. A., Urban, T. J., Fujii, D., and Nerem, R. S. (2002). Low-frequency variations in global mean sea level: 1950–2000. *Journal of Geophysical Research: Oceans*, 107(C4):1–1.

Chambers, D. P., Wahr, J., and Nerem, R. S. (2004). Preliminary observations of global ocean mass variations with GRACE. *Geophysical Research Letters*, 31(13).

Chambers, D. P., Wahr, J., Tamisiea, M. E., and Nerem, R. S. (2010). Ocean mass from GRACE and glacial isostatic adjustment. *Journal of Geophysical Research: Solid Earth*, 115(B11).

Chao, B. F., O'Connor, W. P., Chang, A. T., Hall, D. K., and Foster, J. L. (1987). Snow load effect on the earth's rotation and gravitational field, 1979–1985. *Journal of Geophysical Research: Solid Earth*, 92(B9):9415–9422.

Chen, J., Cazenave, A., Dahle, C., Llovel, W., Panet, I., Pfeffer, J., and Moreira, L. (2022). Applications and challenges of GRACE and GRACE Follow-On satellite gravimetry. *Surveys in Geophysics*, pages 1–41.

Chen, J., Wilson, C., Blankenship, D., and Tapley, B. (2006). Antarctic mass rates from GRACE. *Geophysical Research Letters*, 33(11).

Chen, J., Wilson, C., Blankenship, D., and Tapley, B. (2009a). Accelerated Antarctic ice loss from satellite gravity measurements. *Nature Geoscience*, 2(12):859–862.

Chen, J., Wilson, C., Li, J., and Zhang, Z. (2015). Reducing leakage error in GRACE-observed long-term ice mass change: a case study in West Antarctica. *Journal of Geodesy*, 89(9):925–940.

Chen, J., Wilson, C., Tapley, B., Blankenship, D., and Ivins, E. (2007). Patagonia icefield melting observed by gravity recovery and climate experiment (GRACE). *Geophysical Research Letters*, 34(22).

Chen, J., Wilson, C., Tapley, B., Save, H., and Cretaux, J.-F. (2017). Long-term and seasonal Caspian Sea level change from satellite gravity and altimeter measurements. *Journal of Geophysical Research: solid earth*, 122(3):2274–2290.

Chen, J., Wilson, C., Tapley, B., Yang, Z., and Niu, G.-Y. (2009b). 2005 drought event in the Amazon River basin as measured by GRACE and estimated by climate models. *Journal of Geophysical Research: Solid Earth*, 114(B5).

Chen, J. L., Wilson, C. R., and Tapley, B. D. (2010a). The 2009 exceptional Amazon flood and interannual terrestrial water storage change observed by GRACE. *Water Resources Research*, 46(12).

Chen, J. L., Wilson, C. R., and Tapley, B. D. (2010b). The 2009 exceptional Amazon flood and interannual terrestrial water storage change observed by GRACE. *Water Resources Research*, 46(12).

Chen, Q., Shen, Y., Kusche, J., Chen, W., Chen, T., and Zhang, X. (2021). High-Resolution GRACE Monthly Spherical Harmonic Solutions. *Journal of Geophysical Research: Solid Earth*, 126(1):e2019JB018892.

Cheng, M. and Ries, J. (2017). The unexpected signal in GRACE estimates of C_{20}. *Journal of Geodesy*, 91(8):897–914.

Church, J. A., Clark, P. U., Cazenave, A., Gregory, J. M., Jevrejeva, S., Levermann, A., Merrifield, M. A., Milne, G. A., Nerem, R. S., Nunn, P. D., et al. (2013). Sea level change. In Stocker, T. F., Qin, D., Plattner, G.-K., et al., editors, *Climate change 2013: The physical science basis. Contribution of Working Group I to the Fifth Assessment Report of the Intergovernmental Panel on Climate Change*, pages 1137—-1216. Cambridge University Press, Cambridge; New York.

Ciracì, E., Velicogna, I., and Swenson, S. (2020). Continuity of the mass loss of the world's glaciers and ice caps from the GRACE and GRACE Follow-On missions. *Geophysical Research Letters*, 47(9):e2019GL086926.

Cogley, J. G. (2009). Geodetic and direct mass-balance measurements: Comparison and joint analysis. *Annals of Glaciology*, 50(50):96–100.

Croteau, M., Nerem, R., Loomis, B., and Sabaka, T. (2020). Development of a daily

GRACE mascon solution for terrestrial water storage. *Journal of Geophysical Research: Solid Earth*, 125(3):e2019JB018468.

Croteau, M., Sabaka, T., and Loomis, B. (2021). GRACE fast mascons from spherical harmonics and a regularization design trade study. *Journal of Geophysical Research: Solid Earth*, 126(8):e2021JB022113.

Dahle, C., Flechtner, F., Gruber, C., König, D., König, R., Michalak, G., and Neumayer, K.-H. (2014). GFZ RL05: an improved time-series of monthly GRACE gravity field solutions. In *Observation of the System Earth from Space-CHAMP, GRACE, GOCE and future missions*, pages 29–39. Springer.

Dahle, C., Murböck, M., Flechtner, F., Dobslaw, H., Michalak, G., Neumayer, K. H., Abrykosov, O., Reinhold, A., König, R., Sulzbach, R., et al. (2019). The GFZ GRACE RL06 monthly gravity field time series: Processing details and quality assessment. *Remote Sensing*, 11(18):2116.

De Boor, C. (2001). *A practical guide to splines*. Springer, Berlin, Heidelberg, New York, revised edition.

De Linage, C., Rivera, L., Hinderer, J., Boy, J.-P., Rogister, Y., Lambotte, S., and Biancale, R. (2009). Separation of coseismic and postseismic gravity changes for the 2004 Sumatra–Andaman earthquake from 4.6 yr of GRACE observations and modelling of the coseismic change by normal-modes summation. *Geophysical Journal International*, 176(3):695–714.

Desai, S. D. (2002). Observing the pole tide with satellite altimetry. *Journal of Geophysical Research: Oceans*, 107(C11):7–1.

Ditmar, P., Da Encarnação, J. T., and Farahani, H. H. (2012). Understanding data noise in gravity field recovery on the basis of inter-satellite ranging measurements acquired by the satellite gravimetry mission GRACE. *Journal of Geodesy*, 86(6):441–465.

Dobslaw, H., Bergmann-Wolf, I., Dill, R., Forootan, E., Klemann, V., Kusche, J., and Sasgen, I. (2015). The updated ESA Earth System Model for future gravity mission simulation studies. *Journal of Geodesy*, 89(5):505–513.

Dobslaw, H., Bergmann-Wolf, I., Dill, R., Poropat, L., and Flechtner, F. (2017a). Prod-

uct description document for AOD1B release 06. *GFZ German Research Centre for Geosciences Department*, 1.

Dobslaw, H., Bergmann-Wolf, I., Dill, R., Poropat, L., Thomas, M., Dahle, C., Esselborn, S., König, R., and Flechtner, F. (2017b). A new high-resolution model of non-tidal atmosphere and ocean mass variability for de-aliasing of satellite gravity observations: AOD1B RL06. *Geophysical Journal International*, 211(1):263–269.

Dobslaw, H., Flechtner, F., Bergmann-Wolf, I., Dahle, C., Dill, R., Esselborn, S., Sasgen, I., and Thomas, M. (2013). Simulating high-frequency atmosphere-ocean mass variability for dealiasing of satellite gravity observations: AOD1B RL05. *Journal of Geophysical Research: Oceans*, 118(7):3704–3711.

Döll, P., Mueller Schmied, H., Schuh, C., Portmann, F. T., and Eicker, A. (2014). Global-scale assessment of groundwater depletion and related groundwater abstractions: Combining hydrological modeling with information from well observations and GRACE satellites. *Water Resources Research*, 50(7):5698–5720.

Domingues, C. M., Church, J. A., White, N. J., Gleckler, P. J., Wijffels, S. E., Barker, P. M., and Dunn, J. R. (2008). Improved estimates of upper-ocean warming and multi-decadal sea-level rise. *Nature*, 453(7198):1090–1093.

Dunn, C., Bertiger, W., Bar-Sever, Y., Desai, S., Haines, B., Kuang, D., Franklin, G., Harris, I., Kruizinga, G., and Meehan, T. (2003). Instrument of GRACE GPS augments gravity measurements. *GPS World*, 14(2):16–29.

Famiglietti, J. S. (2014). The global groundwater crisis. *Nature Climate Change*, 4(11):945–948.

Famiglietti, J. S., Lo, M., Ho, S. L., Bethune, J., Anderson, K., Syed, T. H., Swenson, S. C., de Linage, C. R., and Rodell, M. (2011). Satellites measure recent rates of groundwater depletion in California's Central Valley. *Geophysical Research Letters*, 38(3).

Faunt, C. C., Sneed, M., Traum, J., and Brandt, J. T. (2016). Water availability and land subsidence in the Central Valley, California, USA. *Hydrogeology Journal*, 24(3):675–684.

Feng, W., Zhong, M., Lemoine, J.-M., Biancale, R., Hsu, H.-T., and Xia, J. (2013). Evaluation of groundwater depletion in North China using the Gravity Recovery and

Climate Experiment (GRACE) data and ground-based measurements. *Water Resources Research*, 49(4):2110–2118.

Fettweis, X., Franco, B., Tedesco, M., Van Angelen, J., Lenaerts, J. T., van den Broeke, M. R., and Gallée, H. (2013). Estimating the Greenland ice sheet surface mass balance contribution to future sea level rise using the regional atmospheric climate model MAR. *The Cryosphere*, 7(2):469–489.

Flechtner, F. (2007). AOD1B product description document for product releases 01 to 04 (Rev. 3.1, April 13, 2007). *GRACE project document*, pages 327–750.

Flechtner, F., Bettadpur, S., Watkins, M., and Kruizinga, G. (2009). GRACE Science Data System Monthly Report April. Technical report, Jet Propulsion Laboratory, California Institute of Technology.

Flechtner, F., Neumayer, K.-H., Dahle, C., Dobslaw, H., Fagiolini, E., Raimondo, J.-C., and Güntner, A. (2016). What can be expected from the GRACE-FO laser ranging interferometer for earth science applications? *Surveys in Geophysics*, 37(2):453–470.

Flury, J., Bettadpur, S., and Tapley, B. D. (2008). Precise accelerometry onboard the GRACE gravity field satellite mission. *Advances in Space Research*, 42(8):1414–1423.

Folkner, W. M., Williams, J. G., and Boggs, D. H. (2009). The planetary and lunar ephemeris DE 421. *IPN progress report*, 42(178):1–34.

Förste, C., Bruinsma, S., Abrikosov, O., Lemoine, J., Schaller, T., Götze, H., and Balmino, G. (2014). Eigen-6c4. *The latest combined global gravity field model including GOCE data up to degree and order*, 2190.

Fretwell, P., Pritchard, H. D., Vaughan, D. G., Bamber, J. L., Barrand, N. E., Bell, R., Bianchi, C., Bingham, R., Blankenship, D. D., Casassa, G., et al. (2013). Bedmap2: improved ice bed, surface and thickness datasets for Antarctica. *The Cryosphere*, 7(1):375–393.

Frommknecht, B., Oberndorfer, H., Flechtner, F., and Schmidt, R. (2003). Integrated sensor analysis for GRACE–development and validation. *Advances in Geosciences*, 1:57–63.

Fulcher, R. C. (2016). *Temperature fluctuation analysis for GRACE twin satellites*. PhD thesis, The University of Texas at Austin.

Gardner, A. S., Moholdt, G., Cogley, J. G., Wouters, B., Arendt, A. A., Wahr, J., Berthier, E., Hock, R., Pfeffer, W. T., Kaser, G., et al. (2013). A reconciled estimate of glacier contributions to sea level rise: 2003 to 2009. *science*, 340(6134):852–857.

Gardner, A. S., Moholdt, G., Wouters, B., Wolken, G. J., Burgess, D. O., Sharp, M. J., Cogley, J. G., Braun, C., and Labine, C. (2011). Sharply increased mass loss from glaciers and ice caps in the Canadian Arctic Archipelago. *Nature*, 473(7347):357–360.

Ghobadi-Far, K., Han, S.-C., Allgeyer, S., Tregoning, P., Sauber, J., Behzadpour, S., Mayer-Gürr, T., Sneeuw, N., and Okal, E. (2020a). GRACE gravitational measurements of tsunamis after the 2004, 2010, and 2011 great earthquakes. *Journal of Geodesy*, 94(7):1–9.

Ghobadi-Far, K., Han, S.-C., McCullough, C. M., Wiese, D. N., Ray, R. D., Sauber, J., Shihora, L., and Dobslaw, H. (2022). Along-orbit analysis of GRACE Follow-On inter-satellite laser ranging measurements for sub-monthly surface mass variations. *Journal of Geophysical Research: Solid Earth*, 127(2):e2021JB022983.

Ghobadi-Far, K., Han, S.-C., McCullough, C. M., Wiese, D. N., Yuan, D.-N., Landerer, F. W., Sauber, J., and Watkins, M. M. (2020b). GRACE Follow-On laser ranging interferometer measurements uniquely distinguish short-wavelength gravitational perturbations. *Geophysical Research Letters*, 47(16):e2020GL089445.

Ghobadi-Far, K., Han, S.-C., Sauber, J., Lemoine, F., Behzadpour, S., Mayer-Gürr, T., Sneeuw, N., and Okal, E. (2019a). Gravitational changes of the Earth's free oscillation from earthquakes: Theory and feasibility study using GRACE inter-satellite tracking. *Journal of Geophysical Research: Solid Earth*, 124(7):7483–7503.

Ghobadi-Far, K., Han, S.-C., Weller, S., Loomis, B. D., Luthcke, S. B., Mayer-Gürr, T., and Behzadpour, S. (2018). A transfer function between line-of-sight gravity difference and GRACE intersatellite ranging data and an application to hydrological surface mass variation. *Journal of Geophysical Research: Solid Earth*, 123(10):9186–9201.

Ghobadi-Far, K., Šprlák, M., and Han, S.-C. (2019b). Determination of ellipsoidal surface mass change from GRACE time-variable gravity data. *Geophysical Journal International*, 219(1):248–259.

Goswami, S., Devaraju, B., Weigelt, M., and Mayer-Gürr, T. (2018). Analysis of GRACE

range-rate residuals with focus on KBR instrument system noise. *Advances in Space Research*, 62(2):304–316.

Gunter, B., Urban, T., Riva, R., Helsen, M., Harpold, R., Poole, S., Nagel, P., Schutz, B., and Tapley, B. (2009). A comparison of coincident GRACE and ICESat data over Antarctica. *Journal of Geodesy*, 83(11):1051–1060.

Haacker, E. M., Kendall, A. D., and Hyndman, D. W. (2016). Water level declines in the High Plains Aquifer: Predevelopment to resource senescence. *Groundwater*, 54(2):231–242.

Han, S.-C. (2017). Elastic deformation of the Australian continent induced by seasonal water cycles and the 2010–2011 La Niña determined using GPS and GRACE. *Geophysical Research Letters*, 44(6):2763–2772.

Han, S.-C., Jekeli, C., and Shum, C. (2004). Time-variable aliasing effects of ocean tides, atmosphere, and continental water mass on monthly mean GRACE gravity field. *Journal of Geophysical Research: Solid Earth*, 109(B4).

Han, S.-C., Riva, R., Sauber, J., and Okal, E. (2013). Source parameter inversion for recent great earthquakes from a decade-long observation of global gravity fields. *Journal of Geophysical Research: Solid Earth*, 118(3):1240–1267.

Han, S.-C., Sauber, J., and Luthcke, S. (2010). Regional gravity decrease after the 2010 Maule (Chile) earthquake indicates large-scale mass redistribution. *Geophysical Research Letters*, 37(23).

Han, S.-C., Sauber, J., and Pollitz, F. (2015). Coseismic compression/dilatation and viscoelastic uplift/subsidence following the 2012 Indian Ocean earthquakes quantified from satellite gravity observations. *Geophysical Research Letters*, 42(10):3764–3772.

Han, S.-C., Sauber, J. M., Broerse, T., Riva, R., Pollitz, F. F., and Okal, E. (2019). Development of earthquake correction models for GRACE and GRACE Follow-On gravity data time series. In *AGU Fall Meeting Abstracts*, volume 2019, pages G44A–07.

Han, S.-C., Shum, C.-K., Bevis, M., Ji, C., and Kuo, C.-Y. (2006). Crustal dilatation observed by GRACE after the 2004 Sumatra-Andaman earthquake. *Science*, 313(5787):658–662.

Han, S.-C., Yeo, I.-Y., Khaki, M., McCullough, C. M., Lee, E., and Sauber, J. (2021). Novel along-track processing of GRACE Follow-On laser ranging measurements found abrupt water storage increase and land subsidence during the 2021 March Australian flooding. *Earth and Space Science*, 8(11):e2021EA001941.

Hanna, E., Fettweis, X., Mernild, S. H., Cappelen, J., Ribergaard, M. H., Shuman, C. A., Steffen, K., Wood, L., and Mote, T. L. (2014). Atmospheric and oceanic climate forcing of the exceptional Greenland ice sheet surface melt in summer 2012. *International Journal of Climatology*, 34(4):1022–1037.

Harvey, N. (2016). GRACE star camera noise. *Advances in Space Research*, 58(3):408–414.

Harvey, N., Dunn, C. E., Kruizinga, G. L., and Young, L. E. (2017). Triggering conditions for GRACE ranging measurement signal-to-noise ratio dips. *Journal of Spacecraft and Rockets*, 54(1):327–330.

Harvey, N., McCullough, C. M., and Save, H. (2021). Modeling GRACE-FO accelerometer data for the version 04 release. *Advances in Space Research*.

Heki, K. and Matsuo, K. (2010). Coseismic gravity changes of the 2010 earthquake in central Chile from satellite gravimetry. *Geophysical Research Letters*, 37(24).

Herman, J., Davis, A., Chin, K. B., Kinzler, M., Scholz, S., and Steinhoff, M. (2012). Life with a weak heart: prolonging the GRACE mission despite degraded batteries. In *12th International Conference on Space Operations*, Stockholm, Sweden.

Herman, J., Presti, D., Codazzi, A., and Belle, C. (2004). Attitude control for GRACE. In *18th International Symposium on Space Flight Dynamics (ESA SP-548)*, page 27, Munich, Germany.

Hosseini, M. S. and Plataniotis, K. N. (2017). Derivative kernels: Numerics and applications. *IEEE Transactions on Image Processing*, 26(10):4596–4611.

Houborg, R., Rodell, M., Li, B., Reichle, R., and Zaitchik, B. F. (2012). Drought indicators based on model-assimilated Gravity Recovery and Climate Experiment (GRACE) terrestrial water storage observations. *Water Resources Research*, 48(7).

Inácio, P., Ditmar, P., Klees, R., and Farahani, H. H. (2015). Analysis of star camera errors in GRACE data and their impact on monthly gravity field models. *Journal of Geodesy*, 89(6):551–571.

Ivins, E. R. and James, T. S. (2005). Antarctic glacial isostatic adjustment: a new assessment. *Antarctic Science*, 17(4):541.

Ivins, E. R., James, T. S., Wahr, J., O. Schrama, E. J., Landerer, F. W., and Simon, K. M. (2013). Antarctic contribution to sea level rise observed by GRACE with improved GIA correction. *Journal of Geophysical Research: Solid Earth*, 118(6):3126–3141.

Ivins, E. R., Watkins, M. M., Yuan, D.-N., Dietrich, R., Casassa, G., and Rülke, A. (2011). On-land ice loss and glacial isostatic adjustment at the Drake Passage: 2003–2009. *Journal of Geophysical Research: Solid Earth*, 116(B2).

Jacob, T., Wahr, J., Pfeffer, W. T., and Swenson, S. (2012). Recent contributions of glaciers and ice caps to sea level rise. *Nature*, 482(7386):514–518.

Jekeli, C. (1981). Alternative methods to smooth the earth's gravity field. *Unknown*.

Johnson, G. C. and Chambers, D. P. (2013). Ocean bottom pressure seasonal cycles and decadal trends from GRACE Release-05: Ocean circulation implications. *Journal of Geophysical Research: Oceans*, 118(9):4228–4240.

Kaula, W. M. (1971). Dynamical aspects of lunar origin. *Reviews of Geophysics*, 9(2):217–238.

Kim, J. (2000). *Simulation study of a low-low satellite-to-satellite tracking mission*. PhD thesis, The University of Texas at Austin.

Kim, J. and Tapley, B. D. (2002). Error analysis of a low-low satellite-to-satellite tracking mission. *Journal of Guidance, Control, and Dynamics*, 25(6):1100–1106.

King, M., Moore, P., Clarke, P., and Lavallée, D. (2006). Choice of optimal averaging radii for temporal GRACE gravity solutions, a comparison with GPS and satellite altimetry. *Geophysical Journal International*, 166(1):1–11.

Kjeldsen, K. K., Korsgaard, N. J., Bjørk, A. A., Khan, S. A., Box, J. E., Funder, S., Larsen, N. K., Bamber, J. L., Colgan, W., Van Den Broeke, M., et al. (2015). Spatial and temporal distribution of mass loss from the Greenland Ice Sheet since AD 1900. *Nature*, 528(7582):396–400.

Klema, V. and Laub, A. (1980). The singular value decomposition: Its computation and some applications. *IEEE Transactions on automatic control*, 25(2):164–176.

Klinger, B. and Mayer-Gürr, T. (2016). The role of accelerometer data calibration within GRACE gravity field recovery: Results from ITSG-Grace2016. *Advances in Space Research*, 58(9):1597–1609.

Klokočník, J., Wagner, C., Kostelecký, J., Bezděk, A., Novák, P., and McAdoo, D. (2008). Variations in the accuracy of gravity recovery due to ground track variability: GRACE, CHAMP, and GOCE. *Journal of Geodesy*, 82(12):917–927.

Klokočník, J., Wagner, C. A., Kostelecký, J., and Bezděk, A. (2015). Ground track density considerations on the resolvability of gravity field harmonics in a repeat orbit. *Advances in Space Research*, 56(6):1146–1160.

Ko, U. D. (2008). *Analysis of the characteristics of grace dual one-way ranging system.* PhD thesis, The University of Texas at Austin.

Ko, U.-D., Tapley, B. D., Ries, J. C., and Bettadpur, S. V. (2012). High-frequency noise in the gravity recovery and climate experiment intersatellite ranging system. *Journal of Spacecraft and Rockets*, 49(6):1163–1173.

Kovács, P. (2015). Minimum-cost flow algorithms: an experimental evaluation. *Optimization Methods and Software*, 30(1):94–127.

Krabill, W. e., Hanna, E., Huybrechts, P., Abdalati, W., Cappelen, J., Csatho, B., Frederick, E., Manizade, S., Martin, C., Sonntag, J., et al. (2004). Greenland ice sheet: increased coastal thinning. *Geophysical Research Letters*, 31(24).

Krogh, F. T. (1973). On testing a subroutine for the numerical integration of ordinary differential equations. *Journal of the ACM (JACM)*, 20(4):545–562.

Kumar, S. V., Zaitchik, B. F., Peters-Lidard, C. D., Rodell, M., Reichle, R., Li, B., Jasinski, M., Mocko, D., Getirana, A., De Lannoy, G., et al. (2016). Assimilation of gridded GRACE terrestrial water storage estimates in the North American Land Data Assimilation System. *Journal of Hydrometeorology*, 17(7):1951–1972.

Kusche, J. (2007). Approximate decorrelation and non-isotropic smoothing of time-variable GRACE-type gravity field models. *Journal of Geodesy*, 81(11):733–749.

Kusche, J., Schmidt, R., Petrovic, S., and Rietbroek, R. (2009). Decorrelated GRACE time-variable gravity solutions by GFZ, and their validation using a hydrological model. *Journal of Geodesy*, 83(10):903–913.

Kvas, A., Behzadpour, S., Ellmer, M., Klinger, B., Strasser, S., Zehentner, N., and Mayer-Gürr, T. (2019). ITSG-Grace2018: Overview and evaluation of a new GRACE-only gravity field time series. *Journal of Geophysical Research: Solid Earth*, 124(8):9332–9344.

Lambeck, K., Rouby, H., Purcell, A., Sun, Y., and Sambridge, M. (2014). Sea level and global ice volumes from the Last Glacial Maximum to the Holocene. *Proceedings of the National Academy of Sciences*, 111(43):15296–15303.

Landerer, F. W., Flechtner, F. M., Save, H., Webb, F. H., Bandikova, T., Bertiger, W. I., Bettadpur, S. V., Byun, S. H., Dahle, C., Dobslaw, H., et al. (2020). Extending the global mass change data record: GRACE Follow-On instrument and science data performance. *Geophysical Research Letters*, 47(12):e2020GL088306.

Landerer, F. W. and Swenson, S. (2012). Accuracy of scaled grace terrestrial water storage estimates. *Water resources research*, 48(4).

Landerer, F. W., Wiese, D. N., Bentel, K., Boening, C., and Watkins, M. M. (2015). North Atlantic meridional overturning circulation variations from GRACE ocean bottom pressure anomalies. *Geophysical Research Letters*, 42(19):8114–8121.

Leblanc, M. J., Tregoning, P., Ramillien, G., Tweed, S. O., and Fakes, A. (2009). Basin-scale, integrated observations of the early 21st century multiyear drought in southeast Australia. *Water Resources Research*, 45(4).

Lemoine, J.-M., Bourgogne, S., Biancale, R., and Bruinsma, S. (2018). RL04 monthly gravity field solutions from CNES/GRGS. In *The GRACE Science Team Meeting*, Potsdam, Germany.

Lemoine, J.-M., Bruinsma, S., Loyer, S., Biancale, R., Marty, J.-C., Perosanz, F., and Balmino, G. (2007). Temporal gravity field models inferred from GRACE data. *Advances in Space Research*, 39(10):1620–1629.

Lenaerts, J. T., van Angelen, J. H., van den Broeke, M. R., Gardner, A. S., Wouters, B., and van Meijgaard, E. (2013). Irreversible mass loss of Canadian Arctic Archipelago glaciers. *Geophysical Research Letters*, 40(5):870–874.

Liu, X., Ditmar, P., Siemes, C., Slobbe, D., Revtova, E., Klees, R., Riva, R., and Zhao,

Q. (2010). DEOS Mass Transport model (DMT-1) based on GRACE satellite data: methodology and validation. *Geophysical Journal International*, 181(2):769–788.

Llovel, W., K, W. J., F, L., and I, F. (2014). Deep-ocean contribution to sea level and energy budget not detectable over the past decade. *Nature Climate Change*, 4:1031–1035.

Llovel, W., Purkey, S., Meyssignac, B., Blazquez, A., Kolodziejczyk, N., and Bamber, J. (2019). Global ocean freshening, ocean mass increase and global mean sea level rise over 2005–2015. *Scientific Reports*, 9(1):1–10.

Lo, M.-H., Famiglietti, J. S., Yeh, P.-F., and Syed, T. (2010). Improving parameter estimation and water table depth simulation in a land surface model using GRACE water storage and estimated base flow data. *Water Resources Research*, 46(5).

Lombard, A., Garcia, D., Ramillien, G., Cazenave, A., Biancale, R., Lemoine, J., Flechtner, F., Schmidt, R., and Ishii, M. (2007). Estimation of steric sea level variations from combined GRACE and Jason-1 data. *Earth and Planetary Science Letters*, 254(1-2):194–202.

Long, D., Chen, X., Scanlon, B. R., Wada, Y., Hong, Y., Singh, V. P., Chen, Y., Wang, C., Han, Z., and Yang, W. (2016). Have GRACE satellites overestimated groundwater depletion in the Northwest India Aquifer? *Scientific Reports*, 6(1):1–11.

Long, D., Scanlon, B. R., Longuevergne, L., Sun, A. Y., Fernando, D. N., and Save, H. (2013). GRACE satellite monitoring of large depletion in water storage in response to the 2011 drought in Texas. *Geophysical Research Letters*, 40(13):3395–3401.

Long, D., Shen, Y., Sun, A., Hong, Y., Longuevergne, L., Yang, Y., Li, B., and Chen, L. (2014). Drought and flood monitoring for a large karst plateau in Southwest China using extended GRACE data. *Remote Sensing of Environment*, 155:145–160.

Loomis, B., Luthcke, S., and Sabaka, T. (2019a). Regularization and error characterization of GRACE mascons. *Journal of Geodesy*, 93(9):1381–1398.

Loomis, B., Nerem, R., and Luthcke, S. B. (2012). Simulation study of a follow-on gravity mission to GRACE. *Journal of Geodesy*, 86(5):319–335.

Loomis, B. D., Felikson, D., Sabaka, T. J., and Medley, B. (2021). High-spatial-resolution mass rates from GRACE and GRACE-FO: Global and ice sheet analyses. *Journal of Geophysical Research: Solid Earth*, 126(12):e2021JB023024.

Loomis, B. D., Rachlin, K. E., and Luthcke, S. B. (2019b). Improved earth oblateness rate reveals increased ice sheet losses and mass-driven sea level rise. *Geophysical Research Letters*, 46(12):6910–6917.

Loomis, B. D., Rachlin, K. E., Wiese, D. N., Landerer, F. W., and Luthcke, S. B. (2020). Replacing GRACE/GRACE-FO with satellite laser ranging: Impacts on Antarctic ice sheet mass change. *Geophysical Research Letters*, 47(3):e2019GL085488.

Luthcke, S. B., Arendt, A. A., Rowlands, D. D., McCarthy, J. J., and Larsen, C. F. (2008). Recent glacier mass changes in the Gulf of Alaska region from GRACE mascon solutions. *Journal of Glaciology*, 54(188):767–777.

Luthcke, S. B., Rowlands, D. D., Lemoine, F. G., Klosko, S. M., Chinn, D., and McCarthy, J. J. (2006a). Monthly spherical harmonic gravity field solutions determined from GRACE inter-satellite range-rate data alone. *Geophysical Research Letters*, 33(2).

Luthcke, S. B., Sabaka, T. J., Loomis, B., Arendt, A. A., McCarthy, J. J., and Camp, J. (2013). Antarctica, Greenland and Gulf of Alaska land-ice evolution from an iterated GRACE global mascon solution. *Journal of Glaciology*, 59(216):613–631.

Luthcke, S. B., Zwally, H. J., Abdalati, W., Rowlands, D., Ray, R., Nerem, R., Lemoine, F., McCarthy, J., and Chinn, D. (2006b). Recent Greenland ice mass loss by drainage system from satellite gravity observations. *Science*, 314(5803):1286–1289.

Lyard, F., Lefevre, F., Letellier, T., and Francis, O. (2006). Modelling the global ocean tides: modern insights from FES2004. *Ocean Dynamics*, 56:394–415.

Lyard, F. H., Allain, D. J., Cancet, M., Carrère, L., and Picot, N. (2021). FES2014 global ocean tide atlas: design and performance. *Ocean Science*, 17(3):615–649.

Lyman, J. M., Willis, J. K., and Johnson, G. C. (2006). Recent cooling of the upper ocean. *Geophysical Research Letters*, 33(18).

MacGregor, J. A., Colgan, W. T., Fahnestock, M. A., Morlighem, M., Catania, G. A., Paden, J. D., and Gogineni, S. P. (2016). Holocene deceleration of the Greenland ice sheet. *Science*, 351(6273):590–593.

Martín-Español, A., Zammit-Mangion, A., Clarke, P. J., Flament, T., Helm, V., King, M. A., Luthcke, S. B., Petrie, E., Rémy, F., Schön, N., et al. (2016). Spatial and temporal Antarctic Ice Sheet mass trends, glacio-isostatic adjustment, and surface processes from a joint inversion of satellite altimeter, gravity, and GPS data. *Journal of Geophysical Research: Earth Surface*, 121(2):182–200.

Mayer-Gürr, T., Behzadpour, S., Ellmer, M., Klinger, B., Kvas, A., and Zehentner, N. (2016). ITSG-Grace2016-monthly and daily gravity field solutions from GRACE [Data set]. *GFZ Data Services*.

Mayer-Gürr, T., Zehentner, N., Klinger, B., and Kvas, A. (2014). ITSG-GRACE2014. In *GRACE Science Team Meeting*, Potsdam, Germany.

McCarthy, D. D. (1992). IERS Standards (1992). Technical report, Bureau International des Poids et Mesures Sevres (France).

McCullough, C. M., Harvey, N., Save, H., and Bandikova, T. (2019). Description of calibrated GRACE-FO accelerometer data products (ACT). *Level-1 Product Version*, 4.

McGirr, R., Tregoning, P., Allgeyer, S., McQueen, H., and Purcell, A. (2022). Mitigation of thermal noise in GRACE accelerometer observations. *Advances in Space Research*, 69(1):386–401.

Medley, B., McConnell, J. R., Neumann, T., Reijmer, C., Chellman, N., Sigl, M., and Kipfstuhl, S. (2018). Temperature and snowfall in western Queen Maud Land increasing faster than climate model projections. *Geophysical Research Letters*, 45(3):1472–1480.

Menemenlis, D., Campin, J.-M., Heimbach, P., Hill, C., Lee, T., Nguyen, A., Schodlok, M., and Zhang, H. (2008). ECCO2: High resolution global ocean and sea ice data synthesis. *Mercator Ocean Quarterly Newsletter*, 31(October):13–21.

Meyer, U., Jäggi, A., and Beutler, G. (2012). The impact of attitude control on GRACE accelerometry and orbits. In *Geodesy for Planet Earth*, volume 136, pages 139–146. Springer, Berlin, Heidelberg.

Morelli, A. and Danesi, S. (2004). Seismological imaging of the Antarctic continental lithosphere: a review. *Global and Planetary Change*, 42(1-4):155–165.

Moulton, F. R. (1926). *New methods in exterior ballistics*. University Chicago Press.

Muller, P. M. and Sjogren, W. L. (1968). Mascons: Lunar mass concentrations. *Science*, 161(3842):680–684.

National Academies of Sciences, Engineering, and Medicine (2018). *Thriving on our changing planet: A decadal strategy for Earth observation from space*. National Academies Press, Washington, DC.

Nerem, R. S., Beckley, B. D., Fasullo, J. T., Hamlington, B. D., Masters, D., and Mitchum, G. T. (2018). Climate-change–driven accelerated sea-level rise detected in the altimeter era. *Proceedings of the national academy of sciences*, 115(9):2022–2025.

Padman, L., Fricker, H. A., Coleman, R., Howard, S., and Erofeeva, L. (2002). A new tide model for the Antarctic ice shelves and seas. *Annals of Glaciology*, 34:247–254.

Panet, I., Bonvalot, S., Narteau, C., Remy, D., and Lemoine, J.-M. (2018). Migrating pattern of deformation prior to the Tohoku-Oki earthquake revealed by GRACE data. *Nature Geoscience*, 11(5):367–373.

Panet, I., Mikhailov, V., Diament, M., Pollitz, F., King, G., De Viron, O., Holschneider, M., Biancale, R., and Lemoine, J.-M. (2007). Coseismic and post-seismic signatures of the Sumatra 2004 December and 2005 March earthquakes in GRACE satellite gravity. *Geophysical Journal International*, 171(1):177–190.

Pavlis, N. K., Holmes, S. A., Kenyon, S. C., and Factor, J. K. (2012). The development and evaluation of the Earth Gravitational Model 2008 (EGM2008). *Journal of geophysical research: solid earth*, 117(B4).

Peidou, A., Landerer, F., Wiese, D., Ellmer, M., Fahnestock, E., and Yuan, D.-N. (2021). Assessment of GRACE-FO Laser Ranging Interferometer measurements. In *EGU General Assembly Conference Abstracts*, pages EGU21–1249.

Peltier, R. (1982). Dynamics of the ice age Earth. *Advances in Geophysics*, 24:1–146.

Peltier, W. R., Argus, D., and Drummond, R. (2015). Space geodesy constrains ice age terminal deglaciation: The global ICE-6G_C (VM5a) model. *Journal of Geophysical Research: Solid Earth*, 120(1):450–487.

Peltier, W. R., Argus, D. F., and Drummond, R. (2018). Comment on "An assessment of the ICE-6G_C (VM5a) glacial isostatic adjustment model" by Purcell et al. *Journal of Geophysical Research: Solid Earth*, 123(2):2019–2028.

Peralta-Ferriz, C., Morison, J. H., Wallace, J. M., Bonin, J. A., and Zhang, J. (2014). Arctic Ocean circulation patterns revealed by GRACE. *Journal of Climate*, 27(4):1445–1468.

Peterseim, N. (2014). *TWANGS–High-Frequency Disturbing Signals in the 10 Hz Accelerometer Data of the GRACE Satellites.* PhD thesis, Technische Universität München.

Peterseim, N., Flury, J., and Schlicht, A. (2012). Magnetic torquer induced disturbing signals within GRACE accelerometer data. *Advances in Space Research*, 49(9):1388–1394.

Petit, G. and Luzum, B. (2010). IERS conventions (2010). Technical report, Bureau International des Poids et Mesures Sevres (France).

Pie, N., Bettadpur, S., Tamisiea, M., Krichman, B., Save, H., Poole, S., Nagel, P., Kang, Z., Jacob, G., Ellmer, M., et al. (2021). Time variable earth gravity field models from the first spaceborne laser ranging interferometer. *Journal of Geophysical Research: Solid Earth*, 126(12):e2021JB022392.

Pini, A. J. (2012). Investigation of the effect of repeat orbits on GRACE gravity recovery. Master's thesis, The University of Texas at Austin.

Purcell, A., Tregoning, P., and Dehecq, A. (2016). An assessment of the ICE6G_C (VM5a) glacial isostatic adjustment model. *Journal of Geophysical Research: Solid Earth*, 121(5):3939–3950.

Ramillien, G., Lombard, A., Cazenave, A., Ivins, E., Llubes, M., Remy, F., and Biancale, R. (2006). Interannual variations of the mass balance of the Antarctica and Greenland ice sheets from GRACE. *Global and Planetary Change*, 53(3):198–208.

Ray, R. and Ponte, R. (2003). Barometric tides from ECMWF operational analyses. *Annales Geophysicae*, 21(8):1897–1910.

Reager, J. T., Thomas, B. F., and Famiglietti, J. S. (2014). River basin flood potential inferred using GRACE gravity observations at several months lead time. *Nature Geoscience*, 7(8):588–592.

Ries, J., Bettadpur, S., Poole, S., and Richter, T. (2011). Mean background gravity fields for GRACE processing. In *GRACE Science Team Meeting*, Austin, Texas.

Rignot, E., Bamber, J. L., Van Den Broeke, M. R., Davis, C., Li, Y., Van De Berg, W. J., and Van Meijgaard, E. (2008). Recent Antarctic ice mass loss from radar interferometry and regional climate modelling. *Nature geoscience*, 1(2):106–110.

Rignot, E., Mouginot, J., Scheuchl, B., Van Den Broeke, M., Van Wessem, M. J., and Morlighem, M. (2019). Four decades of Antarctic Ice Sheet mass balance from 1979–2017. *Proceedings of the National Academy of Sciences*, 116(4):1095–1103.

Rignot, E., Velicogna, I., van den Broeke, M. R., Monaghan, A., and Lenaerts, J. T. (2011). Acceleration of the contribution of the Greenland and Antarctic ice sheets to sea level rise. *Geophysical Research Letters*, 38(5).

Riser, S. C., Freeland, H. J., Roemmich, D., Wijffels, S., Troisi, A., Belbéoch, M., Gilbert, D., Xu, J., Pouliquen, S., Thresher, A., et al. (2016). Fifteen years of ocean observations with the global Argo array. *Nature Climate Change*, 6(2):145–153.

Riva, R. E., Gunter, B. C., Urban, T. J., Vermeersen, B. L., Lindenbergh, R. C., Helsen, M. M., Bamber, J. L., van de Wal, R. S., van den Broeke, M. R., and Schutz, B. E. (2009). Glacial isostatic adjustment over antarctica from combined icesat and grace satellite data. *Earth and Planetary Science Letters*, 288(3-4):516–523.

Rodell, M., Chen, J., Kato, H., Famiglietti, J. S., Nigro, J., and Wilson, C. R. (2007). Estimating groundwater storage changes in the Mississippi River basin (USA) using GRACE. *Hydrogeology Journal*, 15(1):159–166.

Rodell, M. and Famiglietti, J. S. (2002). The potential for satellite-based monitoring of groundwater storage changes using GRACE: the High Plains aquifer, Central US. *Journal of Hydrology*, 263(1-4):245–256.

Rodell, M., Famiglietti, J. S., Wiese, D. N., Reager, J., Beaudoing, H. K., Landerer, F. W., and Lo, M.-H. (2018). Emerging trends in global freshwater availability. *Nature*, 557(7707):651–659.

Rodell, M., Houser, P., Jambor, U., Gottschalck, J., Mitchell, K., Meng, C.-J., Arsenault, K., Cosgrove, B., Radakovich, J., Bosilovich, M., et al. (2004). The global land data assimilation system. *Bulletin of the American Meteorological society*, 85(3):381–394.

Rodell, M., Velicogna, I., and Famiglietti, J. S. (2009). Satellite-based estimates of groundwater depletion in India. *Nature*, 460(7258):999–1002.

Romans, L. (2003). Optimal combination of quaternions from multiple star cameras. *JPL Interoffice Memorandum*.

Rosat, S., Sato, T., Imanishi, Y., Hinderer, J., Tamura, Y., McQueen, H., and Ohashi, M. (2005). High-resolution analysis of the gravest seismic normal modes after the 2004 mw= 9 sumatra earthquake using superconducting gravimeter data. *Geophysical Research Letters*, 32(13).

Rowlands, D., Luthcke, S., Klosko, S., Lemoine, F. G., Chinn, D., McCarthy, J., Cox, C., and Anderson, O. (2005). Resolving mass flux at high spatial and temporal resolution using GRACE intersatellite measurements. *Geophysical Research Letters*, 32(4).

Rowlands, D., Luthcke, S., McCarthy, J., Klosko, S., Chinn, D., Lemoine, F., Boy, J.-P., and Sabaka, T. (2010). Global mass flux solutions from GRACE: A comparison of parameter estimation strategies—mass concentrations versus stokes coefficients. *Journal of Geophysical Research: Solid Earth*, 115(B1).

Rowlands, D. D., Ray, R. D., Chinn, D. S., and Lemoine, F. G. (2002). Short-arc analysis of intersatellite tracking data in a gravity mapping mission. *Journal of Geodesy*, 76(6):307–316.

Rummel, R. (1979). Determination of short-wavelength components of the gravity field from satellite-to-satellite tracking or satellite gradiometry. *Manuscripta Geodaetica*, 4(2):107–148.

Sabaka, T., Rowlands, D., Luthcke, S., and Boy, J.-P. (2010). Improving global mass flux solutions from Gravity Recovery and Climate Experiment (GRACE) through forward modeling and continuous time correlation. *Journal of Geophysical Research: Solid Earth*, 115(B11).

Sasgen, I., Dobslaw, H., Martinec, Z., and Thomas, M. (2010). Satellite gravimetry observation of Antarctic snow accumulation related to ENSO. *Earth and Planetary Science Letters*, 299(3-4):352–358.

Sasgen, I., Martinec, Z., and Fleming, K. (2006). Wiener optimal filtering of GRACE data. *Studia Geophysica et Geodaetica*, 50(4):499–508.

Sasgen, I., Wouters, B., Gardner, A. S., King, M. D., Tedesco, M., Landerer, F. W., Dahle, C., Save, H., and Fettweis, X. (2020). Return to rapid ice loss in Greenland and

record loss in 2019 detected by the GRACE-FO satellites. *Communications Earth & Environment*, 1(1):1–8.

Save, H. (2020). CSR GRACE and GRACE-FO RL06 Mascon Solutions v02.

Save, H., Bettadpur, S., and Tapley, B. (2006). Single Accelerometer Gravity Solutions for GRACE. In *AGU Fall Meeting Abstracts*, volume 2006, pages G13A–0026.

Save, H., Bettadpur, S., and Tapley, B. D. (2012). Reducing errors in the GRACE gravity solutions using regularization. *Journal of Geodesy*, 86(9):695–711.

Save, H., Bettadpur, S., and Tapley, B. D. (2016). High-resolution CSR GRACE RL05 mascons. *Journal of Geophysical Research: Solid Earth*, 121(10):7547–7569.

Save, H., Poole, S., Bettadpur, S., and Nagel, P. (2019). GRACE-FO Gravity Solutions Using Variational Methods with Range Acceleration Data. In *AGU Fall Meeting Abstracts*, volume 2019, pages G51B–0587.

Scanlon, B., Zhang, Z., Rateb, A., Sun, A., Wiese, D., Save, H., Beaudoing, H., Lo, M., Müller-Schmied, H., Döll, P., et al. (2019). Tracking seasonal fluctuations in land water storage using global models and GRACE satellites. *Geophysical Research Letters*, 46(10):5254–5264.

Scanlon, B. R., Faunt, C. C., Longuevergne, L., Reedy, R. C., Alley, W. M., McGuire, V. L., and McMahon, P. B. (2012). Groundwater depletion and sustainability of irrigation in the US High Plains and Central Valley. *Proceedings of the National Academy of Sciences*, 109(24):9320–9325.

Scanlon, B. R., Rateb, A., Anyamba, A., Kebede, S., MacDonald, A. M., Shamsudduha, M., Small, J., Sun, A., Taylor, R. G., and Xie, H. (2022). Linkages between GRACE water storage, hydrologic extremes, and climate teleconnections in major African aquifers. *Environmental Research Letters*, 17(1):014046.

Schrama, E. J. and Wouters, B. (2011). Revisiting Greenland ice sheet mass loss observed by GRACE. *Journal of Geophysical Research: Solid Earth*, 116(B2).

Schrama, E. J., Wouters, B., and Rietbroek, R. (2014). A mascon approach to assess ice sheet and glacier mass balances and their uncertainties from GRACE data. *Journal of Geophysical Research: Solid Earth*, 119(7):6048–6066.

Selesnick, I. W. (2002). Maximally flat low-pass digital differentiator. *IEEE Transactions on Circuits and Systems II: Analog and Digital Signal Processing*, 49(3):219–223.

Sheard, B., Heinzel, G., Danzmann, K., Shaddock, D., Klipstein, W., and Folkner, W. (2012). Intersatellite laser ranging instrument for the GRACE Follow-On mission. *Journal of Geodesy*, 86(12):1083–1095.

Shen, Y., Chen, Q., and Xu, H. (2015). Monthly gravity field solution from GRACE range measurements using modified short arc approach. *Geodesy and Geodynamics*, 6(4):261–266.

Shepherd, A., Fricker, H. A., and Farrell, S. L. (2018a). Trends and connections across the Antarctic cryosphere. *Nature*, 558(7709):223–232.

Shepherd, A., Ivins, E., Rignot, E., Smith, B., Van Den Broeke, M., Velicogna, I., Whitehouse, P., Briggs, K., Joughin, I., Krinner, G., et al. (2018b). Mass balance of the Antarctic Ice Sheet from 1992 to 2017. *Nature*, 558:219–222.

Shepherd, A., Ivins, E., Rignot, E., Smith, B., Van Den Broeke, M., Velicogna, I., Whitehouse, P., Briggs, K., Joughin, I., Krinner, G., et al. (2020). Mass balance of the Greenland Ice Sheet from 1992 to 2018. *Nature*, 579(7798):233–239.

Shepherd, A., Ivins, E. R., Barletta, V. R., Bentley, M. J., Bettadpur, S., Briggs, K. H., Bromwich, D. H., Forsberg, R., Galin, N., Horwath, M., et al. (2012). A reconciled estimate of ice-sheet mass balance. *Science*, 338(6111):1183–1189.

Spero, R. (2021). Point-mass sensitivity of gravimetric satellites. *Advances in Space Research*, 67(5):1656–1664.

Strassberg, G., Scanlon, B. R., and Chambers, D. (2009). Evaluation of groundwater storage monitoring with the GRACE satellite: Case study of the High Plains aquifer, central United States. *Water Resources Research*, 45(5).

Sun, Y., Ditmar, P., and Riva, R. (2016a). Observed changes in the Earth's dynamic oblateness from GRACE data and geophysical models. *Journal of Geodesy*, 90(1):81–89.

Sun, Y., Riva, R., and Ditmar, P. (2016b). Optimizing estimates of annual variations and trends in geocenter motion and J2 from a combination of GRACE data and geophysical models. *Journal of Geophysical Research: Solid Earth*, 121(11):8352–8370.

Svoboda, M., LeComte, D., Hayes, M., Heim, R., Gleason, K., Angel, J., Rippey, B., Tinker, R., Palecki, M., Stooksbury, D., et al. (2002). The drought monitor. *Bulletin of the American Meteorological Society*, 83(8):1181–1190.

Swarztrauber, P. N. (1982). Vectorizing the FFTs. In Rodrigue, G., editor, *Parallel Computations*, pages 51–83. Academic Press.

Swenson, S., Chambers, D., and Wahr, J. (2008). Estimating geocenter variations from a combination of GRACE and ocean model output. *Journal of Geophysical Research: Solid Earth*, 113(B8).

Swenson, S. and Wahr, J. (2002). Methods for inferring regional surface-mass anomalies from Gravity Recovery and Climate Experiment (GRACE) measurements of time-variable gravity. *Journal of Geophysical Research: Solid Earth*, 107(B9):ETG–3.

Swenson, S. and Wahr, J. (2006). Post-processing removal of correlated errors in GRACE data. *Geophysical research letters*, 33(8).

Swenson, S. and Wahr, J. (2007). Multi-sensor analysis of water storage variations of the Caspian Sea. *Geophysical Research Letters*, 34(16).

Tamisiea, M., Leuliette, E., Davis, J., and Mitrovica, J. (2005). Constraining hydrological and cryospheric mass flux in southeastern Alaska using space-based gravity measurements. *Geophysical Research Letters*, 32(20).

Tapley, B., Flechtner, F., Watkins, M., and Bettadpur, S. (2015). GRACE mission: status and prospects. In *The GRACE Science Team Meeting*, Austin, Texas.

Tapley, B., Ries, J., Bettadpur, S., Chambers, D., Cheng, M., Condi, F., and Poole, S. (2007). The ggm03 mean earth gravity model from grace. In *AGU Fall Meeting Abstracts*, volume 2007, pages G42A–03.

Tapley, B. D., Bettadpur, S., Watkins, M., and Reigber, C. (2004). The gravity recovery and climate experiment: Mission overview and early results. *Geophysical Research Letters*, 31(9).

Tapley, B. D., Watkins, M. M., Flechtner, F., Reigber, C., Bettadpur, S., Rodell, M., Sasgen, I., Famiglietti, J. S., Landerer, F. W., Chambers, D. P., et al. (2019). Contributions of GRACE to understanding climate change. *Nature climate change*, 9(5):358–369.

Tarantola, A. (2005). *Inverse problem theory and methods for model parameter estimation*. SIAM.

Teixeira da Encarnação, J., Save, H., Tapley, B., and Rim, H.-J. (2020). Accelerometer parameterization and the quality of gravity recovery and climate experiment solutions. *Journal of Spacecraft and Rockets*, 57(4):740–752.

Thomas, A. C., Reager, J. T., Famiglietti, J. S., and Rodell, M. (2014). A GRACE-based water storage deficit approach for hydrological drought characterization. *Geophysical Research Letters*, 41(5):1537–1545.

Thomas, B. F., Famiglietti, J. S., Landerer, F. W., Wiese, D. N., Molotch, N. P., and Argus, D. F. (2017). GRACE groundwater drought index: Evaluation of California Central Valley groundwater drought. *Remote Sensing of Environment*, 198:384–392.

Thomas, J. (1999). An analysis of gravity-field estimation based on intersatellite dual-1-way biased ranging. Technical report, Jet Propulsion Laboratory, California Institute of Technology.

Thomas, R., Frederick, E., Krabill, W., Manizade, S., and Martin, C. (2006). Progressive increase in ice loss from Greenland. *Geophysical Research Letters*, 33(10).

Thompson, P., Bettadpur, S., and Tapley, B. (2004). Impact of short period, non-tidal, temporal mass variability on GRACE gravity estimates. *Geophysical Research Letters*, 31(6).

Tian, S., Tregoning, P., Renzullo, L. J., van Dijk, A. I., Walker, J. P., Pauwels, V. R., and Allgeyer, S. (2017). Improved water balance component estimates through joint assimilation of GRACE water storage and SMOS soil moisture retrievals. *Water Resources Research*, 53(3):1820–1840.

Tian, S., Van Dijk, A. I., Tregoning, P., and Renzullo, L. J. (2019). Forecasting dryland vegetation condition months in advance through satellite data assimilation. *Nature Communications*, 10(1):1–7.

Tiwari, V. M., Wahr, J., and Swenson, S. (2009). Dwindling groundwater resources in northern India, from satellite gravity observations. *Geophysical Research Letters*, 36(18).

Touboul, P., Foulon, B., Rodrigues, M., and Marque, J. P. (2004). In orbit nano-g measurements, lessons for future space missions. *Aerospace Science and Technology*, 8(5):431–441.

Touboul, P., Foulon, B., and Willemenot, E. (1999). Electrostatic space accelerometers for present and future missions. *Acta Astronautica*, 45(10):605–617.

Tregoning, P., Allgeyer, S., McQueen, H., McGirr, R., McClusky, S., Purcell, T., and White, H. (2018). Estimating grace temporal gravity fields using adaptive regularisation. In *The GRACE Science Team Meeting*, Potsdam, Germany.

Tregoning, P., McGirr, R., Pfeffer, J., Purcell, A., McQueen, H., Allgeyer, S., and McClusky, S. (2022). ANU GRACE data analysis: Characteristics and benefits of using irregularly shaped mascons. *Journal of Geophysical Research: Solid Earth*, 127(2):e2021JB022412.

Tregoning, P., Purcell, A. P., Allgeyer, S., McQueen, H., and McClusky, S. (2017). The Role of Range Acceleration Observations and Regularisation in the Estimation of Submonthly Temporal Gravity Fields From GRACE Observations. In *AGU Fall Meeting Abstracts*, volume 2017, pages G31B–0900.

Tregoning, P., Ramillien, G., McQueen, H., and Zwartz, D. (2009a). Glacial isostatic adjustment and nonstationary signals observed by GRACE. *Journal of Geophysical Research: Solid Earth*, 114(B6).

Tregoning, P. and Watson, C. (2009). Atmospheric effects and spurious signals in GPS analyses. *Journal of Geophysical Research: Solid Earth*, 114(B9).

Tregoning, P., Watson, C., Ramillien, G., McQueen, H., and Zhang, J. (2009b). Detecting hydrologic deformation using GRACE and GPS. *Geophysical Research Letters*, 36(15).

Vallado, D. A. (2001). *Fundamentals of astrodynamics and applications*, volume 12. Springer Science & Business Media.

Van Dam, T., Wahr, J., and Lavallée, D. (2007). A comparison of annual vertical crustal displacements from GPS and Gravity Recovery and Climate Experiment (GRACE) over Europe. *Journal of Geophysical Research: Solid Earth*, 112(B3).

Van den Broeke, M., Bamber, J., Ettema, J., Rignot, E., Schrama, E., van de Berg, W. J., van Meijgaard, E., Velicogna, I., and Wouters, B. (2009). Partitioning recent Greenland mass loss. *Science*, 326(5955):984–986.

Van Dijk, A. I., Beck, H. E., Crosbie, R. S., de Jeu, R. A., Liu, Y. Y., Podger, G. M., Timbal, B., and Viney, N. R. (2013). The Millennium Drought in southeast Australia (2001–2009): Natural and human causes and implications for water resources, ecosystems, economy, and society. *Water Resources Research*, 49(2):1040–1057.

Van Dijk, A. I., Renzullo, L. J., Wada, Y., and Tregoning, P. (2014). A global water cycle reanalysis (2003–2012) merging satellite gravimetry and altimetry observations with a hydrological multi-model ensemble. *Hydrology and Earth System Sciences*, 18(8):2955–2973.

Van Wessem, J., Ligtenberg, S., Reijmer, C., Van De Berg, W., Van Den Broeke, M., Barrand, N., Thomas, E., Turner, J., Wuite, J., Scambos, T., et al. (2016). The modelled surface mass balance of the Antarctic Peninsula at 5.5 km horizontal resolution. *The Cryosphere*, 10(1):271–285.

Van Wessem, J., Reijmer, C., Morlighem, M., Mouginot, J., Rignot, E., Medley, B., Joughin, I., Wouters, B., Depoorter, M., Bamber, J., et al. (2014). Improved representation of East Antarctic surface mass balance in a regional atmospheric climate model. *Journal of Glaciology*, 60(222):761–770.

Velicogna, I., Mohajerani, Y., Landerer, F., Mouginot, J., Noel, B., Rignot, E., Sutterley, T., van den Broeke, M., van Wessem, M., and Wiese, D. (2020). Continuity of ice sheet mass loss in Greenland and Antarctica from the GRACE and GRACE Follow-On missions. *Geophysical Research Letters*, 47(8):e2020GL087291.

Velicogna, I., Sutterley, T., and Van Den Broeke, M. (2014). Regional acceleration in ice mass loss from Greenland and Antarctica using GRACE time-variable gravity data. *Geophysical Research Letters*, 41(22):8130–8137.

Velicogna, I. and Wahr, J. (2005). Greenland mass balance from GRACE. *Geophysical Research Letters*, 32(18).

Velicogna, I. and Wahr, J. (2006). Measurements of time-variable gravity show mass loss in Antarctica. *Science*, 311(5768):1754–1756.

Visser, P., Schrama, E., Sneeuw, N., and Weigelt, M. (2012). Dependency of resolvable gravitational spatial resolution on space-borne observation techniques. In Kenyon, S., Pacino, M., and Marti, U., editors, *Geodesy for Planet Earth*, volume 136, pages 373–379. Springer, Berlin, Heidelberg.

Volkov, D. L., Lee, S.-K., Landerer, F. W., and Lumpkin, R. (2017). Decade-long deep-ocean warming detected in the subtropical South Pacific. *Geophysical Research Letters*, 44(2):927–936.

Voss, K. A., Famiglietti, J. S., Lo, M., De Linage, C., Rodell, M., and Swenson, S. C. (2013). Groundwater depletion in the Middle East from GRACE with implications for transboundary water management in the Tigris-Euphrates-Western Iran region. *Water Resources Research*, 49(2):904–914.

Wagner, C., McAdoo, D., Klokočník, J., and Kostelecký, J. (2006). Degradation of geopotential recovery from short repeat-cycle orbits: application to GRACE monthly fields. *Journal of Geodesy*, 80(2):94–103.

Wahr, J., Molenaar, M., and Bryan, F. (1998). Time variability of the Earth's gravity field: Hydrological and oceanic effects and their possible detection using GRACE. *Journal of Geophysical Research: Solid Earth*, 103(B12):30205–30229.

Wahr, J., Nerem, R. S., and Bettadpur, S. V. (2015). The pole tide and its effect on GRACE time-variable gravity measurements: Implications for estimates of surface mass variations. *Journal of Geophysical Research: Solid Earth*, 120(6):4597–4615.

Wahr, J., Swenson, S., and Velicogna, I. (2006). Accuracy of GRACE mass estimates. *Geophysical Research Letters*, 33(6).

Wahr, J., Swenson, S., Zlotnicki, V., and Velicogna, I. (2004). Time-variable gravity from GRACE: First results. *Geophysical Research Letters*, 31(11).

Wahr, J., Wingham, D., and Bentley, C. (2000). A method of combining ICESat and GRACE satellite data to constrain Antarctic mass balance. *Journal of Geophysical Research: Solid Earth*, 105(B7):16279–16294.

Wang, G. and Cai, W. (2020). Two-year consecutive concurrences of positive Indian Ocean Dipole and Central Pacific El Niño preconditioned the 2019/2020 Australian "black summer" bushfires. *Geoscience Letters*, 7(1):1–9.

Wang, L. and Burgmann, R. (2019). Statistical significance of precursory gravity changes before the 2011 Mw 9.0 Tohoku-Oki earthquake. *Geophysical Research Letters*, 46(13):7323–7332.

Watkins, M., Yuan, D., Kuang, D., Bertiger, W., Kim, M., and Kruizinga, G. (2005). GRACE harmonic and mascon solutions at JPL. In *AGU Fall Meeting Abstracts*, volume 2005, pages G22A–04.

Watkins, M. M., Wiese, D. N., Yuan, D.-N., Boening, C., and Landerer, F. W. (2015). Improved methods for observing Earth's time variable mass distribution with GRACE using spherical cap mascons. *Journal of Geophysical Research: Solid Earth*, 120(4):2648–2671.

Watkins, M. M. and Yuan, D.-N. (2012). JPL Level-2 processing standards document for Level-2 product release 05. *Report No. GRACE*, pages 327–744.

Weatherall, P., Marks, K. M., Jakobsson, M., Schmitt, T., Tani, S., Arndt, J. E., Rovere, M., Chayes, D., Ferrini, V., and Wigley, R. (2015). A new digital bathymetric model of the world's oceans. *Earth and Space Science*, 2(8):331–345.

Webb, F., Landerer, F., Watkins, M., Save, H., and Dahle, C. (2018). GRACE Follow-On Science Data System Monthly Report: Oct/Nov. Technical report, Jet Propulsion Laboratory, California Institute of Technology.

Whitehouse, P. L., Bentley, M. J., and Le Brocq, A. M. (2012). A deglacial model for Antarctica: geological constraints and glaciological modelling as a basis for a new model of Antarctic glacial isostatic adjustment. *Quaternary Science Reviews*, 32:1–24.

Wiese, D. N., Landerer, F. W., and Watkins, M. M. (2016). Quantifying and reducing leakage errors in the JPL RL05M GRACE mascon solution. *Water Resources Research*, 52(9):7490–7502.

Wijffels, S. E., Willis, J., Domingues, C. M., Barker, P., White, N. J., Gronell, A., Ridgway, K., and Church, J. A. (2008). Changing expendable bathythermograph fall rates and their impact on estimates of thermosteric sea level rise. *Journal of Climate*, 21(21):5657–5672.

Willis, J. K., Lyman, J. M., Johnson, G. C., and Gilson, J. (2007). Correction to "Recent cooling of the upper ocean". *Geophysical Research Letters*, 34(16).

Willis, J. K., Roemmich, D., and Cornuelle, B. (2004). Interannual variability in upper ocean heat content, temperature, and thermosteric expansion on global scales. *Journal of Geophysical Research: Oceans*, 109(C12).

Willis, M. J., Melkonian, A. K., Pritchard, M. E., and Rivera, A. (2012). Ice loss from the Southern Patagonian ice field, South America, between 2000 and 2012. *Geophysical Research Letters*, 39(17).

Wouters, B., Chambers, D., and Schrama, E. (2008). GRACE observes small-scale mass loss in Greenland. *Geophysical Research Letters*, 35(20).

Wouters, B., Gardner, A. S., and Moholdt, G. (2019). Global glacier mass loss during the GRACE satellite mission (2002-2016). *Frontiers in Earth Science*, 7:96.

Wouters, B. and Schrama, E. J. (2007). Improved accuracy of GRACE gravity solutions through empirical orthogonal function filtering of spherical harmonics. *Geophysical Research Letters*, 34(23).

Wu, S.-C., Kruizinga, G., and Bertiger, W. (2006). Algorithm theoretical basis document for GRACE Level-1B data processing V1.2. Technical report, Jet Propulsion Laboratory, California Institute of Technology.

Yeh, P. J.-F., Swenson, S. C., Famiglietti, J. S., and Rodell, M. (2006). Remote sensing of groundwater storage changes in Illinois using the Gravity Recovery and Climate Experiment (GRACE). *Water Resources Research*, 42(12).

Yirdaw, S. Z., Snelgrove, K. R., and Agboma, C. O. (2008). GRACE satellite observations of terrestrial moisture changes for drought characterization in the Canadian Prairie. *Journal of Hydrology*, 356(1-2):84–92.

Yu, Y., Chao, B. F., García-García, D., and Luo, Z. (2018). Variations of the Argentine Gyre observed in the GRACE time-variable gravity and ocean altimetry measurements. *Journal of Geophysical Research: Oceans*, 123(8):5375–5387.

Zaitchik, B. F., Rodell, M., and Reichle, R. H. (2008). Assimilation of GRACE terrestrial water storage data into a land surface model: Results for the Mississippi River basin. *Journal of Hydrometeorology*, 9(3):535–548.

Zlotnicki, V., Wahr, J., Fukumori, I., and Song, Y. T. (2007). Antarctic Circumpolar Current transport variability during 2003–05 from GRACE. *Journal of Physical Oceanography*, 37(2):230–244.